Glacial Ocean Dynamics: Insight from Deep-Sea Coral Reconstructions and A Time-Dependent Dynamical Box Model

Thesis by

Sophia K.V. Hines

In Partial Fulfillment of the Requirements for the
degree of
Doctor of Philosophy

CALIFORNIA INSTITUTE OF TECHNOLOGY
Pasadena, California

2018
Defended September 5, 2017

Sophia K.V. Hines
ORCID: 0000-0001-9357-6399

This thesis is dedicated to all the badass female scientists in my life.

ACKNOWLEDGEMENTS

My graduate studies have been made possible with the love, support, and encouragement of more people than can be named here, but I would like to take the time to acknowledge several who have been especially important.

First, my advisor Jess Adkins. You have pushed me to dig deeper, helped me see the bigger picture when I have gotten frustrated, and shaped me into the scientist that I am today. When you came to visit Carleton my senior year, I knew that I wanted to come to Caltech and work with you, and it is a decision that I have never regretted.

Andy Thompson, you have become a second advisor to me over the past year. Your endless patience and lack of judgment was always appreciated as I made my way from chemistry into the world of ocean physics.

I would like to thank John Eiler and Ken Farley, the other members of my committee. You have helped me think critically about my data and your insight has greatly improved the work that I have done during my time at Caltech.

I had the great fortune of being able to spend time at the KCCAMS lab at UC Irvine. I would like to acknowledge all of the members of the prep lab who have helped me over the years, and I would particularly like to thank John Southon for his generosity of time and lab space. Over the past few years I have also greatly enjoyed the chance to talk science with Patrick Rafter during my visits to UCI.

I always felt that I wouldn't truly be an oceanographer until I got the chance to go to sea, and I am so happy that I got to do it with all the participants of IODP Expedition 361. Thanks to Ian, Sidney, Chad, and Leah for keeping everything running smoothly, and thanks to Andreas, Steve, Melissa, and Jason for keeping my spirits high 12 hours a day for two months.

I have been lucky enough to be a part of two lab groups during my time at Caltech, and I want to thank all the members (and affiliates) of the Adkins and Eiler lab groups. Nami, Guillaume, Stacy, Nithya, Katie, Uri, and Max were always there when I needed help in lab. Andrea, James, and Nithya were always game to talk with me about my data and your insights were always appreciated. I am grateful that I was able to go through grad school with my two classmates Adam and Ted—it won't be the same without you guys.

I want to acknowledge the members of the pit, who helped me survive my first year,

and the members of Steuben House, who welcomed me when I first arrived. Life wouldn't have been the same without all of my friends from the division. I have been grateful to share evening runs, early morning bike rides, trips to the climbing gym, and many backyard barbecues with all of you. Thanks to Jeff for sharing my love of bicycles, thanks to Hayden for matching my enthusiasm, and thanks to Nithya for helping me navigate academia as a woman and going on evening happy hour walks.

I want to say a very special 'merci' to Guillaume. You introduced me to lots of weird cinema and we shared many tasty Belgian beers. Your emotional and scientific support got me here today, and for that I will always be grateful.

Playing frisbee has been a huge part of my life in LA. My teammates have kept my mind and my body healthy through this process and I couldn't imagine it any other way. I would particularly like to thank AJ, Joe, and Connie for helping me keep a good perspective on what is important in life.

I have been lucky enough to get to know Rob, Cyrus, Shannon, and Rachel through Adam and Hot Karate. Family weekends with all of you are always a blast and I hope there are more to come in the future.

I could not have done this without Adam. I am inspired by your creativity and intellect and you can always make me laugh. We have gone on some excellent adventures and cooked some tasty dinners. Plus you got me a dog.

Finally, my family. I owe my parents a million thank yous—your endless love and support has gotten me to where I am today. Thanks to Martha, Adriana, and Arielle for making my family bigger and filling my time at home with good food, tasty cocktails and lots of fun. Thanks to Peter and Barbara and the Miller-Midzik-Hallocks. You all count as family to me too.

ABSTRACT

Glacial-interglacial cycles, occurring at a period of approximately 100,000 years, have dominated Earth's climate over the past 800,000 years. These cycles involve major changes in land ice, global sea level, ocean circulation, and the carbon cycle. While it is generally agreed that the ultimate driver of global climate is changes in insolation, glacial cycles do not look like insolation forcing. Notably, there is a highly non-linear warming response at 100,000 years to a relatively small forcing, implicating a more complicated system of biogeochemical and physical drivers. The ocean plays a pivotal role in glacial-interglacial climate through direct equator-to-pole transport of heat and its role in the carbon cycle. The deep ocean contains 60 times more carbon than the atmosphere, and therefore even small changes in ocean circulation can have a large impact on atmospheric CO_2, a crucial amplifier in the climate system. In order to better understand the role that ocean circulation plays in glacial-interglacial climate we focus on the last glacial-interglacial transition. In this thesis, we present reconstructions of changes in intermediate water circulation and explore a new time-dependent dynamical box model. We reconstruct circulation using radiocarbon and clumped isotope measurements on U/Th dated deep-sea corals from the New England and Corner Rise Seamounts in the western basin of the North Atlantic and from south of Tasmania in the Indo-Pacific sector of the Southern Ocean. Our new time-dependent model contains key aspects of ocean physics, including Southern Ocean Residual Mean theory, and allows us to explore dynamical mechanisms which drive abrupt climate transitions during the last glacial period.

In Chapter 2 we present a compilation of reconnaissance dated deep-sea corals from the Caltech collection. Reconnaissance dating facilitates sample selection for our high-precision radiocarbon and temperature time series and patterns in the depth distribution of deep-sea corals over time contain additional relevant climate information. In Chapter 3, we present a high-resolution radiocarbon record from south of Tasmania which highlights variability in Southern Ocean Intermediate Water radiocarbon during the deglaciation, particularly during the Antarctic Cold Reversal. We use our radiocarbon data, in combination with other deglacial climate records, to infer changes in overturning circulation configuration across this time interval. In Chapter 4 we present our time-dependent dynamical box model. Our model displays hysteresis in basin stratification and Southern Ocean isopycnal outcrop position as

a function of North Atlantic Deep Water formation rate. In a dynamical system, hysteresis implies that there are multiple stable states, and switches between these states can lead to abrupt transitions, such as those observed during the middle of the last glacial period. In Chapter 5 we present paired radiocarbon and temperature time series from the North Atlantic and Southern Ocean spanning the late part of the last glacial. We explore the mechanisms driving trends in radiocarbon and temperature by looking at cross-plots of the data, and we make inferences about changes in circulation configuration using insight gained from our dynamical box model.

PUBLISHED CONTENT AND CONTRIBUTIONS

Hines, Sophia K.V., John R. Southon, and Jess F. Adkins (2015). "A high-resolution record of Southern Ocean intermediate water radiocarbon over the past 30,000 years". In: *Earth and Planetary Science Letters* 432, pp. 46–58. DOI: 10.1016/j.epsl.2015.09.038.

S.K.V.H. helped to design this research, made all of the U/Th and radiocarbon measurements, analyzed the data, worked with J.F.A. to interpret the data, and wrote the manuscript with input from J.F.A. and J.R.S.

Bush, Shari L. et al. (2013). "Simple, rapid, and cost effective: a screening method for ^{14}C analysis of small carbonate samples". In: *Radiocarbon* 55, pp. 631–640. DOI: 10.1017/S0033822200057787.

S.K.V.H. helped prepare samples for radiocarbon analysis and provided some input on the manuscript.

Hines, Sophia K., John M. Eiler, and Jess F. Adkins (*in prep.*). "Deep-sea coral clumped isotope and radiocarbon records from North Atlantic and Southern Ocean intermediate water spanning the most recent glacial termination". In:

S.K.V.H. helped to design this research, made all of the U/Th, radiocarbon, and clumped isotope temperature measurements, analyzed the data, worked with J.F.A. to interpret the data, and wrote the manuscript with input from J.F.A. and J.M.E.

Hines, Sophia K., Andrew F. Thompson, and Jess F. Adkins (*in prep.*). "Abrupt transitions and hysteresis in glacial ocean circulation explained by a two-basin time-dependent dynamical box model". In:

S.K.V.H. helped to design this research, worked with A.F.T. to write the time-dependent box model, ran model experiments, worked with J.F.A. and A.F.T. to interpret the data, and wrote the manuscript with input from J.F.A. and A.F.T.

Thompson, Andrew F., Sophia K. Hines, and Jess F. Adkins (*submitted*). "A Southern Ocean mechanism for climate transients through the last glacial period". In: *Nature*.

S.K.V.H. helped to design this research, worked with A.F.T. to write the time-dependent box model, contributed to the data interpretation, and helped write the manuscript.

TABLE OF CONTENTS

LIST OF ILLUSTRATIONS

Number *Page*

LIST OF TABLES

Chapter 1

INTRODUCTION

For nearly a million years, the earth's climate has been typified by glacial-interglacial cycles, occurring at a period of roughly 100,000 years (Lisiecki and Raymo, 2005). These glacial cycles were accompanied by changes in global temperature, atmospheric CO_2, land-based ice sheets, and global sea level (Jouzel et al., 2007; Lüthi et al., 2008; Rohling et al., 2014). While the ultimate driver of these cycles is generally accepted to be changes in high-latitude insolation, or solar radiation, the character of these late-Pleistocene glaciations does not match the shape of insolation curves (Milanković, 1941; Hays, John Imbrie, and Shackleton, 1976; J Imbrie, Boyle, et al., 1992; J Imbrie, Berger, et al., 1993). In particular, glacial cycles are characterized by an abrupt non-linear response at roughly 100,000 years, while high-latitude insolation has much higher spectral power at 20,000 and 40,000 years. This has led to discussion of whether glacial cycles are paced by sets of 20-kyr procession cycles (Cheng, Edwards, et al., 2016), 40-kyr obliquity cycles (Huybers and Wunsch, 2005), or some combination of both (Huybers, 2011). Recently, some of the discussion has moved away from trying to quantify the exact sequence of events that led to each glacial termination and focused instead on how the build-up of potential energy in the climate system could lead to certain insolation maxima triggering interglacials while others do not (Tzedakis et al., 2017). This potential energy could take the form of deep ocean heat, stored CO_2, large land-based ice sheets, or some other aspect of the climate system that is able to respond in a non-linear way. The question now is: what combination of glaciological, biogeochemical, and physical ocean processes allowed for the necessary build-up of energy in the climate system, and what did that build-up of potential energy look like?

One crucial amplifier in the climate system is the carbon cycle. Although evidence suggests that atmospheric CO_2 does not precede temperature rise at deglaciations (Caillon et al., 2003), CO_2 concentrations have varied along with temperature over the past 800,000 years (Lüthi et al., 2008). Carbon dioxide is a greenhouse gas, and therefore compounds the effects of changes in insolation. Although atmospheric CO_2 has the largest direct effect on global temperature, it is one of the smallest reservoirs in the global carbon system (Sigman and Boyle, 2000). The deep ocean contains 60 times more carbon than the atmosphere, and therefore changes in ocean

circulation and biogeochemistry can have a large impact on atmospheric CO_2. One way that ocean biogeochemistry can impact atmospheric CO_2 is through the efficiency of the biological pump (Sigman, Hain, and Haug, 2010). The "biological pump" refers to the mechanism by which organisms in the surface ocean fix CO_2 into organic matter and the fixed organic carbon is exported into the deep ocean. In the modern ocean, deep water sinking in the North Atlantic has very low dissolved phosphate because organisms living in the surface water have consumed all of it in order to fix CO_2 into organic carbon. In the Southern Ocean, however, newly formed deep water still has unconsumed phosphate, which represents excess CO_2 left in the atmosphere. As was pointed out in the "Harvardton Bears" models, a 100% efficient biological pump cannot achieve the full interglacial-glacial CO_2 draw down—these simple box models require a combination of increased biological pump efficiency and circulation slow-down (Knox and McElroy, 1984; Siegenthaler and Wenk, 1984; Sarmiento and Toggweiler, 1984).

Ocean circulation impacts global climate in two main ways: it provides a means of sequestering CO_2 from the atmosphere via the biological pump and it participates in direct equator-to-pole heat transport (Ganachaud and Wunsch, 2000; L. D. Talley, 2003). The meridional overturning circulation represents the ocean circulation path that transfers water from the surface to the deep and back, and it occurs on timescales of ~1000 years, allowing deeply regenerated CO_2 to be sequestered from the atmosphere for thousands of years (Stuiver, Quay, and Ostlund, 1983). There are two places where deep water is formed in the ocean: the North Atlantic (in the Labrador and Nordic Seas) and the Southern Ocean (on continental shelves in the Weddell Sea, Ross Sea, and around East Antarctica) (Kuhlbrodt et al., 2007). The modern ocean has a "figure-eight" circulation, meaning that its closure involves separate but equally important processes in both the Atlantic and Indo-Pacific basins (Lumpkin and Speer, 2007; L. Talley, 2013). This figure-eight structure involves a central role for the Southern Ocean and is lost in zonally averaged depictions of the overturning circulation, which instead show two stacked counter-rotating cells.

In order to understand the details of the modern overturning circulation and how it may have changed in past climates it is crucial to understand the circulation of the Southern Ocean. The Southern Ocean is unique because it is the only place where there are no continental impediments to zonal flow. Strong westerly winds over the Southern Ocean lead to the generation of the Antarctic Circumpolar Current (ACC), which, at around 140 Sv (1 Sv is 10^6 m^3 s^{-1}), is the largest current in the

world. Because there are no continental boundaries in the Drake Passage latitude band above the depth of the Scotia Ridge, north-south flow cannot be generated via zonal pressure gradients, as is the case in the ocean basins. Modeling and observational data from the Southern Ocean show an interesting density structure—deep isopycnals, or density surfaces, slope to the surface across the ACC, transforming the vertical density gradient, which characterizes the ocean basins, into a meridional density gradient at the surface (Doos and Webb, 1994; Speer, Rintoul, and Sloyan, 2000).

Over the past two decades a new theory has emerged to explain meridional overturning circulation in the Southern Ocean. This Residual Mean theory builds on observations of the Southern Ocean isopycnal structure, and is based on a balance between wind and eddies. Southern Ocean westerly winds drive northward Ekman transport and steepen isopycnals. Steep isopycnals become baroclinically unstable and generate eddies that act to relax isopycnal slopes (Marshall and Radko, 2003). In the subsurface, flow occurs adiabatically along isopycnals. Overturning transport is achieved as a result of buoyancy fluxes at the surface which allow water to be transformed to heavier or lighter density classes according to the equation:

$$\psi_{res} = \bar{\psi} + \psi^*, \quad \text{or rewritten :} \tag{1.1}$$

$$\frac{B_0}{\partial b_0 / \partial y} = -\frac{\tau}{\rho_0 f} + K s_\rho \tag{1.2}$$

where $\bar{\psi}$ is the wind-driven mean component, ψ^* is the eddy-driven component, ψ_{res} is the buoyancy-driven residual component, B_0 is the surface buoyancy flux, $\partial b_0 / \partial y$ is the surface buoyancy gradient, τ is the surface wind stress, ρ_0 is the mean ocean density, f is the coriolis parameter, K is the eddy diffusivity, and s_ρ is the isopycnal slope. There are positive surface buoyancy fluxes in the northern part of the Southern Ocean due to a combination of direct heating by the atmosphere, precipitation minus evaporation, and freshwater from sea ice melt (Abernathey et al., 2016). There are negative surface buoyancy fluxes in the southern part of the Southern Ocean due to brine rejection and direct heat loss to the atmosphere within leads in the sea ice known as polynyas (Abernathey et al., 2016; Nicholls et al., 2009). There is a split in the circulation, therefore, with a clockwise overturning cell in regions of positive surface buoyancy forcing (sometimes called the upper cell) and a counter-clockwise overturning cell in regions of negative surface buoyancy forcing (the lower cell).

In the modern ocean, North Atlantic Deep Water (NADW) upwells in a region of the Southern Ocean where it experiences a negative surface buoyancy forcing, causing it to flow south and sink again as Antarctic Bottom Water (AABW) (L. Talley, 2013). If this newly formed AABW flows back into the Atlantic, it diffusively upwells back into NADW. If, instead, it flows into the Indian or Pacific basins, it is able to diffusively upwell further in the water column to a lighter density class. Therefore, when this water returns to the Southern Ocean as Indian Deep Water or Pacific Deep Water (IDW/PDW), it upwells in a region of positive surface buoyancy forcing (L. Talley, 2013). Finally, this water flows to the north again as Antarctic Intermediate Water (AAIW) and Subantarctic Mode Water (SAMW). These relatively shallow water masses can be transformed, via downward heat diffusion, to upper ocean subtropical waters, which eventually make their way to the North Atlantic, closing the overturning circulation (L. Talley, 2013; Lozier, 2010). This three-dimensional figure-eight structure is lost in some depictions of the overturning circulation where zonal averaging hides the separate but equally important processes that occur in the different ocean basins.

Since ocean circulation has such a strong impact on global climate, a natural question is: how did the structure and rate of ocean circulation change across glacial-interglacial cycles? There is paleoceanographic evidence that ocean circulation looked quite different during the Last Glacial Maximum (LGM, ~22–18 ka) than it does today. A reconstruction of δ^{13}C in the western Atlantic during the LGM shows a shoaled NADW and expanded AABW compared to the modern (Curry and Oppo, 2005). δ^{13}C is a non-conservative circulation tracer, which can track the difference between northern and southern-source water in the Atlantic. Another study combined depth transects of δ^{13}C and δ^{18}O in the Atlantic at the LGM to construct a tracer transport budget and constrain the ratio of overturning transport to vertical mixing (Lund, Adkins, and Ferrari, 2011). They found that in addition to its shoaled configuration, there was also greater stratification between glacial NADW and AABW.

A theoretical scenario has been proposed to explain the change in circulation configuration at the LGM (Ferrari et al., 2014). Ferrari et al. (2014) point out that the switch between negative and positive buoyancy forcing in the Southern Ocean is aligned with the quasi-permanent sea ice edge, and this therefore marks the boundary between the upper and lower circulation cells. To first order, isopycnal slopes are constant across the ACC and therefore the depth of the boundary between the upper

and lower circulation cells can be calculated geometrically (Ferrari et al., 2014). In the modern ocean this depth comes out to around 2200 m, below the mean depth of rough topography on the seafloor (~2000 m). Rough topography greatly increases diapycnal mixing in the deep ocean (Polzin et al., 1997), and the deep boundary between the circulation cells could therefore contribute to the modern figure-eight circulation structure (Ferrari et al., 2014). At the LGM, paleo data and models suggest that sea ice was expanded by at least 5° (Ferrari et al., 2014; Gersonde et al., 2005; Roche, Crosta, and Renssen, 2012). By the same geometric argument, this would shift the surface boundary between the upper and lower circulation cells to the north and shoal it in the basins by around 500 m (Ferrari et al., 2014). This could contribute to the shoaling of NADW and would potentially switch the circulation configuration into a "two-cell" state, with greater stratification and separation between the circulation cells (Ferrari et al., 2014). A switch to two-cell circulation at the LGM should appear in radiocarbon data as an age maximum at mid-depth (Burke et al., 2015), which is indeed what shows up in a recent compilation of LGM data by Skinner et al. (2017).

In this thesis, we investigate two questions: how did the structure of ocean circulation change during the late part of the last glacial cycle and how did this impact global climate? To answer these questions, we employ reconstructions of past ocean circulation and temperature and simple theory-based models. We use deep-sea *Desmophyllum dianthus* corals as our paleoceanographic archive. They are solitary azooxanthellate sclaractinian corals (non-symbiotic stony corals) that live in the deep ocean down to ~2500 m. They are powerful targets for paleoceanographic reconstructions because individual corals are large enough to accommodate multiple measurements using different proxies (e.g. Adkins et al., 2002; Thiagarajan, Adkins, and Eiler, 2011), and they contain sufficient uranium in their skeletons to be precisely U/Th dated for independent calendar age control (Cheng, Adkins, et al., 2000; Lomitschka and Mangini, 1999).

In Chapter 2, we summarize the current state of reconnaissance dated deep-sea corals in the Caltech collection. Much of this work was done by Thiagarajan, Gerlach, et al. (2013), but an additional 331 dates are presented here. Reconnaissance dating is a crucial step in the construction of a paleoceanographic record using deep-sea corals—when samples are collected, their depth and geographical location is well constrained, but their age is entirely unknown. The lack of a priori age information is the biggest disadvantage of deep-sea corals compared with the more

ubiquitous sediment cores. There are several methods of reconnaissance dating, but we use a radiocarbon screening method developed by Bush et al. (2013). In our reconnaissance data, we find shifts in the distribution of deep-sea corals over time that is in line with climatic events and adheres to patterns described by Thiagarajan, Gerlach, et al. (2013). In addition, by comparing radiocarbon-based calendar ages with U/Th ages, we see evidence for a shift in Southern Ocean surface reservoir ages around the time of the Bølling-Allerød/Antarctic Cold Reversal, a key time period during the deglaciation.

In Chapter 3, we reconstruct Southern Ocean intermediate water circulation across the deglaciation using radiocarbon measurements on U/Th dated deep-sea corals from south of Tasmania (Sophia K.V. Hines, Southon, and Adkins, 2015). We find that intermediate water radiocarbon was variable and generally closer to the contemporaneous atmosphere in the time leading up to the LGM (between ~28–23 ka) and during the Antarctic Cold Reversal (~15–13 ka). During the LGM and the majority of Heinrich Stadial 1, intermediate water radiocarbon had a relatively constant offset from the contemporaneous atmosphere. We attribute times of intermediate water radiocarbon variability, particularly during the Antarctic Cold Reversal, to abrupt shifts in Southern Ocean fronts. We also compare our record with other climate reconstructions from the deglaciation in order to make broader inferences about the structure of ocean circulation across this time period.

In Chapter 4, we present a new time-dependent box model of the ocean. It is a coarse resolution isopycnal model with two basins representing the Atlantic and Indo-Pacific and four layers bounded by three isopycnal surfaces. The model is forced by North Atlantic Deep Water formation of variable density and solves for the stratification and the overturning circulation. Importantly, this model contains realistic ocean physics including Residual Mean theory (Marshall and Radko, 2003). Our new time-dependent model is an extension of the steady-state model described in Thompson, Stewart, and Bischoff (2016). We discover an interesting new bipolar seesaw mechanism that explains the interhemispheric time lag (WAIS Divide Project Members, 2015) at rapid climate change events during the middle of the last glacial period (Marine Isotope Stage 3) (Thompson, Sophia K. Hines, and Adkins, *submitted*). This mechanism involves rapid changes in basin stratification and Southern Ocean outcrop position driven by volume convergence upon abrupt changes in NADW formation flux. In order to explore parameter space and better understand the dynamics of our model, we perform a series of experiments where we run our

time-dependent model out to steady state. Notably, we observe hysteresis in the outcrop position of interface 2 (the isopycnal between layers 2 and 3) as a function of NADW flux, reminiscent of the abrupt Dansgaard-Oeschger events that characterize Marine Isotope Stage 3. We look at changes in circulation configuration, identifying regions of NADW flux/density space that are conducive to figure-eight versus two-cell circulation. Finally we compare our results to predictions made by Ferrari et al. (2014).

In Chapter 5, we present paired Intermediate Water radiocarbon and clumped isotope temperature time series from the North Atlantic and Southern Ocean spanning the late part of the last glacial period. These records are constructed using U/Th dated deep-sea corals from the New England and Corner Rise seamounts in the North Atlantic and south of Tasmania in the Southern Ocean. In both the North Atlantic and Southern Ocean, reconstructed radiocarbon and temperature values fall far outside the range of modern radiocarbon and temperature. This emphasizes how different the ocean state was during the late part of the last glacial. The temperature of intermediate water was generally warmer than the modern, supporting the hypothesis that the glacial ocean was salinity stratified rather than temperature stratified (Adkins, 2002). We see a pattern of warming accompanied by older radiocarbon values at intermediate depths during Heinrich Stadial 1, which has been previously observed (Marcott et al., 2011; Thiagarajan, Subhas, et al., 2014). During Heinrich Stadial 2, however, we see cooling at intermediate depth in both the North Atlantic and the Southern Ocean. The variability that we see in radiocarbon and temperature during the deglaciation and preceding the LGM highlight the challenges of trying to interpret paleo data using insight from the modern steady-state ocean. The deglaciation is far from steady-state and therefore strong tracer gradients exist in the ocean. Additionally, some tracers, such as radiocarbon, have a much longer "memory" of past ocean circulation states than others. Nevertheless, by combining our new records with other radiocarbon and temperature data from the North Atlantic and Southern Ocean, we are able to make some inferences about how circulation configuration has changed across the deglaciation.

References

Abernathey, Ryan P. et al. (2016). "Water-mass transformation by sea ice in the upper branch of the Southern Ocean overturning". In: *Nature Geoscience* 9.8, pp. 596–601.

Adkins, Jess F. (2002). "The Salinity, Temperature, and δ^{18}O of the Glacial Deep Ocean". In: *Science* 298.5599, pp. 1769–1773.

Adkins, Jess F. et al. (2002). "Radiocarbon Dating of Deep-Sea Corals". In: *Radiocarbon* 44, pp. 567–580.

Burke, Andrea et al. (2015). "The Glacial Mid-Depth Radiocarbon Bulge and Its Implications for the Overturning Circulation". In: *Paleoceanography*.

Bush, Shari L. et al. (2013). "Simple, rapid, and cost effective: a screening method for ^{14}C analysis of small carbonate samples". In: *Radiocarbon* 55, pp. 631–640. DOI: 10.1017/S0033822200057787.

Caillon, N et al. (2003). "Timing of Atmospheric CO2 and Antarctic Temperature Changes Across Termination III". In: *Science* 299, pp. 1728–1731.

Cheng, Hai, Jess F. Adkins, et al. (2000). "U-Th dating of deep-sea corals". In: *Geochimica et Cosmochimica Acta* 64, pp. 2401–2416.

Cheng, Hai, R Lawrence Edwards, et al. (2016). "The Asian monsoon over the past 640,000 years and ice age terminations". In: *Nature* 534.7609, pp. 640–646.

Curry, William B. and Delia W. Oppo (2005). "Glacial water mass geometry and the distribution of δ13C of ΣCO2 in the western Atlantic Ocean". In: *Paleoceanography*.

Doos, K. and D.J. Webb (1994). "The Deacon Cell and the Other Meridional Cells of the Southern Ocean". In: *Journal of Physical Oceanography* 24, pp. 1–14.

Ferrari, R et al. (2014). "Antarctic sea ice control on ocean circulation in present and glacial climates". In: *PNAS* 111.24, pp. 8753–8758.

Ganachaud, Alexandre and Carl Wunsch (2000). "Improved estimates of global ocean circulation, heat transport and mixing from hydrographic data". In: *Nature* 408, pp. 453–457.

Gersonde, R et al. (2005). "Sea-surface temperature and sea ice distribution of the Southern Ocean at the EPILOG Last Glacial Maximum—A circum-Antarctic view based on siliceous microfossil records". In: *Quaternary Science Reviews* 24.7-9, pp. 869–896.

Hays, J. D., John Imbrie, and N. J. Shackleton (1976). "Variations in the Earth's Orbit: Pacemaker of the Ice Ages". In: *Science* 194, pp. 1121–1132.

Hines, Sophia K.V., John R. Southon, and Jess F. Adkins (2015). "A high-resolution record of Southern Ocean intermediate water radiocarbon over the past 30,000 years". In: *Earth and Planetary Science Letters* 432, pp. 46–58. DOI: 10.1016/j.epsl.2015.09.038.

Huybers, Peter (2011). "Combined obliquity and precession pacing of late Pleistocene deglaciations". In: *Nature* 480.7376, pp. 229–232.

Huybers, Peter and Carl Wunsch (2005). “Obliquity pacing of the late Pleistocene glacial terminations”. In: *Nature* 434.7032, pp. 491–494.

Imbrie, J, A Berger, et al. (1993). “On the structure and origin of major glaciation cycles: 2. The 100,000-year cycle”. In: *Paleoceanography* 8, pp. 699–735.

Imbrie, J, Edward A. Boyle, et al. (1992). “On the structure and origin of major glaciation cycles: 1. Linear responses to Milankovitch forcing”. In: *Paleoceanography* 7, pp. 701–738.

Jouzel, J. et al. (2007). “Orbital and Millennial Antarctic Climate Variability over the Past 800,000 Years”. In: *Science* 317.5839, pp. 793–796.

Knox, Fanny and Michael B McElroy (1984). “Changes in atmospheric CO_2: Influence of the marine biota at high latitude”. In: *Journal of Geophysical Research* 89.D3, p. 4629.

Kuhlbrodt, T et al. (2007). “On the driving processes of the Atlantic meridional overturning circulation”. In: *Reviews of Geophysics* 45.

Lisiecki, Lorraine E and Maureen E Raymo (2005). “A Pliocene-Pleistocene stack of 57 globally distributed benthic δ^{18}O records”. In: *Paleoceanography* 20.1.

Lomitschka, Michael and Augusto Mangini (1999). “Precise Th/U-dating of small and heavily coated samples of deep sea corals”. In: *Earth and Planetary Science Letters* 170.4, pp. 391–401.

Lozier, M. Susan (2010). “Deconstructing the Conveyor Belt”. In: *Science* 328, pp. 1507–1511.

Lumpkin, Rick and Kevin Speer (2007). “Global Ocean Meridional Overturning”. In: *Journal of Physical Oceanography* 37.10, pp. 2550–2562.

Lund, D C, Jess F. Adkins, and R Ferrari (2011). “Abyssal Atlantic circulation during the Last Glacial Maximum: Constraining the ratio between transport and vertical mixing”. In: *Paleoceanography* 26.1.

Lüthi, Dieter et al. (2008). “High-resolution carbon dioxide concentration record 650,000-800,000 years before present”. In: *Nature* 453, pp. 379–382.

Marcott, Shaun A et al. (2011). “Ice-shelf collapse from subsurface warming as a trigger for Heinrich events”. In: *PNAS* 108.33, pp. 13415–13419.

Marshall, John and Timour Radko (2003). “Residual-mean solutions for the Antarctic Circumpolar Current and its associated overturning circulation”. In: *Journal of Physical Oceanography* 33.11, pp. 2341–2354.

Milanković, M (1941). *Kanon der Erdbestrahlung und seine Anwendung auf das Eiszeitenproblem*. Royal Serbian Academy.

Nicholls, Keith W. et al. (2009). “Ice-ocean processes over the continental shelf of the southern Weddell Sea, Antarctica: A revies”. In: *Reviews of Geophysics* 47.

Polzin, K L et al. (1997). "Spatial Variability of Turbulent Mixing in the Abyssal Ocean". In: *Science* 276, pp. 93–96.

Roche, D M, X Crosta, and H Renssen (2012). "Evaluating Southern Ocean sea-ice for the Last Glacial Maximum and pre-industrial climates: PMIP-2 models and data evidence". In: *Quaternary Science Reviews* 56, pp. 99–106.

Rohling, E J et al. (2014). "Sea-level and deep-sea-temperature variability over the past 5.3 million years". In: *Nature* 508.7497, pp. 477–482.

Sarmiento, J. L. and J. R. Toggweiler (1984). "A new model for the role of the oceans in determining atmospheric pCO_2". In: *Nature* 308, pp. 621–624.

Siegenthaler, U and Th Wenk (1984). "Rapid atmospheric CO_2 variations and ocean circulation". In: *Nature* 308.5960, pp. 624–626.

Sigman, Daniel M and Edward A. Boyle (2000). "Glacial/interglacial variations in atmospheric carbon dioxide". In: *Nature* 407, pp. 859–869.

Sigman, Daniel M, Mathis P Hain, and Gerald H Haug (2010). "The polar ocean and glacial cycles in atmospheric CO_2 concentration". In: *Nature* 466.7302, pp. 47–55.

Skinner, L.C. et al. (2017). "Radiocarbon constraints on the glacial ocean circulation and its impact on atmospheric CO_2". In: *Nature Communications*.

Speer, Kevin, Stephen R. Rintoul, and Bernadette Sloyan (2000). "The Diabatic Deacon Cell". In: *Journal of Physical Oceanography*.

Stuiver, M, P D Quay, and H G Ostlund (1983). "Abyssal Water Carbon-14 Distribution and the Age of the World Oceans". In: *Science* 219.4586, pp. 849–851.

Talley, Lynne (2013). "Closure of the Global Overturning Circulation Through the Indian, Pacific, and Southern Oceans: Schematics and Transports". In: *Oceanography* 26.1, pp. 80–97.

Talley, Lynne D. (2003). "Shallow, Intermediate, and Deep Overturning Components of the Global Heat Budget". In: *Journal of Physical Oceanography* 33, pp. 530–560.

Thiagarajan, Nivedita, Jess F. Adkins, and John Eiler (2011). "Carbonate clumped isotope thermometry of deep-sea corals and implications for vital effects". In: *Geochimica et Cosmochimica Acta* 75.16, pp. 4416–4425.

Thiagarajan, Nivedita, Dana Gerlach, et al. (2013). "Movement of deep-sea coral populations on climatic timescales". In: *Paleoceanography* 28, pp. 227–236.

Thiagarajan, Nivedita, Adam V. Subhas, et al. (2014). "Abrupt pre-Bolling-Allerod warming and circulation changes in the deep ocean". In: *Nature* 511, pp. 75–78.

Thompson, Andrew F., Sophia K. Hines, and Jess F. Adkins (*submitted*). "A Southern Ocean mechanism for climate transients through the last glacial period". In: *Nature*.

Thompson, Andrew F., Andrew L. Stewart, and Tobias Bischoff (2016). "A Multi-basin Residual-Mean Model for the Global Overturning Circulation". In: *Journal of Physical Oceanography* 46.9, pp. 2583–2604.

Tzedakis, P C et al. (2017). "A simple rule to determine which insolation cycles lead to interglacials". In: *Nature Publishing Group* 542.7642, pp. 427–432.

WAIS Divide Project Members (2015). "Precise interpolar phasing of abrupt climate change during the last ice age". In: *Nature* 520, pp. 661–664.

Chapter 2

RECONNAISSANCE DATING OF DEEP-SEA CORALS TO DEVELOP A COMPREHENSIVE AGE-DEPTH DISTRIBUTION

2.1 Introduction

Deep-sea corals are a new and versatile paleoceanographic archive. They have large skeletons and growth rates of ~1 mm/yr (Adkins, Henderson, et al., 2004), which allows them to be used for reconstructing decadal shifts in ocean biogeochemistry. Their large size also accommodates measurements from multiple proxies on the same individual, giving temporally synchronous data. They have been successfully used to measure deep ocean proxies for circulation (radiocarbon and ϵ_{Nd}), temperature (clumped isotopes), biological productivity (δ^{15}N, P/Ca, Ba/Ca), and ocean chemistry (δ^{11}B) (Adkins, Griffin, et al., 2002; van de Flierdt, Laura F. Robinson, and Adkins, 2010; Wang et al., 2014; Anagnostou, Sherrell, and Gagnon, 2011; Thiagarajan, Adkins, and Eiler, 2011; van de Flierdt, Laura F. Robinson, Adkins, et al., 2006; McCulloch et al., 2012).

Unlike sediment cores, which have been the staple of paleoceanography since its early days, deep-sea corals incorporate sufficient uranium from seawater to allow precise, independent calendar age determination via U/Th dating (Cheng et al., 2000). Although independent age control is one of the primary advantages of deep-sea corals, their main disadvantage is that there is no a priori way to know their age when they are collected (whereas there is an inherent stratigraphy to deep sea sediments). At Caltech, we have around 16,500 deep-sea corals in our collection. These samples have been collected over several cruises to the New England and Corner Rise Seamounts in the western North Atlantic (in 2003, 2004, and 2005 using the HOV Alvin and ROV Hercules), and to south of Tasmania in the Southern Ocean (in 2008 using the ROV Jason). Since these samples were all collected by deep submergence vehicles, their geographical locations (latitude, longitude, and depth) are very precisely known.

Most paleoceanographic reconstructions aim to either probe the time history of one particular place in the ocean or examine the depth structure during a particular time. When using deep-sea corals, the first step in study design is constructing an age-depth plot of all corals in order to determine which samples to select for the timeseries

or depth transect. To expedite this process, several methods of reconnaissance dating have been established, including radiocarbon age screening (Burke, Laura F. Robinson, et al., 2010; Bush et al., 2013) and laser ablation U/Th dating (Spooner et al., 2016). These methods offer less precise age determinations than high-resolution mass spectrometric U/Th analysis, but much higher throughput. For the Caltech coral collection, initial reconnaissance dating was performed on a subset of samples from the North Atlantic and Southern Ocean (Thiagarajan, Gerlach, et al., 2013) and precise U/Th dating has been performed on many other samples from the North Atlantic (Laura F. Robinson, Adkins, Scheirer, et al., 2007; Eltgroth et al., 2006; Adkins, Cheng, et al., 1998; Laura F. Robinson, Adkins, Keigwin, et al., 2005; Laura F. Robinson, Adkins, Fernandez, et al., 2006).

In addition to providing the information necessary to select samples for paleoceanographic studies, deep-sea coral age-depth distributions have an ecologically meaningful temporal structure (Thiagarajan, Gerlach, et al., 2013). The abundance of deep-sea corals and their depth range has varied in sync with climate over the past ~40,000 yr. Interestingly, coral populations seem to thrive during times of rapid climate change, such as Heinrich Stadial 1 and the Younger Dryas in the Northern Hemisphere and the Antarctic Cold Reversal in the Southern Hemisphere (Thiagarajan, Gerlach, et al., 2013). Thiagarajan, Gerlach, et al. (2013) determined that the dominant controls on deep-sea coral distribution in the Holocene are surface productivity, dissolved oxygen concentration and the aragonite saturation state. These constraints imply that past rapid climate change events were accompanied by changes in deep water chemistry, increasing the suitable coral habitat. On the other hand, gaps in deep-sea coral records—either in depth or in time—imply changes in water chemistry that promote unfavorable growth conditions.

2.2 Methods

In order to further constrain the distribution of deep-sea corals in the North Atlantic and Southern Ocean and select a sample set for radiocarbon and temperature reconstructions, we screened an additional 331 samples—focusing on intermediate (~1400–1750 m; n=72 for N. Atlantic, n=97 for S. Ocean) and deep (>2000 m; n=123 for N. Atlantic, n=39 for S. Ocean) depths.

In preparation for reconnaissance radiocarbon dating by accelerator mass spectrometry at the Keck Carbon Cycle AMS Lab at UC Irvine, approximately 10–20 mg of coral was cut and physically cleaned with a dremel tool. Cut samples were

cleaned by ultrasonication in Mili-Q water for 20-minute increments until the water appeared clear (3–5 times). After cleaning, samples were dried in a laminar flow bench and then powdered with a mortar and pestle. Approximately 3 mg of powder was transferred into a glass vial for radiocarbon screening. Screening was performed according to the method of Bush et al. (2013). In brief, 5–6.5 mg of Sigma Aldrich -400 mesh iron powder was weighed into small borosilicate tubes and then mixed with 0.3 mg of powdered coral. The powdered coral and iron mixture was then pressed into pre-drilled aluminum AMS targets for measurement.

Reconnaissance radiocarbon dates were converted to calendar age using the OxCal online radiocarbon calibration software, version 4.3 (Ramsey, 2009) and the IntCal13 and Marine13 calibration curves (Reimer, Bard, et al., 2013). The IntCal13 calibration curve is an estimate of past atmospheric radiocarbon and was produced from a compilation of terrestrial (tree ring, lake and stalagmite) and surface marine (planktic foraminifera and surface coral) records using a Markov Chain Monte Carlo (MCMC) approach (Reimer, Baillie, et al., 2009; Reimer, Bard, et al., 2013). The Marine13 calibration curve is an estimate of the radiocarbon content of ocean surface water and was produced from an atmosphere-ocean box model and the IntCal13 curve (Reimer, Bard, et al., 2013). Because there tend to be large surface reservoir ages in high-latitude regions, we also added an additional 400-^{14}C year reservoir correction to the ages calculated from the Marine13 curve. We chose to add 400 ^{14}C-years somewhat arbitrarily—it is double the standard reservoir correction and it does not dramatically overcorrect the data.

2.3 Results

The average age error for the Burke, Laura F. Robinson, et al. (2010) method is 1.6% in the Southern Ocean and 1.5% in the North Atlantic (Thiagarajan, Gerlach, et al., 2013). The average age error for the Bush et al. (2013) method is slightly higher: 3.4% for the Southern Ocean and 3.1% for the North Atlantic. 23 of the 72 intermediate depth and 17 of the 123 deep North Atlantic corals we dated were older than the detectable limit of the method. In the Southern Ocean, 17 of the 97 intermediate depth and none of the 39 deep corals were older than the detectable limit.

New reconnaissance radiocarbon dates for the Southern Ocean (Table 2.1) and North Atlantic (Table 2.2) adhere to the basic trends observed previously by Thiagarajan, Gerlach, et al. (2013) (Figure 2.1). The depth range and abundance of the deep-

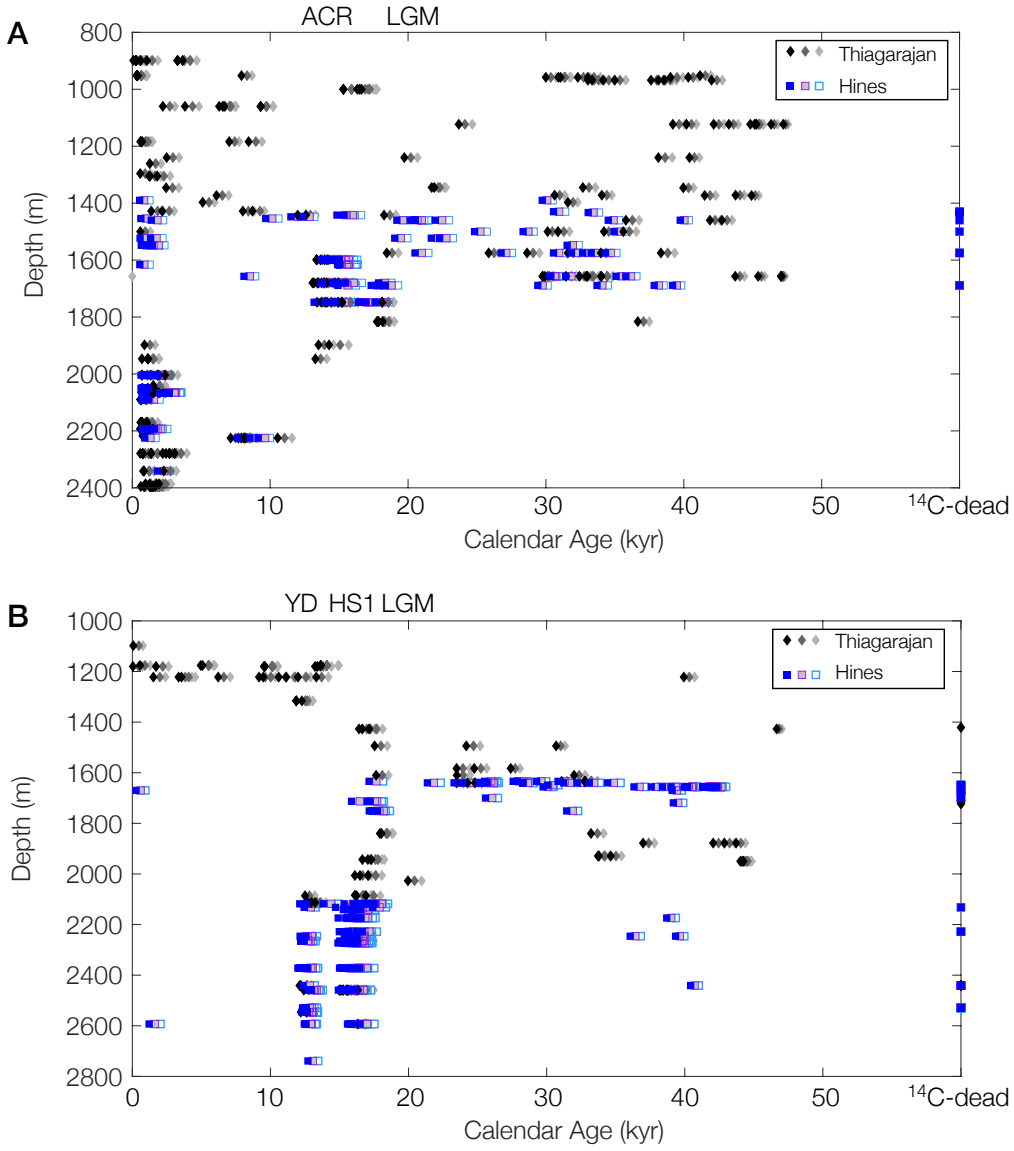

Figure 2.1: Age-depth plot for Southern Ocean (A) and North Atlantic (B) corals. Diamonds are data from Thiagarajan, Gerlach, et al. (2013) and squares are from this study. Lightest colored symbols (legend far right) are calculated using the IntCal13 calibration curve, medium colored symbols (legend center) are calculated using the Marine13 calibration curve, and darkest symbols (legend far left) are calculated using the Marine13 calibration curve and an additional reservoir correction of 400 years.

sea coral population responds to regional climate, particularly rapid climate change events during the deglaciation. In the North Atlantic there are abundance peaks and depth excursions corresponding to the Younger Dryas and Heinrich Stadial 1, and in the Southern Ocean there is an abundance peak corresponding to the Antarctic Cold Reversal. Coral abundances and depth ranges are greatly reduced at the LGM compared to earlier in the glacial and later during the deglaciation.

Since many of the radiocarbon-screened deep-sea corals have since been more precisely and accurately U/Th dated, it is possible to further examine the accuracy of reconnaissance radiocarbon age determinations by making U/Th age versus radiocarbon-derived calendar age plots. Figure 2.2 shows a comparison of Southern Ocean reconnaissance dates and U/Th ages for samples dated using the methodology of Burke, Laura F. Robinson, et al. (2010) (black diamonds) (Thiagarajan, Gerlach, et al., 2013) and Bush et al. (2013) (blue squares). There is generally good correspondence between reconnaissance dates and U/Th dates, except for the oldest samples, where the radiocarbon-derived ages tend to underestimate the age relative to the more precise and accurate U/Th dates. This is not particularly surprising, since the oldest samples push the limit of detection for the radiocarbon methods used. Figure 2.2 D–F are expanded versions of A–C, focusing on the interval between 10 and 30 ka. In these expanded views it is clear that reconnaissance dates using the Marine13 calibration curve with the additional 400-year reservoir correction does the best job of matching the U/Th ages.

There are fewer U/Th dates for comparison in the North Atlantic (Figure 2.3), however the general trends are consistent. The reconnaissance date underestimates the U/Th age for the oldest samples and the Marine13 calibration curve with an additional 400-year reservoir correction gives the best date, particularly for samples in the 10–30 ka age window. One sample, reconnaissance dated to ~26 ka, gave a U/Th date of 11.5±95.0 ka (unfilled square with large x error bars in Figure 2.3). This was due to high ^{232}Th (470,000 ppt), which increases age error due to uncertainty in the initial ^{230}Th/^{232}Th ratio.

This comparison between U/Th and reconnaissance radiocarbon dates focuses primarily on the late glacial and deglaciation, where surface reservoir ages are larger than they are in the Holocene. It should also be noted that reconnaissance ages for deep-sea corals should always be slightly older than U/Th ages because they also record the ventilation age of the water (i.e. the amount of time that has elapsed since the water was at the surface in equilibrium with the atmosphere). Given this, it still

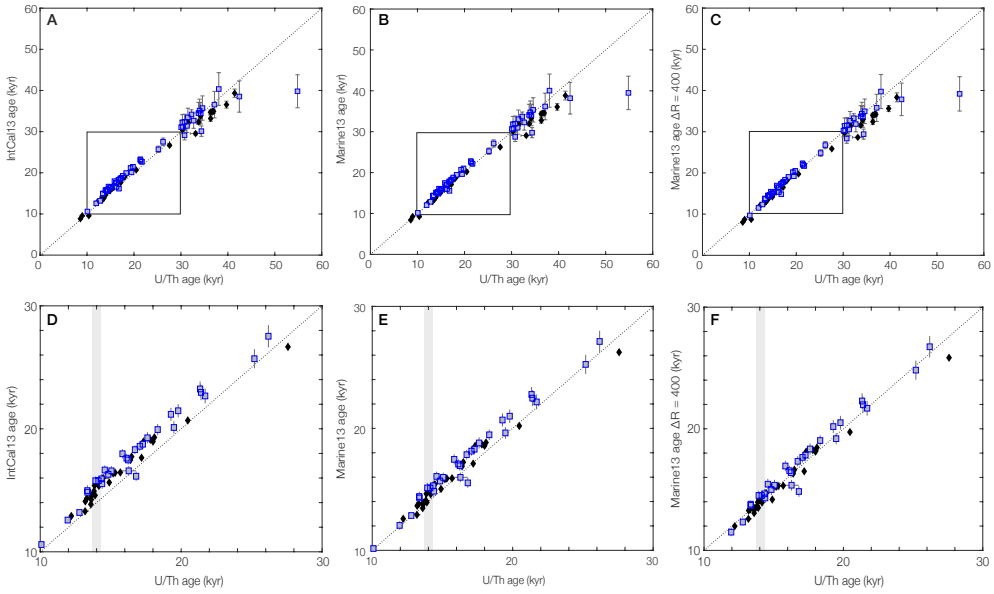

Figure 2.2: Comparison of Southern Ocean radiocarbon reconnaissance dates and precise U/Th ages. A) U/Th ages versus IntCal13-derived calendar ages, B) U/Th ages versus Marine13-derived calendar ages, and C) U/Th ages versus Marine13-derived ages with an additional reservoir age correction of 400 yr. D, E, and F are enlargements of boxed regions in A, B, and C, respectively. In all panels blue squares are dates from this study following the method of Bush et al. (2013) and black filled diamonds are dates from Thiagarajan, Gerlach, et al. (2013) following the method of Burke, Laura F. Robinson, et al. (2010). U/Th ages are reported in Chapter 3. Gray bars mark inflection in U/Th-age ^{14}C-age relationship at ~14 ka.

seems that the Marine13-derived reconnaissance ages with the additional reservoir correction are best for selecting samples to more precisely U/Th date in the ~10–30 kyr age range. This is especially true for the Southern Ocean samples, where surface reservoir ages tend to be higher than in the North Atlantic.

2.4 Discussion

In general, the distribution of deep-sea corals that we observe over the past ~50 kyr are in agreement with previously published data from Thiagarajan, Gerlach, et al. (2013), but the addition of 331 more samples brings a few more interesting patterns to light. The first of these new patterns is the gradual movement of the deep-sea coral population towards shallower and more restricted depths between ~40 and 20 ka (Figure 2.4). One way to explain this trend is by invoking a change in the aragonite saturation horizon. The aragonite saturation state ($\Omega_{\text{arag.}}$) is defined as the in situ ion product of calcium and carbonate divided by the solubility product

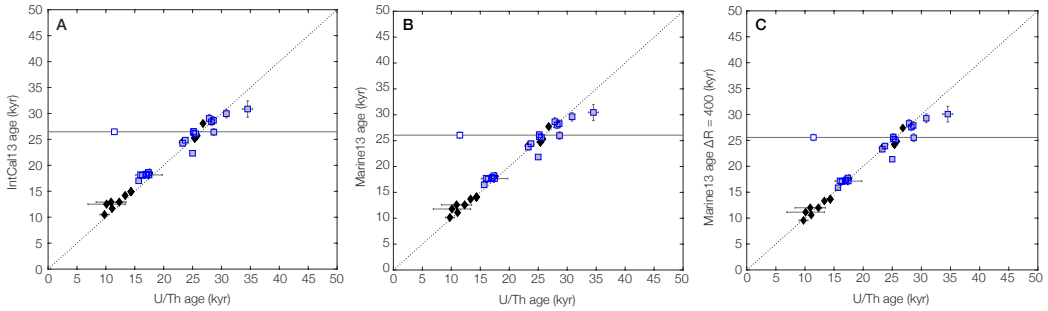

Figure 2.3: Comparison of North Atlantic radiocarbon reconnaissance dates and precise U/Th ages. A) U/Th ages versus IntCal13-derived calendar ages, B) U/Th ages versus Marine13-derived calendar ages, and C) U/Th ages versus Marine13-derived ages with an additional reservoir age correction of 400 yr. In both panels blue squares are dates from this study following the method of Bush et al. (2013) and black filled diamonds are dates from Thiagarajan, Gerlach, et al. (2013) following the method of Burke, Laura F. Robinson, et al. (2010). One sample (blue unfilled square) fell off the 1:1 line but has extremely large error bars (±95,000 yr on an age of 11,500 yr) due to high ^{232}Th (470,000 ppt). U/Th ages are reported in Chapter 5.

of the aragonite mineral. If more CO_2 was stored in the deep ocean during the late glacial period (as has been hypothesized by many, e.g. Broecker, 1982; Sigman and Boyle, 2000; Sigman, Hain, and Haug, 2010), this should drive a decrease in deep ocean $[CO_3^{2-}]$, assuming the rest of the system stays the same. Indeed, Yu, Elderfield, and Piotrowski (2008) observe decreases in deep ocean $[CO_3^{2-}]$ compared to the Holocene in the high-latitude North Atlantic, and there is some evidence for decreases in intermediate water $[CO_3^{2-}]$ in the Indo-Pacific (Allen et al., 2015). There is also evidence for changes in ocean circulation configuration, with shoaled North Atlantic Deep Water and an expansion of Antarctic Bottom Water in the Atlantic bains (Curry and Oppo, 2005; Lund, Adkins, and Ferrari, 2011; L.C. Skinner et al., 2017). This would have a much larger effect on the North Atlantic samples, because there is already a large fraction of southern-source water in the region south of Tasmania. In the modern ocean near Tasmania and the New England and Corner Rise Seamounts, much of the water between ~1000–2000 m is very close to the aragonite saturation horizon (Thiagarajan, Gerlach, et al., 2013), therefore even small changes in $[CO_3^{2-}]$ could drive the water to undersaturation. At the end of the LGM around 18 ka, atmospheric CO_2 begins to rise (Marcott et al., 2014). There is evidence that this CO_2 rise was driven by the degassing of the lower cell (Anderson et al., 2009; Burke and L F Robinson, 2012), which would lead to a deepening of the aragonite saturation horizon again.

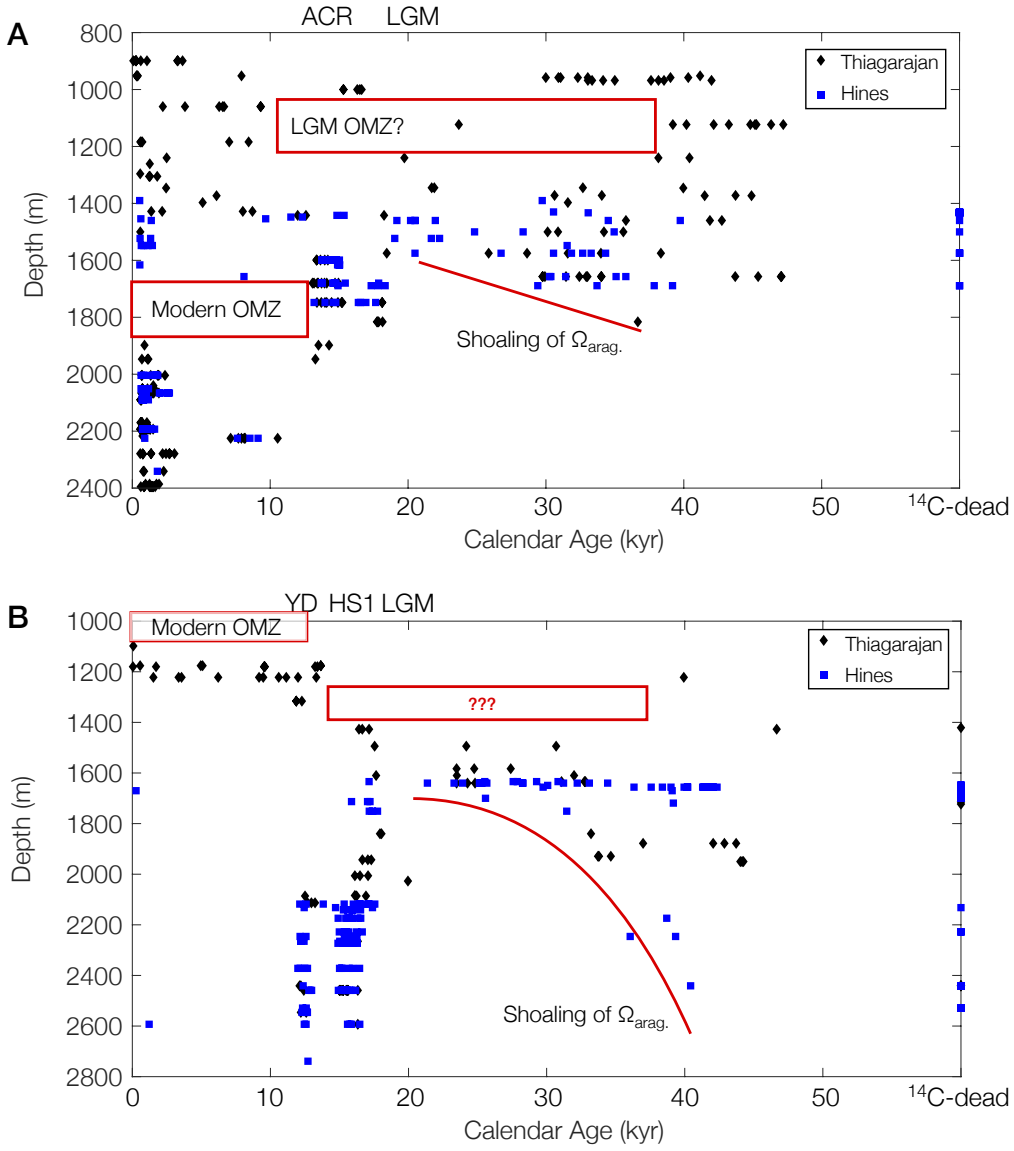

Figure 2.4: Annotated age-depth plot for Southern Ocean (A) and North Atlantic (B). Ages for all samples have been determined using the Marine13 radiocarbon calibration curve (Reimer, Bard, et al., 2013) with an additional reservoir correction of 400 years. Diamonds are from Thiagarajan, Gerlach, et al. (2013) and squares are from this study. Boxes marking the locations of the modern OMZs are based on hydrographic data (Thiagarajan, Gerlach, et al., 2013).

Another pattern that becomes clearer with the addition of new data presented here is the potential shift in the oxygen minimum zone (Figure 2.4). In the Southern Ocean, the OMZ is also associated with the return flow of old Pacific Deep Water (see Figure 3.1). At the LGM, if circulation switched such that NADW was shoaled and the upper and lower circulation cells were less intertwined, then the core of Pacific Deep Water should deepen relative to its modern arrangement in order for the lower cell to close on itself (Ferrari et al., 2014; Talley, 2013). This type of circulation configuration change could explain the presence of corals at the depth of the modern OMZ at other points during the late glacial. A two-cell circulation configuration, and thus a deepening of Pacific Deep Water return flow does not explain a shoaled OMZ during the late glacial. If the OMZ near Tasmania did shift, it is difficult to explain why this might have occurred. In general, as Thiagarajan, Gerlach, et al. (2013) note, the LGM ocean should be more oxygenated due to the temperature dependence of O_2 solubility. Changes in the biological productivity of surface waters could increase or decrease the intensity of an OMZ, but they shouldn't change its depth. That leaves changes in circulation as the most likely explanation, but it is difficult to imagine what these changes might have been.

There is potentially more information that can be gleaned from the radiocarbon age-U/Th age plot as well (Figure 2.2). As was discussed above, the radiocarbon-derived calendar ages depend on both the ventilation age of the water (the amount of time that has elapsed since the water was at the surface) and the surface reservoir age (the depletion in surface water radiocarbon relative to the atmosphere). Southern Ocean reservoir ages tend to be old, because the amount of time that water typically spends at the surface is shorter than the isotopic equilibration time ($O(10)$ years). During the LGM, Southern Ocean reservoir ages were thought to be much older because the deep ocean was more depleted in radiocarbon and expanded sea ice could have further impeded isotopic equilibration with the atmosphere (L Skinner et al., 2015; Sikes et al., 2000). If we look at the bottom panels of Figure 2.2, there seems to be a slight inflection in the data at around 14 ka, marked with gray bars. This coincides with the Bølling-Allerød/Antarctic Cold Reversal, a time of resumed North Atlantic Deep Water formation and warm temperatures in the Northern Hemisphere and cooling in the Southern Hemisphere. It is also a time when circulation appears to have shifted towards a more modern-like configuration (Thiagarajan, Subhas, et al., 2014) and much of the CO_2-rich, radiocarbon depleted LGM water has been ventilated (Burke and L F Robinson, 2012). It would make sense, therefore, that this time period would be associated with a shift toward younger surface reservoir

ages in the Southern Ocean.

2.5 Conclusion

As we have discussed, radiocarbon screening is a vital tool for the construction of paleoceanographic records using deep-sea corals, and its usefulness extends beyond merely enabling sample selection. The screening method developed by Bush et al. (2013) allows high sample throughput (we prepared 331 samples for AMS measurement in 3 days) and relatively low error (~3‰). Newly screened North Atlantic and Southern Ocean deep-sea corals adhere to the same basic trends in depth and time highlighted by Thiagarajan, Gerlach, et al. (2013). The abundance of deep-sea corals and the depth range of the coral population is contracted during the LGM and expanded during the deglaciation, particularly at abrupt cooling events—the Antarctic Cold Reversal in the Southern Ocean and the Younger Dryas and Heinrich Stadial 1 in the North Atlantic.

The addition of 331 samples presented here also reveal some new patterns in the deep-sea coral population distribution over the past ~50 ka. We see evidence for a shoaling of the aragonite saturation horizon starting around 40 ka and reaching a maximum at the LGM. This trend is likely driven by CO_2 storage in the deep ocean, which drives the carbonate system toward lower $[CO_3^{2-}]$. We also see potential evidence for a shift in the oxygen minimum zone to a shallower depth during the LGM compared to the modern. This shift is somewhat difficult to explain. It is unlikely that changes in surface productivity would shift the depth of the oxygen minimum zone, and in general, the LGM ocean should be more oxygenated due to the temperature dependence of oxygen solubility. The most likely explanation, therefore, is changes to local circulation. In the modern ocean, the local oxygen minimum zone is associated with the return flow of Pacific Deep Water. During the LGM, however, Pacific Deep Water should return at a deeper depth, making the source of this low-oxygen water mass mysterious.

Because many of the reconnaissance dated deep-sea corals have subsequently been U/Th dated, we are able to assess different methods of converting our radiocarbon ages to calendar age. We find the best match between samples converted using the Marine13 radiocarbon calibration curve with an additional reservoir correction of 400 years. We also see evidence for a systematic shift in Southern Ocean reservoir ages toward younger values around the start of the Bølling-Allerød/Antarctic Cold Reversal. By this time in the deglaciation, much of the old, radiocarbon-depleted

water from the deep ocean has been ventilated via the Southern Ocean, releasing its stored CO_2 to the atmosphere.

Table 2.1: Southern Ocean reconnaissance dates. Samples marked with reference "NT" were screened according to the method of Burke, Laura F. Robinson, et al. (2010) by Thiagarajan, Gerlach, et al. (2013). Samples with reference "SH" were screened for this study according to the method of Bush et al. (2013). Radiocarbon-dead samples are assigned a dummy value of 60,000 with no error on the age.

Sample Name	Depth (m)	Lab Code	^{14}C age (yr)	1σ err	IntCal13 age (yr)	1σ err	Marine13 age (yr)	1σ err	Marine13 age ΔR=400 (yr)	1σ err	Ref.
TN228-J2-386-1223-1345-011-899-003	899	NTWH2-H45	871	23	782	45	492	19	75	51	NT
TN228-J2-386-1223-1345-011-0899-009	899	esh05	995	27	901	45	581	30	230	45	NT
TN228-J2-386-1223-1345-011-0899-007	899	ESH02	1449	41	1347	36	999	51	613	38	NT
TN228-J2-386-1223-1345-011-0899-006	899	NTWH2-H46	1028	17	944	11	601	28	275	22	NT
TN228-J2-386-1223-1345-011-0899-010	899	NTWH2-H47	1038	18	947	13	609	29	283	23	NT
TN228-J2-386-1223-1345-001-0899-004	899	esh03	1909	23	1855	27	1455	40	1062	45	NT
TN228-J2-386-1223-1345-011-0899-008	899	esh04	3794	30	4177	54	3738	52	3263	48	NT
TN228-J2-386-1223-1345-011-0899-002	899	esh01	3833	33	4243	71	3782	55	3302	49	NT
TN228-J2-386-1223-1345-011-0899-001	899	ESG03	4124	26	4672	82	4182	52	3645	46	NT
TN228-J2-384-1218-0950-02-0952-03	952	ESF05	1057	17	957	21	626	26	301	29	NT
TN228-J2-384-1218-0950-02-0952-06	952	ESG02	1090	24	1000	33	652	24	340	38	NT
TN228-J2-384-1218-0950-02-0952-04	952	esf07	1156	22	1075	54	700	26	396	40	NT
TN228-J2-384-1218-0950-02-0952-05	952	ESG01	7861	39	8666	75	8324	45	7918	44	NT
TN228-J2-389-1218-0950-02-0952-01	952	ESF06	37332	1573	41956	1548	41565	1555	41182	1569	NT
TN228-J2-386-1223-0739-07-0958-001	958	esh06	26580	330	30737	290	30357	365	29991	404	NT
TN228-J2-386-1223-0739-07-0958-003	958	ESH07	27625	482	31730	532	31323	468	30902	434	NT
TN228-J2-386-1223-0739-07-0958-004	958	esh07	27804	374	31797	452	31396	357	31063	271	NT
TN228-J2-386-1223-0739-07-0958-009	958	esi02	29116	432	33184	514	32721	567	32313	551	NT
TN228-J2-386-1223-0739-07-0958-005	958	ESH08	29841	618	33954	616	33484	677	33037	702	NT
TN228-J2-386-1223-0739-07-0958-008	958	esi01	35287	940	39934	974	39508	1052	39034	1125	NT
TN228-J2-386-1223-0739-07-0958-005	958	ESH08-2	36506	1088	41035	983	40680	1013	40322	1059	NT
TN228-J2-390-0104-0815-16-968-006	968	ESJ05	29846	620	33959	618	33490	679	33042	704	NT
TN228-J2-390-0104-0815-16-968-005	968	NTWH2-H44	30126	635	34254	602	33815	657	33347	706	NT
TN228-J2-390-0104-0815-016-968-002	968	ESJ04	30824	709	34943	708	34560	686	34147	713	NT
TN228-J2-390-0104-0815-16-968-008	968	esj07	31746	607	35787	709	35373	637	34995	597	NT

Sample Name	Depth (m)	Lab Code	^{14}C age (yr)	1σ err	IntCal13 age (yr)	1σ err	Marine13 age (yr)	1σ err	Marine13 age ΔR=400 (yr)	1σ err	Ref.
TN228-J2-390-0104-0815-16-968-004	968	NTWH2-H43	33998	1066	38476	1281	38034	1277	37621	1271	NT
TN228-J2-390-0104-0815-16-968-009	968	esj08	34586	853	39167	1014	38653	1066	38163	1062	NT
TN228-J2-390-0104-0815-16-968-007	968	ESJ06	34860	1160	39466	1287	39012	1344	38564	1370	NT
TN228-J2-390-0104-0815-16-968-003	968	NTWH2-H42	38087	1745	42793	1757	42401	1774	42010	1787	NT
TN228-J2-386-1223-0515-04-1000-003	1000	esj01	13627	61	16432	122	15894	107	15299	114	NT
TN228-J2-386-1223-0515-04-1000-008	1000	esj03	13639	69	16451	132	15909	115	15323	127	NT
TN228-J2-386-123-0515-04-1000-002	1000	esi04	14342	81	17471	131	16892	156	16315	138	NT
TN228-J2-386-1223-0515-04-1000-007	1000	esj02	14476	85	17650	126	17109	156	16503	156	NT
TN228-J2-386-1223-0515-04-1000-001	1000	ESI03	14562	105	17737	134	17228	165	16633	184	NT
TN228-J2-385-1221-0558-05-1060-001	1060	NTWH2-C01	2936	24	3090	47	2719	23	2213	47	NT
TN228-J2-385-1221-0558-05-1060-002	1060	NTWH2-C02	4261	30	4833	36	4368	53	3820	54	NT
TN228-J2-385-1221-0558-05-1060-007	1060	NTWH2-h02	6280	39	7209	47	6735	55	6300	45	NT
TN228-J2-385-1221-0558-05-1060-006	1060	NTWH2-h01	6525	42	7440	46	7040	63	6554	58	NT
TN228-J2-385-1221-0558-05-1060-005	1060	ntwh2-c05	6612	26	7508	34	7143	48	6658	42	NT
TN228-J2-385-1221-0558-05-1060-004	1060	ntwh2-c04	9028	35	10208	28	9708	77	9299	60	NT
TN228-J2-385-1221-0558-05-1060-003	1060	ntwh2-c03	9050	36	10218	20	9745	79	9324	55	NT
TN228-J2-385-1221-0229-04-1123-001	1123	ntwh2-c06	20464	144	24656	233	24126	180	23680	192	NT
TN228-J2-385-1221-0229-04-1123-006	1123	ntwh2-c11	35430	968	40072	979	39662	1053	39206	1132	NT
TN228-J2-385-1221-0229-04-1123-004	1123	ntwh2-c09	36367	1096	40913	1000	40557	1035	40192	1088	NT
TN228-J2-385-1221-0229-04-1123-009	1123	ntwh2-c14	38456	1385	42913	1266	42545	1279	42167	1290	NT
TN228-J2-385-1221-0229-04-1123-007	1123	ntwh2-c12	39518	1591	43935	1514	43609	1517	43268	1528	NT
TN228-J2-385-1221-0229-04-1123-008	1123	ntwh2-c13	41166	1945	45408	1805	45114	1822	44823	1839	NT
TN228-J2-385-1221-0229-04-1123-005	1123	NTWH2-C10	41530	2452	45777	1988	45523	2038	45266	2089	NT
TN228-J2-385-1221-0229-04-1123-002	1123	ntwh2-c07	41566	2049	45730	1830	45445	1860	45164	1885	NT
TN228-J2-385-1221-0229-04-1123-010	1123	ntwh2-c15	43249	2518	46799	1756	46566	1824	46331	1885	NT
TN228-J2-385-1221-0229-04-1123-003	1123	ntwh2-c08	45306	3251	47561	1557	47390	1633	47214	1709	NT
TN228-J2-385-1221-026-02-1184-002	1184	ntwh2-c17	1397	21	1308	14	944	29	582	28	NT
TN228-J2-385-1221-026-02-1184-004	1184	ntwh2-c19	1474	25	1358	26	1018	42	638	27	NT
TN228-J2-385-1221-026-02-1184-003	1184	ntwh2-c18	1587	22	1470	37	1151	41	724	30	NT
TN228-J2-385-1221-026-02-1184-001	1184	NTWH2-C16	6913	32	7741	39	7425	36	7028	57	NT
TN228-J2-385-1221-026-02-1184-005	1184	ntwh2-c20	8376	38	9399	54	8961	64	8436	45	NT

Sample Name	Depth (m)	Lab Code	^{14}C age (yr)	1σ err	IntCal13 age (yr)	1σ err	Marine13 age (yr)	1σ err	Marine13 age ΔR=400 (yr)	1σ err	Ref.
TN228-J2-385-1220-2749-01-1240-003	1240	ntwh2-c23	3162	26	3392	32	2948	50	2490	72	NT
TN228-J2-385-1220-2749-01-1240-001	1240	NTWH2-C21	17141	119	20683	162	20199	160	19731	157	NT
TN228-J2-385-1220-2749-01-1240-002	1240	ntwh2-c22	34579	856	39158	1019	38644	1069	38156	1065	NT
TN228-J2-385-1220-2749-01-1240-004	1240	ntwh2-c24	36605	1111	41124	1000	40768	1027	40412	1069	NT
TN228-J2-389-0101-1024-10-1261-001	1261	NTWH2-G30	2112	24	2084	45	1693	48	1267	27	NT
TN228-J2-389-0101-0930-07-1296-001	1296	NTWH2-G31	1380	23	1299	13	927	31	572	30	NT
TN228-J2-382-1216-1930-16-1305-002	1305	ntwh2-c26	2058	24	2027	42	1627	42	1222	31	NT
TN228-J2-382-1216-1930-16-1305-002	1305	ntwh2-C26-2	2127	20	2107	50	1715	44	1280	24	NT
TN228-J2-382-1216-1930-16-1305-001	1305	NTWH2-C25	2608	24	2747	10	2288	42	1806	42	NT
TN228-J2-395-0114-0555-17-1345-009	1345	esm02	18736	120	22622	141	22182	149	21715	171	NT
TN228-J2-395-0114-0555-17-1345-010	1345	esm03	18873	119	22742	153	22318	146	21904	177	NT
TN228-J2-395-0114-0555-17-1345-005	1345	esm01	29479	451	33588	470	33126	543	32679	582	NT
TN228-J2-383-1217-1800-09-1346-001	1346	NTWH2-C27	3141	26	3362	41	2920	48	2450	66	NT
TN228-J2-383-1217-1800-09-1346-002	1346	ntwh2-c28	36126	1038	40700	963	40341	1006	39962	1069	NT
TN228-J2-382-1216-1820-14-1372-001	1372	NTWH2-C29	27321	416	31365	394	30997	331	30625	387	NT
TN228-J2-382-1216-1820-14-1372-002	1372	ntwh2-c30	30734	536	34773	509	34418	478	34053	499	NT
TN228-J2-382-1216-1820-14-1372-003	1372	ntwh2-c31	40011	1683	44386	1619	44074	1619	43752	1626	NT
TN228-J2-389-0101-0732-04-1373-002	1373	NTWH2-G38-2	6101	33	6986	71	6528	51	6108	57	NT
TN228-J2-389-0101-0732-04-1373-005	1373	NTWH2-g39	37572	1763	42305	1802	41908	1816	41514	1832	NT
TN228-J2-389-0101-0732-04-1373-006	1373	NTWH2-g40	40956	2607	45437	2119	45178	2180	44910	2245	NT
TN228-J2-383-1217-1611-07-1397-003	1397	esl02	5208	31	5963	40	5567	40	5102	74	NT
TN228-J2-383-1217-1611-07-1397-001	1397	ESL01-2	28263	507	32304	601	31962	575	31591	538	NT
TN228-J2-389-0101-0330-01-1428-002	1428	esj10	2234	26	2235	51	1836	41	1373	42	NT
TN228-J2-389-0101-0330-01-1428-001	1428	ESJ09	2894	26	3027	47	2680	42	2165	56	NT
TN228-J2-389-0101-0330-01-1428-007	1428	esk01	7956	35	8829	96	8416	42	8015	48	NT
TN228-J2-389-0101-0330-01-1428-010	1428	esk02	8605	38	9568	38	9265	68	8713	80	NT
TN228-J2-393-0112-0730-13-1442-008	1442	NTWH2-H41	11047	58	12910	78	12590	56	11993	136	NT
TN228-J2-393-0112-0730-13-1442-007	1442	NTWH2-H40	11450	58	13294	69	12916	89	12593	56	NT
TN228-J2-393-0112-0730-13-1442-001	1442	NTWH2-G37	15830	126	19117	161	18684	129	18258	159	NT
TN228-J2-383-1217-1320-05-1460-003	1460	ntwh2-c37	32520	668	36759	860	36269	850	35802	786	NT
TN228-J2-383-1217-1320-05-1460-002	1460	ntwh2-c36	38188	1339	42648	1215	42272	1228	41893	1237	NT

Sample Name	Depth (m)	Lab Code	^{14}C age (yr)	1σ err	IntCal13 age (yr)	1σ err	Marine13 age (yr)	1σ err	Marine13 age ΔR=400 (yr)	1σ err	Ref.
TN228-J2-383-1217-1320-05-1460-001	1460	NTWH2-C35	38850	1756	43501	1728	43137	1752	42760	1773	NT
TN228-J2-383-1217-1024-04-1500-01	1500	NTWH2-D01-2	1391	29	1308	18	939	37	578	31	NT
TN228-J2-395-0114-0057-9-1500-004	1500	ESK03-2	26753	428	30844	363	30465	418	30124	458	NT
TN228-J2-395-0114-0057-9-1500-004	1500	ESK03	27601	477	31702	524	31295	456	30877	427	NT
TN228-J2-395-0114-0057-9-1500-005	1500	esk04	30896	538	34922	523	34558	490	34208	484	NT
TN228-J2-395-0114-0057-9-1500-009	1500	esk06	32360	646	36556	841	36059	802	35614	725	NT
TN228-J2-383-1217-0725-01-1575-006	1575	ntwh2-d07	15995	81	19303	127	18840	84	18454	106	NT
TN228-J2-383-1217-0725-01-1575-001	1575	NTWH2-D02	22366	221	26663	285	26243	246	25845	204	NT
TN228-J2-383-1217-0725-01-1575-002	1575	ntwh2-d03	25393	269	29535	372	29069	303	28631	303	NT
TN228-J2-383-1217-0725-01-1575-003	1575	ntwh2-d04	28376	391	32359	526	31973	487	31582	426	NT
TN228-J2-383-1217-0725-01-1575-004	1575	ntwh2-d05	30669	537	34715	504	34362	478	33987	509	NT
TN228-J2-383-1217-0725-01-1575-005	1575	ntwh2-d06	34729	873	39338	1009	38836	1075	38338	1089	NT
TN228-J2-387-1226-1635-23-1599-003	1599	ntwh2-d10	12290	51	14253	137	13755	82	13351	58	NT
TN228-J2-387-1226-1635-23-1599-004	1599	ntwh2-d11	12331	58	14354	170	13803	86	13384	64	NT
TN228-J2-387-1226-1635-23-1599-002	1599	ntwh2-d09	12596	54	14936	143	14082	85	13646	86	NT
TN228-J2-357-1226-1635-23-1599-001	1599	NTWH2-D08	12876	67	15385	128	14637	215	13958	87	NT
TN228-J2-387-1226-1635-23-1599-005	1599	ntwh2-d12-2	13058	56	15639	128	15033	125	14183	124	NT
TN228-J2-393-0112-0124-06-1657-009	1657	NTWH2-f09	26350	420	30470	411	30123	452	29749	500	NT
TN228-J2-393-0112-0124-06-1657-007	1657	NTWH2-f07-2	26374	413	30495	403	30146	444	29774	492	NT
TN228-J2-393-0112-0124-06-1657-007	1657	NTWH2-f07	26528	419	30635	388	30274	433	29925	479	NT
TN228-J2-393-0112-0124-06-1657-001	1657	NTWH2-F01	28173	460	32203	561	31844	527	31455	466	NT
TN228-J2-393-0112-0124-06-1657-004	1657	NTWH2-f04	29172	590	33188	672	32771	679	32424	663	NT
TN228-J2-393-0112-0124-06-1657-010	1657	NTWH2-f10-2	29725	630	33821	650	33347	701	32920	712	NT
TN228-J2-393-0112-0124-06-1657-010	1657	NTWH2-f10	29817	637	33925	645	33452	701	33011	719	NT
TN228-J2-393-0112-0124-06-165-006	1657	NTWH2-f06	30693	711	34821	699	34431	692	34000	732	NT
TN228-J2-393-0112-0124-06-165-006	1657	NTWH2-f06-2	30717	715	34846	706	34456	696	34028	735	NT
TN228-J2-393-0112-0124-06-1657-005	1657	NTWH2-f05-2	39619	2185	44391	2074	44068	2123	43730	2174	NT
TN228-J2-393-0112-0124-06-1657-005	1657	NTWH2-f05	41666	2823	45866	2084	45632	2147	45392	2213	NT
TN228-J2-393-0112-0124-06-1657-008	1657	NTWH2-f08-2	46145	4934	47333	1751	47187	1822	47040	1891	NT
TN228-J2-393-0112-0124-06-1657-008	1657	NTWH2-f08	46407	5116			47230	1808	47086	1877	NT
TN228-J2-387-1226-1148-20-1680-009	1680	NTWH2-H21	11997	92	13860	120	13457	103	13068	112	NT

Sample Name	Depth (m)	Lab Code	^{14}C age (yr)	1σ err	IntCal13 age (yr)	1σ err	Marine13 age (yr)	1σ err	Marine13 age ΔR=400 (yr)	1σ err	Ref.
TN228-J2-387-1226-1148-20-1680-07	1680	NTWH2-H23	12094	64	13945	96	13547	88	13181	76	NT
TN228-J2-387-1226-1148-20-1680-001	1680	ESE01	12369	61	14432	184	13847	86	13417	70	NT
TN228-J2-387-1226-1148-20-1680-004	1680	ESE04	12429	64	14548	203	13911	86	13478	83	NT
TN228-J2-387-1126-1148-20-1680-06	1680	NTWH2-H24	12667	70	15044	145	14228	163	13724	100	NT
TN228-J2-387-1226-1148-20-1680-08	1680	NTWH2-H25	12856	90	15366	153	14601	237	13938	110	NT
TN228-J2-387-1226-1148-20-1680-010	1680	NTWH2-H22	12998	75	15547	142	14898	189	14103	128	NT
TN228-J2-387-1226-1148-20-1680-003	1680	ESE03	13306	70	16001	116	15421	131	14704	219	NT
TN228-J2-387-1226-1148-20-1680-002	1680	ESE02	13421	70	16148	115	15571	139	14950	166	NT
TN228-J2-387-1226-0615-017-1748-002	1748	ntwh2-e02	12342	51	14365	163	13817	79	13392	60	NT
TN228-J2-387-1226-0615-017-1748-012	1748	ntwh2-e10	12651	53	15032	121	14165	112	13708	86	NT
TN228-J2-387-1226-0615-017-1748-008	1748	ntwh2-e06	12893	59	15406	120	14680	207	13974	81	NT
TN228-J2-387-1226-0615-017-1748-005	1748	ntwh2-e04	13007	57	15558	126	14943	146	14098	94	NT
TN228-J2-387-1226-0615-017-1748-007	1748	ntwh2-e05	13181	68	15839	120	15231	117	14452	195	NT
TN228-J2-387-1226-0615-017-1748-010	1748	ntwh2-e08	13393	58	16112	101	15531	125	14915	156	NT
TN228-J2-387-1226-0615-017-1748-001	1748	NTWH2-E01	13548	71	16328	126	15779	134	15177	125	NT
TN228-J2-387-1226-0615-017-1748-009	1748	ntwh2-e07	13583	71	16377	128	15833	125	15235	123	NT
TN228-J2-387-1226-0615-017-01748-011	1748	ntwh2-e09	15704	78	18956	96	18568	95	18117	112	NT
TN228-J2-387-1226-0615-017-1748-004	1748	ntwh2-e03	15710	79	18963	98	18574	96	18124	113	NT
TN228-J2-393-0111-1851-02-1816-002	1816	NTWH2-G32	15371	98	18636	106	18190	131	17742	127	NT
TN228-J2-393-0111-1851-2-1816-005	1816	NTWH2-g34	15428	99	18691	102	18252	136	17798	128	NT
TN228-J2-393-0111-1851-2-1816-007	1816	NTWH2-g35	15490	100	18749	100	18325	138	17867	133	NT
TN228-J2-393-0111-1851-2-1816-004	1816	NTWH2-g33	15732	104	18998	127	18591	115	18151	134	NT
TN228-J2-393-0111-1851-2-1816-008	1816	NTWH2-g36	33111	966	37494	1159	37081	1162	36666	1167	NT
TN 228-J2-387-1225-1253-11-1898-003	1898	ESA03	1739	17	1652	32	1289	22	883	32	NT
TN 228-J2-387-1225-1253-11-1898-002	1898	ESA02	12452	62	14595	206	13934	84	13502	84	NT
TN 228-J2-387-1225-1253-11-1898-001	1898	ESA01	13089	67	15689	139	15078	133	14269	169	NT
TN228-J2-395-0113-1830-5-1947-004	1947	ESD05	1553	17	1465	38	1113	36	696	23	NT
TN228-J2-395-0113-1830-5-1947-009	1947	ESD07	1945	17	1894	23	1493	38	1105	36	NT
TN228-J2-395-0113-1830-5-1947-002	1947	ESD03	1997	19	1946	27	1559	34	1164	39	NT
TN228-J2-395-0113-1830-5-1947-003	1947	ESD04	12204	60	14102	104	13655	90	13278	65	NT
TN228-J2-387-1225-0439-04-2004-009	2004	ntwh2-e18	1517	20	1405	41	1073	42	671	21	NT

Sample Name	Depth (m)	Lab Code	^{14}C age (yr)	1σ err	IntCal13 age (yr)	1σ err	Marine13 age (yr)	1σ err	Marine13 age ΔR=400 (yr)	1σ err	Ref.
TN228-J2-387-1225-0439-04-2004-007	2004	ntwh2-e17	1565	26	1465	38	1125	43	707	29	NT
TN228-J2-387-1225-0439-04-2004-001	2004	NTWH2-E11	2194	24	2229	52	1790	42	1333	31	NT
TN228-J2-387-1225-0439-04-2004-006	2004	ntwh2-e16	2633	21	2756	9	2319	30	1836	37	NT
TN228-J2-387-1225-0439-04-2004-010	2004	ntwh2-e19	2705	24	2804	27	2399	46	1917	39	NT
TN228-J2-387-1225-0439-04-2004-011	2004	NTWH2-E20	3079	22	3293	38	2843	41	2371	39	NT
TN228-J2-387-1225-0318-3-2040-001	2040	ESK07	2369	24	2389	43	1994	45	1525	42	NT
TN228-J2-387-1224-2355-1-2051-02	2051	ESC03	1565	33	1463	42	1125	49	710	34	NT
TN228-J2-387-1224-2355-1-2051-09	2051	NTWH2-H39	1601	28	1479	43	1167	44	739	38	NT
TN228-J2-387-1224-2355-1-2051-03	2051	ESC04	1605	37	1484	49	1169	50	748	47	NT
TN 228-J2-387-1224-2355-1-2051-01	2051	ESC02	1941	24	1889	30	1487	42	1100	42	NT
TN228-J2-387-1224-2355-1-2051-06	2051	NTWH2-H27	2429	24	2483	101	2065	44	1596	42	NT
TN228-J2-387-1225-0147-02-2066-008	2066	NTWH2-e23	1511	29	1404	49	1064	49	668	27	NT
TN228-J2-387-1225-0147-02-2066-006	2066	ESD12	1523	25	1421	49	1080	45	677	24	NT
TN228-J2-387-1225-0147-02-2066-001	2066	NTWH2-E21	1726	24	1637	40	1279	26	867	37	NT
TN228-J2-387-1225-0147-02-2066-007	2066	NTWH2-E22	1870	23	1809	42	1417	43	1013	39	NT
TN228-J2-387-1225-0147-02-2066-003	2066	ESD09	2078	19	2049	36	1648	40	1239	27	NT
TN228-J2-387-1225-0147-02-2066-010	2066	NTWH2-e25	2144	20	2151	69	1736	41	1294	24	NT
TN228-J2-387-1225-0147-02-2066-010	2066	NTWH2-e25-2	2153	21	2179	74	1746	40	1301	25	NT
TN228-J2-387-1225-0147-02-2066-005	2066	ESD11	2184	19	2232	55	1778	38	1324	26	NT
TN228-J2-387-1225-0147-02-2066-004	2066	ESD10	2344	21	2353	17	1961	41	1491	40	NT
TN228-J2-387-1225-0147-02-2066-009	2066	NTWH2-e24	2392	21	2410	51	2023	42	1554	36	NT
TN228-J2-387-1225-0147-02-2066-002	2066	ESD08	2716	18	2811	24	2407	44	1928	35	NT
TN228-J2-395-0113-1530-03-2090-007	2090	NTWH2-h30	1384	72	1300	71	932	85	576	53	NT
TN228-J2-395-0113-1530-03-2090-010	2090	NTWH2-H33	1450	22	1338	21	994	36	618	29	NT
TN228-J2-395-0113-1530-03-2090-008	2090	NTWH2-h31	1461	69	1378	67	1019	79	626	59	NT
TN228-J2-395-0113-1530-03-2090-009	2090	NTWH2-h32	1473	65	1386	65	1030	75	635	58	NT
TN228-J2-395-0113-1530-03-2090-005	2090	NTWH2-H28	1487	33	1375	42	1036	50	648	32	NT
TN228-J2-395-0113-1530-03-2090-006	2090	NTWH2-H29	1510	29	1402	48	1063	49	668	27	NT
TN228-J2-390-1615-06-2170-005	2170	NTWH2-f15	1463	20	1348	21	1006	36	631	26	NT
TN228-J2-390-1615-06-2170-001	2170	NTWH2-F11	1414	23	1318	16	960	33	591	29	NT
TN228-J2-390-0103-1615-06-2170-007	2170	NTWH2-h05	1488	52	1392	60	1042	65	648	49	NT

Sample Name	Depth (m)	Lab Code	^{14}C age (yr)	1σ err	IntCal13 age (yr)	1σ err	Marine13 age (yr)	1σ err	Marine13 age ΔR=400 (yr)	1σ err	Ref.
TN228-J2-390-1615-06-2170-002	2170	NTWH2-f12	1515	31	1412	52	1069	50	672	29	NT
TN228-J2-390-1615-06-2170-004	2170	NTWH2-f14	1580	20	1468	35	1142	40	717	28	NT
TN228-J2-390-0103-1615-06-2170-006	2170	NTWH2-H04-2	1538	25	1446	47	1097	43	688	26	NT
TN228-J2-390-1615-06-2170-003	2170	NTWH2-f13	1906	20	1853	24	1452	38	1058	43	NT
TN228-J2-395-0113-1206-01-2193-023	2193	NTWH2-H13	1366	24	1292	14	912	33	562	31	NT
TN228-J2-395-0113-1206-01-2193-029	2193	NTWH2-H19	1461	39	1354	38	1010	51	623	38	NT
TN228-J2-395-0113-0902-01-2193-001	2193	ESC07	1500	18	1379	23	1049	42	659	19	NT
TN228-J2-395-0113-0902-01-2193-006	2193	ESD02	1521	21	1414	46	1078	42	674	22	NT
TN228-J2-395-0113-0902-01-2193-007	2193	ESD02	1532	17	1434	47	1091	38	681	21	NT
TN228-J2-395-0113-0902-01-2193-005	2193	NTWH2-E26	1538	23	1446	47	1097	41	687	25	NT
TN228-J2-395-0113-0902-01-2193-09	2193	NTWH2-H10	1571	24	1467	37	1131	42	711	29	NT
TN228-J2-395-0113-1206-01-2193-021	2193	NTWH2-H11	1571	33	1466	41	1131	49	715	36	NT
TN228-J2-395-0113-0902-01-2193-05	2193	NTWH2-H07-2	1624	39	1506	57	1187	48	769	51	NT
TN228-J2-395-0113-1206-01-2193-025	2193	NTWH2-e28	1624	20	1512	45	1195	33	761	37	NT
TN228-J2-395-0113-0902-01-2193-010	2193	NTWH2-H06-2	1686	23	1592	35	1245	28	832	39	NT
TN228-J2-395-0113-1206-01-2193-026	2193	NTWH2-H16	1704	24	1613	41	1260	27	847	38	NT
TN228-J2-395-0113-0902-01-2193-004	2193	ESD01	1713	23	1623	42	1268	26	855	37	NT
J2-395-395-0113-1206-01-2193-025	2193	NTWH2-H15-2	1718	40	1631	50	1271	40	856	48	NT
TN228-J2-395-0113-0902-01-2193-08	2193	NTWH2-H09-2	1788	32	1711	57	1331	36	936	40	NT
TN228-J2-395-0113-0902-01-2193-07	2193	NTWH2-H08-2	1796	24	1726	51	1335	31	943	32	NT
TN228-J2-395-0113-1206-01-2193-024	2193	NTWH2-H14	1793	31	1719	56	1335	36	942	39	NT
TN228-J2-395-0113-0902-01-2193-002	2193	ESC08	1899	17	1848	21	1446	37	1047	41	NT
TN228-J2-395-0113-1206-01-2193-028	2193	NTWH2-H18	1897	24	1844	32	1444	41	1046	45	NT
TN228-J2-395-0113-1206-01-2193-027	2193	NTWH2-H17	1901	24	1848	30	1448	41	1051	45	NT
TN228-J2-385-0113-0902-01-2193-007	2193	NTWH2-E27	1819	28	1757	44	1358	40	967	37	NT
TN228-J2-395-0113-1206-01-2193-022	2193	NTWH2-H12	1976	26	1927	31	1534	43	1137	44	NT
TN228-J2-395-0113-0902-01-2193-003	2193	ESC09	2127	17	2107	43	1715	42	1280	22	NT
TN228-J2-395-0113-0902-01-2193-004	2193	esc09	2150	31	2167	81	1741	49	1300	32	NT
TN228-J2-395-0113-1206-01-2193-030	2193	NTWH2-H20	2358	28	2383	46	1981	48	1508	46	NT
TN228-J2-392-0110-1547-10-2217-001	2217	NTWH2-H26	1598	29	1477	42	1163	45	737	38	NT
TN228-J2-392-0110-1409-08-2225-08	2225	NTWH2-H37	7007	35	7851	50	7499	37	7132	56	NT

Sample Name	Depth (m)	Lab Code	^{14}C age (yr)	1σ err	IntCal13 age (yr)	1σ err	Marine13 age (yr)	1σ err	Marine13 age ΔR=400 (yr)	1σ err	Ref.
TN228-J2-392-01140-1409-08-2225-05	2225	NTWH2-H36	7630	30	8422	28	8084	45	7691	41	NT
TN228-J2-392-0110-1409-08-2225-09	2225	NTWH2-H38	7857	55	8687	106	8315	60	7914	59	NT
TN228-J2-392-0110-1409-08-2225-03	2225	ESE06	8063	32	8970	74	8513	46	8114	49	NT
TN228-J2-392-0110-1409-08-2225-02	2225	NTWH2-H35	8112	32	9052	42	8574	51	8181	54	NT
TN228-J2-392-0110-1409-08-2225-01	2225	NTWH2-H34	10052	51	11576	136	11044	82	10542	72	NT
TN228-J2-390-0113-1145-04-2279-03	2279	NTWH2-G03	1384	23	1301	13	932	30	574	29	NT
TN228-J2-390-0113-1145-04-2279-08	2279	NTWH2-G08	1619	33	1498	51	1185	44	761	46	NT
TN228-J2-390-0113-1145-04-2279-09	2279	NTWH2-G09	2220	27	2230	49	1820	43	1358	39	NT
TN228-J2-390-0113-1145-04-2279-002	2279	NTWH2-g02	2226	20	2228	47	1828	37	1362	35	NT
TN228-J2-390-0113-1145-04-2279-06	2279	NTWH2-G06	2918	24	3062	49	2706	27	2196	50	NT
TN228-J2-390-0113-1145-04-2279-10	2279	NTWH2-G10	3138	24	3358	39	2916	46	2443	62	NT
TN228-J2-390-0113-1145-04-2279-001	2279	NTWH2-G01	3298	29	3522	37	3133	53	2682	44	NT
TN228-J2-390-0113-1145-04-2279-004	2279	NTWH2-G04	3312	32	3536	43	3154	57	2695	41	NT
TN228-J2-390-0113-1145-04-2279-07	2279	NTWH2-G07	3319	25	3541	39	3164	49	2706	27	NT
TN228-J2-390-0113-1145-04-2279-05	2279	NTWH2-G05	3638	24	3954	46	3536	42	3054	51	NT
TN228-J2-390-0103-1024-03-2281-001	2281	NTWH2-G11	1622	34	1502	53	1188	44	765	47	NT
TN228-J2-392-0110-1120-07-2341-004	2341	NTWH2-G15	1645	28	1543	45	1211	35	790	45	NT
TN228-J2-392-0110-1120-07-2341-001	2341	NTWH2-G12	1712	23	1622	42	1267	26	854	37	NT
TN228-J2-392-0110-1120-07-2341-003	2341	NTWH2-G14	2999	24	3182	49	2770	30	2276	44	NT
TN228-J2-391-0109-0930-25-2386-003	2386	NTWH2-g18	1809	29	1745	49	1348	38	958	37	NT
TN228-J2-391-0109-0930-25-2386-001	2386	NTWH2-G16	2095	26	2066	42	1670	48	1252	29	NT
TN228-J2-391-0109-0930-25-2386-004	2386	NTWH2-g19	2557	24	2695	68	2230	46	1750	42	NT
TN228-J2-391-0109-0930-25-2386-002	2386	NTWH2-g17	2726	24	2817	27	2425	55	1940	41	NT
TN228-J2-390-0103-0815-02-2395-006	2395	NTWH2-G25	1447	27	1338	23	992	39	614	32	NT
TN228-J2-390-0103-0815-02-2395-003	2395	NTWH2-g22	1692	27	1601	40	1249	30	837	40	NT
TN228-J2-390-0103-0815-02-2395-009	2395	NTWH2-G28	1737	34	1647	46	1289	34	875	44	NT
TN228-J2-390-0103-0815-02-2395-008	2395	NTWH2-G27	2089	24	2060	39	1662	45	1247	29	NT
TN228-J2-390-0103-0815-02-2395-005	2395	NTWH2-g24	2172	24	2217	65	1766	41	1316	28	NT
TN228-J2-390-0103-0815-02-2395-001	2395	NTWH2-g20	2231	23	2232	49	1833	39	1369	39	NT
TN228-J2-390-0103-0815-02-2395-010	2395	NTWH2-G29	2285	25	2300	53	1895	40	1433	43	NT
TN228-J2-390-0103-0815-02-2395-004	2395	NTWH2-g23	2354	25	2371	36	1975	45	1503	44	NT

Sample Name	Depth (m)	Lab Code	^{14}C age (yr)	1σ err	IntCal13 age (yr)	1σ err	Marine13 age (yr)	1σ err	Marine13 age ΔR=400 (yr)	1σ err	Ref.
TN228-J2-390-0103-0815-02-2395-002	2395	NTWH2-g21	2356	24	2371	35	1977	45	1506	43	NT
TN228-J2-390-0103-0815-02-2395-007	2395	NTWH2-G26	2485	26	2588	76	2150	57	1657	46	NT
TN228-J2-383-1217-1710-08-1390-001	1390	SH_IR2_A01	1320	50	1240	49	857	57	533	43	SH
TN228-J2-383-1217-1710-08-1390-003	1390	SH_IR2_A02	26100	1300	30482	1420	30093	1386	29732	1361	SH
TN228-J2-395-0114-0354-15-1430-001	1430	SH_IR2_A03	60000		60000		60000		60000		SH
TN228-J2-395-0114-0354-15-1430-002	1430	SH_IR2_A04	60000		60000		60000		60000		SH
TN228-J2-395-0114-0354-15-1430-003	1430	SH_IR2_A05	26900	1400	31389	1586	30958	1578	30551	1553	SH
TN228-J2-382-1216-1619-11-1433-001	1433	SH_IR2_A06	60000		60000		60000		60000		SH
TN228-J2-382-1216-1619-11-1433-002	1433	SH_IR2_A07	60000		60000		60000		60000		SH
TN228-J2-382-1216-1619-11-1433-003	1433	SH_IR2_A08	60000		60000		60000		60000		SH
TN228-J2-382-1216-1619-11-1433-004	1433	SH_IR2_A09	60000		60000		60000		60000		SH
TN228-J2-382-1216-1619-11-1433-005	1433	SH_IR2_A10	60000		60000		60000		60000		SH
TN228-J2-382-1216-1619-11-1433-006	1433	SH_IR2_A11	29000	1800	33845	2249	33456	2236	33066	2234	SH
TN228-J2-382-1216-1619-11-1433-007	1433	SH_IR2_A12	60000		60000		60000		60000		SH
TN228-J2-382-1216-1619-11-1433-008	1433	SH_IR2_A13	60000		60000		60000		60000		SH
TN228-J2-382-1216-1619-11-1433-009	1433	SH_IR2_A14	60000		60000		60000		60000		SH
TN228-J2-393-0112-0730-13-1442-002	1442	SH_IR2_A16	13400	250	16143	376	15531	399	14842	436	SH
TN228-J2-393-0112-0730-13-1442-003	1442	SH_IR2_A17	13700	260	16584	378	15984	390	15358	444	SH
TN228-J2-387-1226-2330-25-1448-001	1448	SH_IR2_A15	10720	210	12580	259	12044	344	11500	339	SH
TN228-J2-387-1226-2330-25-1448-002	1448	SH_IR2_B01	11340	210	13196	205	12855	206	12332	291	SH
TN228-J2-395-0114-0134-10-1454-001	1454	SH_IR2_B02	1450	70	1369	67	1008	80	618	58	SH
TN228-J2-395-0114-0134-10-1454-004	1454	SH_IR2_B03	9340	140	10591	218	10149	199	9673	186	SH
TN228-J2-383-1217-1320-05-1460-004	1460	SH_IR2_B04	60000		60000		60000		60000		SH
TN228-J2-383-1217-1320-05-1460-005	1460	SH_IR2_B05	34300	3600	40357	3974	40048	4051	39743	4130	SH
TN228-J2-383-1217-1320-05-1460-006	1460	SH_IR2_B06	17740	430	21468	529	20996	545	20500	549	SH
TN228-J2-383-1217-1320-05-1460-007	1460	SH_IR2_B07	18970	540	22965	633	22475	652	21977	657	SH
TN228-J2-383-1217-1320-05-1460-008	1460	SH_IR2_B08	17490	420	21178	528	20686	538	20182	528	SH
TN228-J2-383-1217-1320-05-1460-009	1460	SH_IR2_B09	16630	400	20108	500	19627	475	19188	459	SH
TN228-J2-383-1217-1320-05-1460-010	1460	SH_IR2_B10	17740	430	21468	529	20996	545	20500	549	SH
TN228-J2-383-1217-1320-05-1460-012	1460	SH_IR2_B11	30100	2100	35308	2793	34909	2802	34521	2808	SH
TN228-J2-383-1217-1320-05-1460-014	1460	SH_IR2_B12	2225	50	2232	62	1824	66	1375	59	SH

Sample Name	Depth (m)	Lab Code	^{14}C age (yr)	1σ err	IntCal13 age (yr)	1σ err	Marine13 age (yr)	1σ err	Marine13 age ΔR=400 (yr)	1σ err	Ref.
TN228-J2-395-0114-0057-09-1500-001	1500	SH_IR2_B13	30400	2200	35732	2949	35335	2970	34948	2985	SH
TN228-J2-395-0114-0057-09-1500-003	1500	SH_IR2_B14	24700	1100	29104	1108	28736	1126	28345	1148	SH
TN228-J2-395-0114-0057-09-1500-007	1500	SH_IR2_B15	60000		60000		60000		60000		SH
TN228-J2-395-0114-0057-09-1500-010	1500	SH_IR2_B16	21400	700	25700	779	25245	782	24823	786	SH
TN228-J2-382-1216-1350-03-1523-001	1523	SH_IR2_B17	1365	45	1284	40	907	56	564	38	SH
TN228-J2-382-1216-1350-03-1523-003	1523	SH_IR2_B18	18730	500	22674	594	22168	607	21687	606	SH
TN228-J2-382-1216-1350-03-1523-005	1523	SH_IR2_B19	19220	520	23241	606	22780	614	22284	631	SH
TN228-J2-382-1216-1350-03-1523-007	1523	SH_IR2_B20	16500	370	19940	457	19473	432	19034	426	SH
TN228-J2-382-1216-1350-03-1523-009	1523	SH_IR2_B21	2170	60	2181	89	1759	77	1326	62	SH
TN228-J2-383-1217-0852-03-1548-001	1548	SH_IR2_B22	1980	50	1935	59	1538	69	1138	62	SH
TN228-J2-383-1217-0852-03-1548-002	1548	SH_IR2_B23	1695	45	1610	57	1249	45	835	52	SH
TN228-J2-383-1217-0852-03-1548-003	1548	SH_IR2_B24	2300	80	2325	136	1919	102	1454	89	SH
TN228-J2-383-1217-0852-03-1548-004	1548	SH_IR2_B25	1490	60	1398	64	1046	71	650	56	SH
TN228-J2-383-1217-0852-03-1548-005	1548	SH_IR2_B26	27700	1600	32373	1873	31956	1885	31538	1887	SH
TN228-J2-383-1217-0725-01-1575-007	1575	SH_IR2_B27	26900	1400	31389	1586	30958	1578	30551	1553	SH
TN228-J2-383-1217-0725-01-1575-009	1575	SH_IR2_B28	30000	1000	34184	1130	33705	1118	33282	1077	SH
TN228-J2-383-1217-0725-01-1575-011	1575	SH_IR2_B29	60000		60000		60000		60000		SH
TN228-J2-383-1217-0725-01-1575-013	1575	SH_IR2_C01	28600	1800	33460	2236	33066	2234	32665	2240	SH
TN228-J2-383-1217-0725-01-1575-015	1575	SH_IR2_C02	60000		60000		60000		60000		SH
TN228-J2-383-1217-0725-01-1575-017	1575	SH_IR2_C03	23200	890	27527	911	27124	883	26746	880	SH
TN228-J2-383-1217-0725-01-1575-019	1575	SH_IR2_C04	60000		60000		60000		60000		SH
TN228-J2-383-1217-0725-01-1575-021	1575	SH_IR2_C05	29900	2100	35110	2798	34714	2805	34327	2812	SH
TN228-J2-383-1217-0725-01-1575-023	1575	SH_IR2_C06	17740	440	21469	541	20997	556	20503	561	SH
TN228-J2-383-1217-0725-01-1575-025	1575	SH_IR2_C07	28000	1600	32672	1865	32266	1876	31852	1886	SH
TN228-J2-387-1226-1635-23-1599-006	1599	SH_IR2_C08	13360	240	16080	361	15471	392	14781	417	SH
TN228-J2-387-1226-1635-23-1599-008	1599	SH_IR2_C09	13510	250	16311	374	15700	378	15021	451	SH
TN228-J2-387-1226-1635-23-1599-010	1599	SH_IR2_C10	13050	250	15617	386	14920	445	14379	410	SH
TN228-J2-387-1226-1635-23-1599-012	1599	SH_IR2_C11	12660	220	14941	411	14378	374	13767	276	SH
TN228-J2-387-1226-1635-23-1599-014	1599	SH_IR2_C12	12680	230	14976	426	14411	385	13802	302	SH
TN228-J2-387-1226-1635-23-1599-016	1599	SH_IR2_C13	13000	260	15535	416	14846	449	14313	422	SH
TN228-J2-387-1226-1635-23-1599-018	1599	SH_IR2_C14	12650	220	14923	410	14363	375	13755	272	SH

Sample Name	Depth (m)	Lab Code	^{14}C age (yr)	1σ err	IntCal13 age (yr)	1σ err	Marine13 age (yr)	1σ err	Marine13 age ΔR=400 (yr)	1σ err	Ref.
TN228-J2-387-1226-1635-23-1599-020	1599	SH_IR2_C15	13160	230	15781	341	15115	426	14517	384	SH
TN228-J2-387-1226-1507-22-1616-001	1616	SH_IR2_D01	13430	250	16189	376	15579	391	14888	442	SH
TN228-J2-387-1226-1507-22-1616-002	1616	SH_IR2_D02	13520	250	16326	373	15715	377	15038	452	SH
TN228-J2-387-1226-1507-22-1616-003	1616	SH_IR2_D03	1335	50	1253	47	872	59	545	42	SH
TN228-J2-387-1226-1507-22-1616-004	1616	SH_IR2_D04	13500	250	16296	374	15685	379	15003	450	SH
TN228-J2-393-0112-0124-06-1657-002	1657	SH_IR2_D05	8030	120	8905	180	8526	150	8098	123	SH
TN228-J2-393-0112-0124-06-1657-003	1657	SH_IR2_D06	27600	1600	32272	1876	31852	1886	31433	1885	SH
TN228-J2-393-0112-0124-06-1657-011	1657	SH_IR2_D07	31000	2400	36560	3224	36174	3265	35795	3300	SH
TN228-J2-393-0112-0124-06-1657-013	1657	SH_IR2_D08	26600	1400	31068	1582	30651	1561	30262	1530	SH
TN228-J2-393-0112-0124-06-1657-015	1657	SH_IR2_D09	26700	1400	31174	1585	30752	1567	30357	1538	SH
TN228-J2-393-0112-0124-06-1657-017	1657	SH_IR2_D10	30400	2300	35859	3117	35470	3144	35088	3167	SH
TN228-J2-387-1226-1148-20-1680-005	1680	SH_IR2_D11	12600	230	14842	415	14295	387	13705	273	SH
TN228-J2-387-1226-1148-20-1680-012	1680	SH_IR2_D12	12620	230	14874	419	14325	387	13728	280	SH
TN228-J2-387-1226-1148-20-1680-013	1680	SH_IR2_D13	13260	250	15929	374	15291	438	14651	414	SH
TN228-J2-387-1226-1148-20-1680-014	1680	SH_IR2_E01	13350	270	16069	406	15439	448	14778	453	SH
TN228-J2-387-1226-1148-20-1680-016	1680	SH_IR2_E02	13170	240	15795	357	15130	438	14533	396	SH
TN228-J2-387-1226-1148-20-1680-017	1680	SH_IR2_E03	13750	260	16652	376	16060	391	15444	431	SH
TN228-J2-387-1226-1148-20-1680-018	1680	SH_IR2_E04	12660	240	14941	437	14388	398	13787	312	SH
TN228-J2-387-1226-1148-20-1680-020	1680	SH_IR2_E05	15490	330	18783	380	18322	365	17867	402	SH
TN228-J2-382-1216-1010-01-1689-001	1689	SH_IR2_E06	33660	3480	39807	4015	39493	4093	39182	4172	SH
TN228-J2-382-1216-1010-01-1689-002	1689	SH_IR2_E07	15070	320	18306	353	17844	392	17325	430	SH
TN228-J2-382-1216-1010-01-1689-003	1689	SH_IR2_E08	13450	250	16220	376	15609	387	14920	445	SH
TN228-J2-382-1216-1010-01-1689-004	1689	SH_IR2_E09	15460	340	18749	391	18290	378	17828	418	SH
TN228-J2-382-1216-1010-01-1689-005	1689	SH_IR2_E10	60000		60000		60000		60000		SH
TN228-J2-382-1216-1010-01-1689-006	1689	SH_IR2_E11	60000		60000		60000		60000		SH
TN228-J2-382-1216-1010-01-1689-007	1689	SH_IR2_E12	25800	1200	30124	1266	29757	1236	29409	1222	SH
TN228-J2-382-1216-1010-01-1689-008	1689	SH_IR2_E13	32500	3000	38533	3805	38192	3875	37854	3944	SH
TN228-J2-382-1216-1010-01-1689-009	1689	SH_IR2_E14	15900	400	19270	460	18805	462	18338	454	SH
TN228-J2-382-1216-1010-01-1689-010	1689	SH_IR2_E15	29400	2000	34488	2623	34095	2621	33705	2624	SH
TN228-J2-387-1226-0615-17-1748-003	1748	SH_IR2_E16	13330	290	16041	437	15396	486	14759	474	SH
TN228-J2-387-1226-0615-17-1748-006	1748	SH_IR2_E17	13190	240	15825	357	15167	436	14558	396	SH

Sample Name	Depth (m)	Lab Code	^{14}C age (yr)	1σ err	IntCal13 age (yr)	1σ err	Marine13 age (yr)	1σ err	Marine13 age ΔR=400 (yr)	1σ err	Ref.
TN228-J2-387-1226-0615-17-1748-014	1748	SH_IR2_E18	14770	310	17973	367	17458	410	16937	431	SH
TN228-J2-387-1226-0615-17-1748-015	1748	SH_IR2_E19	14370	280	17470	371	16936	396	16396	413	SH
TN228-J2-387-1226-0615-17-1748-016	1748	SH_IR2_E20	15320	330	18581	372	18137	375	17651	421	SH
TN228-J2-387-1226-0615-17-1748-018	1748	SH_IR2_E21	12780	260	15151	465	14554	421	13978	391	SH
TN228-J2-387-1226-0615-17-1748-019	1748	SH_IR2_E22	12120	220	14144	373	13613	239	13186	225	SH
TN228-J2-387-1226-0615-17-1748-020	1748	SH_IR2_E23	14480	280	17613	360	17080	392	16552	406	SH
TN228-J2-387-1225-0439-04-2004-002	2004	SH_IR2_F01	2590	60	2667	101	2257	80	1782	77	SH
TN228-J2-387-1225-0439-04-2004-004	2004	SH_IR2_F02	2380	70	2475	124	2015	93	1540	89	SH
TN228-J2-387-1225-0439-04-2004-008	2004	SH_IR2_F03	2640	70	2751	97	2337	106	1843	89	SH
TN228-J2-387-1225-0439-04-2004-013	2004	SH_IR2_F04	2400	60	2493	113	2036	83	1564	79	SH
TN228-J2-387-1225-0439-04-2004-015	2004	SH_IR2_F05	1920	60	1861	74	1467	72	1076	72	SH
TN228-J2-387-1225-0439-04-2004-017	2004	SH_IR2_F06	2490	80	2562	111	2148	102	1670	97	SH
TN228-J2-387-1225-0439-04-2004-019	2004	SH_IR2_F07	1470	70	1386	69	1028	79	634	61	SH
TN228-J2-387-1225-0439-04-2004-021	2004	SH_IR2_F08	1670	80	1578	100	1218	84	816	79	SH
TN228-J2-387-1224-2355-01-2051-004	2051	SH_IR2_F09	1470	60	1380	62	1026	70	632	53	SH
TN228-J2-387-1224-2355-01-2051-005	2051	SH_IR2_F10	1540	80	1445	79	1095	87	705	77	SH
TN228-J2-387-1224-2355-01-2051-007	2051	SH_IR2_G01	1600	60	1488	69	1155	68	754	63	SH
TN228-J2-387-1224-2355-01-2051-010	2051	SH_IR2_G02	2020	60	1987	77	1589	78	1174	66	SH
TN228-J2-387-1224-2355-01-2051-012	2051	SH_IR2_G03	1690	60	1603	77	1242	61	830	64	SH
TN228-J2-387-1224-2355-01-2051-014	2051	SH_IR2_G04	1730	60	1649	74	1284	61	867	68	SH
TN228-J2-387-1224-2355-01-2051-017	2051	SH_IR2_G05	1520	60	1425	65	1076	72	680	57	SH
TN228-J2-387-1224-2355-01-2051-018	2051	SH_IR2_G06	1590	60	1479	66	1145	69	745	62	SH
TN228-J2-387-1224-2355-01-2051-020	2051	SH_IR2_G07	1840	70	1768	84	1396	75	997	80	SH
TN228-J2-387-1225-0147-02-2066-011	2066	SH_IR2_G08	2850	70	2980	96	2588	96	2102	97	SH
TN228-J2-387-1225-0147-02-2066-013	2066	SH_IR2_G09	2740	60	2850	62	2476	96	1965	78	SH
TN228-J2-387-1225-0147-02-2066-015	2066	SH_IR2_G10	1560	60	1456	63	1116	71	719	59	SH
TN228-J2-387-1225-0147-02-2066-017	2066	SH_IR2_G11	3270	80	3506	91	3096	111	2605	106	SH
TN228-J2-387-1225-0147-02-2066-019	2066	SH_IR2_G12	1860	80	1789	95	1416	85	1019	89	SH
TN228-J2-387-1225-0147-02-2066-021	2066	SH_IR2_G13	3240	70	3473	79	3057	100	2578	97	SH
TN228-J2-387-1225-0147-02-2066-023	2066	SH_IR2_G14	3330	70	3568	86	3174	98	2689	93	SH
TN228-J2-395-0113-1530-03-2090-001	2090	SH_IR2_G15	1580	70	1474	75	1133	78	740	69	SH

Sample Name	Depth (m)	Lab Code	^{14}C age (yr)	1σ err	IntCal13 age (yr)	1σ err	Marine13 age (yr)	1σ err	Marine13 age ΔR=400 (yr)	1σ err	Ref.
TN228-J2-395-0113-1530-03-2090-002	2090	SH_IR2_G16	2010	60	1974	76	1577	79	1165	67	SH
TN228-J2-395-0113-1530-03-2090-003	2090	SH_IR2_G17	1555	50	1453	55	1112	64	710	49	SH
TN228-J2-395-0113-1530-03-2090-004	2090	SH_IR2_G18	1660	60	1563	81	1212	62	805	64	SH
TN228-J2-395-0113-0902-01-2193-011	2193	SH_IR2_H01	2100	70	2091	102	1681	87	1251	72	SH
TN228-J2-395-0113-0902-01-2193-013	2193	SH_IR2_H02	2440	70	2531	112	2090	97	1613	88	SH
TN228-J2-395-0113-0902-01-2193-015	2193	SH_IR2_H03	2230	80	2226	99	1831	101	1389	83	SH
TN228-J2-395-0113-0902-01-2193-017	2193	SH_IR2_H04	1810	60	1737	76	1365	65	963	71	SH
TN228-J2-395-0113-0902-01-2193-019	2193	SH_IR2_H05	1610	60	1498	71	1165	67	763	63	SH
TN228-J2-395-0113-0902-01-2193-020	2193	SH_IR2_H06	1570	80	1469	83	1122	86	733	77	SH
TN228-J2-392-0110-1409-08-2225-004	2225	SH_IR2_H07	7540	110	8338	111	8008	117	7624	104	SH
TN228-J2-392-0110-1409-08-2225-006	2225	SH_IR2_H08	8420	150	9384	181	9005	206	8528	186	SH
TN228-J2-392-0110-1409-08-2225-007	2225	SH_IR2_H09	1760	70	1683	85	1318	73	902	81	SH
TN228-J2-392-0110-1409-08-2225-010	2225	SH_IR2_H10	8910	150	9976	205	9638	199	9122	193	SH
TN228-J2-392-0110-1120-07-2341-002	2341	SH_IR2_H11	2620	70	2713	108	2304	103	1818	89	SH

Table 2.2: North Atlantic reconnaissance dates. Samples marked with reference "NT" were screened according to the method of Burke, Laura F. Robinson, et al. (2010) by Thiagarajan, Gerlach, et al. (2013). Samples with reference "SH" were screened for this study according to the method of Bush et al. (2013). Radiocarbon-dead samples are assigned a dummy value of 60,000 with no error on the age.

Sample Name	Depth (m)	Lab Code	^{14}C age (yr)	1σ err	IntCal13 age (yr)	1σ err	Marine13 age (yr)	1σ err	Marine13 age ΔR=400 (yr)	1σ err	Ref.
RBDASS05-H05_0818-1926-103-001-1098	1098	UBA06	845	40	764	53	472	34	72	54	NT
ALV-3891-1459-003-012	1176	UAM14	1370	25	1294	14	916	34	565	31	NT
ALV-3891-1459-003-008	1176	UAM19	5130	25	5868	58	5504	37	4956	53	NT
ALV-3891-1459-003-008	1176	UAM19	5200	25	5954	27	5559	35	5089	70	NT
ALV-3891-1459-003-018	1176	UAN06	12600	65	14927	164	14095	107	13651	93	NT
ALV-3891-1459-003-018	1176	UAN06	12600	65	14927	164	14095	107	13651	93	NT
ALV-3891-1646-004-005	1180	UAJ10	830	20	735	24	468	20	46	31	NT
ALV-3891-1646-004-B1	1180	UBA02	2530	30	2622	81	2206	51	1717	51	NT
ALV-3891-1646-004-002	1180	UAO05	9280	50	10457	83	10096	78	9537	57	NT
ALV-3891-1646-004-006	1180	UAO04	9310	40	10509	66	10148	54	9564	52	NT
ALV-3891-1646-004-002	1180	UAO05	9340	45	10554	69	10178	50	9599	63	NT
ALV-3891-1646-004-001	1180	UAO01	12150	65	14016	105	13602	91	13232	70	NT
ALV-3891-1646-004-007	1180	UAN11	12350	75	14414	199	13823	101	13404	80	NT
ALV-3891-1758-006-004	1222	UAM13	2370	30	2404	60	1996	50	1525	48	NT
ALV-3891-1758-006-011	1222	UBB07	3870	20	4314	54	3835	44	3352	35	NT
ALV-3891-1758-006-012	1222	UBB08	4060	30	4552	88	4089	58	3565	49	NT
ALV-3891-1758-006-002	1222	UAM18	6190	25	7084	48	6630	43	6218	32	NT
ALV-3891-1758-006-010	1222	UBB06	8940	75	10039	121	9625	101	9177	102	NT
ALV-3891-1758-006-010	1222	UBB06	9220	45	10382	73	10027	81	9479	39	NT
ALV-3891-1758-006-009	1222	UBB05	10100	50	11689	148	11098	68	10601	67	NT
ALV-3891-1725-005-B2	1222	UBB10	10550	50	12518	77	11789	143	11148	57	NT
ALV-3891-1758-006-001	1222	UAM20	11050	55	12913	76	12594	53	11999	130	NT
ALV-3891-1725-005-006	1222	UAN10	12250	65	14194	143	13705	95	13318	68	NT
ALV-3891-1725-005-009	1222	UAI08	36100	1400	40720	1366	40332	1414	39932	1475	NT
RBDASS05-H05_0818-1450-101-004-1316	1316	UBA04	11200	55	13066	58	12692	58	12278	126	NT

Sample Name	Depth (m)	Lab Code	^{14}C age (yr)	1σ err	IntCal13 age (yr)	1σ err	Marine13 age (yr)	1σ err	Marine13 age ΔR=400 (yr)	1σ err	Ref.
RBDASS05-H05-0818-1450-101-003-1316	1316	NTWH2-A09	10989	51	12856	75	12541	65	11872	127	NT
RBDASS05-H05-0818-1450-101-001-1316	1316	UBA01	10984	45	12846	71	12541	59	11868	115	NT
ALV-3890-1718-006-004	1421	UAL01	60000		60000		60000		60000		NT
RBDASS05-H03-0815-1004-314-3-003-1427	1427	NTWH2-A08	44216	3450	47024	1805	46841	1877	46657	1947	NT
RBDASS05-H03-0815-1004-314-3-001-1427	1427	NTWH2-H48	14899	90	18120	122	17670	128	17143	158	NT
RBDASS05-H03-0815-1004-314-3-002-1427	1427	NTWH2-H49	14576	88	17753	118	17250	142	16651	165	NT
RBDASS05-H03-0815-1004-314-3-002-1427	1427	NTWH2-h49-2	14402	125	17548	177	16986	212	16412	199	NT
RBDASS05-h09-0823-0349-217-012-1494	1494	NTWH2-B15	20906	183	25191	263	24706	267	24182	234	NT
RBDASS05-h09-0823-0349-217-007-1494	1494	NTWH2-B19	15200	89	18463	113	18005	122	17545	138	NT
RBDASS05-h09-0823-0349-217-009-1494	1494	ntwh2-b20	27346	351	31326	308	31018	243	30687	321	NT
RBDASS05-H03-0815-0156-304-001-1583	1583	NTWH2-A02	21349	194	25656	185	25237	265	24755	274	NT
RBDASS05-H03-0815-0156-304-005-1583	1583	NTWH2-A04	23953	272	28070	256	27726	228	27401	234	NT
RBDASS05-h03-0815-0156-304-007-1583	1583	NTWH2-B24	20302	184	24448	270	23942	226	23479	245	NT
RBDASS05-H09-0823-0225-216-022-1610	1610	NTWH2-B10	15283	89	18549	106	18098	120	17652	129	NT
RBDASS05-h09-0823-0225-216-006-1610	1610	ntwh2-b22	20316	142	24442	223	23957	183	23497	206	NT
RBDASS05-h09-0823-0225-216-002-1610	1610	ntwh2-b23-2	28770	414	32792	551	32357	542	31986	506	NT
RBDASS05-H03-0814-2151-301-003-1634	1634	NTWH2-A07	27806	439	31860	513	31467	446	31079	369	NT
RBDASS05-H03-0814-2151-301-007-1634	1634	NTWH2-H50	29534	454	33648	464	33188	536	32738	582	NT
RBDASS05-H03-0814-2151-301-011-1634	1634	NTWH2-H51	29600	457	33721	457	33262	528	32809	582	NT
RBDASS05-H06-0819-1631-210-5-012-1640	1640	NTWH2-A05	21406	195	25707	182	25309	252	24816	274	NT
RBDASS05-H06-0819-1631-210-5-020-1640	1640	NTWH2-B06	20974	187	25280	249	24781	266	24269	250	NT
RBDASS05-H06-0819-1631-210-5-019-1640	1640	NTWH2-B07	20303	170	24441	254	23943	210	23480	232	NT
ALV-3889-1353-003-002	1714	UAM02	60000		60000		60000		60000		NT
ALV-3889-1326-002-001	1723	UAM03	60000		60000		60000		60000		NT
RBDASS05-h09-0822-1800-201-001-1840	1840	NTWH2-B11	29997	578	34121	543	33678	607	33213	659	NT
RBDASS05-h09-0822-1800-201-002-1840	1840	NTWH2-B13	15541	92	18796	93	18389	126	17931	128	NT
RBDASS05-h09-0822-1800-201-003-1840	1840	NTWH2-B25	15628	101	18883	110	18484	123	18040	134	NT
ALV-3885-1452-004-027	1878	UAN02	33400	1000	37804	1202	37391	1197	36984	1201	NT
ALV-3885-1452-004-028	1878	UAN05	38100	1800	42841	1827	42450	1846	42058	1862	NT
ALV-3885-1452-004-025	1878	UAN03	38800	2000	43615	2002	43249	2040	42872	2075	NT
ALV-3885-1452-004-026	1878	UAN04	39600	2200	44384	2087	44060	2138	43721	2190	NT

Sample Name	Depth (m)	Lab Code	^{14}C age (yr)	1σ err	IntCal13 age (yr)	1σ err	Marine13 age (yr)	1σ err	Marine13 age ΔR=400 (yr)	1σ err	Ref.
RBDASS05-H07-0821-0513-112-007-1929	1929	NTWH2-A01	30441	614	34545	569	34161	584	33720	644	NT
RBDASS05-H07-0821-0513-112-013-1929	1929	NTWH2-A03	31325	689	35411	745	35021	692	34648	662	NT
RBDASS05-H07-0821-0513-112-008-1929	1929	NTWH2-A10	30503	618	34603	577	34224	583	33792	640	NT
ALV-4162-1916-008-033-1943	1943	NTWH2-B08	15019	91	18246	129	17790	121	17302	142	NT
ALV-4162-1916-008-009-1943	1943	NTWH2-B12	14843	94	18062	126	17602	140	17055	171	NT
ALV-4162-1916-008-030-1943	1943	NTWH2-B21	14581	99	17756	128	17254	155	16659	178	NT
RBDASS05-H06-0819-1019-205-001-1950	1950	NTWH2-A06	40251	2168	44853	1995	44557	2036	44248	2081	NT
RBDASS05-H06-0819-1019-205-017-1950	1950	NTWH2-B03	40060	2041	44654	1927	44347	1959	44027	1996	NT
RBDASS05-H06-0819-1019-205-012-1950	1950	NTWH2-B05	40189	2078	44768	1942	44466	1976	44152	2015	NT
ALV-4162-1628-003-014-2006	2006	NTWH2-B09	14851	86	18069	118	17614	130	17069	159	NT
ALV-4162-1628-003-034-2006	2006	NTWH2-B17	14465	80	17638	123	17092	151	16485	148	NT
ALV-4162-1628-003-024-2006	2006	NTWH2-B18	14201	89	17287	140	16687	166	16116	137	NT
ALV-3885-1239-001-010	2027	UAH19	17350	130	20949	192	20433	174	19957	177	NT
ALV-3884-1638-004-154	2084	UAK17	14200	85	17286	136	16686	162	16115	132	NT
ALV-4162-1457-001-003-2086	2086	NTWH2-B14	11366	60	13208	61	12827	79	12506	87	NT
ALV-4162-1457-001-004-2086	2086	NTWH2-B16	14291	78	17401	128	16816	151	16240	132	NT
ALV-4162-1457-001-002-2086	2086	NTWH2-B26	14757	90	17958	126	17484	142	16916	168	NT
RBDASS05-H06-0819-0534-201-5-001-2113	2113	NTWH2-B01	12148	60	14015	98	13599	87	13231	65	NT
RBDASS05-H06-0819-0534-201-5-007-2113	2113	NTWH2-B02	11894	65	13704	91	13355	68	12966	94	NT
RBDASS05-H06-0819-0534-201-5-004-2113	2113	NTWH2-B04-2	11596	56	13423	61	13073	84	12689	57	NT
ALV-3887-1652-005-B8	2265	UAN08	13900	90	16837	166	16255	146	15692	165	NT
ALV-3887-1652-005-B2	2265	UAN07	14350	90	17481	142	16905	167	16328	149	NT
ALV-3887-1436-003-020	2441	UBA11	11100	55	12957	76	12628	49	12110	134	NT
ALV-3887-1436-003-017	2441	UBA08	11150	60	13004	75	12659	54	12203	135	NT
ALV-3887-1436-003-021	2441	UBA12	60000		60000		60000		60000		NT
ALV-3887-1436-003-022	2441	UBA13	60000		60000		60000		60000		NT
ALV-3887-1436-003-002	2441	UBA19	60000		60000		60000		60000		NT
RBDASS05-H15_0831-2045-605-053-2459	2459	UCA06	11300	60	13161	57	12772	71	12417	115	NT
RBDASS05-H15_0831-2045-605-003-2459	2459	UCA03	13450	75	16188	124	15614	147	14998	163	NT
RBDASS05-H15_0831-2045-605-035-2459	2459	UCB17	13450	75	16188	124	15614	147	14998	163	NT
RBDASS05-H15_0831-2045-605-034-2459	2459	UCB16	13500	75	16260	129	15696	148	15091	145	NT

Sample Name	Depth (m)	Lab Code	^{14}C age (yr)	1σ err	IntCal13 age (yr)	1σ err	Marine13 age (yr)	1σ err	Marine13 age ΔR=400 (yr)	1σ err	Ref.
RBDASS05-H15_0831-2045-605-036-2459	2459	UCB18	13550	75	16332	131	15781	139	15180	132	NT
RBDASS05-H15_0831-2045-605-013-2459	2459	UBB20	13600	80	16402	140	15855	134	15266	140	NT
RBDASS05-H15_0831-2045-605-033-2459	2459	UCB15	13600	85	16404	146	15853	141	15267	149	NT
RBDASS05-H15_0831-2045-605-008-2459	2459	UBB18	13750	75	16618	153	16050	120	15479	137	NT
RBDASS05-H15_0831-2045-605-037-2459	2459	UCB19	13800	80	16693	156	16114	126	15543	147	NT
RBDASS05-H15_0831-2045-605-001-2459	2459	UCA01	13850	85	16765	160	16182	136	15613	158	NT
RBDASS05-H15_0831-2045-605-007-2459	2459	UCA10	13850	85	16765	160	16182	136	15613	158	NT
RBDASS05-H15_0831-2045-605-020-2459	2459	UCA05	14350	85	17482	136	16905	161	16327	143	NT
ALV-3887-1324-002-001	2546	UBB02	11150	55	13008	69	12658	51	12203	130	NT
ALV-3887-1324-002-006	2546	UBA18	11450	60	13294	71	12917	91	12592	58	NT
RBDASS05-H15_0831-1616-601_3-003-2593	2593	UBB17	14350	90	17481	142	16905	167	16328	149	NT
RBDASS05-H03_0814-2151-301-001-1634	1634	SHIRI-B10	22050	670	26409	662	25983	728	25519	752	SH
RBDASS05-H03_0814-2151-301-002-1634	1634	SHIRI-C01	24400	700	28664	723	28284	700	27876	704	SH
RBDASS05-H03_0814-2151-301-008-1634	1634	SHIRI-F15	25810	830	29967	818	29621	828	29273	844	SH
RBDASS05-H03_0814-2151-301-010-1634	1634	SHIRI-F16	27400	1000	31762	1068	31299	1110	30826	1100	SH
RBDASS05-H03_0814-2151-301-006-1634	1634	SHIRI-F17	24130	680	28402	682	28007	676	27578	682	SH
RBDASS05-H03_0814-2151-301-005-1634	1634	SHIRI-F23	14920	210	18153	242	17669	265	17143	307	SH
RBDASS05-H06_0819-1631-210_5-005-1640	1640	SHIRI-F01	21720	500	26075	543	25581	567	25133	557	SH
RBDASS05-H06_0819-1631-210_5-003-1640	1640	SHIRI-F02	21860	520	26230	544	25755	589	25283	582	SH
RBDASS05-H06_0819-1631-210_5-009-1640	1640	SHIRI-F03	20630	430	24849	495	24413	533	23913	541	SH
RBDASS05-H06_0819-1631-210_5-010-1640	1640	SHIRI-F04	30700	1500	35346	1853	34874	1861	34418	1842	SH
RBDASS05-H06_0819-1631-210_5-004-1640	1640	SHIRI-F05	18460	350	22322	414	21838	427	21366	445	SH
RBDASS05-H06_0819-1631-210_5-007-1640	1640	SHIRI-F06	24750	750	29016	785	28640	769	28257	760	SH
RBDASS05-H06_0819-1631-210_5-008-1640	1640	SHIRI-F07	22190	540	26537	518	26149	576	25670	613	SH
RBDASS05-H06_0819-1631-210_5-001-1640	1640	SHIRI-F08	21780	500	26143	535	25654	567	25196	558	SH
RBDASS05-H06_0819-1631-210_5-006-1640	1640	SHIRI-F09	28600	1200	32895	1246	32565	1229	32216	1252	SH
RBDASS05-H06_0819-1631-210_5-002-1640	1640	SHIRI-F10	27700	1100	32090	1138	31678	1192	31223	1221	SH
RBDASS05-H06_0819-1631-210_5-013-1640	1640	SHIRI-F12	20110	410	24270	520	23756	509	23297	476	SH
RBDASS05-H06_0819-1631-210_5-014-1640	1640	SHIRI-F21	24770	750	29035	785	28659	770	28277	760	SH
RBDASS05-H06_0819-1631-210_5-016-1640	1640	SHIRI-F22	29520	1330	33851	1555	33450	1494	33092	1443	SH
ALV-3889-1444-005-001	1649	SHIRI-E08	60000		60000		60000		60000		SH

Sample Name	Depth (m)	Lab Code	^{14}C age (yr)	1σ err	IntCal13 age (yr)	1σ err	Marine13 age (yr)	1σ err	Marine13 age ΔR=400 (yr)	1σ err	Ref.
ALV-3889-1444-005-002	1649	SHIRI-E09	60000		60000		60000		60000		SH
ALV-3889-1444-005-003	1649	SHIRI-E10	60000		60000		60000		60000		SH
ALV-3889-1444-005-005	1649	SHIRI-F11	60000		60000		60000		60000		SH
ALV-3889-1444-005-004	1649	SHIRI-F14	26400	1400	30859	1573	30453	1546	30075	1516	SH
ALV-3892-1421-002-002	1656	SHIRI-C02	37000	3400	42472	3359	42126	3444	41788	3522	SH
ALV-3892-1421-002-003	1656	SHIRI-C03	60000		60000		60000		60000		SH
ALV-3892-1421-002-004	1656	SHIRI-C04	37300	3500	42737	3341	42397	3433	42062	3517	SH
ALV-3892-1421-002-005	1656	SHIRI-C05	36700	3300	42195	3368	41845	3447	41504	3518	SH
ALV-3892-1421-002-006	1656	SHIRI-C06	36600	3200	42082	3329	41727	3404	41381	3472	SH
ALV-3892-1421-002-007	1656	SHIRI-C07	36700	3300	42195	3368	41845	3447	41504	3518	SH
ALV-3892-1421-002-008	1656	SHIRI-C08	35500	2800	40916	3208	40552	3254	40202	3297	SH
ALV-3892-1421-002-009	1656	SHIRI-C09	36700	3300	42195	3368	41845	3447	41504	3518	SH
ALV-3892-1421-002-010	1656	SHIRI-C10	37600	3700	42992	3359	42663	3458	42338	3549	SH
ALV-3892-1421-002-012	1656	SHIRI-D01	37100	3400	42557	3337	42211	3424	41872	3503	SH
ALV-3892-1421-002-013	1656	SHIRI-D02	26300	1000	30501	1069	30101	1026	29744	1002	SH
ALV-3892-1421-002-014	1656	SHIRI-D03	32100	1900	37122	2307	36731	2349	36326	2393	SH
ALV-3892-1421-002-015	1656	SHIRI-D04	33900	2300	39083	2768	38729	2793	38382	2823	SH
ALV-3892-1421-002-016	1656	SHIRI-D05	60000		60000		60000		60000		SH
ALV-3892-1421-002-017	1656	SHIRI-D06	34400	2500	39703	2995	39348	3025	39004	3057	SH
ALV-3892-1421-002-018	1656	SHIRI-D07	60000		60000		60000		60000		SH
ALV-3892-1421-002-022	1656	SHIRI-D08	37100	3500	42569	3387	42229	3475	41896	3557	SH
ALV-3892-1421-002-024	1656	SHIRI-D09	36500	3200	41994	3349	41640	3422	41295	3488	SH
ALV-3892-1421-002-026	1656	SHIRI-D10	60000		60000		60000		60000		SH
ALV-3892-1421-002-025	1656	SHIRI-E01	33200	2100	38286	2522	37930	2549	37571	2584	SH
ALV-3892-1421-002-028	1656	SHIRI-E02	35500	2800	40916	3208	40552	3254	40202	3297	SH
ALV-3892-1421-002-029	1656	SHIRI-E03	35300	2700	40669	3136	40303	3177	39952	3215	SH
ALV-3892-1421-002-030	1656	SHIRI-E04	60000		60000		60000		60000		SH
OE2003-3905-1805-112-002-1670	1670	SHIRI-A02	60000		60000		60000		60000		SH
OE2003-3905-1805-112-001-1670	1670	SHIRI-A03	60000		60000		60000		60000		SH
OE2003-3905-1805-112-007-1670	1670	SHIRI-A05	60000		60000		60000		60000		SH
OE2003-3905-1805-112-017-1670	1670	SHIRI-A06	60000		60000		60000		60000		SH

Sample Name	Depth (m)	Lab Code	^{14}C age (yr)	1σ err	IntCal13 age (yr)	1σ err	Marine13 age (yr)	1σ err	Marine13 age ΔR=400 (yr)	1σ err	Ref.
OE2003-3905-1805-112-005-1670	1670	SHIRI-A07	60000		60000		60000		60000		SH
OE2003-3905-1805-112-009-1670	1670	SHIRI-A10	60000		60000		60000		60000		SH
OE2003-3905-1805-112-003-1670	1670	SHIRI-B02	60000		60000		60000		60000		SH
OE2003-3905-1805-112-006-1670	1670	SHIRI-B03	60000		60000		60000		60000		SH
OE2003-3905-1805-112-008-1670	1670	SHIRI-B04	60000		60000		60000		60000		SH
OE2003-3905-1805-112-010-1670	1670	SHIRI-B05	60000		60000		60000		60000		SH
OE2003-3905-1805-112-011-1670	1670	SHIRI-B06	34500	2500	39792	2988	39435	3017	39089	3049	SH
OE2003-3905-1805-112-012-1670	1670	SHIRI-B07	60000		60000		60000		60000		SH
OE2003-3905-1805-112-013-1670	1670	SHIRI-B08	1030	60	942	75	602	47	269	82	SH
OE2003-3905-1805-112-015-1670	1670	SHIRI-B09	60000		60000		60000		60000		SH
ALV-3889-1404-004-003	1700	SHIRI-F13	60000		60000		60000		60000		SH
ALV-3889-1404-004-001	1700	SHIRI-F18	60000		60000		60000		60000		SH
ALV-3889-1404-004-002	1700	SHIRI-F20	22110	540	26469	527	26058	588	25573	613	SH
ALV-3892-1315-001-004	1713	SHIRI-E05	14970	220	18205	249	17729	275	17210	314	SH
ALV-3892-1315-001-009	1713	SHIRI-E06	14030	180	17029	277	16467	272	15872	270	SH
ALV-3892-1315-001-012	1713	SHIRI-E07	14840	210	18064	249	17568	272	17032	312	SH
ALV-3889-1311-001-009	1719	SHIRI-F19	34600	2500	39882	2981	39522	3010	39175	3041	SH
RBDASS05-H01_0812-2157-101-002-1751	1751	SHIRI-A04	15390	220	18644	243	18220	248	17754	274	SH
RBDASS05-H01_0812-2157-101-004-1751	1751	SHIRI-A08	27900	1100	32270	1116	31890	1165	31454	1212	SH
RBDASS05-H01_0812-2157-101-003-1751	1751	SHIRI-A09	15100	220	18337	242	17890	269	17384	301	SH
RBDASS05-H01_0812-2157-101-001-1751	1751	SHIRI-B01	14930	210	18163	242	17681	264	17157	306	SH
RBDASS05-H15_0901-0248-615_2-004-2118	2118	SH_IR2_H12	14830	300	18045	349	17538	391	17014	418	SH
RBDASS05-H15_0901-0248-615_2-008-2118	2118	SH_IR2_H13	15250	350	18506	393	18055	406	17556	453	SH
RBDASS05-H15_0901-0248-615_2-012-2118	2118	SH_IR2_H14	14910	330	18132	375	17638	422	17116	450	SH
RBDASS05-H15_0901-0248-615_2-016-2118	2118	SH_IR2_H15	11520	200	13372	199	13003	190	12589	248	SH
RBDASS05-H15_0901-0248-615_2-020-2118	2118	SH_IR2_H16	11160	180	13022	169	12656	209	12125	301	SH
RBDASS05-H15_0901-0248-615_2-024-2118	2118	SH_IR2_H17	14450	300	17571	389	17040	417	16512	436	SH
RBDASS05-H15_0901-0248-615_2-028-2118	2118	SH_IR2_H18	14400	310	17504	407	16975	430	16441	453	SH
RBDASS05-H15_0901-0248-615_2-032-2118	2118	SH_IR2_H19	14110	280	17126	391	16593	405	16001	421	SH
RBDASS05-H15_0901-0248-615_2-036-2118	2118	SH_IR2_H20	12650	290	14931	498	14398	457	13826	397	SH
RBDASS05-H15_0901-0248-615_2-040-2118	2118	SH_IR2_H21	13690	260	16571	378	15968	390	15340	447	SH

Sample Name	Depth (m)	Lab Code	^{14}C age (yr)	1σ err	IntCal13 age (yr)	1σ err	Marine13 age (yr)	1σ err	Marine13 age ΔR=400 (yr)	1σ err	Ref.
RBDASS05-H15_0901-0144-613_2-001-2132	2132	SH_IR2_H22	60000		60000		60000		60000		SH
RBDASS05-H15_0901-0144-613_2-003-2132	2132	SH_IR2_H23	11420	200	13273	195	12923	188	12445	264	SH
RBDASS05-H15_0901-0144-613_2-005-2132	2132	SH_IR2_H24	13310	250	16005	375	15381	425	14716	421	SH
RBDASS05-H15_0901-0144-613_2-007-2132	2132	SH_IR2_I01	14450	310	17569	402	17040	429	16512	449	SH
RBDASS05-H15_0901-0144-613_2-009-2132	2132	SH_IR2_I02	14190	280	17232	386	16701	401	16124	421	SH
RBDASS05-H15_0901-0144-613_2-011-2132	2132	SH_IR2_I03	15120	320	18359	352	17905	386	17390	426	SH
ALV-3884-1531-003-001	2141	SH_IR2_I04	13660	260	16529	380	15923	389	15287	453	SH
ALV-3884-1531-003-017	2141	SH_IR2_I05	13850	280	16786	399	16216	420	15600	443	SH
ALV-3884-1531-003-026	2141	SH_IR2_I06	14090	270	17101	380	16565	392	15970	406	SH
ALV-3884-1531-003-035	2141	SH_IR2_I07	14460	290	17586	375	17053	405	16525	421	SH
ALV-3884-1531-003-042	2141	SH_IR2_I08	14080	270	17088	380	16551	393	15954	406	SH
ALV-3884-1531-003-074	2141	SH_IR2_I09	14060	290	17060	405	16525	421	15926	439	SH
OE2003-3904-1351-201-004-2174	2174	SH_IR2_I10	13760	270	16667	389	16077	406	15456	446	SH
OE2003-3904-1351-201-008-2174	2174	SH_IR2_I11	13920	270	16877	385	16321	402	15712	413	SH
OE2003-3904-1351-201-012-2174	2174	SH_IR2_I12	13440	260	16206	391	15591	408	14906	455	SH
OE2003-3904-1351-201-016-2174	2174	SH_IR2_I13	14320	290	17402	388	16872	409	16323	431	SH
OE2003-3904-1351-201-020-2174	2174	SH_IR2_J01	14030	280	17021	394	16482	409	15879	423	SH
OE2003-3904-1351-201-024-2174	2174	SH_IR2_J02	14470	280	17600	361	17067	393	16538	407	SH
OE2003-3904-1351-201-028-2174	2174	SH_IR2_J03	33300	3200	39347	3860	39021	3933	38696	4006	SH
OE2003-3904-1351-201-032-2174	2174	SH_IR2_J04	13840	270	16772	387	16200	405	15587	427	SH
OE2003-3904-1351-201-036-2174	2174	SH_IR2_J05	13940	270	16903	385	16351	401	15742	411	SH
ALV-3884-1411-002-008	2228	SH_IR2_J06	13890	270	16838	386	16276	404	15666	417	SH
ALV-3884-1411-002-032	2228	SH_IR2_J07	13710	280	16600	404	16001	421	15366	474	SH
ALV-3884-1411-002-068	2228	SH_IR2_J08	60000		60000		60000		60000		SH
ALV-3884-1411-002-085	2228	SH_IR2_J09	13780	270	16693	388	16108	406	15489	441	SH
ALV-3884-1411-002-086	2228	SH_IR2_J10	13490	270	16283	403	15666	417	14988	473	SH
ALV-3884-1411-002-088	2228	SH_IR2_J11	13730	270	16626	390	16031	406	15405	453	SH
ALV-3884-1411-002-090	2228	SH_IR2_J12	13780	280	16694	401	16109	421	15485	459	SH
ALV-3884-1411-002-094	2228	SH_IR2_J13	14260	280	17324	380	16793	399	16231	419	SH
ALV-3884-1411-002-116	2228	SH_IR2_J14	60000		60000		60000		60000		SH
ALV-3884-1411-002-119	2228	SH_IR2_J15	14550	310	17699	392	17169	424	16649	442	SH

Sample Name	Depth (m)	Lab Code	^{14}C age (yr)	1σ err	IntCal13 age (yr)	1σ err	Marine13 age (yr)	1σ err	Marine13 age ΔR=400 (yr)	1σ err	Ref.
RBDASS05-H10_0825-0131-101-001-2246	2246	SH_IR2_J16	13750	290	16655	415	16064	437	15430	482	SH
RBDASS05-H10_0825-0131-101-003-2246	2246	SH_IR2_J17	33900	3430	39965	3935	39650	4010	39338	4087	SH
RBDASS05-H10_0825-0131-101-005-2246	2246	SH_IR2_J18	13830	260	16758	374	16183	391	15575	410	SH
RBDASS05-H10_0825-0131-101-007-2246	2246	SH_IR2_J19	11510	200	13362	198	12995	190	12574	250	SH
RBDASS05-H10_0825-0131-101-009-2246	2246	SH_IR2_J20	14220	280	17272	384	16740	400	16170	420	SH
RBDASS05-H10_0825-0131-101-011-2246	2246	SH_IR2_J21	13700	260	16584	378	15984	390	15358	444	SH
RBDASS05-H10_0825-0131-101-013-2246	2246	SH_IR2_K01	31200	2450	36809	3279	36427	3325	36050	3365	SH
RBDASS05-H10_0825-0131-101-015-2246	2246	SH_IR2_K02	14280	280	17351	379	16819	398	16262	418	SH
RBDASS05-H10_0825-0131-101-017-2246	2246	SH_IR2_K03	13980	270	16956	384	16409	399	15803	408	SH
RBDASS05-H10_0825-0131-101-019-2246	2246	SH_IR2_K04	11190	200	13054	187	12688	231	12147	316	SH
ALV-3887-1652-005-001	2265	SH_IR2_K05	13860	270	16799	386	16230	405	15619	423	SH
ALV-3887-1652-005-003	2265	SH_IR2_K06	13800	270	16720	388	16138	406	15523	436	SH
ALV-3887-1652-005-005	2265	SH_IR2_K07	11210	180	13066	175	12721	195	12194	283	SH
ALV-3887-1652-005-007	2265	SH_IR2_K08	13730	270	16626	390	16031	406	15405	453	SH
ALV-3887-1652-005-009	2265	SH_IR2_K09	11240	190	13097	184	12754	202	12222	287	SH
ALV-3887-1652-005-011	2265	SH_IR2_K10	11410	200	13264	195	12915	189	12432	265	SH
ALV-3887-1652-005-014	2265	SH_IR2_K11	13510	250	16311	374	15700	378	15021	451	SH
ALV-3887-1652-005-015	2265	SH_IR2_K12	14200	270	17247	373	16713	388	16138	406	SH
ALV-3887-1652-005-017	2265	SH_IR2_K13	13850	260	16785	374	16214	390	15606	406	SH
ALV-3887-1652-005-019	2265	SH_IR2_K14	14230	290	17283	395	16754	412	16187	435	SH
ALV-3884-1330-001-001	2273	SH_IR2_K15	14000	290	16982	407	16440	425	15833	442	SH
ALV-3884-1330-001-003	2273	SH_IR2_K16	13670	260	16543	379	15938	390	15304	451	SH
ALV-3884-1330-001-005	2273	SH_IR2_L01	13880	260	16824	374	16260	389	15653	400	SH
ALV-3884-1330-001-007	2273	SH_IR2_L02	14110	280	17126	391	16593	405	16001	421	SH
ALV-3884-1330-001-009	2273	SH_IR2_L03	13660	260	16529	380	15923	389	15287	453	SH
ALV-3884-1330-001-011	2273	SH_IR2_L04	14300	290	17376	390	16846	410	16293	432	SH
ALV-3884-1330-001-013	2273	SH_IR2_L05	13860	310	16801	435	16235	463	15607	496	SH
ALV-3884-1330-001-015	2273	SH_IR2_L06	13430	260	16191	391	15575	410	14891	454	SH
ALV-3887-1549-004-001	2372	SH_IR2_L07	14070	290	17073	404	16539	421	15941	438	SH
ALV-3887-1549-004-003	2372	SH_IR2_L08	13590	270	16431	398	15818	407	15158	476	SH
ALV-3887-1549-004-010	2372	SH_IR2_L09	14410	300	17519	393	16988	418	16455	439	SH

Sample Name	Depth (m)	Lab Code	^{14}C age (yr)	1σ err	IntCal13 age (yr)	1σ err	Marine13 age (yr)	1σ err	Marine13 age ΔR=400 (yr)	1σ err	Ref.
ALV-3887-1549-004-011	2372	SH_IR2_L10	11070	180	12952	156	12528	228	11988	326	SH
ALV-3887-1549-004-013	2372	SH_IR2_L11	11590	210	13446	217	13063	203	12683	245	SH
ALV-3887-1549-004-015	2372	SH_IR2_L12	13910	260	16864	373	16305	388	15698	396	SH
ALV-3887-1549-004-016	2372	SH_IR2_L13	11450	200	13303	196	12947	188	12487	260	SH
ALV-3887-1549-004-017	2372	SH_IR2_L14	13500	280	16299	417	15679	434	15005	486	SH
ALV-3887-1549-004-019	2372	SH_IR2_L15	11180	180	13039	172	12683	203	12153	294	SH
ALV-3887-1549-004-020	2372	SH_IR2_L16	13600	260	16444	383	15833	390	15179	462	SH
ALV-3887-1436-003-001	2441	SH_IR2_M01	60000		60000		60000		60000		SH
ALV-3887-1436-003-005	2441	SH_IR2_M02	60000		60000		60000		60000		SH
ALV-3887-1436-003-008	2441	SH_IR2_M03	60000		60000		60000		60000		SH
ALV-3887-1436-003-012	2441	SH_IR2_M04	60000		60000		60000		60000		SH
ALV-3887-1436-003-016	2441	SH_IR2_M05	60000		60000		60000		60000		SH
ALV-3887-1436-003-018	2441	SH_IR2_M06	35000	4000	41012	4048	40716	4131	40425	4215	SH
ALV-3887-1436-003-020	2441	SH_IR2_M07	11350	180	13204	176	12863	173	12367	244	SH
ALV-3887-1436-003-021	2441	SH_IR2_M08	60000		60000		60000		60000		SH
ALV-3887-1436-003-022	2441	SH_IR2_M09	60000		60000		60000		60000		SH
RBDASS05-H15_0831-2045-605-002-2459	2459	SH_IR2_M10	13760	270	16667	389	16077	406	15456	446	SH
RBDASS05-H15_0831-2045-605-006-2459	2459	SH_IR2_M11	13770	260	16679	376	16091	391	15478	425	SH
RBDASS05-H15_0831-2045-605-011-2459	2459	SH_IR2_M12	13850	270	16786	386	16215	405	15603	425	SH
RBDASS05-H15_0831-2045-605-016-2459	2459	SH_IR2_M13	13720	260	16612	377	16014	391	15393	439	SH
RBDASS05-H15_0831-2045-605-019-2459	2459	SH_IR2_M14	14030	270	17022	382	16481	396	15879	406	SH
RBDASS05-H15_0831-2045-605-023-2459	2459	SH_IR2_M15	13740	260	16639	377	16045	391	15427	434	SH
RBDASS05-H15_0831-2045-605-026-2459	2459	SH_IR2_M16	14220	290	17270	396	16741	412	16172	435	SH
RBDASS05-H15_0831-2045-605-029-2459	2459	SH_IR2_M17	11770	190	13633	213	13234	199	12881	181	SH
RBDASS05-H15_0831-2045-605-038-2459	2459	SH_IR2_M18	13600	250	16443	369	15832	373	15182	449	SH
RBDASS05-H15_0831-2045-605-042-2459	2459	SH_IR2_M19	13560	270	16387	400	15773	409	15106	477	SH
RBDASS05-H15_0831-2045-605-046-2459	2459	SH_IR2_M20	13450	250	16220	376	15609	387	14920	445	SH
RBDASS05-H15_0831-2045-605-049-2459	2459	SH_IR2_M21	13940	270	16903	385	16351	401	15742	411	SH
RBDASS05-H15_0831-2045-605-054-2459	2459	SH_IR2_M22	11890	210	13790	276	13369	222	12981	197	SH
RBDASS05-H15_0831-2045-605-057-2459	2459	SH_IR2_M23	11670	210	13531	226	13135	211	12783	222	SH
RBDASS05-H11_0826-0029-201_4-002-2529	2529	SH_IR2_N01	60000		60000		60000		60000		SH

Sample Name	Depth (m)	Lab Code	^{14}C age (yr)	1σ err	IntCal13 age (yr)	1σ err	Marine13 age (yr)	1σ err	Marine13 age ΔR=400 (yr)	1σ err	Ref.
RBDASS05-H11_0826-0029-201_4-004-2529	2529	SH_IR2_N02	11330	200	13185	195	12846	196	12327	278	SH
RBDASS05-H11_0826-0029-201_4-006-2529	2529	SH_IR2_N03	11520	190	13369	187	13001	182	12594	234	SH
RBDASS05-H11_0826-0029-201_4-008-2529	2529	SH_IR2_N04	60000		60000		60000		60000		SH
RBDASS05-H11_0826-0029-201_4-010-2529	2529	SH_IR2_N05	60000		60000		60000		60000		SH
RBDASS05-H11_0826-0029-201_4-012-2529	2529	SH_IR2_N06	60000		60000		60000		60000		SH
RBDASS05-H11_0826-0029-201_4-014-2529	2529	SH_IR2_N07	60000		60000		60000		60000		SH
RBDASS05-H11_0826-0029-201_4-016-2529	2529	SH_IR2_N08	60000		60000		60000		60000		SH
RBDASS05-H11_0826-0029-201_4-018-2529	2529	SH_IR2_N09	60000		60000		60000		60000		SH
ALV-3887-1324-002-003	2546	SH_IR2_N10	11280	180	13135	178	12798	180	12282	260	SH
ALV-3887-1324-002-004	2546	SH_IR2_O01	11580	190	13429	192	13051	186	12679	219	SH
ALV-3887-1324-002-007	2546	SH_IR2_O02	11570	200	13422	203	13044	193	12660	236	SH
ALV-3887-1324-002-009	2546	SH_IR2_O03	11550	200	13402	201	13027	192	12632	241	SH
RBDASS05-H15_0831-1616-601_3-001-2593	2593	SH_IR2_O04	13840	280	16773	399	16201	420	15584	445	SH
RBDASS05-H15_0831-1616-601_3-002-2593	2593	SH_IR2_O05	11510	190	13360	187	12993	182	12580	236	SH
RBDASS05-H15_0831-1616-601_3-004-2593	2593	SH_IR2_O06	11420	190	13273	184	12922	180	12452	249	SH
RBDASS05-H15_0831-1616-601_3-005-2593_UP	2593	SH_IR2_O07	14420	300	17532	392	17001	418	16469	438	SH
RBDASS05-H15_0831-1616-601_3-005-2593_LO	2593	SH_IR2_O08	2065	55	2040	78	1640	71	1218	56	SH
RBDASS05-H15_0831-1616-601_3-006-2593	2593	SH_IR2_O09	13950	270	16917	385	16365	401	15758	410	SH
RBDASS05-H15_0831-1616-601_3-007-2593	2593	SH_IR2_O10	14030	260	17022	371	16480	382	15878	389	SH
ALV-3888-1714-006-002	2739	SH_IR2_O11	11610	190	13460	195	13077	188	12718	210	SH

References

Adkins, Jess F., Hai Cheng, et al. (1998). "Deep-Sea Coral Evidence for Rapid Change in Ventilation of the Deep North Atlantic 15,400 Years Ago". In: *Science* 280, pp. 725–728.

Adkins, Jess F., Sheila Griffin, et al. (2002). "Radiocarbon Dating of Deep-Sea Corals". In: *Radiocarbon* 44, pp. 567–580.

Adkins, Jess F., G M Henderson, et al. (2004). "Growth rates of the deep-sea scleractinia Desmophyllum cristagalli and Enallopsammia rostrata". In: *Earth and Planetary Science Letters* 227.3-4, pp. 481–490.

Allen, Katherine A. et al. (2015). "Southwest Pacific deep water carbonate chemistry linked to high southern latitude climate and atmospheric CO_2 during the Last Glacial Termination". In: *Quaternary Science Reviews* 122, pp. 180–191.

Anagnostou, E, R M Sherrell, and A Gagnon (2011). "Seawater nutrient and carbonate ion concentrations recorded as P/Ca, Ba/Ca, and U/Ca in the deep-sea coral Desmophyllum dianthus". In: *Geochimica et Cosmochimica Acta*.

Anderson, Robert F. et al. (2009). "Wind-Driven Upwelling in the Southern Ocean and the Deglacial Rise in Atmospheric CO_2". In: *Science* 323.5920, pp. 1443–1448.

Broecker, Wallace S. (1982). "Glacial to Interglacial Changes in Ocean Chemistry". In: *Progress in Oceanography* 11.2, pp. 151–197.

Burke, Andrea and L F Robinson (2012). "The Southern Ocean's Role in Carbon Exchange During the Last Deglaciation". In: *Science* 335.6068, pp. 557–561.

Burke, Andrea, Laura F. Robinson, et al. (2010). "Reconnaissance dating: A new radiocarbon method applied to assessing the temporal distribution of Southern Ocean deep-sea corals". In: *Deep-Sea Research Part I-Oceanographic Research Papers* 57.11, pp. 1510–1520.

Bush, Shari L. et al. (2013). "Simple, rapid, and cost effective: a screening method for ^{14}C analysis of small carbonate samples". In: *Radiocarbon* 55, pp. 631–640. DOI: 10.1017/S0033822200057787.

Cheng, Hai et al. (2000). "U-Th dating of deep-sea corals". In: *Geochimica et Cosmochimica Acta* 64, pp. 2401–2416.

Curry, William B. and Delia W. Oppo (2005). "Glacial water mass geometry and the distribution of δ13C of ΣCO2 in the western Atlantic Ocean". In: *Paleoceanography*.

Eltgroth, Selene F et al. (2006). "A deep-sea coral record of North Atlantic radiocarbon through the Younger Dryas: Evidence for intermediate water/deepwater reorganization". In: *Paleoceanography* 21.4.

Ferrari, R et al. (2014). "Antarctic sea ice control on ocean circulation in present and glacial climates". In: *PNAS* 111.24, pp. 8753–8758.

van de Flierdt, Tina, Laura F. Robinson, and Jess F. Adkins (2010). "Deep-sea coral aragonite as a recorder for the neodymium isotopic composition of seawater". In: *Geochimica et Cosmochimica Acta* 74.21, pp. 6014–6032.

van de Flierdt, Tina, Laura F. Robinson, Jess F. Adkins, et al. (2006). "Temporal stability of the neodymium isotope signature of the Holocene to glacial North Atlantic". In: *Paleoceanography* 21.4, PA4102.

Lund, D C, Jess F. Adkins, and R Ferrari (2011). "Abyssal Atlantic circulation during the Last Glacial Maximum: Constraining the ratio between transport and vertical mixing". In: *Paleoceanography* 26.1.

Marcott, Shaun A et al. (2014). "Centennial-scale changes in the global carbon cycle during the last deglaciation". In: *Nature* 514, pp. 616–619.

McCulloch, Malcolm et al. (2012). "Resilience of cold-water scleractinian corals to ocean acidification: Boron isotopic systematics of pH and saturation state up-regulation". In: *Geochimica et Cosmochimica Acta* 87, pp. 21–34.

Ramsey, Christopher Bronk (2009). "Bayesian Analysis of Radiocarbon Dates". In: *Radiocarbon* 51.1, pp. 337–360.

Reimer, Paula J., Mike G. L. Baillie, et al. (2009). "IntCal09 and Marine09 radiocarbon age calibration curves, 0–50,000 years cal BP". In: *Radiocarbon* 51.

Reimer, Paula J., Edouard Bard, et al. (2013). "IntCal13 and Marine13 radiocarbon age calibration curves 0–50,000 years cal BP". In: *Radiocarbon* 55.4, pp. 1869–1887.

Robinson, Laura F., Jess F. Adkins, Diego P Fernandez, et al. (2006). "Primary U distribution in scleractinian corals and its implications for U series dating". In: *Geochemistry Geophysics Geosystems* 7.5, Q05022.

Robinson, Laura F., Jess F. Adkins, Lloyd D. Keigwin, et al. (2005). "Radiocarbon Variability in the Western North Atlantic During the Last Deglaciation". In: *Science* 310, pp. 1469–1473.

Robinson, Laura F., Jess F. Adkins, Daniel S. Scheirer, et al. (2007). "Deep-sea scleractinian coral age and depth distributions in the WN Atlantic for the last 225 thousand years". In: *Bulletin of Marine Science* 81, pp. 371–391.

Sigman, Daniel M and Edward A. Boyle (2000). "Glacial/interglacial variations in atmospheric carbon dioxide". In: *Nature* 407, pp. 859–869.

Sigman, Daniel M, Mathis P Hain, and Gerald H Haug (2010). "The polar ocean and glacial cycles in atmospheric CO_2 concentration". In: *Nature* 466.7302, pp. 47–55.

Sikes, Elisabeth L et al. (2000). "Old radiocarbon ages in the southwest Pacific Ocean during the last glacial period and deglaciation". In: *Nature* 405.6786, pp. 555–559.

Skinner, L.C. et al. (2017). “Radiocarbon constraints on the glacial ocean circulation and its impact on atmospheric CO_2”. In: *Nature Communications*.

Skinner, L et al. (2015). “Reduced ventilation and enhanced magnitude of the deep Pacific carbon pool during the last glacial period”. In: *Earth and Planetary Science Letters* 411.C, pp. 45–52.

Spooner, P T et al. (2016). “Rapid uranium-series age screening of carbonates by laser ablation mass spectrometry”. In: *Quaternary Geochronology*.

Talley, Lynne (2013). “Closure of the Global Overturning Circulation Through the Indian, Pacific, and Southern Oceans: Schematics and Transports”. In: *Oceanography* 26.1, pp. 80–97.

Thiagarajan, Nivedita, Jess F. Adkins, and John Eiler (2011). “Carbonate clumped isotope thermometry of deep-sea corals and implications for vital effects”. In: *Geochimica et Cosmochimica Acta* 75.16, pp. 4416–4425.

Thiagarajan, Nivedita, Dana Gerlach, et al. (2013). “Movement of deep-sea coral populations on climatic timescales”. In: *Paleoceanography* 28, pp. 227–236.

Thiagarajan, Nivedita, Adam V. Subhas, et al. (2014). “Abrupt pre-Bolling-Allerod warming and circulation changes in the deep ocean”. In: *Nature* 511, pp. 75–78.

Wang, Xingchen T et al. (2014). “Isotopic composition of carbonate-bound organic nitrogen in deep-sea scleractinian corals: A new window into past biogeochemical change”. In: *Earth and Planetary Science Letters* 400, pp. 243–250.

Yu, Jimin, Henry Elderfield, and Alexander M. Piotrowski (2008). “Seawater carbonate ion-δ^{13}C systematics and application to glacial-interglacial North Atlantic ocean circulation”. In: *Earth and Planetary Science Letters* 271, pp. 209–220.

Chapter 3

A HIGH-RESOLUTION RECORD OF SOUTHERN OCEAN INTERMEDIATE WATER RADIOCARBON OVER THE PAST 30,000 YEARS

Hines, Sophia K.V., John R. Southon, and Jess F. Adkins (2015). "A high-resolution record of Southern Ocean intermediate water radiocarbon over the past 30,000 years". In: *Earth and Planetary Science Letters* 432, pp. 46–58. DOI: 10.1016/j.epsl.2015.09.038.

3.1 Introduction

The ocean is an important driver of global climate on a variety of timescales. Water has a large heat capacity, which allows the oceans to transport significant amounts of sensible heat from the tropics to the poles. Relative to its volume transport, intermediate water carries a large amount of heat due to the large temperature difference between its formation and upwelling regions (L. Talley, 2013; L. D. Talley, 2003). In addition to the ocean's direct effect on climate through heat transport, the deep ocean stores 60 times more carbon than the atmosphere, so changes in ocean circulation can have dramatic impacts on the global carbon cycle. Carbon is stored in the deep ocean via the biological, solubility, and alkalinity pumps, and deeply regenerated CO_2 returns to the atmosphere when deep water upwells to the surface as part of the meridional overturning circulation (Sigman, Hain, and Haug, 2010; Hain, Sigman, and Haug, 2014).

One important tracer that is useful both for reconstructing mean and local ocean circulation is radiocarbon. Radiocarbon (^{14}C) is cosmogenically produced in the atmosphere where it is quickly converted to $^{14}CO_2$. Its 5730-yr half-life makes ^{14}C well suited as a tracer for deep ocean circulation, which occurs on time scales of $\sim$1000 yr. The rate of change of radiocarbon in the atmosphere is a balance between ^{14}C production (which is variable in time), exchange with the ocean, and self-decay, which makes the radiocarbon value of the atmosphere a very sensitive recorder of globally integrated ocean overturning. Reconstructions of ^{14}C production through time (Hain, Sigman, and Haug, 2014; Laj et al., 2002; Muscheler et al., 2004) are helpful for disentangling these competing processes that imprint themselves

on atmospheric $\Delta^{14}C$. However, production rate records are difficult to generate. Although mean ocean circulation changes can help explain global shifts in climate, the specific regions involved and the timing of regional changes is also crucial for understanding the mechanisms at work. Measurements of radiocarbon in the ocean are therefore important because they provide local information that can be combined with the atmospheric record to generate a global understanding of how the ocean behaves over millennial timescales.

We provide an intermediate water $\Delta^{14}C$ reconstruction from south of Tasmania in the Indo-Pacific region of the Southern Ocean (Figure 3.1). In the modern ocean, Antarctic Intermediate Water (AAIW) ventilates this region between ~500 and 1500 m. Intermediate waters are defined by extrema in salinity, and AAIW can be easily seen in the middle panel of Figure 3.1A as the tongue of low-salinity water extending from the surface of the Southern Ocean to between ~500—1500 m. At the sample location this water has a bomb-corrected $\Delta^{14}C$ value of around $-150‰$ (3.1A, top panel), and underlying Circumpolar Deep Water (CDW) and Antarctic Bottom Water (AABW) are more depleted in radiocarbon. The core of Pacific Deep Water is marked by an oxygen minimum (L. Talley, 2013), and its return flow to the Southern Ocean intersects with our sample location (Figure 3.1A, bottom panel). As Talley points out, the modern meridional overturning circulation (MOC) does not consist of two separate cells stacked on top of one another; instead both cells are intertwined (Figure 3.1D, top panel).

Through the application of simple box models, it has been shown that increasing the meridional overturning strength and reducing the efficiency of the biological pump together are able to accomplish the full glacial to interglacial CO_2 change (Knox and McElroy, 1984; Sarmiento and Toggweiler, 1984; Siegenthaler and Wenk, 1984). The configuration of the ocean during the Last Glacial Maximum (LGM) was distinct from the modern (Curry and Oppo, 2005), and it is thought that the ocean circulation was near steady state during this time. Benthic carbon and oxygen isotope measurements show a shoaling of the boundary between the northern and southern source water masses and a sharper gradient between them (Curry and Oppo, 2005; Lund, Adkins, and Ferrari, 2011). Recently, a mechanism has been proposed to move between the interglacial and glacial circulation schemes. It builds on the observation that the boundary between the upper and lower cells is defined by the switch between positive and negative buoyancy forcing at the surface of the Southern Ocean, and that this location generally aligns with the summertime

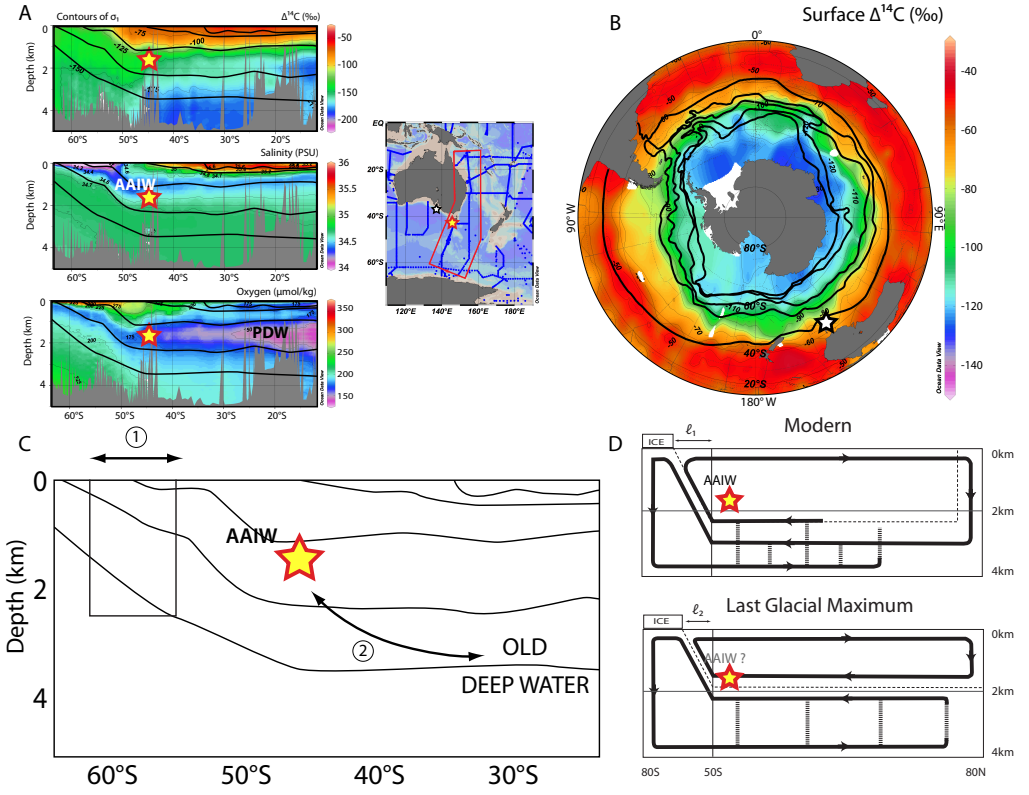

Figure 3.1: Hydrography for the broader region around our sample location. A) Sections of bomb-corrected Δ^{14}C (top), salinity (middle), and oxygen (bottom) from ~65°S to 10°S for the region marked on the inset map (Key et al., 2004). Sample location marked with a yellow star. Thick black contour lines are isopycnals (σ_1). In this region, tracers largely move along density surfaces. Map to the right shows the location of the sections, the Tasmanian coral location (yellow star) and the location of core MD-03-2611 (black star). B) Surface map of bomb-corrected Δ^{14}C for the whole Southern Ocean. Thick black lines mark the positions of the major Southern Ocean fronts (from furthest north to furthest south: Subtropical Front (STF), Subantarctic Front (SAF), Polar Front (PF), Southern ACC Front (SACCF), and the Southern Boundary (SB)). C) Schematic Southern Ocean section with contours of density (taken from panel A). Coral location is marked with yellow star, and arrows show the two main ways to change radiocarbon values. D) Schematic of modern and glacial meridional overturning circulation with coral location marked with yellow star (adapted from (Ferrari et al., 2014)). In the modern, upper and lower cells are intertwined whereas in the glacial, cells are separated. This is due to increased sea ice extent (note: ℓ_1 in the upper panel is greater than ℓ_2 in the lower panel).

sea ice edge (Ferrari et al., 2014). To first order, isopycnals have a constant slope across the Southern Ocean and are flat in the rest of the ocean basin, so it is possible to calculate the depth of the boundary between deep cells based on the high latitude buoyancy forcing. In the modern ocean, this boundary sits at around 2200 m, which is deep enough for the rough topography at the bottom of the ocean to effectively mix water between the cells. Expanded sea ice during the LGM shoals this boundary out of the rough region and allows for separation between the upper and lower cells 3.1D (Ferrari et al., 2014).

In this paper, we use the results of age screening deep-sea corals from the Caltech collection to select samples for a continuous well-dated time series of $\Delta^{14}C$ from a narrow depth range in the region south of Tasmania. This high-resolution time series is then used to examine glacial climate and the behavior of the Southern Ocean during the deglaciation. Our sample location lies within the modern and glacial upper cell but near its lower boundary, so it is quite sensitive to the interconnectedness of the meridional overturning circulation. We assess this interconnectedness by comparing our Tasmanian intermediate water $\Delta^{14}C$ record to other Southern Ocean records from different depths as well as atmospheric CO_2.

3.2 Methods

Deep-sea corals used in this study were collected from seamounts south of Tasmania (43°S–47°S 144°E–152°E) during cruise TN-228 in 2008–2009 on the R/V Thompson using the remotely operated deep submergence vehicle JASON. During this cruise over 10,000 deep-sea corals were collected from between 898-2395 m. All corals used for the construction of this time series were the scleractinian azooxanthellate *Desmophyllum dianthus*. The time series presented here encompasses samples from 1430–1950 m with 80% of samples between 1500 and 1700 m (marked with a star in 3.1A sections).

Previous reconnaissance radiocarbon dating (Thiagarajan, Gerlach, et al., 2013) was performed at the National Ocean Sciences Accelerator Mass Spectrometry Laboratory at the Woods Hole Oceanographic Institute following the method of Burke, Laura F. Robinson, et al. (2010) using an Elemental Analyzer. Additional radiocarbon age screening was performed at the UC Irvine Keck Carbon Cycle AMS facility following the 'rapid survey' method of (Bush et al., 2013). Reconnaissance ^{14}C dates were converted into calendar ages using IntCal13 and the Calib 7.0 software and reservoir age offsets according to Thiagarajan, Gerlach, et al. (2013)

for consistency (1250 yr for the Holocene and 1900 yr for all samples older than 10 kyr).

In preparation for U/Th and high-precision radiocarbon dating, all coral samples were physically and chemically cleaned following previously established methods (Cheng et al., 2000; Shen and Boyle, 1988). U/Th dating was performed using previously established methods (Cheng et al., 2000; Laura F. Robinson et al., 2007). Approximately 100 mg of coral was weighed, dissolved in Seastar HNO_3, and spiked with a mixed ^{229}Th–^{236}U spike. Uranium and thorium were separated from the rest of the coral matrix by iron co-precipitation and anion exchange chromatography. Purified U and Th fractions were dried and re-dissolved in 5% Seastar nitric acid and measured on a Thermo Scientific Neptune MC-ICPMS. Bracketing CRM-145 standards for uranium and SGS standards for thorium were used to correct for instrumental drift, mass bias and gain. Uranium samples were intensity matched to within ~10% of the CRM-145 standard for ^{234}U, which was measured on the center position secondary electron multiplier with a retarding potential quadruple to reduce scattered ion effects. ^{235}U, ^{236}U, and ^{238}U were measured on Faraday cups with 10^{11} ohm resistors. ^{229}Th and ^{230}Th were measured on channeltron ion counters and ^{232}Th was measured on a Faraday cup with a 10^{11} ohm resistor. Four procedural blanks were run with each set of samples and the average of the blank values was subtracted from each of the samples. Samples and standards were also corrected for instrumental blank using the average of bracketing 5% Seastar nitric used to dilute samples and standards. Samples were corrected for initial thorium using a ^{230}Th/^{232}Th atom ratio of $80\pm80\times10^{-6}$ (Cheng et al., 2000).

High-precision ^{14}C dating was performed at the Keck Carbon Cycle AMS facility at UC Irvine. Approximately 11 mg of cleaned coral was weighed into a 3 mL rubber septum top vial and leached in 0.01% HCl to remove 10% of the coral mass. Samples were then dried, evacuated and hydrolyzed in phosphoric acid. The resulting CO_2 was purified and graphitized with H_2 and an iron catalyst (Santos et al., 2007). Graphite was pressed into aluminum targets for ^{14}C analysis on the accelerator mass spectrometer. Measured radiocarbon activities are normalized for mass-dependent fractionation using δ^{13}C values measured on the AMS, and normalized to a $\delta^{13}C_{PDB}$ value of -25 ‰. Radiocarbon activities are reported as fraction modern (F_m) relative to 95% of the activity of NBS oxalic acid standard in the year 1950 (normalized to $\delta^{13}C_{PDB} = -19$ ‰). Fraction modern is converted to a ^{14}C age using the formula ^{14}C age = -8033 ln(Fm). Radiocarbon blanks measured on ^{14}C-dead deep-sea

corals tend to be larger and more variable than those measured on ^{14}C-dead calcite (e.g. (Adkins, Griffin, et al., 2002; Eltgroth et al., 2006)). Therefore, corals are background corrected using the average and standard deviation of radiocarbon values measured on replicate samples (n = 8) of a "radiocarbon dead" deep-sea coral (F_m = 0.0034±0.0007) with a U/Th age of 205,000±3000 yr.

Intermediate water Δ^{14}C values were reconstructed using measured U/Th ages and high-precision radiocarbon dates on coral samples according to the expression:

$$\Delta^{14}C = \left(\frac{e^{-^{14}\text{C age/Libby Mean Life}}}{e^{-\text{U/Th age/True Mean Life}}} - 1 \right) \times 1000\,, \tag{3.1}$$

where the Libby Mean Life is 8033 yr and the True Mean Life is 8266 yr (Stuiver and Polach, 1977). This Δ^{14}C value corrects for the time elapsed since each coral sample grew, thereby extracting the Δ^{14}C value of the water it grew in, relying on the assumption that both the carbon isotope system and the U/Th isotope system have remained closed. For corals with top, middle, and bottom dates, a single U/Th age is measured on the top of the coral and middle and bottom dates are inferred using measured distances between subsamples and a growth rate of 1 mm/yr (Adkins, Henderson, et al., 2004). Age errors for middle and bottom subsamples are assigned to be 50 yr. Error in the Δ^{14}C value incorporates both error from U/Th dating and ^{14}C dating. Because calculating Δ^{14}C involves taking a ratio of exponentials, error in either of the dates can cause the total error to greatly increase (Supplemental Figure 3.8). When comparing these intermediate water Δ^{14}C values to the contemporaneous atmosphere, it is most appropriate to transform the Δ^{14}C data into epsilon values, which are similar to $\Delta\Delta^{14}$C. Epsilon values are the proper way of differencing delta values and are calculated by converting the Δ^{14}C of each sample and the contemporaneous atmosphere into ratios, and taking the ratio of the ratios:

$$\epsilon = \left(\left[\frac{\frac{\Delta^{14}C_{sample}}{1000} + 1}{\frac{\Delta^{14}C_{atm}}{1000} + 1} \right] - 1 \right) \times 1000\,. \tag{3.2}$$

Epsilon is a more correct measure of past ocean circulation changes than $\Delta\Delta^{14}$C because it takes into account changes in atmospheric Δ^{14}C value itself. It is therefore the parameter that stays constant (for sufficiently slow ^{14}C production changes) if ocean circulation does not change.

3.3 Results

Radiocarbon age screening reveals patterns consistent with those published by Thiagarajan, Gerlach, et al. (2013) (Figure 3.2). 97 corals were selected for ^{14}C screening from between 1390-1748 m, and 162 corals were selected from between 2004-2739 m. Previously, an additional 249 samples from between the depths of 899–2395 m were measured by Thiagarajan, Gerlach, et al. (2013). All of the corals deeper than 2000 m are Holocene-age with most younger than 5000 yr. There is an abundance peak with a greater depth range (1450–1950 m) that roughly coincides with the ACR and HS1. The LGM on the other hand has a much more restricted depth range, with most corals between 1450-1575 m. Average uncertainties were 300 ^{14}C-yr for samples screened at NOSAMS using the EA method, and 500 ^{14}C-yr for samples screened at UC Irvine using the 'rapid survey' method. The average offset between screened ages (converted into calendar age) and U/Th ages is 1500 yr. This discrepancy is most likely the result of our choice of reservoir age through time, in addition to changes in ventilation age.

In order to have a sufficient age range and sampling frequency for the Δ^{14}C time series, 103 individual corals were U/Th dated (Supplemental Table 3.1). Samples were selected for U/Th dating based on their depth and reconnaissance age. Dates were assessed based on two main criteria: the amount of ^{232}Th, which increases errors due to uncertainty in the initial ^{232}Th/^{230}Th ratio, and the initial δ^{234}U value, which provides information about whether or not the sample has behaved as a closed system (a primary assumption for U/Th dates). If the sample has behaved as a closed system, then the calculated initial δ^{234}U ($\delta^{234}U_{init} = \delta^{234}U_{meas}e^{\lambda t}$) should be within error of the marine δ^{234}U value. 14 samples had ^{232}Th concentrations above the cutoff value of 2000 ppt, and 3 samples had $\delta^{234}U_{init}$ values that were non-marine using the selection criteria from IntCal09, which is defined as 147±7‰ for corals younger than 17 kyr and 141.7±7.8‰ for corals older than 17 kyr (Reimer et al., 2009). The average relative error for all dates was 6.64‰ and the average relative error for all samples that met the ^{232}Th and δ^{234}U criteria was 5.26‰. Procedural blanks account for 0.05% or less of the total error for ^{238}U and ^{234}U, 0.14% of the total error for ^{230}Th, and 1.97% of the total error for ^{232}Th, with average values of 38 fmol for ^{232}Th and 0.29 pmol for ^{238}U.

Out of the 103 individual corals that were U/Th dated, 44 were selected for high-precision radiocarbon dating. Keeping with the goal of creating a high-resolution continuous time series, samples were selected for high-precision radiocarbon dating

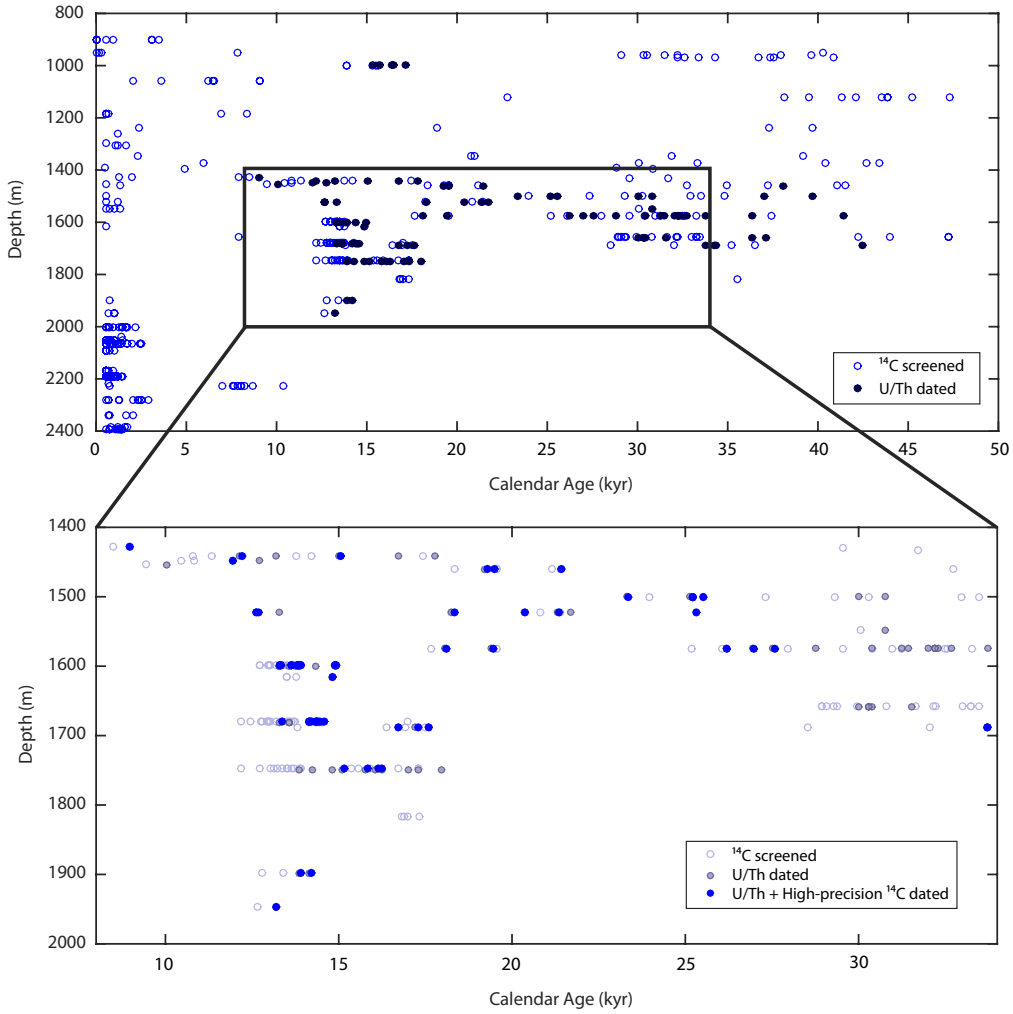

Figure 3.2: Age-depth distribution for ^{14}C screened corals. Upper panel shows all screened corals (blue open circles; n = 508) and individuals that were selected for U/Th dating (blue filled circles; n = 112). Lower panel is an expanded view of the boxed region in the upper panel. In the lower panel, ^{14}C screened and U/Th dated corals from the upper panel are shown in lighter blue, and filled blue circles represent the subset of U/Th dated samples that were also high-precision ^{14}C dated (n = 44).

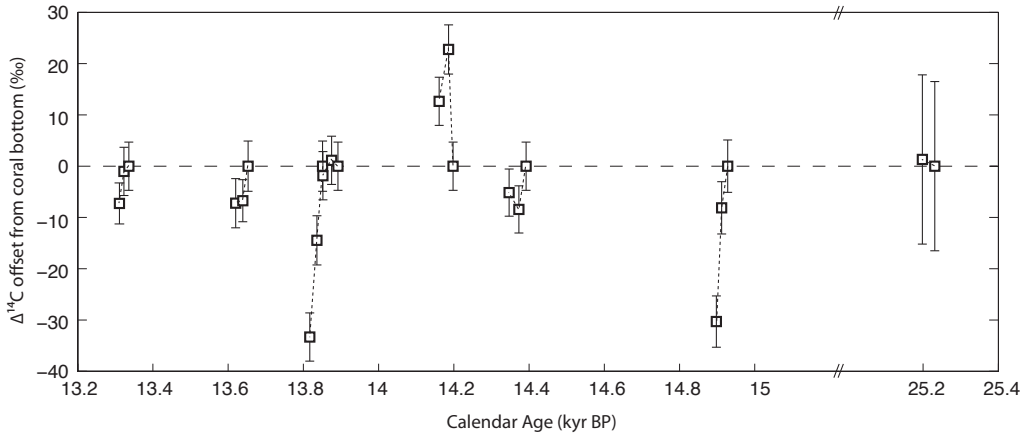

Figure 3.3: Changes in Δ^{14}C over the lifetime of single deep-sea coral specimens. Seven corals were sub-sampled for top–middle–bottom ^{14}C dates and one for top–bottom ^{14}C dates. Calculated Δ^{14}C values are plotted as differences from the bottom of the coral with 1σ error bars based only on uncertainty from radiocarbon dating. Of these eight corals, three show distinguishable changes in Δ^{14}C over the lifetime of the coral, two show no change, and three show slight changes that are not resolvable within error. (Note break in x-axis between 15 and 25.2 ka.)

based on their U/Th ages, ^{232}Th concentrations, and uranium isotope values. Of these 44 samples, eight were subsampled for top, middle, and bottom dates (Figure 3.4). Average relative errors radiocarbon dates were 2.7‰ for samples less than 15,000 ^{14}C-yr, 3.6‰ for samples between 15,000-25,000 ^{14}C-yr, 4.6‰ for samples between 20,000-25,000 ^{14}C-yr, and 8.4‰ for samples older than 25,000 ^{14}C-yr.

The Δ^{14}C dataset presented here is the highest resolution record that has been produced for this time in the Southern Ocean. It contains 68 ^{14}C dates on 44 individual corals between 9000–33,790 yr with an average sampling resolution of 575 yr (average resolution of 295 yr between 9000-15,170 yr and 590 yr between 15,830-27,580 yr) (Figure 3.3). Eight of these 44 corals were also subsampled for even higher resolution radiocarbon dating during times of increased Δ^{14}C variability, and three of these corals reveal resolvable changes in intermediate water radiocarbon occurring on decadal timescales (Figure 3.3; depicted as separate Δ^{14}C points connected by lines on subsequent figures).

The full record can be broken up into three main segments based on chronology and Δ^{14}C behavior during these periods: the Marine Isotope Stage (MIS) 3–2 transition, the LGM/early HS1, and the ACR. The MIS 3–2 transition segment is characterized by one large drop in intermediate water radiocarbon of ~250‰ starting at 27.6

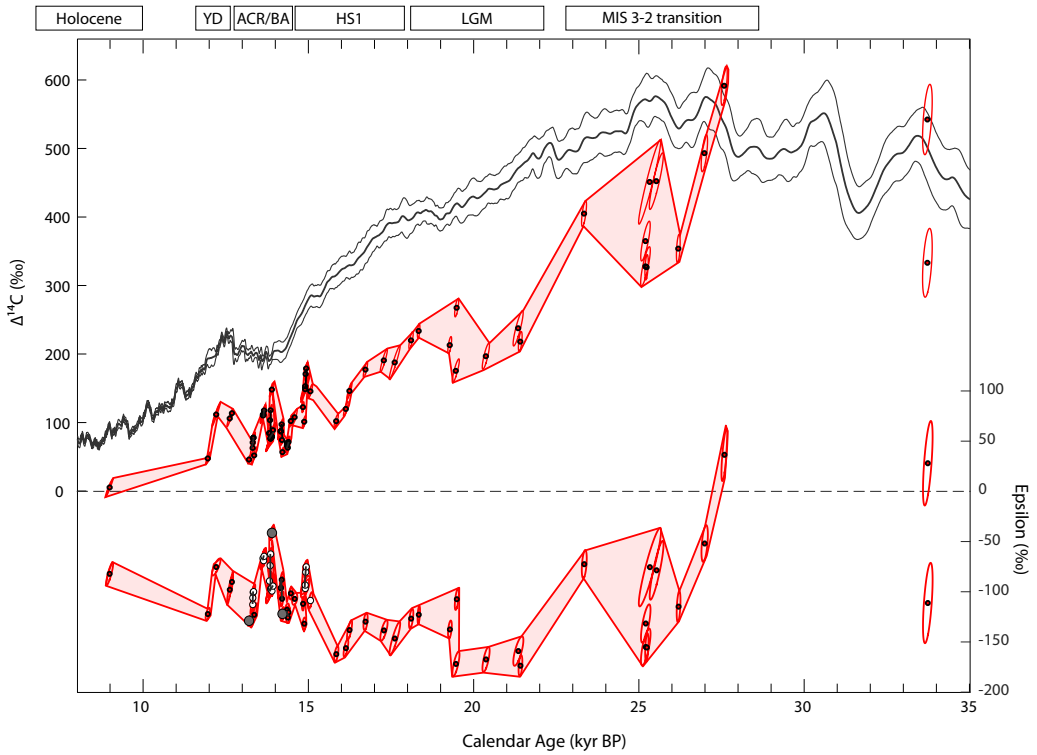

Figure 3.4: A) Tasmanian $\Delta^{14}C$ record plotted with IntCal13 atmospheric $\Delta^{14}C$ record, and B) converted into epsilon values. Error ellipses represent 1σ correlated U/Th and $\Delta^{14}C$ errors. For epsilon values, these ellipses also take into account uncertainty in the IntCal13 atmospheric $\Delta^{14}C$ record. Despite coming from between 1442 and 1947 m, epsilon variability between ~15–13 ka is not depth dependent. The deepest samples (at 1947 and 1898 m) are shown in panel B with dark gray filled circles, and they encompass nearly the full range in epsilon (including the highest point). The shallowest samples (at 1442 and 1599 m) are shown with white circles. 25 of the 30 samples from this time interval come from a depth range of less than 100 m (1599–1680 m).

ka. This drop is followed by a period of intermediate water variability and then a gap between 23.6-21.5 ka. Between 21.5–16 ka, the LGM/early HS1 segment, intermediate waters roughly follow the atmosphere with an offset of around 200‰ (with a ~40‰ jump at around 19 ka). Then there is an 800-yr gap in the record, after which intermediate waters are on average less offset from the atmosphere but far more variable. This final ACR segment contains three corals that record abrupt changes in intermediate radiocarbon within their lifetimes. There is a drop of 30‰ at 14.9 ka, a rise of 23‰ at 14.2 ka, and a drop of 35‰ at 13.9 ka (Figure 3.3 and Figure 3.4).

3.4 Discussion

The Southern Ocean is a region where deep water upwells to the surface and exchanges with the atmosphere, making it important to global climate. The Southern Ocean is also important in setting atmospheric CO_2 values over glacial-interglacial timescales (Sarmiento and Toggweiler, 1984). In the Southern Ocean, surface $\Delta^{14}C$ values are generally aligned with isopycnals and fronts (Figure 3.1B). This is the result of Southern Ocean overturning, where the oldest water upwells close to Antarctica, and the residence time of water at the surface, which is not long enough for the full exchange of carbon isotopes. This leads to a meridional surface gradient in $\Delta^{14}C$ with more negative values closest to Antarctica (Figure 3.1B). When water leaves the surface of the Southern Ocean, the surface $\Delta^{14}C$ gradient is transformed into a vertical gradient (Figure 3.1A). Because of this pattern, there are two main mechanisms to generate changes in intermediate water $\Delta^{14}C$ at our sampling location—one of them able to produce abrupt changes on annual to decadal timescales and the other tending to produce more gradual changes over centennial to millennial timescales (Figure 3.1C). On short timescales, meridional shifts in the position of Southern Ocean fronts can change the $\Delta^{14}C$ value of the water ventilating a particular region (Figure 3.1C; mechanism 1). On longer timescales, $\Delta^{14}C$ changes could also reflect the degree of mixing between Tasmanian intermediate water and older Pacific deep water below and to the north (Figure 3.1C; mechanism 2). The amount of mixing between Tasmanian intermediate water and older, deeper water masses also dictates how responsive intermediate waters will be to changes in atmospheric CO_2, since older deep waters carry the majority of regenerated CO_2. In general, the positions of fronts in the Southern Ocean are dictated by bathymetry (Graham et al., 2012). However in the absence of strong bathymetric features, fronts are less constrained and respond to the position of Southern Ocean westerly winds (Sallée, Speer, and Morrow, 2008). This latter scenario is the case for the Subantarctic and Polar Fronts in the region south of Tasmania, between which Antarctic Intermediate Water is formed.

LGM steady state and early frontal shifts

Beginning at 21.5 ka, the Tasmanian coral $\Delta^{14}C$ record generally follows the atmosphere at a constant offset. This trend can be easily seen by converting the $\Delta^{14}C$ record into epsilon units. Between ~21.5 and 19 ka, intermediate waters have an epsilon of ~–170‰. After an abrupt jump of ~40‰ at 19 ka, intermediate water $\Delta^{14}C$ continues to follow the atmosphere, now with epsilon values of around -130‰.

Correcting the IntCal13 atmospheric $\Delta^{14}C$ reconstruction for the contribution from production rate changes, the residual atmospheric $\Delta^{14}C$ is flat across most of the LGM, consistent with an ocean–atmosphere system at steady state (Hain, Sigman, and Haug, 2014) (Figure 3.5A). Together, the consistency between the atmosphere and the coral $\Delta^{14}C$ and the constant value of production-corrected atmospheric $\Delta^{14}C$ imply that the ocean was at or near steady state during the LGM.

The jump in intermediate water radiocarbon at ~19 ka is a conspicuous departure from the otherwise steady–state-like conditions of the LGM. This timing is coincident with 10-15 m of sea level rise measured using a series of sediment cores off the northern coast of Australia (Yokoyama et al., 2000). It also corresponds to an abrupt and permanent poleward shift of the Subantarctic (SAF) and Polar Fronts (PF) as shown by foram faunal assemblage data from a core located south of Australia (MD03-2611, 36°43.8'S, 136°32.9'E, 2420 m; Figure 3.5D)(De Deckker et al., 2012). A southward shift of the Subantarctic and Polar Fronts would lead to a rise in intermediate water $\Delta^{14}C$ south of Tasmania. The decrease in subpolar foraminifera beginning at 19 ka also marks the first appearance of subtropical fauna, which dominate the rest of the deglaciation.

Based on the relative timing of Northern and Southern Hemisphere ice sheet and mountain glacier retreat following the Last Glacial Maximum, it is thought that the sea level rise at ~19 ka originated from ice sheet retreat in the north (Clark et al., 2009). This influx of fresh water to the North Atlantic caused a reduction in the strength of the Atlantic meridional overturning circulation (AMOC) and initiated warming in the Southern Hemisphere via the bipolar seesaw (Broecker, 1998; Shakun et al., 2012). Atmospheric models show that the ITCZ and other aspects of tropical circulation responds to changes in extratropical temperature, shifting toward the warmer hemisphere (Kang et al., 2008). Shifts in the position of the ITCZ can in turn affect other atmospheric wind belts, shifting them in the same direction (Ceppi et al., 2013). This is consistent both with our $\Delta^{14}C$ record and with foram assemblages from south of Australia (De Deckker et al., 2012). Our data is consistent with melting of Northern Hemisphere ice sheets reducing the strength of the AMOC, which shifted atmospheric winds to the south and caused a southward shift in Southern Ocean fronts.

Although this initial pulse of meltwater at ~19 ka prompts a shift in Tasmanian intermediate water $\Delta^{14}C$, the bulk of the carbon system stays in steady state through this interval, as indicated by the production-corrected IntCal13 record and atmo-

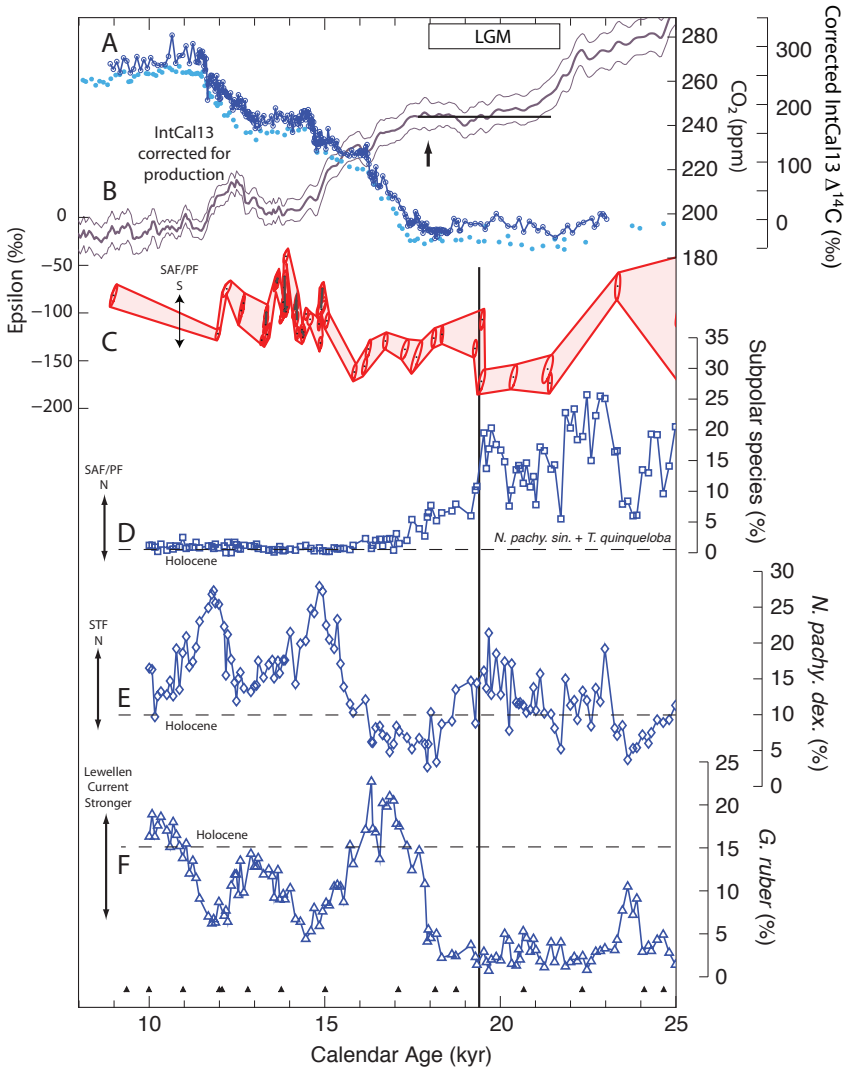

Figure 3.5: $\Delta^{14}C$ changes and frontal movement in the Southern Ocean. A) Atmospheric CO_2 curves from EPICA Dome C (through 22 ka) on the timescale of Lemieux-Dudon and Taylor Dome (20–25 ka) (Indermühle et al., 2000; Lemieux-Dudon et al., 2010; Monnin et al., 2001) (light blue dots) and WAIS (Marcott et al., 2014) (dark blue circles and line) B) The IntCal13 atmospheric $\Delta^{14}C$ reconstruction corrected for changes in atmospheric ^{14}C production (Hain, Sigman, and Haug, 2014). Arrow at top marks the initiation of CO_2 rise at ~18 ka. C) The Tasmanian coral $\Delta^{14}C$ record, converted into epsilon. D-F) Foraminiferal species assemblages from core MD03-2611 (36°43.8'S, 136°32.9'E; 2420 m) located south of Australia (De Deckker et al., 2012). D) Percent abundance of subpolar foraminiferal species assemblage (*N. pachyderma sinestral* and *T. quinqueloba*), indicative of SAF/PF movement. E) *N. pacyderma dextral* percent abundance, indicative of STF movement. F) *G. ruber* percent abundance, representative of the strength of the Lewellen Current. Black triangles at the bottom of the figure are age control points for MD03-2611 based on calibrated $\Delta^{14}C$ ages.

spheric CO_2. The deep ocean exerts the strongest influence on the $\Delta^{14}C$ value of the atmosphere and CO_2 because it is old and contains a large volume of regenerated CO_2. The disconnect between intermediate water Δ^{14} C and atmospheric Δ^{14} C at ~19 ka indicates that deep and intermediate waters are not acting together and the upper and lower circulation cells are separate.

Early in the deglaciation atmospheric CO_2 begins to rise as recorded in the Epica Dome C and WAIS divide ice cores (at ~17.5 ka according to EDC and ~18 ka according to WAIS) (Figure 3.5A) (Lemieux-Dudon et al., 2010; Marcott et al., 2014; Monnin et al., 2001). Despite this big change in the ocean– atmosphere carbon system, there is very little change in intermediate water Δ^{14} C. The insensitivity of intermediate water $\Delta^{14}C$ to early changes in atmospheric CO_2 indicates, again, that intermediate water is behaving independently from deep water. A comparison of epsilon values from Tasmania to other deglacial radiocarbon records from the Chilean Margin, Drake Passage, deep South Atlantic, and the Chatham Rise, shows this general pattern, with the deepest water getting younger most dramatically at the start of HS1 and shallower water not changing (Figure 3.6C, 3.9) (Burke and L F Robinson, 2012; De Pol-Holz et al., 2010; L. C. Skinner et al., 2010; L. Skinner et al., 2015).

Rapid variability and zonal asymmetry during the ACR

In the Tasmanian coral $\Delta^{14}C$ record, the ACR stands out compared to the rest of the deglaciation due to its large and abrupt changes in $\Delta^{14}C$, and unprecedented resolution (Figure 3.6C). Average sample resolution during the ACR (14.7–12.9 ka) is 55 yr, including 6 corals that have been sub-sampled (excluding the 6 sub-sampled corals decreases the average sample resolution to 105 yr, which is still high compared to most marine records). The variability during this time period is not only seen between corals but also within the lifetimes of several individuals (Figure 3.3 and Figure 3.6C). Because of the inherent stratigraphy of each skeleton, top middle and bottom dates are able to resolve changes in intermediate water radiocarbon that would otherwise be within calendar age measurement error. The largest of these jumps occurs at 13.9 ka and has a magnitude of 35‰ over approximately 35 yr. The standard deviation of detrended inter-sample epsilon values during the ACR (i.e. excluding middle and bottom samples) is twice as large as during the LGM and HS1, and a Levene's Test (Levene, 1960) comparing the detrended inter-sample epsilon variability during the ACR to that of the LGM/HS1 rejects the null hypothesis that the variances are equal at the 82% confidence level ($p = 0.177$). It cannot

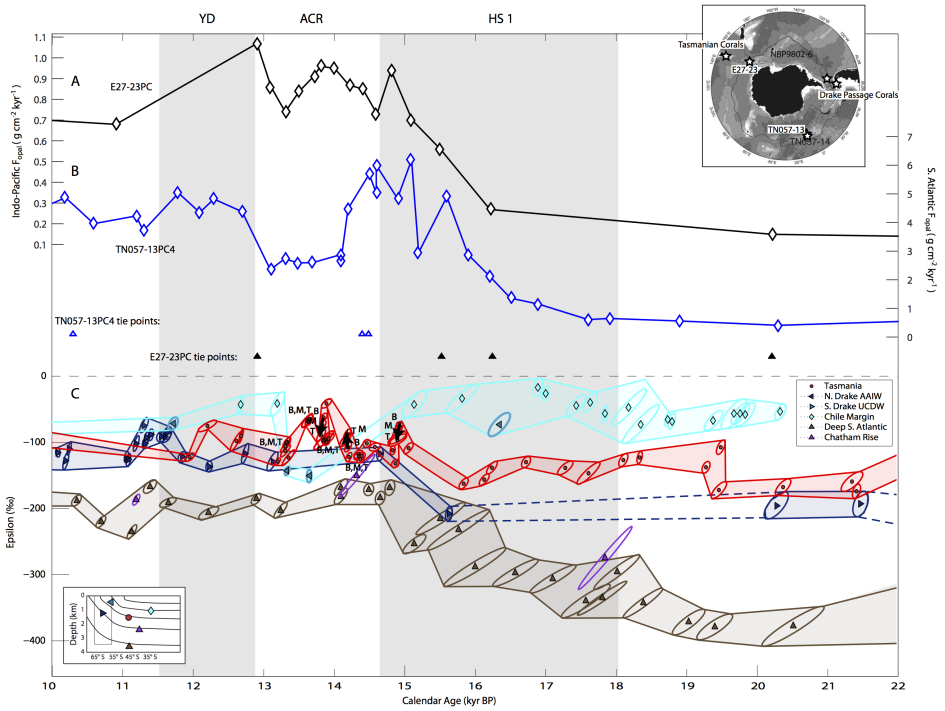

Figure 3.6: Opal flux and epsilon radiocarbon records from the Southern Ocean across the deglaciation. A) Opal flux record from Indo-Pacific core E27-23 (59.62°S 155.24°E, 3182 m). B) Opal flux record from South Atlantic core TN057-13 (53.1728°S 5.1275°E, 2848 m). Error bars on opal flux values are the size of the points. Also included are chronological constraints (from calibrated ^{14}C dates) for both cores, with E27-23 tie points in filled black triangles and TN057-13 tie points in open blue triangles. C) Tasmanian coral Δ^{14}C record shown as epsilon units offset from the atmosphere with other Southern Ocean records Δ^{14}C records. Deep South Atlantic (L. C. Skinner et al., 2010) (brown ellipses and upward-facing triangles; core MD07-3076; 44.1°S 14.2°E, 4981 m), southern Drake Passage UCDW (Burke and L F Robinson, 2012) (dark blue ellipses and right-facing triangles; ~60°S, ~1000 m), northern Drake passage AAIW (Burke and L F Robinson, 2012) (dark teal ellipses and left-facing triangles; ~55°S, 500 m), Chilean Margin (De Pol-Holz et al., 2010) (teal ellipses and diamonds; core SO161-SL22; 36.2°S 73.7°W, 1000 m), Chatham Rise (L. Skinner et al., 2015) (purple ellipses and upward-facing triangles; core MD97-2121; 40.4°S 178.0°E, 2314 m), and Tasmania (this study) (red ellipses and circles; ~45°S, ~1600 m). "T, M, B" labels refer to top, middle, and bottom ^{14}C values for individual corals. Of corals with top, middle, and bottom dates, only three show resolvable changes over the coral's lifespan (see Figure 3.3). The direction of these changes is marked with an arrow. Top right: map showing the locations of cores TN057-13 and E27-23, Drake Passage Corals and Tasmanian corals. Bottom left: schematic showing modern Southern Ocean zonally-averaged isopycnal structure, Drake Passage location, and locations of epsilon records (in color-coded symbols).

completely be ruled out, however, that this difference is the result of the three-fold higher sampling resolution during the ACR compared to the LGM/HS1.

The rapidity of these radiocarbon fluctuations implicates frontal shifts, rather than changes in circulation strength, either at the surface or at depth. In the modern ocean south of Tasmania, a 30‰ shift in $\Delta^{14}C$ would require fronts to move ~10° latitude based on the surface meridional $\Delta^{14}C$ gradient of ~3‰ per degree (Figure 3.1). However, some of the inter-sample $\Delta^{14}C$ shifts during this time are as large as 80‰, which would require a frontal shift of over 25° latitude based on this same gradient. Given that the Southern Ocean is only about 20° of latitude wide south of Tasmania, it is clearly unreasonable to assume that the surface $\Delta^{14}C$ gradient was the same during the ACR. It seems very likely that frontal gradients would have been enhanced during this time because older deep water upwelling around the Antarctic continent would reduce $\Delta^{14}C$ values to the south thereby increasing the total gradient across the Southern Ocean. This would decrease the magnitude of SAF/PF shift required to fit our data.

Frontal shifts of 5–10° over the deglaciation have been previously suggested for the Southern Ocean by several different studies (Kohfeld et al., 2013; Sikes et al., 2009). In the most comprehensive frontal reconstructions, shifts of 4–5° have been suggested for the SAF and PF and shifts of 3–5° have been suggested for the Subtropical Front (STF) (Kohfeld et al., 2013). Differences between the exact location and the temporal resolution of these frontal reconstructions compared to our record makes comparisons of the timing of these frontal shifts less informative than the magnitude of change. There are high-resolution data from south of Australia (De Deckker et al., 2012) through this time period, but the foram abundances indicate that subtropical waters are primarily influencing the core region. Our Tasmanian intermediate water corals are not especially sensitive to Subtropical Front position (NPD percent abundance) or Lewellen Current intensity (*G. ruber* percent abundance), so we do not expect these foram records to be directly comparable to our $\Delta^{14}C$ record during this time period.

Shifts in the position of Southern Ocean fronts, driven by the position of the westerly winds are thought to influence the rate of Southern Ocean upwelling and CO_2 degassing (Anderson et al., 2009; Toggweiler, Russell, and Carson, 2006). This is exemplified in the opal flux record from core TN057-13 (53.1728°S 5.1275°E, 2848 m) in the South Atlantic (Anderson et al., 2009). This record shows low opal fluxes during the LGM, consistent with Southern Ocean westerly winds shifted north, out-

side of the Drake Passage latitude band (Anderson et al., 2009; Toggweiler, Russell, and Carson, 2006). At the start of HS1, Northern Hemisphere cooling shifts the westerlies to the south, prompting increased upwelling and higher opal fluxes. This process is reversed at the Bølling–Allerød/ACR, where the Northern Hemisphere warms, and then reversed again at the Younger Dryas, causing a pattern of reduced then increased opal flux (Anderson et al., 2009). Other Southern Ocean records from near this core location highlight the ACR as a time of surface stratification and reduced upwelling (Anderson et al., 2009; Burke and L F Robinson, 2012; Siani et al., 2013).

During the end of HS1, leading up to the ACR, there seems to be a coherent Southern Ocean response. Upwelling leading to increased opal flux in the South Atlantic (Anderson et al., 2009) and increases in UCDW epsilon values seen in the Drake Passage (Burke and L F Robinson, 2012) are mirrored by increased opal flux in Indo-Pacific sector core E27-23 (Anderson et al., 2009) (Figure 3.6A; 59.62°S 155.24°E, 3182 m) and increases in epsilon south of Tasmania. However, the classic Southern hemisphere pattern of reduced upwelling and enhanced stratification during the middle of the ACR, typified by the South Atlantic opal flux record, is distinctly different from the pattern seen in the Indo-Pacific sector core (Figure 3.6A, B). In E27-23 there is upwelling throughout the ACR with some amount of temporal variability. It is tempting to look for a correlation between the Indo-Pacific opal flux record, as an indicator of front position, and the rapid, short-timescale variability in the Tasmanian coral epsilon record. Indeed, the Indo-Pacific opal flux and Tasmanian coral epsilon records do seem to line up; however, the age model for Indo-Pacific core E27-23 is much less well constrained than that of South Atlantic core TN057-13. There are three calendar age tie points for E27-23 between 12–17 ka, so if the opal flux data from E27-23 were shifted to better match the patterns in TN057-13, it would require two abrupt changes in sedimentation rate during this time period. The observation that Indo-Pacific opal fluxes do not look the same as South Atlantic opal fluxes, and their close correspondence with the Tasmanian coral $\Delta^{14}C$, indicates that there is zonal asymmetry across the Southern Ocean during the ACR.

Although the Drake Passage UCDW record looks quite similar to our Tasmanian coral record during the end of HS1, a comparison of Tasmanian coral epsilon values to both the UCDW and AAIW records from Drake Passage during this time shows potential differences (Figure 3.6C). This is most obvious at ~13.6 ka, where

one Drake Passage AAIW sample falls almost 100‰ below the contemporaneous Tasmanian coral samples. The Drake Passage corals more closely resemble the South Atlantic opal flux record, while the Tasmanian corals more closely resemble the Indo-Pacific opal flux record (Figure 3.6), despite the fact that the Tasmanian record should fall between the two Drake Passage records according to a zonally symmetric view of the modern hydrography (Figure 3.6, inset at lower left). Drake Passage is unique in the Southern Ocean, as it steers all the volume of the ACC and many of the Southern Ocean fronts through a fairly narrow channel, so one might expect fronts to behave differently in this region than they would south of Tasmania. Although there are some important topographic features south of Tasmania, such as the Tasman Plateau, this primarily influences the position of the Subtropical Front, leaving the Subantarctic and Polar Fronts free to move. It is also important to note that the discrepancy between the Drake Passage and Tasmanian coral records is largely driven by a gap in the UCDW record between 14.7–13.1 ka, so it is also possible that apparent zonal differences are simply driven by a lack of temporal overlap between the records. For the foraminiferal records (De Pol-Holz et al., 2010; L. C. Skinner et al., 2010; L. Skinner et al., 2015), fronts near the Chile Margin and Chatham Rise should be less affected by topography than those in the Southeast Atlantic; however, sampling gaps make it impossible to determine the extent to which frontal movement influences Δ^{14} C values at these locations.

Intermediate water perspectives on deglacial overturning circulation

One of the strongest climate signals through the deglaciation is the rise in atmospheric CO_2 and its connection with Southern Hemisphere warming and deep ocean ventilation (Figure 3.7C, D, F) (Marcott et al., 2014; L. C. Skinner et al., 2010; WAIS Divide Project Members, 2013). On top of this broad signal there are abrupt ~12 ppm rises in pCO_2 at ~16 ka and ~14.7 ka (Marcott et al., 2014). This first abrupt CO_2 increase occurs at about the same time as Heinrich Event 1 and the associated maximum weak monsoon interval seen in the Hulu cave record (Figure 3.7B) (Wang et al., 2001). This interval is thought to be associated with a southward shift of the ITCZ and other atmospheric wind systems (McGee et al., 2014), which should show up in Tasmanian intermediate water Δ^{14}C as a positive shift in epsilon values. Instead intermediate water Δ^{14}C gets gradually older.

This somewhat surprising observation could be the result of mechanism 2 in Figure 3.1C—at this time there is convergence between deeper and shallower water masses (Figure 3.7F) (Burke and L F Robinson, 2012), indicating that the deep overturning

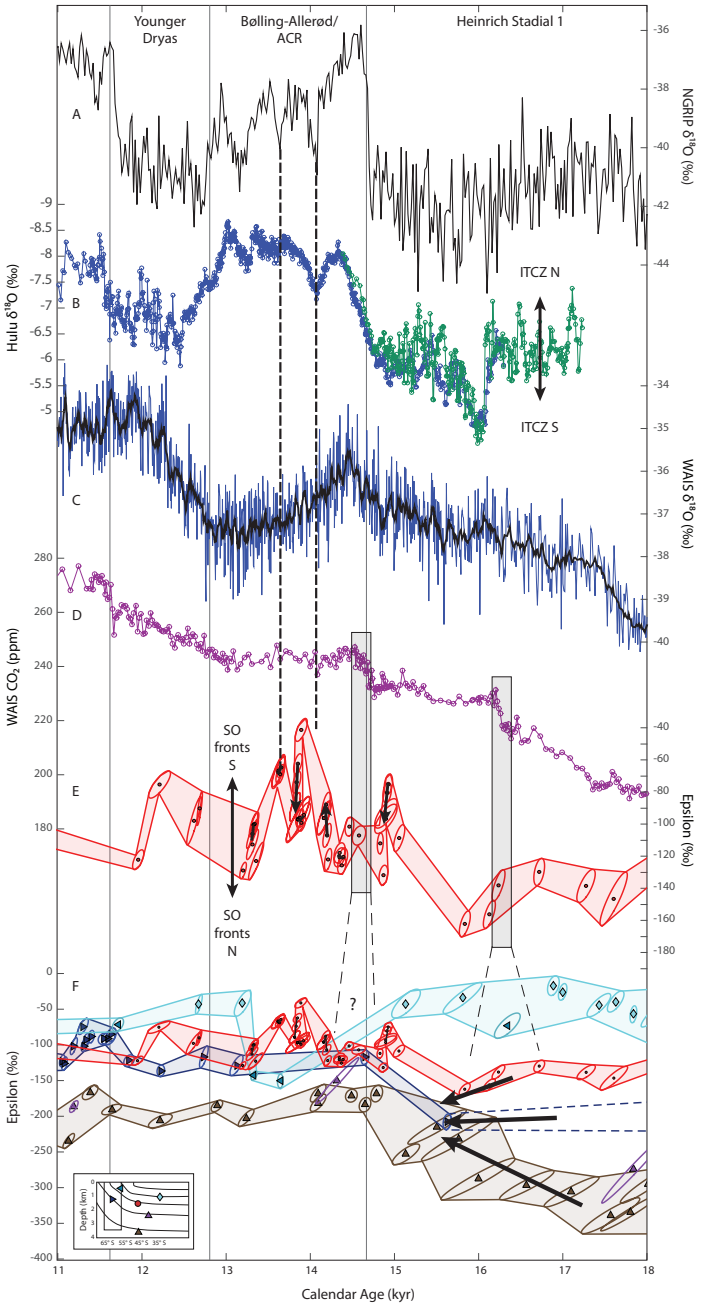

Figure 3.7: Records of the full deglacial period showing changes in overturning circulation. A) NGRIP δ^{18}O from Greenland (Andersen et al., 2006; Rasmussen et al., 2006). B) Hulu cave δ^{18}O from stalagmites H82 (blue) and YT (green) (Wang et al., 2001). C) WAIS Divide δ^{18}O from west Antarctica (WAIS Divide Project Members, 2013). D) Atmospheric CO_2 from WAIS Divide (Marcott et al., 2014). E) Δ^{14}C record from south of Tasmania represented as epsilon (this study). F) Tasmanian Δ^{14}C record with other Southern Ocean Δ^{14}C records (same colors and symbols as Figure 3.6C) (Burke and L F Robinson, 2012; De Pol-Holz et al., 2010; L. C. Skinner et al., 2010; L. Skinner et al., 2015).

cells have become temporarily more interconnected. After this convergence, there is a pause in atmospheric CO_2 rise, indicating less ventilation of deep water, perhaps due to expanded sea ice, which shoals the boundary between the upper and lower cells and reduces mixing between intermediate and deep waters. Without the influence of old deep water, Tasmanian intermediate water $\Delta^{14}C$ returns to the value dictated by the position of the fronts in the Southern Ocean (Figure 3.7E). At ~15 ka, the ITCZ starts to move north and intermediate water epsilon values drop.

At the start of the Bølling, there is another 12 ppm increase in atmospheric CO_2. This could be the result of deep convection in the North Atlantic, possibly associated with thermobaric capacitance and stored heat at mid-depths (Thiagarajan, Subhas, et al., 2014). There is also a slight convergence of intermediate and deeper waters in the Southern Ocean at this time, so perhaps there is also a southern source to this atmospheric CO_2 rise. During the rest of the ACR and Bølling–Allerød, atmospheric CO_2 stays constant and Antarctic $\delta^{18}O$ drops (Figure 3.7C, D, F). Intermediate water $\Delta^{14}C$, on the other hand, is highly variable and generally younger than earlier in the deglaciation. As indicated by the constant pCO_2, there is separation between the upper and lower circulation cells, while intermediate waters respond to atmospheric forcing unbuffered by mixing of deeper and older waters.

If the rapid fluctuations in Tasmanian coral $\Delta^{14}C$ record during the ACR are due to frontal movement in the Southern Ocean, then the question of what drives these shifts arises. Antarctic $\delta^{18}O$ drops during the ACR, but there is no resolvable second-order variability on top of the broader shift in isotope value (Figure 3.7C). On the other hand, there is structure within the Greenland $\delta^{18}O$ record during the Bølling–Allerød (Figure 3.7A). During the early part of the ACR/Bølling, there is some correspondence between Greenland $\delta^{18}O$ and Tasmanian coral $\Delta^{14}C$, as illustrated by vertical dashed lines in Figure 3.7. By the same mechanism previously discussed to explain the frontal shift at 19 ka, a sharp drop in Greenland $\delta^{18}O$ should shift winds and fronts to the south and lead to an increase in Tasmanian coral epsilon. While this correspondence between Tasmanian coral epsilon and Greenland $\delta^{18}O$ holds for the first two sharp drops (at 14.1 and 13.6 ka), by about 13.3 ka Southern Ocean intermediate water records have converged again and there is no longer a connection between Tasmanian corals and Greenland, though there is a slight gap in the coral record at this time.

Other times of intermediate water variability

The earliest part of the Tasmanian coral $\Delta^{14}C$ record is also characterized by rapid, albeit more ambiguous, variability. This variability directly contrasts with the LGM section of the record where intermediate water $\Delta^{14}C$ clearly follows the atmosphere, and indicates that the ocean is most likely not in steady state during this interval (~28–23 ka). The timing of variability and non-steady state behavior seen early in the Tasmanian coral record is not surprising, however, since it follows the transition between Marine Isotope Stages 3 and 2 (Lisiecki and Raymo, 2005). Around 25 ka in particular there is a large range of $\Delta^{14}C$ values. While this spread in $\Delta^{14}C$ may be driven by the same mechanisms that lead to intermediate water variability later in the record, it is difficult to resolve specific changes in intermediate water radiocarbon due to uncertainty in the radiocarbon dates driven by error associated with deep-sea coral blanks (Supplemental Figure 3.8). Therefore, it is hard to determine a specific forcing or mechanism for $\Delta^{14}C$ change. It is worth noting that two of the earliest samples in the record overlap with the IntCal13 atmospheric $\Delta^{14}C$ record. This is quite unusual due to old surface reservoir ages in the Southern Ocean, however, there is a great deal of scatter among the datasets that comprise the IntCal13 atmospheric $\Delta^{14}C$ compilation during this time period, so the apparent overlap between our record and the atmosphere is not necessarily representative of intermediate water of zero age.

Probably the most striking feature of the record during this time is the ~250‰ drop in intermediate water $\Delta^{14}C$ between 27.6–26.2 ka. The trajectory of this drop closely matches that of ^{14}C decay, implicating in situ ageing of a water mass. It also closely matches the initial portion of a $\Delta^{14}C$ drop from the Brazil Margin observed by Mangini et al. starting at 27.9 ka (Supplemental Figure 3.10) (Mangini et al., 2010). Mangini et al. suggest that this drop in intermediate water $\Delta^{14}C$ is related to a slowdown in the meridional overturning circulation during Heinrich 2. Yet a circulation slowdown that would give decay-like $\Delta^{14}C$ trajectories implies complete stagnation of the water, or an unlikely mixing scenario between multiple water masses. In addition, deep circulation changes in the North Atlantic and southern sourced intermediate waters are not expected to be in phase if the 'seesaw' mechanism (Broecker, 1998) is still at work during this time. Another possible mechanism is mixing with ^{14}C-dead water. While it would be difficult to simulate a decay-like $\Delta^{14}C$ trajectory by mixing water masses that contain radiocarbon, a 50:50 mixture with ^{14}C-dead water over 5730 yr naturally mimics decay. If mixing with ^{14}C-dead water was the cause of the decay-like drop in $\Delta^{14}C$ at ~27.6 ka, however,

the source of this water remains elusive.

The 250‰ ^{14}C drop at 27.6 ka is similar in magnitude to some of the intermediate water variability observed during the ACR. However, the high-resolution data during the deglaciation clearly distinguish the intermediate water changes from the stagnation signature of ^{14}C decay. It is therefore not hard to imagine that higher-resolution data at 27.6 ka might also differentiate this three-point $\Delta^{14}C$ drop from a decay trajectory. Likewise, more data could potentially change the interpretation of the Brazil Margin record, however, the longer duration of each stagnation event and repetition of decay trajectories over their entire interval sets their dataset apart from the alternating variability and steady–state behavior observed in our intermediate water record.

3.5 Conclusion

Our high-resolution $\Delta^{14}C$ record from south of Tasmania highlights times during the deglaciation when the upper and lower cells of the MOC are more or less interconnected. It also emphasizes the importance of fronts in the Southern Ocean for determining the radiocarbon values and short-term variability of intermediate waters.

During much of the Last Glacial Maximum we see evidence for steady state circulation. Tasmanian intermediate water $\Delta^{14}C$ follows the contemporaneous atmosphere, and production-corrected atmospheric $\Delta^{14}C$ is nearly constant in time. There is however one obvious departure from steady–state at around 19 ka, where a 10–15 m sea level rise (Yokoyama et al., 2000) is accompanied by a southward shift of the Subantarctic and Polar Fronts (De Deckker et al., 2012) and a 40‰ rise in intermediate water $\Delta^{14}C$. This abrupt shift only impacts the upper cell however—-production-corrected atmospheric $\Delta^{14}C$ values and atmospheric CO_2 are unaffected.

Intermediate water south of Tasmania is much more dynamic beginning late in HS1 and continuing through the Antarctic Cold Reversal. Fronts are aligned with the large-scale density structure of the Southern Ocean, and because of the pattern of upwelling, these fronts are also aligned with radiocarbon gradients. Frontal position is strongly influenced by topography (Graham et al., 2012), but in the absence of large topographic features, fronts are free to move in response to Southern Ocean westerly winds (Sallée, Speer, and Morrow, 2008). Although on a large scale the Southern Ocean is zonally symmetric there is important regional variability, largely driven by topography. This zonal asymmetry helps explain why Tasmanian

intermediate water $\Delta^{14}C$ and Indo-Pacific upwelling records deviate from similar South Atlantic records (Anderson et al., 2009; Burke and L F Robinson, 2012; L. C. Skinner et al., 2010; L. Skinner et al., 2015; De Pol-Holz et al., 2010).

Tasmanian intermediate water $\Delta^{14}C$ shows that the classic view of weakened overturning in the Southern Ocean during the Antarctic Cold Reversal is not appropriate for all regions. The timing of intermediate water $\Delta^{14}C$ variability south of Tasmania during parts of the ACR matches with $\delta^{18}O$ values measured in Greenland ice and Chinese speleothems. This upper cell variability and connection to Northern Hemisphere records indicates a separation between the circulation cells and less of a deep water influence at the sample location during this time. Earlier in the deglaciation, at ~16 ka, atmospheric signals associated with Heinrich Event 1 are not immediately seen in Tasmanian intermediate waters because they are overprinted by the effects of mixing with old deeper water masses. By the end of the ACR, overturning circulation more closely matches the modern and intermediate and deep water masses are organized accordingly.

Early in the record, following the Marine Isotope Stage 3–2 transition at 29 ka, there is also a great deal of variability in intermediate water $\Delta^{14}C$, however it is more difficult to resolve clear patterns and connect them to specific forcings. One discernable feature is a 1400-yr 250‰ drop starting at 27.6 ka, which closely follows the trajectory of ^{14}C decay. This $\Delta^{14}C$ drop corresponds to the first half of a drop observed off the coast of Brazil (Mangini et al., 2010). We hesitate to interpret our signal as intermediate water stagnation since it is difficult to imagine physical mechanisms wherein this could be achieved. The magnitude of this drop is similar to some of the variability observed during the ACR section of the record. Whereas the high-resolution data during the deglaciation clearly distinguish intermediate water ^{14}C variability from ^{14}C decay, the lack of data density at 27.6 ka makes this distinction difficult. More $\Delta^{14}C$ measurements could lead to a better understanding of the mechanisms at play during this time period, but we recovered few corals that grew during this time.

References

Adkins, Jess F., Sheila Griffin, et al. (2002). “Radiocarbon Dating of Deep-Sea Corals”. In: *Radiocarbon* 44, pp. 567–580.

Adkins, Jess F., G M Henderson, et al. (2004). “Growth rates of the deep-sea scleractinia Desmophyllum cristagalli and Enallopsammia rostrata”. In: *Earth and Planetary Science Letters* 227.3-4, pp. 481–490.

Andersen, Katrine K et al. (2006). "The Greenland ice core chronology 2005, 15–42ka. Part 1: constructing the time scale". In: *Quaternary Science Reviews* 25.23-24, pp. 3246–3257.

Anderson, Robert F. et al. (2009). "Wind-Driven Upwelling in the Southern Ocean and the Deglacial Rise in Atmospheric CO_2". In: *Science* 323.5920, pp. 1443–1448.

Broecker, Wallace S. (1998). "Paleocean circulation during the last deglaciation: A bipolar seesaw?" In: *Paleoceanography* 13, pp. 119–121.

Burke, Andrea and L F Robinson (2012). "The Southern Ocean's Role in Carbon Exchange During the Last Deglaciation". In: *Science* 335.6068, pp. 557–561.

Burke, Andrea, Laura F. Robinson, et al. (2010). "Reconnaissance dating: A new radiocarbon method applied to assessing the temporal distribution of Southern Ocean deep-sea corals". In: *Deep-Sea Research Part I-Oceanographic Research Papers* 57.11, pp. 1510–1520.

Bush, Shari L. et al. (2013). "Simple, rapid, and cost effective: a screening method for ^{14}C analysis of small carbonate samples". In: *Radiocarbon* 55, pp. 631–640. DOI: 10.1017/S0033822200057787.

Ceppi, P et al. (2013). "The relationship between the ITCZ and the Southern Hemispheric eddy-driven jet". In: *Journal of Geophysical Research* 118, pp. 1–11.

Cheng, Hai et al. (2000). "U-Th dating of deep-sea corals". In: *Geochimica et Cosmochimica Acta* 64, pp. 2401–2416.

Clark, Peter U et al. (2009). "The Last Glacial Maximum". In: *Science* 325.5941, pp. 710–714.

Curry, William B. and Delia W. Oppo (2005). "Glacial water mass geometry and the distribution of δ13C of ΣCO2 in the western Atlantic Ocean". In: *Paleoceanography*.

De Deckker, Patrick et al. (2012). "Influence of the tropics and southern westerlies on glacial interhemispheric asymmetry". In: *Nature Geoscience* 5.4, pp. 266–269.

De Pol-Holz, Ricardo et al. (2010). "No signature of abyssal carbon in intermediate waters off Chile during deglaciation". In: *Nature Geoscience* 3.3, pp. 192–195.

Eltgroth, Selene F et al. (2006). "A deep-sea coral record of North Atlantic radiocarbon through the Younger Dryas: Evidence for intermediate water/deepwater reorganization". In: *Paleoceanography* 21.4.

Ferrari, R et al. (2014). "Antarctic sea ice control on ocean circulation in present and glacial climates". In: *PNAS* 111.24, pp. 8753–8758.

Graham, Robert M et al. (2012). "Southern Ocean fronts: Controlled by wind or topography?" In: *Journal of Geophysical Research* 117.

Hain, Mathis P, Daniel M Sigman, and Gerald H Haug (2014). "Distinct roles of the Southern Ocean and North Atlantic in the deglacial atmospheric radiocarbon decline". In: *Earth and Planetary Science Letters* 394.C, pp. 198–208.

Indermühle, Andreas et al. (2000). "Atmospheric CO_2 concentration from 60 to 20 kyr BP from the Taylor Dome Ice Core, Antarctica". In: *Geophysical Research Letters* 27.5, pp. 735–738.

Kang, Sarah M et al. (2008). "The Response of the ITCZ to Extratropical Thermal Forcing: Idealized Slab-Ocean Experiments with a GCM". In: *Journal of Climate* 21.14, pp. 3521–3532.

Key, RM et al. (2004). "A global ocean carbon climatology: Results from Global Data Analysis Project (GLODAP)". In: *Global Biogeochemical Cycles* 18.4.

Knox, Fanny and Michael B McElroy (1984). "Changes in atmospheric CO_2: Influence of the marine biota at high latitude". In: *Journal of Geophysical Research* 89.D3, p. 4629.

Kohfeld, K E et al. (2013). "Southern Hemisphere westerly wind changes during the Last Glacial Maximum: paleo-data synthesis". In: *Quaternary Science Reviews* 68, pp. 76–95.

Laj, C et al. (2002). "Geomagnetic field intensity, North Atlantic Deep Water circulation and atmospheric $\Delta^{14}C$ during the last 50 kyr". In: *Earth and Planetary Science Letters* 200, pp. 177–190.

Lemieux-Dudon, Benedicte et al. (2010). "Consistent dating for Antarctic and Greenland ice cores". In: *Quaternary Science Reviews* 29.1-2, pp. 8–20.

Levene, H (1960). "Robust tests for equality of variances". In: *Contributions to probability and statistics*.

Lisiecki, Lorraine E and Maureen E Raymo (2005). "A Pliocene-Pleistocene stack of 57 globally distributed benthic $\delta^{18}O$ records". In: *Paleoceanography* 20.1.

Lund, D C, Jess F. Adkins, and R Ferrari (2011). "Abyssal Atlantic circulation during the Last Glacial Maximum: Constraining the ratio between transport and vertical mixing". In: *Paleoceanography* 26.1.

Mangini, A et al. (2010). "Deep sea corals off Brazil verify a poorly ventilated Southern Pacific Ocean during H2, H1 and the Younger Dryas". In: *Earth and Planetary Science Letters* 293.3-4, pp. 269–276.

Marcott, Shaun A et al. (2014). "Centennial-scale changes in the global carbon cycle during the last deglaciation". In: *Nature* 514, pp. 616–619.

McGee, David et al. (2014). "Changes in ITCZ location and cross-equatorial heat transport at the Last Glacial Maximum, Heinrich Stadial 1, and the mid-Holocene". In: *Earth and Planetary Science Letters* 390.2, pp. 69–79.

Monnin, Eric et al. (2001). "Atmospheric CO_2 concentrations over the last glacial termination". In: *Science* 291.5501, pp. 112–114.

Muscheler, R et al. (2004). "Changes in the carbon cycle during the last deglaciation as indicated by the comparison of ^{10}Be and ^{14}C records". In: *Earth and Planetary Science Letters* 219, pp. 325–240.

Rasmussen, S O et al. (2006). "A new Greenland ice core chronology for the last glacial termination". In: *Journal of Geophysical Research* 111.

Reimer, Paula J. et al. (2009). "IntCal09 and Marine09 radiocarbon age calibration curves, 0–50,000 years cal BP". In: *Radiocarbon* 51.

Robinson, Laura F. et al. (2007). "Deep-sea scleractinian coral age and depth distributions in the WN Atlantic for the last 225 thousand years". In: *Bulletin of Marine Science* 81, pp. 371–391.

Rose, Kathryn A et al. (2010). "Upper-ocean-to-atmosphere radiocarbon offsets imply fast deglacial carbon dioxide release". In: *Nature* 466.7310, pp. 1093–1097.

Sallée, J B, K Speer, and R Morrow (2008). "Response of the Antarctic Circumpolar Current to atmospheric variability". In: *Journal of Climate* 21.12, pp. 3020–3039.

Santos, G M et al. (2007). "Evaluation of iron and cobalt powders as catalysts for ^{14}C-AMS target preparation". In: *Nuclear Instruments and Methods in Physics Research Section B: Beam Interactions with Materials and Atoms* 259.1, pp. 308–315.

Sarmiento, J. L. and J. R. Toggweiler (1984). "A new model for the role of the oceans in determining atmospheric pCO_2". In: *Nature* 308, pp. 621–624.

Shakun, Jeremy D et al. (2012). "Global warming preceded by increasing carbon dioxide concentrations during the last deglaciation". In: *Nature* 484.7392, pp. 49–54.

Shen, Glen T and Edward A. Boyle (1988). "Determination of lead, cadmium and other trace metals in annually-banded corals". In: *Chemical Geology* 67.1-2, pp. 47–62.

Siani, Giuseppe et al. (2013). "Carbon isotope records reveal precise timing of enhanced Southern Ocean upwelling during the last deglaciation". In: *Nature Communications* 4, pp. 1–9.

Siegenthaler, U and Th Wenk (1984). "Rapid atmospheric CO_2 variations and ocean circulation". In: *Nature* 308.5960, pp. 624–626.

Sigman, Daniel M, Mathis P Hain, and Gerald H Haug (2010). "The polar ocean and glacial cycles in atmospheric CO_2 concentration". In: *Nature* 466.7302, pp. 47–55.

Sikes, E L et al. (2009). "Southern Ocean seasonal temperature and Subtropical Front movement on the South Tasman Rise in the late Quaternary". In: *Paleoceanography* 24.2.

Skinner, L C et al. (2010). "Ventilation of the Deep Southern Ocean and Deglacial CO_2 Rise". In: *Science* 328.5982, pp. 1147–1151.

Skinner, L et al. (2015). "Reduced ventilation and enhanced magnitude of the deep Pacific carbon pool during the last glacial period". In: *Earth and Planetary Science Letters* 411.C, pp. 45–52.

Stuiver, M and H A Polach (1977). "Reporting of ^{14}C Data—Discussion". In: *Radiocarbon* 19.3, pp. 355–363.

Talley, Lynne (2013). "Closure of the Global Overturning Circulation Through the Indian, Pacific, and Southern Oceans: Schematics and Transports". In: *Oceanography* 26.1, pp. 80–97.

Talley, Lynne D. (2003). "Shallow, Intermediate, and Deep Overturning Components of the Global Heat Budget". In: *Journal of Physical Oceanography* 33, pp. 530–560.

Thiagarajan, Nivedita, Dana Gerlach, et al. (2013). "Movement of deep-sea coral populations on climatic timescales". In: *Paleoceanography* 28, pp. 227–236.

Thiagarajan, Nivedita, Adam V. Subhas, et al. (2014). "Abrupt pre-Bolling-Allerod warming and circulation changes in the deep ocean". In: *Nature* 511, pp. 75–78.

Toggweiler, J. R., Joellen L Russell, and S R Carson (2006). "Midlatitude westerlies, atmospheric CO_2, and climate change during the ice ages". In: *Paleoceanography* 21.2.

WAIS Divide Project Members (2013). "Onset of deglacial warming in West Antarctica driven by local orbital forcing". In: *Nature* 500, pp. 440–444.

Wang, Y J et al. (2001). "A High-Resolution Absolute-Dated Late Pleistocene Monsoon Record from Hulu Cave, China". In: *Science* 294.5550, pp. 2345–2348.

Yokoyama, Yusuke et al. (2000). "Timing of the Last Glacial Maximum from observed sea-level minima". In: *Nature* 406.6797, pp. 713–716.

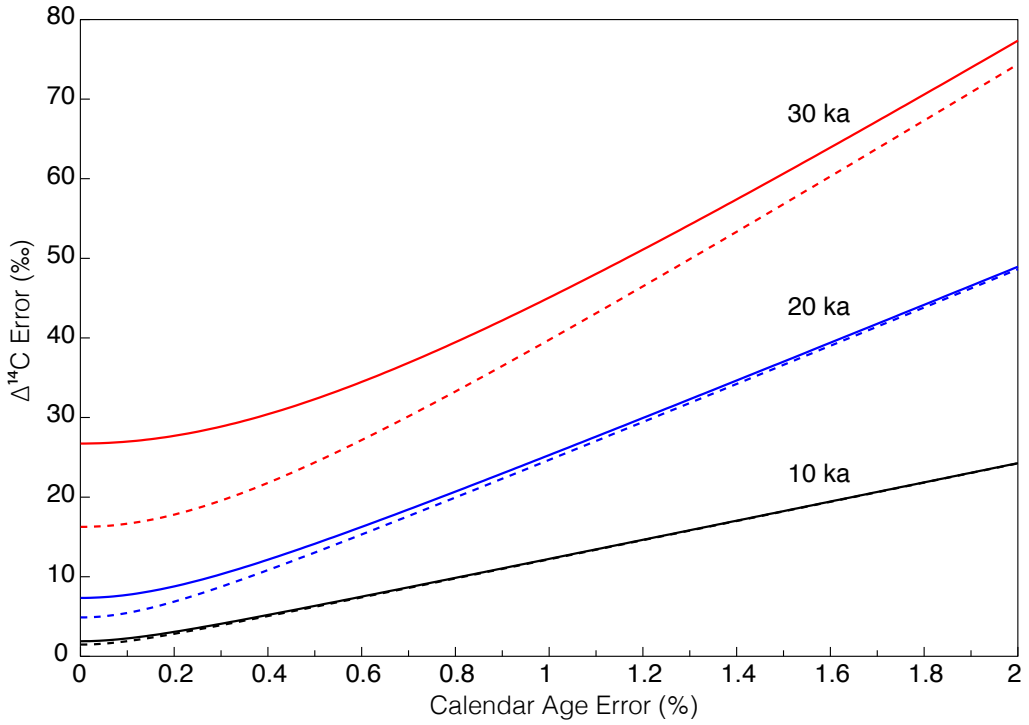

Figure 3.8: Error on $\Delta^{14}C$ as a function of coral age, calendar age error, and radiocarbon age error. Error on $\Delta^{14}C$ is calculated as a function of relative calendar age error for corals of three different ages. The dashed line is for a F_m of ± 0.0002 based on calcite blanks and the solid line is for a F_m error of ±0.0007 based on measured deep-sea corals.

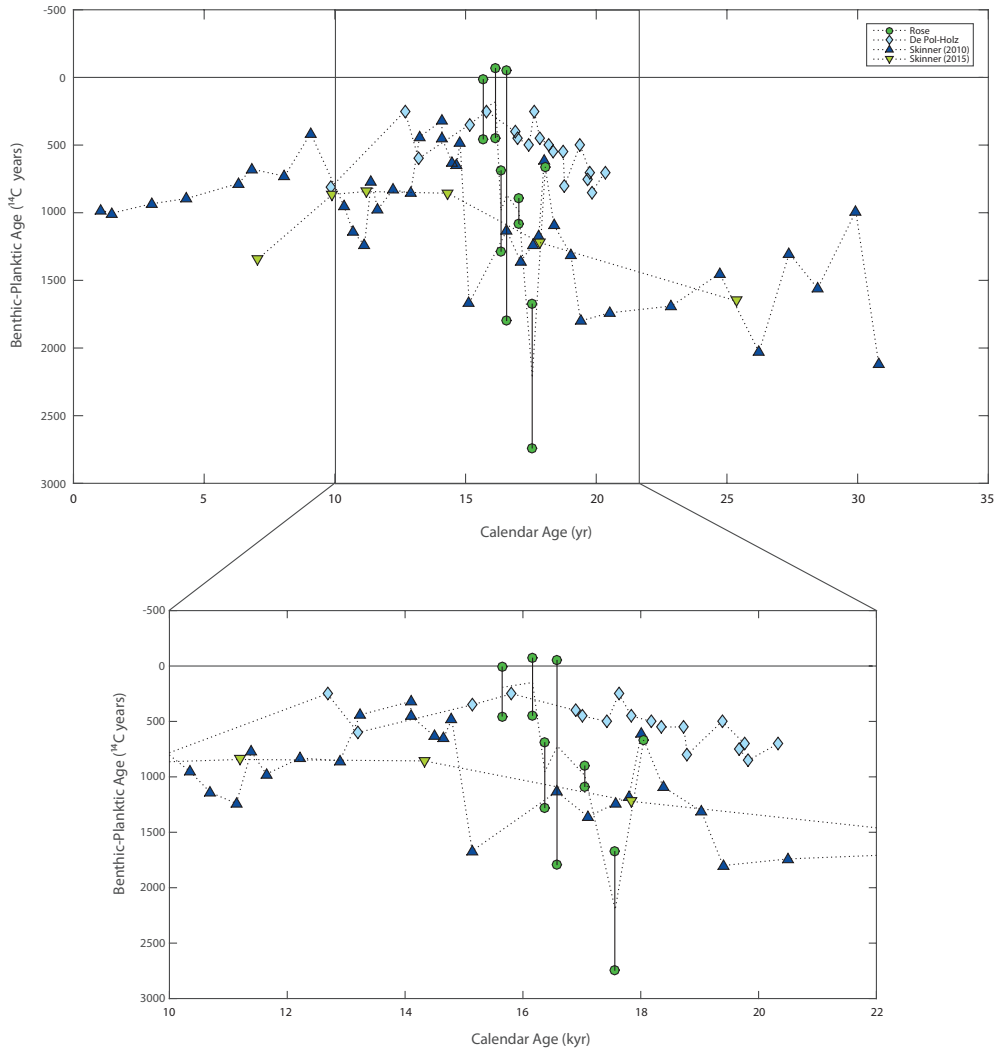

Figure 3.9: Benthic-Planktic age offsets for Southern Ocean foram records. Data from De Pol-Holz (De Pol-Holz et al., 2010) (light blue diamonds, core SO161-SL22; 36.2°S 73.7°W, 1000m), Skinner (L. Skinner et al., 2015) (light green inverted triangles, core MD97-2121; 40.4°S 178.0°E, 2314m) and (L. C. Skinner et al., 2010)(dark blue triangles, core MD07-3076; 44.1°S 7.8°E, 4981m), and Rose (Rose et al., 2010) (green circles with black vertical lines connecting B-P ages calculated using different planktic foram species from the same core depth, core MD97-2120; 43.5°S 174.9°E, 1210 m). Rose et al. B-P data plotted using a δ^{18}O-based age model that is independent of ^{14}C (from their Table S2). These results cover a limited period from 18 to 16 ka and the planktic data show interspecies age differences of up to 1800 ^{14}C-years.

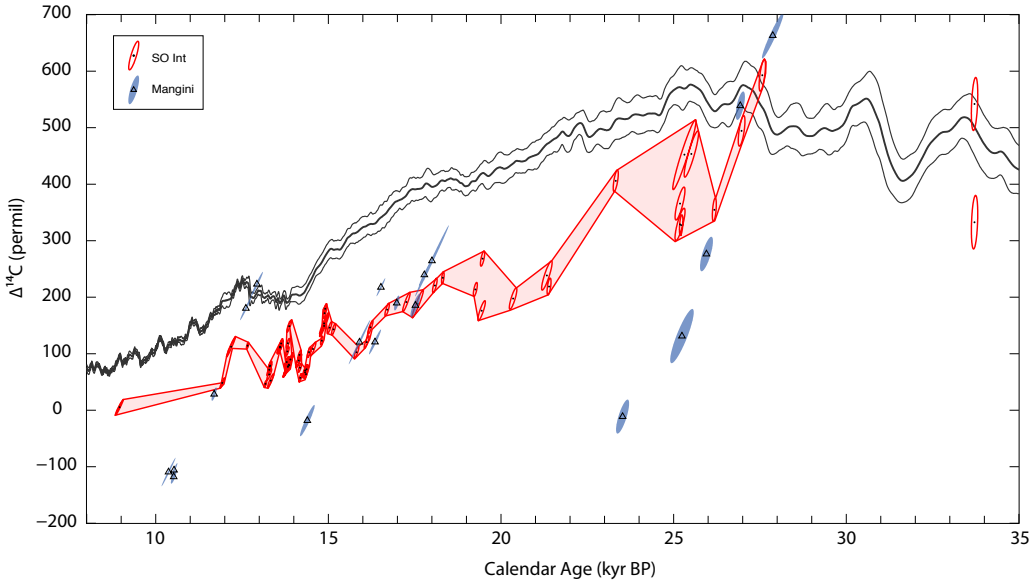

Figure 3.10: Δ^{14}C records from south of Tasmania and the Brazil Margin (Mangini et al., 2010). Black curve is IntCal13, red ellipses are Tasmanian coral Δ^{14}C data, and blue ellipses are Brazil Margin Δ^{14}C data. Ellipses drawn with 1σ U/Th and ^{14}C errors.

Table 3.1: Summary of U/Th dates including measured uranium and thorium concentration and uranium isotope ratios. Corrected age takes into account initial thorium using an atom ratio of $^{230}Th/^{232}Th$ = 80±80. $\delta^{234}U_i$ is initial $\delta^{234}U$ corrected using measured age. Both raw and corrected ages are in yr since 1980.

$*$ samples flagged for high ^{232}Th (>2000 ppt). † samples flagged for non-marine $\delta^{234}U_i$ (where marine is defined as 147±7 for samples younger than 17 ka and 141.7±7.8 for samples older than 17 ka by IntCal09). ‡ samples are flagged for both criteria.

Name	Depth	Lab Code	^{238}U	err.	^{232}Th	err.	$\delta^{234}U_m$	err.	$^{230}Th/^{238}U$	err.	Age raw	Age Corr.	Age err.	$\delta^{234}U_i$	err.	Note
			ppb		ppt		‰		Activity		years BP	years BP		‰		
TN228-J2-386-1223-0515-04-1000-001	1000	SH_SOI_I05	3676.8	2.2	335.2	2.7	143.47	0.68	0.1617	0.0002	16527	16485	50	150.34	0.72	
TN228-J2-386-1223-0515-04-1000-002	1000	SH_SOI_I03	4144.9	3.6	870.8	4.2	144.28	0.73	0.1615	0.0003	16495	16398	102	151.16	0.77	
TN228-J2-386-1223-0515-04-1000-003	1000	SH_SOI_I01	4212.4	3.9	620.2	4.5	141.70	0.70	0.1510	0.0003	15380	15312	76	147.99	0.73	
TN228-J2-386-1223-0515-04-1000-007	1000	SH_SOI_I04	3817.6	2.8	558.2	3.6	145.74	0.62	0.1686	0.0003	17256	17189	73	153.02	0.65	
TN228-J2-386-1223-0515-04-1000-008	1000	SH_SOI_I02	3721.4	2.4	812.6	3.3	143.68	0.60	0.1549	0.0002	15849	15683	104	150.22	0.63	
TN228-J2-385-1220-2749-01-1240-001	1240	SH_SOI_K10	3650.3	2.4	1173.6	5.2	143.60	0.59	0.1980	0.0002	20619	20471	147	152.18	0.63	†
TN228-J2-389-0101-0330-01-1428-007	1428	SH_SOI_I06	5338.6	4.4	2460.2	3.8	146.99	0.95	0.0896	0.0002	8799	8587	216	150.62	0.98	$*$
TN228-J2-389-0101-0330-01-1428-010	1428	SH_SOI_I07	4198.1	3.7	3613.1	5.6	149.68	0.61	0.1089	0.0003	10783	10387	399	154.17	0.65	$*$
TN228-J2-389-0101-0330-01-1428-010	1428	SH_SOI_I07-2	3729.2	12.2	852.5	6.1	146.14	0.92	0.0923	0.0002	9151	8981	107	149.93	0.94	
TN228-J2-393-0112-0730-13-1442-001	1442	SH_SOI_A07	4166.4	4.2	693.5	5.4	139.58	0.48	0.1732	0.0004	17881	17805	88	146.81	0.50	
TN228-J2-393-0112-0730-13-1442-002	1442	SH_SOI_J01	3828.7	2.9	1713.8	3.9	145.57	0.70	0.1663	0.0003	17010	16804	202	152.68	0.74	
TN228-J2-393-0112-0730-13-1442-003	1442	SH_SOI_J02	4243.8	3.0	4845.6	5.1	143.87	0.44	0.1642	0.0002	16805	16279	523	150.68	0.51	$*$
TN228-J2-393-0112-0730-13-1442-003	1442	SH_SOI_J02-2	4750.9	9.04	671.2	3.4	140.50	0.71	0.1485	0.0002	15121	15056	67	146.63	0.74	
TN228-J2-393-0112-0730-13-1442-007	1442	SH_SOI_A02	3455.3	3.6	1960.6	5.8	143.39	0.59	0.1334	0.0004	13444	13183	264	148.86	0.62	
TN228-J2-393-0112-0730-13-1442-008	1442	SH_SOI_A01	4515.8	3.4	1251.6	3.5	142.78	0.77	0.1229	0.0002	12333	12205	131	147.82	0.80	
TN228-J2-387-1226-2330-25-1448-001	1448	SH_SOI_J03	4246.7	2.4	606.0	2.7	144.55	0.54	0.1201	0.0002	12017	11951	67	149.54	0.56	
TN228-J2-387-1226-2330-25-1448-002	1448	SH_SOI_J04	3612.5	2.3	1020.1	6.1	145.55	0.56	0.1287	0.0002	12977	12782	134	150.93	0.58	
TN228-J2-395-0114-0134-10-1454-004	1454	SH_SOI_J05	4514.9	5.5	1867.5	10.7	145.52	0.55	0.1037	0.0003	10340	10084	192	149.76	0.57	
TN228-J2-383-1217-1320-05-1460-005	1460	SH_SOI_E01	4558.6	3.7	761.1	12.7	130.37	0.92	0.3357	0.0002	38138	38061	93	145.20	1.03	
TN228-J2-383-1217-1320-05-1460-007	1460	SH_SOI_E02	4568.6	5.6	303.0	11.5	135.11	1.81	0.2036	0.0002	21439	21408	57	143.57	1.92	
TN228-J2-383-1217-1320-05-1460-008	1460	SH_SOI_E03	4426.3	4.5	475.1	15.3	138.06	1.25	0.1858	0.0002	19323	19274	57	145.81	1.32	
TN228-J2-383-1217-1320-05-1460-009	1460	SH_SOI_E04	4543.4	4.2	542.1	13.7	137.45	1.11	0.1875	0.0002	19538	19483	61	145.26	1.17	
TN228-J2-395-0114-0057-09-1500-001	1500	SH_SOI_E05	4100.8	3.2	2812.5	14.3	129.70	0.71	0.3113	0.0002	34906	34588	322	143.04	0.79	$*$

Name	Depth	Lab Code	^{238}U	err.	^{232}Th	err.	$\delta^{234}U_m$	err.	^{230}Th/^{238}U	err.	Age raw	Age Corr.	Age err.	$\delta^{234}U_i$	err.	Note
			ppb		ppt		‰		Activity		years BP	years BP		‰		
TN228-J2-395-0114-0057-09-1500-002	1500	SH_SOI_E06	3576.8	2.7	535.4	12.3	136.23	0.86	0.2206	0.0002	23408	23338	75	145.55	0.92	
TN228-J2-395-0114-0057-09-1500-003	1500	SH_SOI_E07	4237.6	3.1	1725.4	12.6	132.47	0.80	0.2815	0.0002	30956	30767	190	144.53	0.88	
TN228-J2-395-0114-0057-09-1500-005	1500	SH_SOI_E08	3039.6	2.1	572.8	10.6	138.54	0.61	0.3280	0.0003	36764	36678	98	153.70	0.68	†
TN228-J2-395-0114-0057-09-1500-005	1500	SH_SOI_E08	3697.6	3.5	468.6	17.3	130.30	0.86	0.3274	0.0003	37017	36958	77	144.68	0.95	
TN228-J2-395-0114-0057-09-1500-006	1500	SH_SOI_E09	5460.3	5.0	1712.1	9.6	129.58	1.32	0.2743	0.0002	30147	30002	155	141.07	1.44	
TN228-J2-395-0114-0057-09-1500-008	1500	SH_SOI_E10	4492.0	3.4	2011.1	14.1	132.10	0.67	0.2392	0.0001	25733	25526	209	142.01	0.72	
TN228-J2-395-0114-0057-09-1500-009	1500	SH_SOI_E11	4112.8	3.1	1355.1	11.8	131.46	0.94	0.3487	0.0002	39854	39702	158	147.09	1.06	
TN228-J2-395-0114-0057-09-1500-010	1500	SH_SOI_E12	4400.5	4.0	1308.0	12.2	133.92	1.21	0.2363	0.0002	25336	25198	144	143.84	1.30	
TN228-J2-382-1216-1350-03-1523-002	1523	SH_SOI_F01	3695.0	3.3	1046.0	14.6	145.87	1.04	0.1336	0.0001	13436	13306	130	151.49	1.08	
TN228-J2-382-1216-1350-03-1523-002	1523	SH_SOI_F01-2	4443.0	8.7	808.0	3.7	144.04	3.66	0.1265	0.0001	12764	12615	86	149.29	0.85	
TN228-J2-382-1216-1350-03-1523-003	1523	SH_SOI_F02	5581.2	3.7	1955.0	8.9	136.47	0.69	0.2076	0.0002	21932	21704	164	145.13	0.73	
TN228-J2-382-1216-1350-03-1523-004	1523	SH_SOI_F03	4548.0	3.0	1053.3	9.7	120.54	0.54	0.5225	0.0003	67587	67480	134	145.89	0.66	
TN228-J2-382-1216-1350-03-1523-005	1523	SH_SOI_F04	5663.8	3.6	2238.5	8.7	135.82	0.66	0.2050	0.0002	21582	21399	183	144.31	0.71	∗
TN228-J2-382-1216-1350-03-1523-005	1523	SH_SOI_F04-2	6048.8	7.9	1919.9	3.2	135.42	1.18	0.2041	0.0002	21491	21344	153	143.87	1.26	
TN228-J2-382-1216-1350-03-1523-006	1523	SH_SOI_F05	4427.0	2.8	996.2	9.2	136.58	0.55	0.1955	0.0002	20471	20367	109	144.70	0.58	
TN228-J2-382-1216-1350-03-1523-007	1523	SH_SOI_F06	3958.0	2.3	222.7	8.2	140.36	0.53	0.1776	0.0002	18359	18333	38	147.86	0.56	
TN228-J2-382-1216-1350-03-1523-008	1523	SH_SOI_F07	3521.7	1.9	157.1	7.3	147.10	0.54	0.1269	0.0002	12703	12682	33	152.50	0.56	
TN228-J2-382-1216-1350-03-1523-010	1523	SH_SOI_F08	3723.7	2.4	3025.0	10.0	139.98	0.51	0.2443	0.0003	26144	25769	378	150.58	0.57	∗
TN228-J2-382-1216-1350-03-1523-010	1523	SH_SOI_F08-2	3855.9	9.2	2732.1	7.8	141.42	0.74	0.2406	0.0003	25650	25324	333	151.94	0.81	‡
TN228-J2-383-1217-0852-03-1548-005	1548	SH_SOI_F09	4656.1	2.7	483.6	8.8	130.49	0.46	0.2799	0.0002	30819	30771	58	142.37	0.50	
TN228-J2-383-1217-0725-01-1575-001	1575	SH_SOI_A05	2214.2	1.6	394.0	11.6	127.75	0.60	0.2540	0.0003	27661	27579	92	138.13	0.65	
TN228-J2-383-1217-0725-01-1575-002	1575	SH_SOI_A06	3594.0	3.1	8764.4	15.4	136.97	0.55	0.3083	0.0004	34250	33122	1122	150.44	0.77	∗
TN228-J2-383-1217-0725-01-1575-003	1575	SH_SOI_A03	4983.4	2.5	1353.0	7.6	129.05	0.45	0.3033	0.0002	33889	33763	128	141.99	0.50	
TN228-J2-383-1217-0725-01-1575-004	1575	SH_SOI_A10	4122.4	2.6	1607.5	9.6	131.56	0.45	0.3237	0.0003	36477	36297	190	145.80	0.51	
TN228-J2-383-1217-0725-01-1575-005	1575	SH_SOI_A08	5136.6	2.9	1122.7	8.4	125.36	0.46	0.3588	0.0002	41544	41443	109	140.96	0.51	
TN228-J2-383-1217-0725-01-1575-006	1575	SH_SOI_A04	4143.4	2.9	500.4	10.8	138.25	0.54	0.1755	0.0003	18157	18102	65	145.53	0.57	
TN228-J2-383-1217-0725-01-1575-007	1575	SH_SOI_F10	4577.8	2.9	1602.0	13.5	131.35	0.60	0.2850	0.0002	31449	31286	166	143.52	0.66	
TN228-J2-383-1217-0725-01-1575-008	1575	SH_SOI_F11	5415.9	3.2	1845.6	11.1	129.38	0.72	0.2651	0.0002	29055	28832	163	140.39	0.78	
TN228-J2-383-1217-0725-01-1575-009	1575	SH_SOI_F12	5486.5	3.4	1378.6	12.6	131.81	0.62	0.2923	0.0002	32363	32247	120	144.42	0.68	
TN228-J2-383-1217-0725-01-1575-010	1575	SH_SOI_F13	4539.3	3.5	905.7	16.6	134.09	0.60	0.2507	0.0002	27072	26980	96	144.74	0.65	
TN228-J2-383-1217-0725-01-1575-012	1575	SH_SOI_G01	4911.3	2.8	873.1	11.2	128.66	0.62	0.2893	0.0002	32088	32006	88	140.87	0.67	

Name	Depth	Lab Code	^{238}U	err.	^{232}Th	err.	$\delta^{234}U_m$	err.	^{230}Th/^{238}U	err.	Age raw	Age Corr.	Age err.	$\delta^{234}U_i$	err.	Note
			ppb		ppt		‰		Activity		years BP	years BP		‰		
TN228-J2-383-1217-0725-01-1575-013	1575	SH_SOI_G02	3766.6	2.7	747.1	15.4	131.85	0.63	0.2861	0.0002	31561	31469	99	144.15	0.69	
TN228-J2-383-1217-0725-01-1575-014	1575	SH_SOI_G03	5638.1	3.1	2073.4	10.4	130.31	0.65	0.2947	0.0002	32724	32554	171	142.89	0.72	*
TN228-J2-383-1217-0725-01-1575-016	1575	SH_SOI_G04	3897.8	2.3	895.9	11.9	133.79	0.61	0.2781	0.0002	30491	30385	108	145.82	0.67	
TN228-J2-383-1217-0725-01-1575-017	1575	SH_SOI_G05	4124.1	3.0	422.7	14.9	134.74	0.68	0.2440	0.0002	26238	26191	57	145.12	0.73	
TN228-J2-383-1217-0725-01-1575-018	1575	SH_SOI_G06	4067.3	2.3	662.4	11.8	132.05	0.61	0.2930	0.0002	32442	32367	82	144.72	0.67	
TN228-J2-383-1217-0725-01-1575-020	1575	SH_SOI_G07	4340.3	3.2	2307.0	16.0	132.07	0.62	0.2801	0.0002	30800	30554	244	144.01	0.68	*
TN228-J2-383-1217-0725-01-1575-021	1575	SH_SOI_G08	4870.8	3.1	3169.9	13.9	131.55	0.60	0.3070	0.0002	34270	33969	302	144.83	0.67	*
TN228-J2-383-1217-0725-01-1575-022	1575	SH_SOI_G09	4598.6	2.8	1329.3	12.2	127.58	0.64	0.4442	0.0002	54037	53903	146	148.60	0.75	
TN228-J2-383-1217-0725-01-1575-023	1575	SH_SOI_G10	5628.4	4.0	2197.2	13.8	141.39	0.52	0.1920	0.0001	19969	19789	185	149.55	0.56	*
TN228-J2-383-1217-0725-01-1575-023	1575	SH_SOI_G10-2	6284.6	8.5	1368.0	2.6	137.25	1.29	0.1877	0.0002	19557	19457	108	145.04	1.36	
TN228-J2-383-1217-0725-01-1575-024	1575	SH_SOI_G11	4773.8	2.8	1067.4	10.0	135.43	0.60	0.2932	0.0002	32411	32243	105	148.38	0.66	
TN228-J2-383-1217-0725-01-1575-025	1575	SH_SOI_G12	4940.0	3.5	3820.8	14.2	132.33	0.43	0.2979	0.0002	33130	32707	364	145.18	0.50	
TN228-J2-387-1226-1635-23-1599-001	1599	SH_ACR_01	4443.6	4.0	1344.8	8.0	144.21	1.47	0.1385	0.0001	13992	13852	139	149.99	1.53	
TN228-J2-387-1226-1635-23-1599-002	1599	SH_ACR_02	4436.3	4.1	582.8	7.4	142.08	1.55	0.1372	0.0001	13878	13817	63	147.77	1.62	
TN228-J2-387-1226-1635-23-1599-003	1599	SH_ACR_03	4392.4	4.5	698.9	9.9	142.29	1.61	0.1355	0.0001	13693	13620	79	147.90	1.68	
TN228-J2-387-1226-1635-23-1599-004	1599	SH_ACR_04	4791.9	3.8	676.5	5.7	143.29	1.35	0.1327	0.0001	13376	13311	70	148.81	1.40	
TN228-J2-387-1226-1635-23-1599-005	1599	SH_ACR_05	4489.1	3.3	1267.3	6.6	143.03	1.19	0.1479	0.0001	15028	14898	132	149.21	1.24	
TN228-J2-387-1226-1635-23-1599-014	1599	SH_SOI_G13	3864.5	2.3	158.9	11.1	148.34	0.55	0.1332	0.0001	13366	13347	25	154.07	0.57	
TN228-J2-387-1226-1635-23-1599-016	1599	SH_SOI_G14	4356.0	2.8	742.3	12.3	141.17	0.55	0.1426	0.0001	14468	14390	80	147.06	0.58	
TN228-J2-387-1226-1635-23-1599-020	1599	SH_SOI_G15	4612.3	3.4	2364.9	14.5	141.73	0.53	0.1417	0.0002	14371	14134	240	147.53	0.56	*
TN228-J2-387-1226-1635-23-1599-020	1599	SH_SOI_G15-2	4895.4	7.0	813.5	2.6	143.29	0.76	0.1385	0.0001	14064	13922	79	149.07	0.79	
TN228-J2-387-1226-1507-22-1616-004	1616	SH_SOI_G16	4170.4	2.2	285.6	9.1	140.22	0.54	0.1461	0.0001	14863	14831	35	146.25	0.57	
TN228-J2-393-0112-0124-06-1657-001	1657	SH_SOI_B02	4120.4	3.0	655.4	14.3	134.67	0.48	0.2876	0.0002	31663	31590	79	147.28	0.52	
TN228-J2-393-0112-0124-06-1657-003	1657	SH_SOI_G17	4798.2	3.3	1390.9	13.7	132.57	0.43	0.2774	0.0002	30445	30311	137	144.46	0.48	
TN228-J2-393-0112-0124-06-1657-004	1657	SH_SOI_B03	5344.2	3.4	1270.4	12.8	126.33	0.45	0.3218	0.0002	36436	36325	115	140.01	0.50	
TN228-J2-393-0112-0124-06-1657-007	1657	SH_SOI_B01	4722.7	3.3	671.5	13.3	132.33	0.55	0.2767	0.0002	30359	30294	71	144.19	0.59	
TN228-J2-393-0112-0124-06-1657-010	1657	SH_SOI_B04	4772.2	2.8	2137.5	11.4	130.37	0.40	0.3076	0.0002	34397	34190	208	143.62	0.45	*
TN228-J2-393-0112-0124-06-1657-011	1657	SH_SOI_G18	4295.4	3.6	1260.1	16.6	125.69	0.59	0.3279	0.0002	37278	37141	142	139.62	0.66	
TN228-J2-393-0112-0124-06-1657-013	1657	SH_SOI_G19	5689.1	3.8	1406.6	13.3	126.53	0.46	0.2738	0.0002	30175	30060	119	137.78	0.50	
TN228-J2-393-0112-0124-06-1657-015	1657	SH_SOI_G20	4032.2	3.1	362.6	34.8	130.53	0.81	0.2770	0.0006	30523	30417	92	142.27	0.89	
TN228-J2-387-1226-1148-20-1680-003	1680	SH_SOI_B09	3054.5	2.4	316.1	12.7	145.79	0.62	0.1436	0.0002	14512	14464	52	151.90	0.64	

Name	Depth	Lab Code	^{238}U	err.	^{232}Th	err.	$\delta^{234}U_m$	err.	^{230}Th/^{238}U	err.	Age raw	Age Corr.	Age err.	$\delta^{234}U_i$	err.	Note
			ppb		ppt		‰		Activity		years BP	years BP		‰		
TN228-J2-387-1226-1148-20-1680-004	1680	SH_SOI_B07	4700.2	16.4	1665.2	168.0	139.63	3.04	0.1362	0.0025	13800	13636	318	145.15	3.17	
TN228-J2-387-1226-1148-20-1680-005	1680	SH_SOI_H01	4994.9	3.4	846.2	30.4	147.00	0.79	0.1337	0.0004	13496	13354	90	152.68	0.82	
TN228-J2-387-1226-1148-20-1680-009	1680	SH_SOI_C03	3698.8	2.9	266.9	34.2	145.23	0.89	0.1353	0.0007	13626	13593	78	150.94	0.93	
TN228-J2-387-1226-1148-20-1680-013	1680	SH_SOI_H02	4195.0	2.8	344.6	28.9	143.43	0.76	0.1421	0.0005	14385	14347	66	149.39	0.79	
TN228-J2-387-1226-1148-20-1680-017	1680	SH_SOI_H03	3333.0	2.5	288.5	30.6	147.19	0.88	0.1447	0.0006	14617	14578	80	153.40	0.92	
TN228-J2-387-1226-1148-20-1680-08	1680	SH_SOI_C02	5670.3	4.0	855.7	32.4	140.82	0.74	0.1403	0.0004	14231	14161	82	146.59	0.77	
TN228-J2-382-1216-1010-01-1689-001	1689	SH_SOI_H04	4890.9	3.1	940.9	30.5	119.13	0.63	0.4463	0.0005	54924	54834	128	139.12	0.74	
TN228-J2-382-1216-1010-01-1689-002	1689	SH_SOI_H05	4189.8	3.0	187.9	31.5	142.92	0.80	0.1635	0.0005	16743	16722	64	149.86	0.84	
TN228-J2-382-1216-1010-01-1689-004	1689	SH_SOI_H06	3867.6	3.1	691.4	35.2	141.14	0.87	0.1688	0.0006	17361	17279	109	148.23	0.92	
TN228-J2-382-1216-1010-01-1689-007	1689	SH_SOI_H07	5018.7	3.3	1595.6	31.0	125.33	0.67	0.3070	0.0005	34509	34362	163	138.13	0.74	
TN228-J2-382-1216-1010-01-1689-008	1689	SH_SOI_H08	4997.6	3.0	1560.2	28.4	125.60	0.60	0.3663	0.0004	42587	42443	158	141.64	0.68	
TN228-J2-382-1216-1010-01-1689-009	1689	SH_SOI_H09	4593.2	3.1	1502.5	29.6	138.45	0.77	0.1720	0.0005	17759	17608	164	145.54	0.81	
TN228-J2-382-1216-1010-01-1689-010	1689	SH_SOI_H10	4494.9	2.4	1279.9	24.8	130.97	0.59	0.3075	0.0004	34422	34225	145	144.29	0.65	
TN228-J2-382-1216-1010-01-1689-010	1689	SH_SOI_H10-2	5043.0	7.3	705.1	2.4	127.83	1.25	0.3023	0.0003	33860	33730	91	140.64	1.37	
TN228-J2-387-1226-0615-017-01748-011	1748	SH_SOI_C05	4229.1	3.4	632.2	6.8	138.83	0.50	0.1688	0.0002	17397	17328	74	145.83	0.53	
TN228-J2-387-1226-0615-017-1748-004	1748	SH_SOI_C12	3473.9	4.3	308.0	10.7	140.48	0.51	0.1748	0.0004	18042	18001	65	147.84	0.53	
TN228-J2-387-1226-0615-017-1748-005	1748	SH_SOI_C10	4187.2	3.6	473.4	7.0	142.27	0.63	0.1381	0.0002	13969	13916	59	148.01	0.66	
TN228-J2-387-1226-0615-017-1748-007	1748	SH_SOI_C08	3991.4	4.6	258.8	9.9	142.64	0.54	0.1414	0.0003	14318	14289	48	148.55	0.57	
TN228-J2-387-1226-0615-17-1748-009	1748	SH_SOI_C09	2713.6	1.6	290.4	9.2	142.13	0.56	0.1468	0.00018	14918	14869	53	148.25	0.58	
TN228-J2-387-1226-0615-17-1748-009	1748	SH_SOI_C09-2	5054.7	22.4	598.1	7.9	143.65	0.94	0.1498	0.0002	15227	15172	62	149.97	0.98	
TN228-J2-387-1226-0615-17-1748-014	1748	SH_SOI_K05	5474.6	4.6	710.8	6.7	139.45	0.67	0.1554	0.0002	15897	15837	65	145.86	0.70	
TN228-J2-387-1226-0615-17-1748-015	1748	SH_SOI_K03	4341.5	4.2	639.7	8.2	140.93	0.57	0.1593	0.0003	16306	16238	76	147.58	0.60	
TN228-J2-387-1226-0615-17-1748-016	1748	SH_SOI_K06	4260.4	3.2	345.8	6.3	138.91	0.50	0.1662	0.0002	17103	17065	46	145.80	0.52	
TN228-J2-387-1226-0615-17-1748-020	1748	SH_SOI_K04	3996.7	3.4	560.5	7.0	139.91	0.65	0.1581	0.0003	16194	16129	71	146.46	0.68	
TN 228-J2-387-1225-1253-11-1898-001	1898	SH_SOI_K08	5011.2	3.5	401.1	4.8	142.60	0.86	0.1407	0.0002	14247	14210	43	148.47	0.90	
TN 228-J2-387-1225-1253-11-1898-002	1898	SH_SOI_K07	3511.8	3.2	490.1	7.5	144.34	0.63	0.1382	0.0003	13955	13891	72	150.15	0.66	
TN228-J2-395-0113-1830-5-1947-003	1947	SH_SOI_K09	4878.4	3.3	348.1	5.2	143.04	0.63	0.1314	0.0002	13232	13199	39	148.51	0.66	

Table 3.2: Summary of radiocarbon dates used for calculating $\Delta^{14}C$.

Name	Lab Code	Depth (m)	Age (yrBP)	Age err.	^{14}C age (^{14}C yr)	^{14}C err.
TN228-J2-389-0101-0330-01-1428-010	SH_SOI_I07-2	1428	8981	107	8685	20
TN228-J2-387-1226-2330-25-1448-001	SH_SOI_J03	1448	11951	67	11240	25
TN228-J2-393-0112-0730-13-1442-008	SH_SOI_A01	1442	12205	131	11010	25
TN228-J2-382-1216-1350-03-1523-002	SH_SOI_F01-2	1523	12615	86	11450	30
TN228-J2-382-1216-1350-03-1523-008	SH_SOI_F07	1523	12682	33	11460	30
TN228-J2-395-0113-1830-05-1947-003	SH_SOI_K09	1947	13199	39	12465	30
TN228-J2-387-1226-1635-23-1599-004	SH_ACR_04-T	1599	13311	70	12385	30
TN228-J2-387-1226-1635-23-1599-004	SH_ACR_04C	1599	13311	70	12445	35
TN228-J2-387-1226-1635-23-1599-004	SH_ACR_04-M	1599	13323	50	12350	35
TN228-J2-387-1226-1635-23-1599-004	SH_ACR_04-B	1599	13336	50	12355	35
TN228-J2-387-1226-1148-20-1680-005	SH_SOI_H01	1680	13354	90	12570	35
TN228-J2-387-1226-1635-23-1599-003	SH_ACR_03-T	1599	13620	79	12395	35
TN228-J2-387-1226-1635-23-1599-003	SH_ACR_03C	1599	13620	79	12385	35
TN228-J2-387-1226-1635-23-1599-003	SH_ACR_03-M	1599	13639	50	12410	30
TN228-J2-387-1226-1635-23-1599-003	SH_ACR_03-B	1599	13653	50	12375	35
TN228-J2-387-1226-1635-23-1599-002	SH_ACR_02-T	1599	13817	63	12775	35
TN228-J2-387-1226-1635-23-1599-002	SH_ACR_02C	1599	13817	63	12775	35
TN228-J2-387-1226-1635-23-1599-002	SH_ACR_02-M	1599	13836	50	12655	35
TN228-J2-387-1226-1635-23-1599-002	SH_ACR_02-B	1599	13851	50	12565	35
TN228-J2-387-1226-1635-23-1599-001	SH_ACR_01-T	1599	13852	139	12865	35
TN228-J2-387-1226-1635-23-1599-001	SH_ACR_01C	1599	13852	139	12870	35
TN228-J2-387-1226-1635-23-1599-001	SH_ACR_01-M	1599	13875	50	12865	35
TN228-J2-387-1225-1253-11-1898-002	SH_SOI_K07	1898	13891	72	12390	30

Name	Lab Code	Depth (m)	Age (yrBP)	Age err.	^{14}C age (^{14}C yr)	^{14}C err.
TN228-J2-387-1226-1635-23-1599-001	SH_ACR_01-B	1599	13892	50	12890	35
TN228-J2-387-1226-1635-23-1599-020	SH_SOI_G15-2	1599	13922	79	12845	35
TN228-J2-387-1226-1148-20-1680-008	SH_SOI_C02	1680	14161	82	13090	45
TN228-J2-387-1226-1148-20-1680-008	SH_SOI_C02-T	1680	14161	82	13090	35
TN228-J2-387-1226-1148-20-1680-008	SH_SOI_C02-M	1680	14186	50	13040	35
TN228-J2-387-1226-1148-20-1680-008	SH_SOI_C02-B	1680	14198	50	13220	35
TN228-J2-387-1225-1253-11-1898-001	SH_SOI_K08	1898	14210	43	13365	35
TN228-J2-387-1226-1148-20-1680-013	SH_SOI_H02	1680	14347	66	13400	40
TN228-J2-387-1226-1148-20-1680-013	SH_SOI_H02-T	1680	14347	66	13425	35
TN228-J2-387-1226-1148-20-1680-013	SH_SOI_H02-M	1680	14373	50	13475	35
TN228-J2-387-1226-1148-20-1680-013	SH_SOI_H02-B	1680	14392	50	13430	35
TN228-J2-387-1226-1148-20-1680-003	SH_SOI_B09	1680	14464	52	13275	40
TN228-J2-387-1226-1148-20-1680-017	SH_SOI_H03	1680	14578	80	13345	40
TN228-J2-387-1226-1507-22-1616-004	SH_SOI_G16	1616	14831	35	13485	45
TN228-J2-387-1226-0615-17-1748-009	SH_SOI_C09	1748	14869	53	13675	40
TN228-J2-387-1226-1635-23-1599-005	SH_ACR_05-T	1599	14898	132	13365	35
TN228-J2-387-1226-1635-23-1599-005	SH_ACR_05C	1599	14898	132	13335	35
TN228-J2-387-1226-1635-23-1599-005	SH_ACR_05-M	1599	14912	50	13225	35
TN228-J2-387-1226-1635-23-1599-005	SH_ACR_05-B	1599	14928	50	13185	35
TN228-J2-393-0112-0730-13-1442-003	SH_SOI_J02-2	1442	15056	67	13540	35
TN228-J2-387-1226-0615-17-1748-014	SH_SOI_K05	1748	15837	65	14610	40
TN228-J2-387-1226-0615-17-1748-020	SH_SOI_K04	1748	16129	71	14765	40
TN228-J2-387-1226-0615-17-1748-015	SH_SOI_K03	1748	16238	76	14685	40
TN228-J2-382-1216-1010-01-1689-002	SH_SOI_H05	1689	16722	64	14940	45
TN228-J2-382-1216-1010-01-1689-004	SH_SOI_H06	1689	17279	109	15390	45

Name	Lab Code	Depth (m)	Age (yrBP)	Age err.	^{14}C age (^{14}C yr)	^{14}C err.
TN228-J2-382-1216-1010-01-1689-009	SH_SOI_H09	1689	17608	164	15730	50
TN228-J2-383-1217-0725-01-1575-006	SH_SOI_A04	1575	18102	65	15995	55
TN228-J2-382-1216-1350-03-1523-007	SH_SOI_F06	1523	18333	38	16130	60
TN228-J2-383-1217-1320-05-1460-008	SH_SOI_E03	1460	19274	57	17180	60
TN228-J2-383-1217-0725-01-1575-023	SH_SOI_G10-2	1575	19457	108	17610	60
TN228-J2-383-1217-1320-05-1460-009	SH_SOI_E04	1460	19483	61	17030	60
TN228-J2-382-1216-1350-03-1523-006	SH_SOI_F05	1523	20367	109	18350	70
TN228-J2-382-1216-1350-03-1523-005	SH_SOI_F04-2	1523	21344	153	19030	80
TN228-J2-383-1217-1320-05-1460-007	SH_SOI_E02	1460	21408	57	19220	80
TN228-J2-395-0114-0057-09-1500-002	SH_SOI_E06	1500	23338	75	19950	80
TN228-J2-395-0114-0057-09-1500-010	SH_SOI_E12	1500	25198	144	21990	100
TN228-J2-395-0114-0057-09-1500-010	SH_SOI_E12-T	1500	25198	144	22210	100
TN228-J2-395-0114-0057-09-1500-010	SH_SOI_E12-B	1500	25231	50	22250	100
TN228-J2-382-1216-1350-03-1523-010	SH_SOI_F08-2	1523	25324	333	21620	100
TN228-J2-395-0114-0057-09-1500-008	SH_SOI_E10	1500	25526	209	21810	100
TN228-J2-383-1217-0725-01-1575-017	SH_SOI_G05	1575	26191	57	23020	110
TN228-J2-383-1217-0725-01-1575-010	SH_SOI_F13	1575	26980	96	23000	110
TN228-J2-383-1217-0725-01-1575-001	SH_SOI_A05	1575	27579	92	23070	110
TN228-J2-382-1216-1010-01-1689-010	SH_SOI_H10-2A	1689	33730	145	30470	270
TN228-J2-382-1216-1010-01-1689-010	SH_SOI_H10-2B	1689	33730	145	29300	230

Chapter 4

ABRUPT TRANSITIONS AND HYSTERESIS IN GLACIAL OCEAN CIRCULATION EXPLAINED BY A TWO-BASIN TIME-DEPENDENT DYNAMICAL BOX MODEL

4.1 Introduction

During the last glacial period there were a series of abrupt changes in Northern Hemisphere high-latitude temperature, as recorded in Greenland ice cores (Dansgaard et al., 1993; NGRIP members, 2004). Ice core records from Greenland and Antarctica show that changes in inferred temperature during the last glacial period were not in phase between the hemispheres (Blunier and Brook, 2001). During cold periods in Greenland (known as "stadials"), temperature in Antarctica gradually rose, and during warm periods in Greenland ("interstadials"), temperature in Antarctica gradually fell (Figure 4.1) (Blunier and Brook, 2001). This observation has been coined the bipolar seesaw (Broecker, 1998; Thomas F Stocker and Johnsen, 2003; T F Stocker, 1998).

The simplest mechanism to explain this phenomenon is the asymmetry of equator-to-pole heat transport by the ocean in the Atlantic (Crowley, 1992). Because deep water is formed in the North Atlantic, there is net transport of warm surface water north across the equator and net transport of cold deep water south. In order to match the abrupt transitions in the north with the gradual transitions in the south, a heat reservoir was added to the simple bipolar seesaw model to damp the signal in the south (Thomas F Stocker and Johnsen, 2003). This "thermal" bipolar seesaw was able to qualitatively match ice core records from Greenland and Antarctica. Recent efforts to more precisely align high-resolution Northern and Southern Hemisphere ice core records have allowed for a better determination of the interhemispheric phasing at these abrupt climate change events (WAIS Divide Project Members, 2015). WAIS Divide Project Members (2015) found a Northern Hemisphere lead of $\sim 200 \pm 100$ years at these abrupt transitions. However, the origin of this 200-year timescale has been somewhat difficult to explain because it is slow for a typical atmospheric adjustment timescale, $O(\leq 1$ yr), but short for a full diffusive ocean adjustment timescale, $O(1000$ yr) (Zhengyu Liu and Alexander, 2007).

The global overturning circulation involves a central role for the Southern Ocean

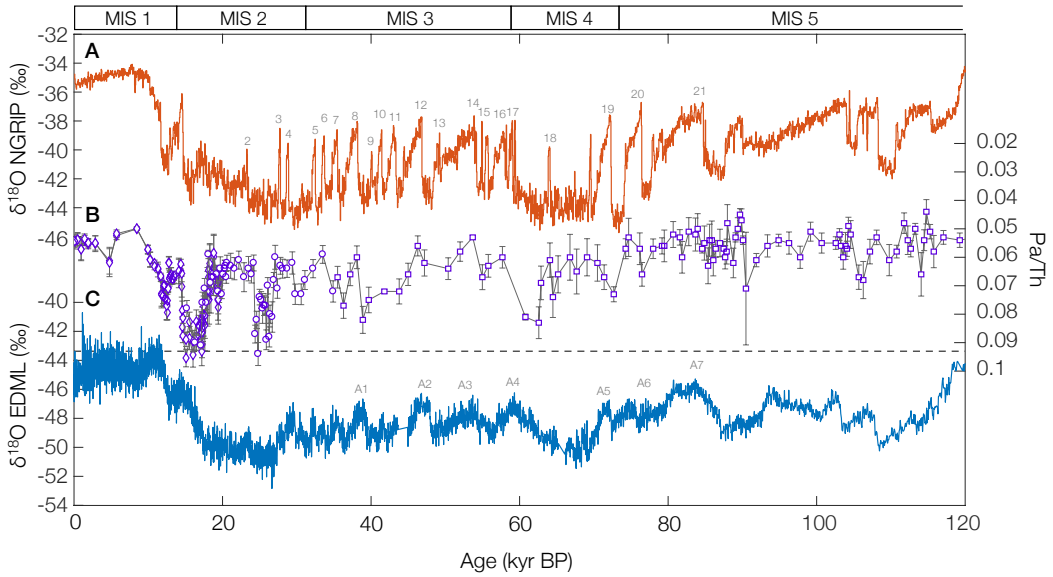

Figure 4.1: Greenland and Antarctic δ^{18}O records with Pa/Th circulation tracer. Oxygen isotopic composition of NGRIP ice core in Greenland (A) and EDML ice core in Antarctica (C). The δ^{18}O composition of ice is a proxy for regional temperature. Numbers mark the Dansgaard-Oeschger (DO) events in Greenland and corresponding AIM events in Antarctica. B) Compilation of Pa/Th records from the Bermuda Rise (youngest section from McManus et al. (2004) (diamonds), middle section from Lippold et al. (2009) (circles), oldest section from Böhm et al. (2015) (squares)). Pa/Th ratio is a proxy for the strength of North Atlantic Deep Water (NADW). Horizontal dashed line marks the Pa/Th production ratio of 0.093. Bar at top shows the Marine Isotope Stage boundaries.

(J. Marshall and Speer, 2012; Kuhlbrodt et al., 2007). In the Southern Ocean, strong westerly winds drive the vigorous Antarctic Circumpolar Current (ACC), the largest current on the planet. However, unlike the rest of the ocean, these strong zonal winds cannot drive mean geostrophic meridional flow because there are no continents to create sustained pressure gradients. Therefore, other transport mechanisms are required. Over the past decade, great strides have been made in our understanding of Southern Ocean dynamics and circulation. Notably, we now have a theoretical framework that describes circulation as a balance between Southern Ocean westerly winds, that steepen isopycnals via Ekman processes, and eddies, that act to relax them (J. Marshall and Radko, 2003).

The wind-driven, or mean, component of the overturning circulation is defined as $\bar{\psi} = -\tau/\rho_0 f$, where τ is the surface wind stress, ρ_0 is the mean ocean density, and f is the Coriolis parameter. The counteracting eddy-driven component can be parameterized as $\psi* = Ks$, where K is the eddy diffusivity and s is the isopycnal

slope. At steady-state, the balance between wind and eddies leads to a structure where isopycnals slope from the surface to depth across the Southern Ocean, and the surface meridional distribution of density classes is mapped into a vertical stratification at the northern edge of the ACC. Importantly, though, this steady-state isopycnal structure does not necessarily allow for meridional overturning—in fact if $\bar{\psi}$ perfectly matches ψ^*, then there is no net meridional transport. The balance between the wind and eddy-driven circulation is known as the residual circulation: $\psi_{res} = \bar{\psi} + \psi^*$. Residual flow occurs largely along isopycnals in the subsurface and then crosses isopycnals in the mixed layer as a result of surface buoyancy fluxes (J. Marshall and Radko, 2003; Speer, Rintoul, and Sloyan, 2000). Where there is a positive surface buoyancy flux, water in the mixed layer can be converted from a heavier density class to a lighter density class, and vice versa. Because the residual circulation above the sill depth occurs along isopycnals in the ACC, it allows for adiabtic pole-to-pole upwelling along the subset of isopycnals that outcrop both in the Southern Ocean and in the North Atlantic (Wolfe and Cessi, 2011). In a zonally averaged depiction of the meridional overturning circulation, this adiabatic circulation is the upper circulation cell. The lower cell is necessarily diabatic because it involves isopycnals that only outcrop in the Southern Ocean.

In the modern ocean, we observe that closure of the overturning circulation requires water mass modification in both the Atlantic and Indo-Pacific basins (Lumpkin and Speer, 2007; Talley, 2013). This is because North Atlantic Deep Water (NADW) is dense enough that it upwells in a region of the Southern Ocean where it experiences a negative surface buoyancy forcing. This water therefore moves to the south and sinks again as Antarctic Bottom Water (AABW), part of the lower circulation cell. If this AABW flows back into the Atlantic basin, then it upwells back into NADW. It is only once AABW flows into the Indian and Pacific basins that it is able to diffusively upwell to a density class where it can close the overturning loop. It does this either via Pacific Deep Water (PDW), which upwells in a positive buoyancy forcing region of the Southern Ocean and returns north as Antarctic Intermediate Water (AAIW), or via the Indonesian Throughflow, flowing first from the surface of the Western Equatorial Pacific into the Indian Ocean, and then from the Indian Ocean into the Atlantic through the Agulhas Leakage (Talley, 2013).

Building upon the work of Curry and Oppo (2005), Talley (2013), and J. Marshall and Radko (2003), Ferrari et al. (2014) recently put forth a theoretical model for changes in overturning circulation structure at the Last Glacial Maximum (LGM)

compared to today. This model relies on two key observations: (1) that the change from positive surface buoyancy forcing to negative surface buoyancy forcing aligns roughly with the quasi-permanent sea ice edge (defined as ice-covered 70% of the time) (Ferrari et al., 2014), and (2) that there is dramatically higher diapycnal mixing over rough bottom topography (Polzin et al., 1997). The Ferrari et al. (2014) model also relies on the simplification of a constant slope for isopycnals in the Southern Ocean (approximately equal to $\tau/\rho_0 fK$). Using the observation that the boundary between the positive and negative buoyancy forcing regions (and thus the upper and lower circulation cells) lies at the summertime sea ice edge and the approximate isopycnal slope, Ferrari et al. (2014) calculate the depth of the boundary between the upper and lower circulation cells in the northern basins. For the modern ocean this depth comes out to ~2200 m, below the mean depth of the mid-ocean ridges (2000 m). If sea ice was expanded at the LGM, as is implied by data and models, then this geometric argument predicts a shoaling of the boundary between the upper and lower circulation cells. Ferrari et al. (2014) estimate a 5° latitude shift of the summertime sea ice edge (based on output from the National Center for Atmospheric Research Community Climate System Model version 3), which would lead to a 500-m shoaling of the boundary between the upper and lower circulation cells—enough to raise it above the region of rough topography in the ocean and reduce diapycnal mixing. One potential result of this change in diapycnal diffusivity, driven by a shoaling of the boundary between the circulation cells, is a change from an intertwined "figure-eight" overturning circulation, as described by Talley (2013), into a two-cell overturning circulation, where there is less connection between upper and lower circulation cells and more potential to sequester CO_2 in the deep ocean.

In order to understand the complex interplay of physics and biogeochemistry that lead to glacial-interglacial cycles, we rely on models as well as paleoceanographic reconstructions, but it can be difficult to accurately model processes that occur on millennial timescales. On one end of the modeling continuum are general circulation models (GCMs), which attempt to capture all the physics of the ocean (and/or atmosphere), but are faced with the dilemma of run duration versus model resolution. It is widely understood that small-scale processes are crucial for accurately representing the Southern Ocean residual circulation and Antarctic Bottom Water formation, yet the computational cost is prohibitive to run these high-resolution models that explicitly resolve these processes for thousands of years. The most recent and comprehensive GCM modeling effort to understand ocean dynamics

during the most recent deglaciation, the TraCE simulation (Z Liu et al., 2009), ran the Community Climate System Model, version 3 (CCSM3) for 11,000 years with a nominal ocean resolution of 3° (for comparison, 1/4–1/6° models are considered "eddy permitting" and 1/10° are considered "eddy resolving"). On the other end are simple theoretical models, that parameterize fluxes based on theoretical relations rather than attempting to resolve them based on the equations of motion. An early and well-known example of this type of model is from Gnanadesikan (1999), who sought to understand the depth of the main pycnocline. His model was essentially 1-dimensional, with two layers and a single basin. Subsequent efforts by D. P. Marshall and Zanna (2014) expanded the Gnanadesikan model to multiple layers, but kept the same general model geometry and did not attempt to include Antarctic Bottom Water formation. Another example of a simple physical model is the dynamical box model of Goodwin (2012), which looks to solve the problem of prescribed box volumes and fluxes in biogeochemical models.

Recently, a simple but powerful new model has been developed by Thompson, Andrew L. Stewart, and Bischoff (2016). It uses residual mean theory in the Southern Ocean (J. Marshall and Radko, 2003), but keeps the Atlantic and Pacific basins separate, unlike most models, which reduce dimensionality by zonally averaging. This added dimension enables the model to occupy the figure-eight circulation configuration of Talley (2013). It is an isopycnal model with very coarse resolution—density surfaces are flat-lying in the Atlantic and Pacific basins, and slope to the surface (with a constant slope) in the ACC. Since there are two basins (the Atlantic and Indo-Pacific), the model allows exchange via zonal convergence or divergence in the ACC and through a simulated Indonesian Throughflow. Each density surface can be defined by two points: a depth, z, in the basin, and an outcrop position, y, in the ACC. Thompson, Andrew L. Stewart, and Bischoff (2016) choose four density classes (three isopycnal surfaces), because that is the minimum number that allows two overturning cells to close within a single basin. This means that the model can occupy either the figure-eight configuration or the two-cell configuration. They solve both the overturning circulation and the stratification at steady-state by solving for each isopycnal depth and outcrop position in each basin and the zonal convergence. The model also calculates the water mass modification and transport from the basin stratification (z) and ACC outcrop position (y).

In this chapter we modify the Thompson, Andrew L. Stewart, and Bischoff (2016) model in order to investigate the ocean response to transient changes in circulation.

In particular, we simulate the abrupt changes in NADW formation rate associated with the Heinrich and Dansgaard-Oeschger events during the last glacial period (Figure 4.1) (Dansgaard et al., 1993; Böhm et al., 2015). In these simulations, we look at the timescale associated with communicating the signal of an abrupt change in NADW strength from north to south. The transient model response to abrupt NADW flux changes occurs much faster than a full diffusive ocean adjustment, and provides a mechanistic explanation to the observations of WAIS Divide Project Members (2015) (Thompson, Hines, and Adkins, *submitted*). Then we perform a series of experiments to determine which regions of parameter space allow for abrupt transitions in basin stratification and circulation configuration, focusing on how the density of NADW and the strength of NADW interact. We compare our results to the predictions made by Ferrari et al. (2014).

4.2 Model Description

We build upon the steady-state model described in Thompson, Andrew L. Stewart, and Bischoff (2016), keeping similar architecture with four isopycnal layers and two basins, representing the Atlantic and Indo-Pacific. Each basin is two-dimensional and divided into two regions: a northern basin region, where isopycnals are flat-lying, and an Antarctic Circumpolar Current (ACC) region, where isopycnals slope and outcrop at the surface. In the ACC region, mass may be transferred between the Atlantic and Indo-Pacific basins. The model is driven by an imposed buoyancy and wind forcing at the surface of the Southern Ocean, and imposed North Atlantic Deep Water (NADW) forcing in the northern end of the Atlantic basin. Based on these imposed forcings, the model adjusts to find a steady-state circulation and stratification by solving for the depth of each isopycnal in the basin, z, and each outcrop position in the ACC, y. The depths and outcrop positions for each isopycnal can differ between the Atlantic and Pacific sectors. Together, the depth and outcrop position determine a slope for each isopycnal, which is constant across the ACC.

Diffusive upwelling

In the basin, the only process that modifies water density (and thus adjusts the basin stratification) is diffusive upwelling, which is defined as:

$$T_{diff} = \frac{\kappa(z)A}{\Delta z}, \tag{4.1}$$

where κ is the diapycnal diffusivity, A is the horizontal area of the basin, and Δz is the thickness of the layer above the interface. The diapycnal diffusivity varies with

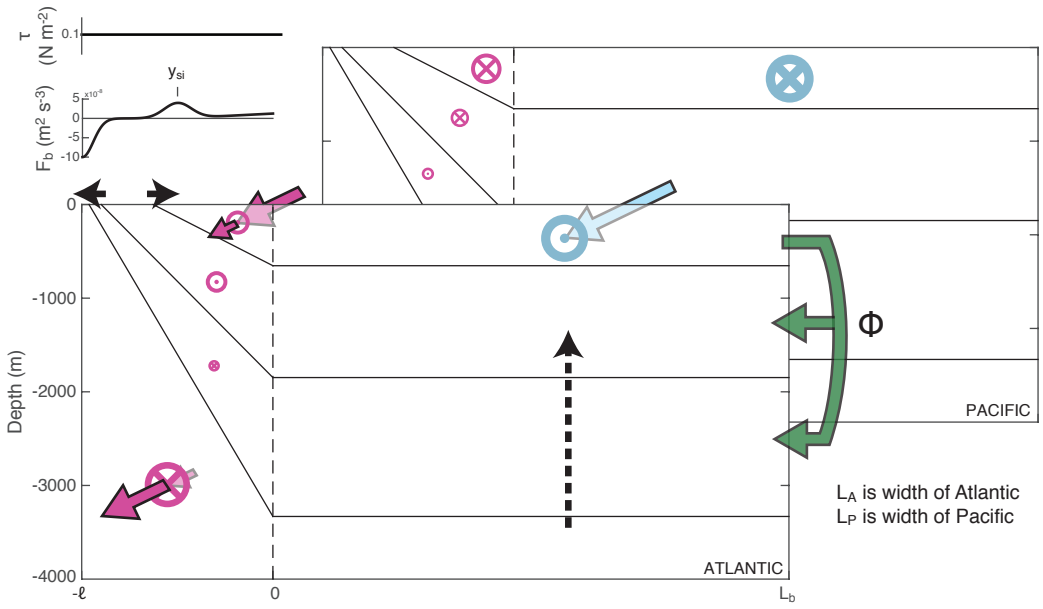

Figure 4.2: Schematic of model architecture. Model domain is split into an Atlantic sector and an Indo-Pacific sector. Each basin has a channel region with sloping isopycnals that outcrop at the surface (from -ℓ to 0), and a basin region where isopycnals are flat-lying (from 0 to L_b). Within each basin, water can move between density classes due to diabatic processes at the surface of the channel region or due to diapycnal diffusion in the basin region. Water can move between the Atlantic and Indo-Pacific due to zonal convergence in the channel (pink arrows) or via the Indonesian Throughflow (blue arrow). At the northern end of the Atlantic basin, North Atlantic Deep Water is formed with variable density (green arrow; density specified by parameter ϕ). Two plots in upper left show wind stress, τ, (top) and surface buoyancy flux, F_b, (bottom) as a function of y for the channel region of the model. Model solves for the outcrop positions of isopycnals in the channel, y, and depths of isopycnals in the basin, z.

depth according to the equation:

$$\kappa(z) = \kappa_0 - \frac{\Delta\kappa}{2} \tanh\left(\frac{z - z_0}{d}\right), \tag{4.2}$$

where κ_0 is the mean diapycnal diffusivity, $\Delta\kappa$ is the change in diapycnal diffusivity over depth interval d, and z_0 is the depth of the transition. Diapycnal diffusivity is enhanced in the deep ocean due to interaction with rough bottom topography (Polzin et al., 1997), and this has been implicated as an important mechanism for changes in ocean circulation configuration during glacial times (Ferrari et al., 2014).

Table 4.1: Values and definitions of parameters used in model.

Parameter	Value	Description
L_y	1×10^7 m	Meridional basin length
ℓ	2×10^6 m	Meridional ACC length
L_A	3×10^6 m	Width of Atlantic basin
L_P	10×10^6 m	Width of Pacific basin
H	4000 m	Ocean depth
h_m	100 m	Depth of Southern Ocean mixed layer
τ_0	0.1 N m^{-2}	Reference wind stress
f	-1×10^{-4} s^{-1}	Coriolis parameter
ρ_0	1025 kg m^{-2}	Reference seawater density
F_0	1×10^-7 m^2 s^{-3}	Reference surface buoyancy flux
τ_r	$2 * 2.6 \times 10^6$ s	Relaxation timescale for atmospheric heat flux (2.6×10^6 s is equal to 1 month)
Δb_{atm}	1.3×10^{-3} m s^{-2}	Range of atmospheric buoyancy forcing (choice of value corresponds to atmospheric heat flux of 50 W m^{-2} at northern boundary of ACC.)
b_1, b_2, b_3, b_4	$(5, 1, -1, -2.5) \times 10^{-3}$ m s^2	Buoyancy of AAIW, UCDW/PDW, LCDW/NADW, and AABW density classes, respectively
a_N, a_S	$(2, 1.6) \times 10^5$ m	Widths of the sea ice melting and formation regions, respectively
K	1000 m^2 s^{-2}	ACC along-isopycnal diffusivity
κ_0	1×10^{-4} m^2 s^{-1}	Mean diapycnal diffusivity
$\Delta\kappa$	8×10^{-5} m^2 s^{-1}	Change in diapycnal diffusivity
z_0	1600 m	Depth of transition in diapycnal diffusivity
d	300 m	Thickness of transition in diapycnal diffusivity
C_{ITF}	5×10^4 m^2 s^{-1}	Indonesian Throughflow parameter
U_0	0.05 m s^{-1}	Mean (barotropic) zonal velocity
ϕ	1	NADW splitting parameter (varied in experiments)
T_{NADW}	10×10^6 m^3 s^{-1}	NADW flux (varied in experiments)
y_{si}	-1×10^6 m	Meridional position of sea ice edge in Southern Ocean (varied in experiments)
R_{AABW}	1	Parameter for relative bottom water formation in Atlantic versus Pacific

Zonal transport

Zonal flow in the Southern Ocean has a mean (barotropic) component and a baroclinic component which is related to the relative slopes of the isopycnals in the ACC and the relative thicknesses of the layers in the Atlantic and Indo-Pacific basins. Thompson, Andrew L. Stewart, and Bischoff (2016) solve for both components of zonal flow in order to calculate the zonal convergence for each layer, but we simplify this expression by assuming a mean zonal flow, $U_0 = 0.05$ m s^{-1}, and convergence or divergence of mass driven by the relative difference in layer thickness between the Atlantic and Indo-Pacific basins. Therefore we define zonal transport as:

$$T_{zonal} = -U_0 \, (\Delta A_{ACC}), \tag{4.3}$$

where ΔA_{ACC} is the difference in cross-sectional area (in the depth-latitude plane) between the two basins of a layer in the ACC. Zonal transport is defined as positive from Pacific to Atlantic

In addition to zonal transport in the Southern Ocean, we also define an Indonesian Throughflow transport, which flows from the uppermost layer in the Pacific to the uppermost layer in the Atlantic. Because the zonal transport in the ACC is

simply given by the differences in cross-sectional area of a given density class in the Atlantic and Pacific, the zonal budget need not close in the ACC. The Indonesian Throughflow transport is defined to close the zonal budget:

$$T_{ITF} = -\left(\sum T_{zonal}\right). \tag{4.4}$$

Total zonal transport for a given layer, ΔT_{zonal} is the sum of T_{ITF}, the zonal transport in that layer, and the zonal transports for all layers above. Zonal transport is defined as positive from Pacific to Atlantic.

Southern Ocean buoyancy fluxes and residual transport

Buoyancy fluxes in the Southern Ocean have two components—one driven by sea ice and one due to atmospheric heating. Sea ice formation near the Antarctic continent leads to a strong negative buoyancy flux due to brine rejection, and freshwater from sea ice melt drives a positive buoyancy flux. The importance of sea ice dynamics to the meridional overturning circulation has recently been diagnosed from the Southern Ocean State Estimate (SOSE) (Abernathey et al., 2016). Abernathey et al. (2016) show that negative buoyancy fluxes from sea ice formation are concentrated around the Antarctic continent, particularly in the Weddell and Ross Seas (key known sites of bottom water formation). Freshwater fluxes from sea ice melt are located further to the north in a band at roughly 60°S (Abernathey et al., 2016). North of the sea ice edge, direct heating from the atmosphere provides an additional heat flux, but its contribution to the overall buoyancy flux budget for the Southern Ocean is smaller than that of sea ice (Abernathey et al., 2016; Sun, Eisenman, and A L Stewart, 2016). The buoyancy fluxes are defined as:

$$F_{\text{atm}} = \frac{h_m}{\tau_r}\left(\hat{b} - b^*\right), \quad y_{si} < y < 0, \tag{4.5}$$

$$\hat{b} = \Delta b_{atm}\left(\frac{y - y_{si}}{\ell}\right), \tag{4.6}$$

$$F_{\text{SI}} = mF_0 \exp\left[-\left(\frac{y - y_{si}}{a_N}\right)^2\right] - R_{AABW}F_0 \exp\left[-\left(\frac{y + \ell}{a_S}\right)^2\right], \quad -\ell < y < 0, \tag{4.7}$$

$$F_b(y) = F_{\text{atm}} + F_{\text{SI}}, \tag{4.8}$$

where y_{si} is the meridional position of the sea ice edge in the Southern Ocean, $\hat{b}$ is the meridional buoyancy distribution for the atmospheric component of the buoyancy forcing, Δb_{atm} is the range of atmospheric buoyancy forcing (chosen such

that the northern boundary of the ACC corresponds to an atmospheric heat flux of 50 W m^{-2}), $b^* = (b_n + b_{n+1})/2$ is the buoyancy associated with the interface, h_m is the depth of the mixed layer in the Southern Ocean, and τ_r is the relaxation timescale (set to be equal to 2 months).

In equation 4.7, the pre-factor m sets the strength of buoyancy forcing in the sea ice melting and formation regions (set to a value of 0.4), and a_N and a_S are the widths of the sea ice melting and formation regions, respectively. The pre-factor R_{AABW} sets the relative strength of bottom water formation in the Atlantic and Pacific basins. It has value R_{AABW} in the Atlantic, and $(1 + L_A/L_P\,(1 - R_{AABW}))$ in the Pacific. This accounts for the difference in Atlantic and Pacific basin widths and ensures that the zonally integrated negative buoyancy flux is equal to the zonally integrated positive buoyancy flux. This expression also sets limits for R_{AABW} of $0 < R_{AABW} < 13/3$.

According to the residual-mean theory of J. Marshall and Radko (2003), the residual transport at the base of the mixed layer in the ACC is defined as $B/\partial_y b_s$—the net surface buoyancy flux over the meridional buoyancy gradient. In our model we use the net surface buoyancy flux, F_b, as defined in equations 4.5–4.8, and follow the simplification of Thompson, Andrew L. Stewart, and Bischoff (2016), approximating the meridional buoyancy gradient as: $\Delta b/\ell^{ml}$ where $\Delta b = b_n - b_{n+1}$ and $\ell^{ml} = (y_{n-1} - y_{n+1})/2$. Buoyancy-driven transport in the Southern Ocean, T_{res}, is therefore defined as:

$$T_{res} = F_b \left(\frac{\ell^{ml}}{\Delta b}\right) L_{A,P}. \tag{4.9}$$

Evolution equations for y and z

In the Atlantic and Pacific basins, isopycnal depths are defined as a balance between diffusive upwelling and the combination of buoyancy driven exchange and zonal convergence/divergence in the Southern Ocean. In the Atlantic basin, North Atlantic Deep Water formation also influences isopycnal depths. Interface depths in the basin evolve according to the general equation:

$$\frac{dz}{dt} = \frac{1}{A}\left[\Delta T_{diff} + \Delta T_{res} + \Delta T_{zonal} + (T_{NADW})\right], \tag{4.10}$$

where A is the horizontal area of the basin and the ΔTs refer to the net volume transport for a given layer. In our model, T_{NADW} is an external parameter and is the main independent forcing. The full NADW flux, T_{NADW}, is added to the evolution equation for z_1, and multiplied by a prefactor ϕ in the evolution equation for z_2. This prefactor determines the relative amount of the total NADW flux that is added

to layer 2 versus layer 3. A ϕ value of 1 means that all of T_{NADW} goes into layer 3 and a ϕ value of 0 means that all of T_{NADW} goes into layer 2.

At the surface in the Southern Ocean, we calculate the isopycnal outcrop position by solving the full residual-mean equation. At steady-state, transport in the Southern Ocean, ψ_{res}, is the balance between mean wind-driven flow, $\bar{\psi}$, and eddy-driven flow, ψ^* (J. Marshall and Radko, 2003). If $\bar{\psi}$ and ψ^* are exactly equal, then there is no overturning transport. However, if the system is not in steady-state, this need not hold. Therefore, all three components of the residual circulation ($\bar{\psi}$, ψ^*, and ψ_{res}) can contribute to the isopycnal outcropping position (although ψ_{res} is the only one of the three that modifies water masses). Outcropping positions evolve according to the equation:

$$\frac{dy}{dt} = \frac{1}{h_m}\left(\bar{\psi} + \psi^* - \psi_{res}\right) = \frac{1}{h_m}\left(-\frac{\tau}{\rho_0 f} + Ks - \frac{T_{res}}{L_{A,P}}\right), \tag{4.11}$$

where h_m is the depth of the mixed layer, τ is the wind stress (held at a constant value of τ_0 for the experiments presented here), ρ_0 is the reference density, f is the coriolis parameter, K is the along-isopycnal diffusivity, s is the isopycnal slope, and T_{res} is as defined in Equation 4.9.

The evolution equations for y and z are solved using a fourth-order Runge-Kutta method. We initialize the model for 10 years using a time step of 0.1 days, then run with a time step of 0.5 days for the rest of the simulation (5000 years). In order to speed up the run time of our model, for the full simulation we only save output every 50 model years. Our relatively simple model allows us to explore parameter space and run simulations for durations that would be out of reach for more complex GCMs. As a point of comparison, we can run our model for 100,000 years at 0.5-day resolution in ≈6.5 hours on a single processor. Compare this to the CCSM3 model configuration used to run the TraCE simulation, which requires 62 CPU hours to simulate a single year (Z Liu et al., 2009; Collins et al., 2006; Yeager et al., 2006).

4.3 Results

In order to explore the behavior of the model in scenarios relevant to glacial-interglacial climate, we performed two sets of experiments. The first set examined the model response to transient changes in forcing. We looked at the timescale of interhemispheric response and basin stratification adjustment (Thompson, Hines, and Adkins, *submitted*). For our second set of experiments, we ran the time-dependent model out to steady-state. In these steady-state experiments, we varied

the strength of North Atlantic Deep water formation, T_{NADW}, the density of North Atlantic Deep Water, ϕ, and the position of the sea ice edge y_{si}. We also looked at the effect of having variable vertical diffusivity in the basin. Specifically, we wanted to assess which conditions led to abrupt changes in basin stratification and which conditions were associated with a "figure-eight" and "two-cell" circulation configuration.

Transient interhemispheric adjustment

In our first set of experiments, we examine the delay time between the Northern Hemisphere forcing and the Southern Hemisphere response at DO events (which are characterized by abrupt changes in NADW flux). We find an adjustment timescale that is associated with volume convergence into a density class due to an abrupt change in NADW formation flux. This timescale goes as the volume of the density class into which the flux perturbation occurs over the magnitude of the perturbation: $\tau_{trans} \sim V/F_V$. For our generalized Atlantic basin geometry and typical NADW flux values, this timescale is ≈200 years. Mechanistically, this adjustment arises because flux convergence advects isopycnals in the basin, rapidly altering basin stratification. If, for example, NADW rapidly decreases, mass converges in the upper ocean and diverges at mid-depth. This causes an increase in mid-depth stratification and a decrease in upper ocean stratification. In the Southern Ocean, these changes in basin stratification are mapped to the surface by sloping isopycnals. Isopycnal slopes are generally constant in time due to eddy saturation (Munday, Johnson, and D. P. Marshall, 2013; Thompson, Hines, and Adkins, *submitted*).

These changes in isopycnal outcrop position could lead to changes in Southern Hemisphere temperature, consistent with the bipolar seesaw. When NADW is strong (in a Northern Hemisphere warm phase), isopycnals tend to outcrop further to the north exposing more of the Southern Ocean surface to colder, denser layers (Figure 4.3). This should lead to cooling in the Southern Hemisphere. When NADW is weak (in a Northern Hemisphere cold phase), isopycnals tend to outcrop closer to the Antarctic continent, exposing more of the Southern Ocean surface area to warmer, lighter layers. This should lead to warming the Southern Hemisphere (Thompson, Hines, and Adkins, *submitted*).

There is an interesting feedback between changes in basin stratification and changes in residence time of different density classes. For a Northern Hemisphere cooling event, where NADW flux abruptly decreases, mass converges in the uppermost layer,

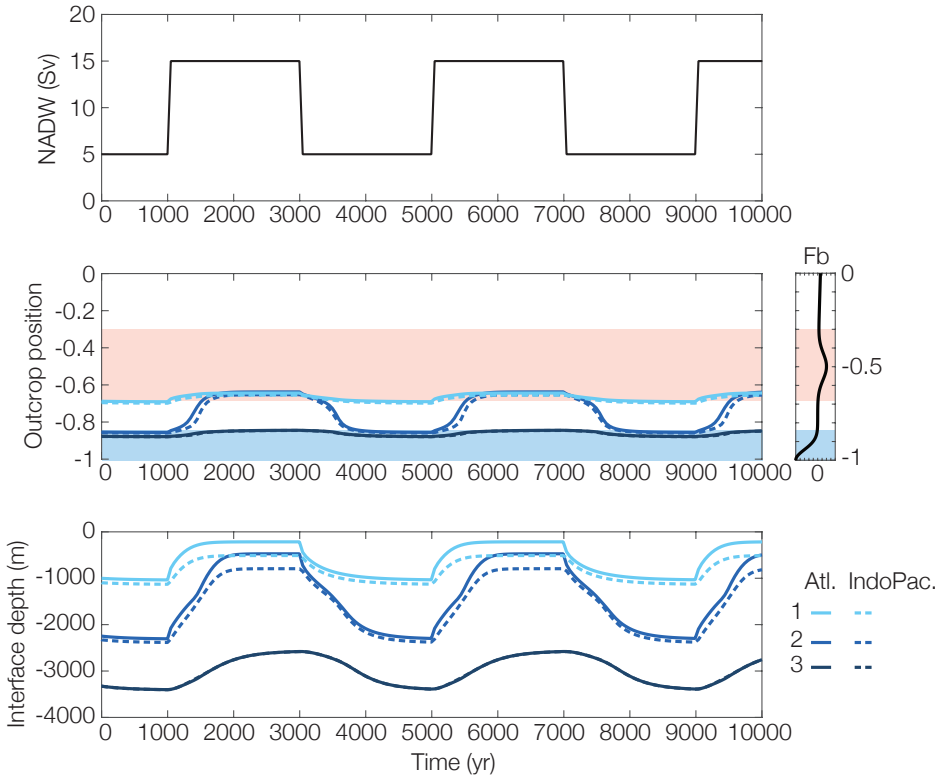

Figure 4.3: Example of model response in transient experiment. Top panel shows NADW forcing, middle panel shows outcrop position (as fraction of total ACC width), and bottom panel shows interface depth in the basin. Legend shows colors for the three interfaces and shading in middle panel indicates regions of positive and negative buoyancy forcing at the surface of the Southern Ocean, F_b plotted to right. This experiment was run at $\phi = 1$, meaning all of the NADW flux went from layer 1 into layer 3.

reducing stratification in the upper ocean and increasing stratification in the deep ocean (see Figure 4.3). As a consequence, diffusive upwelling for the deepest layers increases, since it is inversely dependent on the layer thickness (Thompson, Hines, and Adkins, *submitted*). This increase in deep circulation as a result of a deepening of basin stratification is another mechanism to explain the bipolar seesaw, and it is perhaps more physical than the "density vacuum" mechanism (Broecker, 1998), which relies on heat from the thermocline mixing down to the deep ocean.

We tested the idea that this same mechanism could be responsible for radiocarbon observations from the deep and abyssal South Atlantic during the late part of the last glacial period by adding a simple radiocarbon tracer to the model. Unlike a simple residence time calculation, radiocarbon tracer has a strong "memory" of past

changes in circulation, since it decays with a 5730-year half-life. We simulated a 25 kyr period from 35 ka to 10 ka, encompassing Heinrich Stadial 2 (an abrupt shut-down in NADW formation preceding the LGM), the LGM, and Heinrich Stadial 1 (a second abrupt shut-down in NADW formation immediately following the LGM). Our simulation was able to qualitatively match deep (layer 3) and abyssal (layer 4) radiocarbon records from the South Atlantic (L. C. Skinner et al., 2010; Barker et al., 2010). These records show similar radiocarbon values preceding the LGM, separation in radiocarbon during the LGM, with oldest values in the deep (layer 3), and convergence in radiocarbon following the LGM (Thompson, Hines, and Adkins, *submitted*).

Abrupt transitions in steady-state experiments

As can be seen in Figure 4.3, interface 2 is more sensitive to changes in NADW flux than any of the other interfaces. In an attempt to more precisely determine the response of interface 2 to changes in NADW flux, we conducted a series of experiments where we ran the time-dependent model out to steady-state. In particular, we were interested in the model response to different NADW fluxes and different NADW densities (ϕ). We varied ϕ between 0 (all NADW goes into layer 2) and 1 (all NADW goes into layer 3), in increments of 0.1. For each value of ϕ we ran a 'loop' of NADW values—starting at a NADW flux of 4 Sv, we ran the model for 5000 years, we saved the final values for each interface depth and outcrop position, and then we used them as initial conditions for the next iteration, with a NADW flux of 5 Sv. To start, we ran each loop from a NADW flux of 4 Sv to 20 Sv and back to 4 Sv, in increments of 1 Sv. In some loops, there were abrupt transitions, particularly in the outcrop position of interface 2. For these loops, we re-ran them with increased NADW resolution (down to 0.25 Sv) in the vicinity of the transition (Figure 4.4).

For values of ϕ between 0.4 and 1, the NADW loop is characterized by an abrupt transition in the outcrop position of interface 2 in the Atlantic (y_2^A) from a region of negative surface buoyancy forcing to a region of positive surface buoyancy forcing. For these loops with abrupt transitions in outcrop position, there is also hysteresis in outcrop position as a function of NADW flux—the transition from outcropping in a negative buoyancy flux region to a positive buoyancy flux region occurs at a higher NADW flux when NADW is increasing than when NADW is decreasing (Figure 4.4). The width of the hysteresis loop increases as ϕ decreases from 1 to 0.4, but once ϕ is below 0.4, the hysteresis (and the abrupt transition in outcrop position)

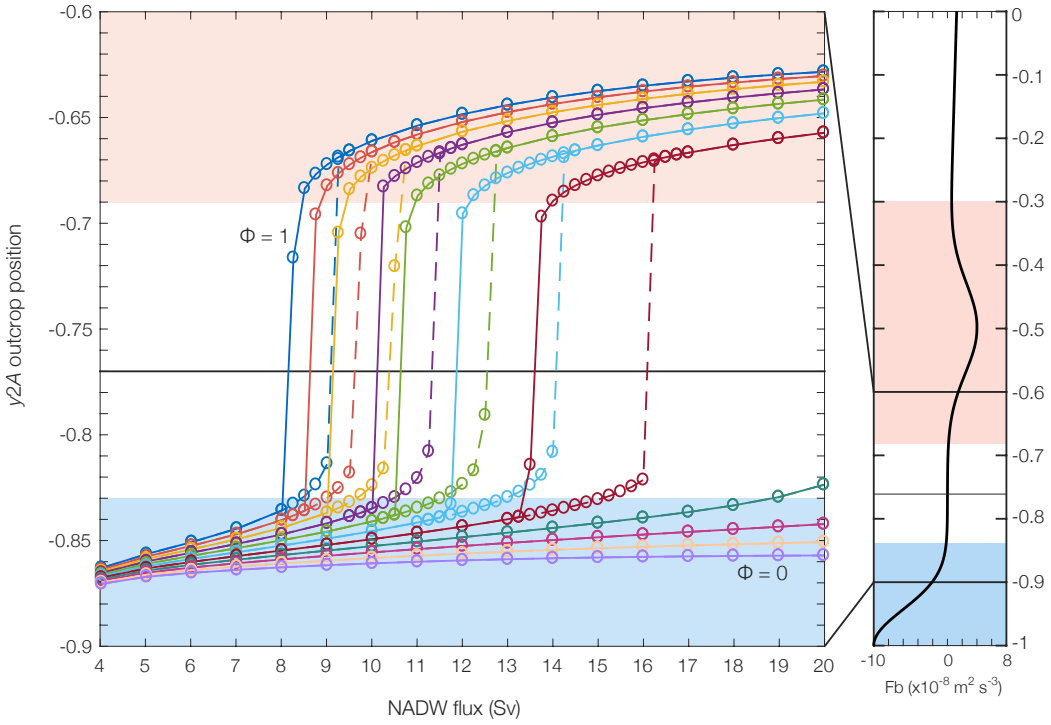

Figure 4.4: Outcrop position of interface 2 in the Atlantic (y_2^A) for all values of ϕ. ϕ varies from 0 to 1 in increments of 0.1. Each loop is a different single color; dashed lines mark the up-going limb of the loop (i.e. increasing from 4 Sv to 20 Sv) and solid lines mark the down-going limb of the loop. Circles mark each NADW flux value that was run. Shading in the background indicates regions of positive and negative surface buoyancy flux, F_b (plotted in full to right). Horizontal line marks the $F_b = 0$ contour.

disappears.

In the vicinity of the hysteresis loop, the amount of time it takes for the model to reach steady-state also increases (Figure 4.5). For ϕ values of 0–0.3, where there is no abrupt transition in y_2^A or hysteresis, equilibration times are short (50–100 years). The equilibration time was calculated by finding the maximum in the first derivative of the timeseries for y_2^A.

To test the Ferrari et al. (2014) mechanism, we ran a series of experiments where we changed the extent of sea ice in the Southern Ocean (y_{si}, see Eq. 4.7). Increasing this parameter extends sea ice further across the Southern Ocean and decreasing this parameter (to more negative values) contracts sea ice closer to the southern boundary of the domain. As y_{si} increases, the magnitude of the jump in y_2^A also increases; as y_{si} decreases, the magnitude of the jump in y_2^A decreases. The hysteresis in y_2^A

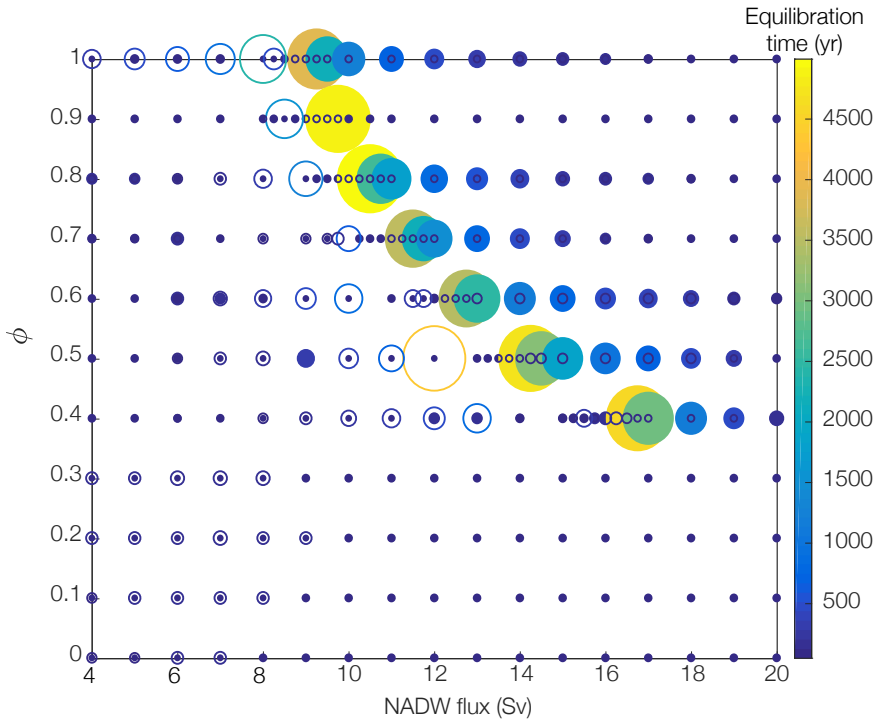

Figure 4.5: Equilibration time for interface y_2^A for all values of ϕ as a function of NADW flux. Filled circles are for the up-going limb of the loop and unfilled circles are for the down-going limb. Color and size of circle corresponds to equilibration time.

outcrop position still remains, however (Figure 4.6).

4.4 Discussion

The primary goal of our experiments was to elucidate the fundamental physics driving abrupt transitions in circulation during the last glacial period. While some simple models of the bipolar seesaw are able to generate signals that match climate records (e.g. Thomas F Stocker and Johnsen, 2003), the physics of these models do not very closely match that of the ocean. Although our model is also fairly simple, we have kept many important aspects of ocean physics including both an Atlantic and Indo-Pacific basin, the residual circulation in the Southern Ocean, differences in vertical diffusivity in the northern basins, and sea ice-driven buoyancy forcing in the Southern Ocean.

The origin of hysteresis and abrupt transitions in the model

One of the most notable and interesting results of the experiments where we ran our model out to steady-state is the emergence of hysteresis. In dynamical systems,

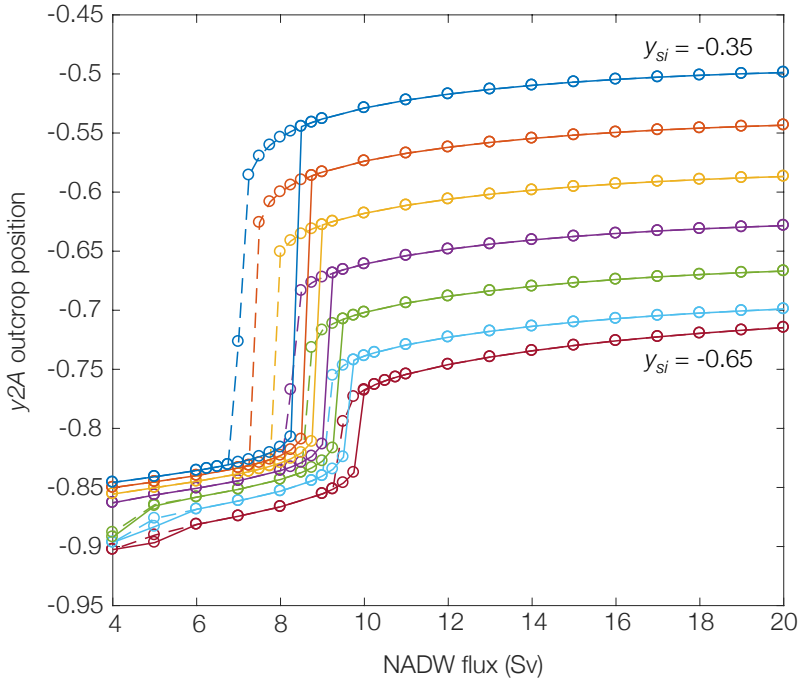

Figure 4.6: Outcrop position of y_2^A as a function of NADW flux for different sea ice extents (y_{si}). A y_{si} value of -0.5 means that the maximum of F_b associated with sea ice melt is centered at the middle of the ACC and is an equivalent position to -0.5 on the y axis (see Equation 4.7). From bottom to top, y_{si} position increases in increments of 0.05. $\phi = 1$ for all experiments.

hysteresis indicates the presence of multiple steady states, and rapid flips between these states can give rise to abrupt transitions in the system. During Marine Isotope Stage (MIS) 3, there were many such abrupt transitions in the climate system, as recorded in isotope records from the Greenland ice sheet (Figure 4.1).

The most striking consequence of this hysteresis in our model is the abrupt jumps in the Southern Ocean outcrop position of interface 2 between a region of positive buoyancy forcing and a region of negative buoyancy forcing. At steady-state, the surface buoyancy forcing in the Southern Ocean imposes a constraint on the slope of each interface ($-z/y$), given its outcrop position. From Equation 4.11, we see that when $\partial y/\partial t = 0$, $F_b\left(\ell^{ml}/\Delta b\right) = -\tau/(\rho_0 f) + Ks$. From this we can define a cut-off slope value where $F_b = 0$: $s_0 = -\tau/(\rho_0 f K) = -9.8 \times 10^{-4}$. If interface 2 (the only interface that switches between positive and negative buoyancy forcing regions) is in a region where $F_b > 0$, then $s > s_0$, if interface 2 is in a region where $F_b < 0$, then $s < s_0$. Indeed, looking at the hysteresis loop for $\phi = 1$ from Figure 4.4 as slope versus NADW we see that the loop splits around $s = s_0$ (Figure 4.7).

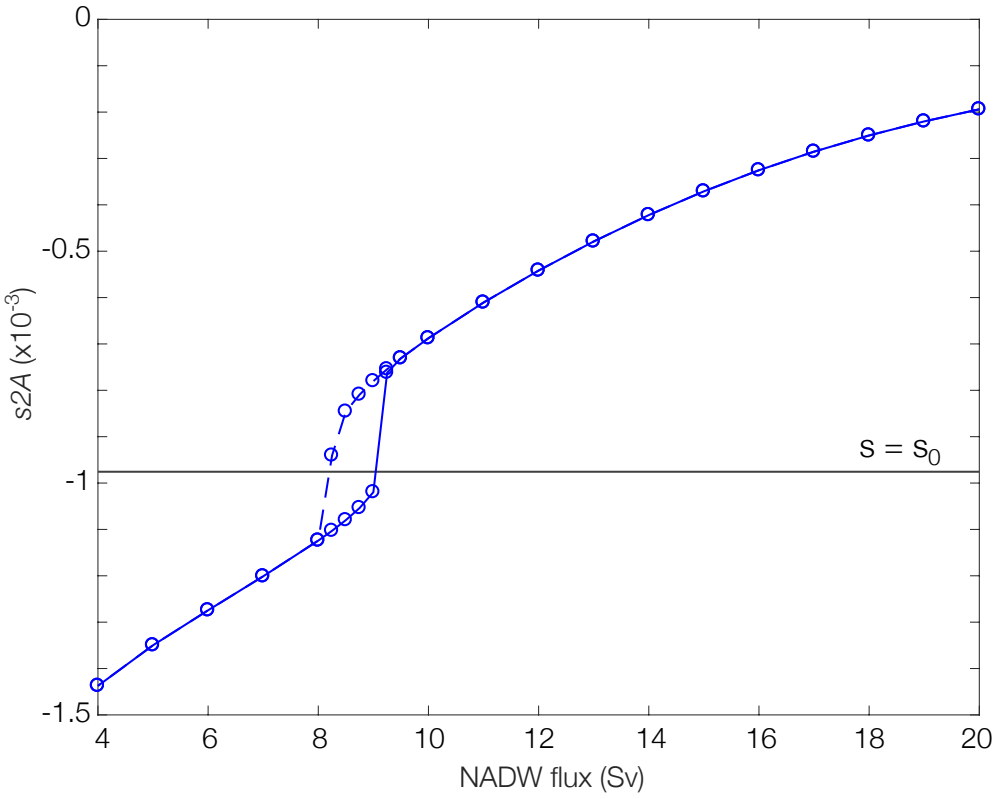

Figure 4.7: Interface 2A slope as a function of NADW flux for $\phi = 1$. The slope for interface 2 in the Atlantic is defined as $-z_2^A/y_2^A$. Horizontal line marks $s = s_0$.

Within a hysteresis loop there are actually 3 steady-state solutions, two of which are stable. From Figure 4.7, we see that the two stable solutions are where $s > s_0$ and $s < s_0$. The third solution lies between the two stable solutions, so it must therefore be where s is very close to or equal to s_0, i.e. where F_b is very close to zero. This solution is unstable because any perturbation to the isopycnal outcrop position moves it to a region with a larger buoyancy flux (either positive or negative), which then requires the slope to adjust further.

To test the stability of the hysteresis loop, we do a series of perturbation experiments to z_2 in both the Atlantic and Pacific. We have chosen to perturb the z position instead of the y position of interface 2 because the timescale for the diffusive adjustment of z is much longer than the eddy-induced relaxation of y. This longer adjustment timescale means that the perturbation has a larger affect. For a NADW flux of 8.75 Sv (in the middle of the hysteresis loop for $\phi = 1$), we displace the z position of interface 2 downward from its steady state on the upper (down-going) limb of the loop by 100–500 m and allow it to relax back towards equilibrium. We run the

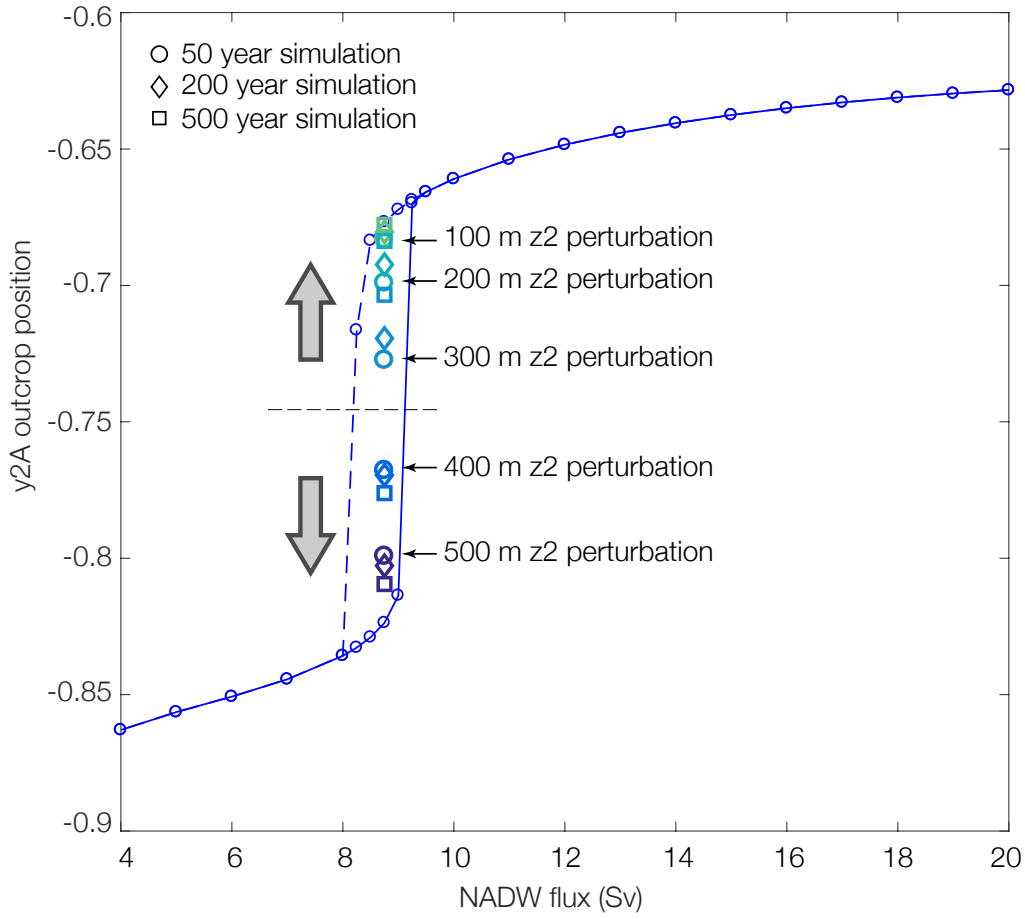

Figure 4.8: Perturbation experiments to test the stability of the hysteresis loop. Starting with the steady-state interface positions for a NADW flux of 8.75 Sv on the upper limb of the hysteresis loop, z_2^A and z_2^P were displaced and then allowed to relax for 50, 200, and 500 years (y_2^A for each of these simulations are plotted in circles, diamonds and squares, respectively).

simulation for 50, 200, and 500 years so we can ascertain the direction that the model is relaxing toward (since none of them fully reach steady state). We find that there is indeed a bifurcation in the middle of the hysteresis loop—displacements of 100–300 m relax back towards the original state, while 400 and 500 m perturbations relax toward the other limb of the loop (Figure 4.8).

While the surface buoyancy flux distribution in the Southern Ocean plays a large part in the dynamics of the hysteresis loop it is not solely responsible for generating hysteresis. The other major non-linearity that contributes to generating hysteresis in the model is the distribution of vertical diffusivity in the basin, $\kappa(z)$. If we look at the same perturbation experiment in z space instead of y space (Figure 4.9), we see that

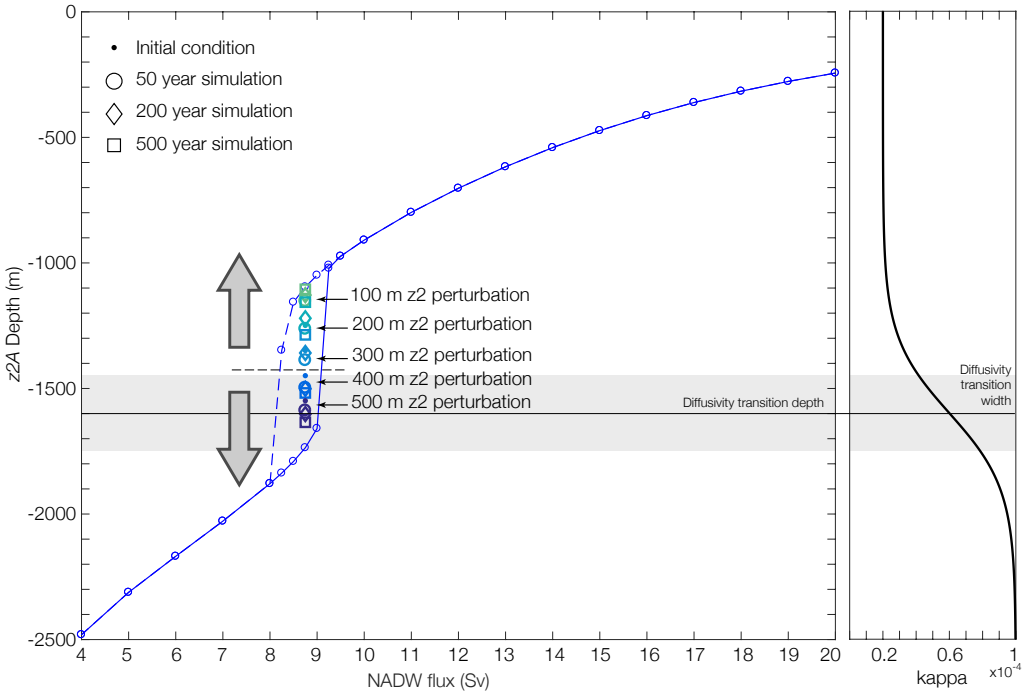

Figure 4.9: Perturbation experiments in z space. Same experiment as shown in Figure 4.8. Vertical diffusivity profile is also shown with diffusivity transition depth (1600 m) and diffusivity transition width (d = 300 m) marked.

the bifurcation in z_2 occurs once the initial z position enters the κ transition region (where the κ transition region is defined by the parameter d, see Table 4.1). Indeed, if we run the same NADW loop, but keep κ fixed or have a linear distribution of vertical diffusivity, the hysteresis and the abrupt transition in outcrop position goes away (Figure 4.10).

In general, as NADW flux increases there is a tendency for y_2 to move north and z_2 to shoal. In the basin, shoaling z_2 tends to increase diffusive transport across that interface, since T_{diff} is inversely proportional to the thickness of the layer above. This helps to balance the additional NADW flux. As z_2 approaches the κ transition region, shoaling the interface becomes less effective at increasing T_{diff}, since it moves z_2 into a less diffusive region. Therefore z_2 has to shoal much more rapidly to balance the additional NADW input. Since there are strong constraints on the slope of interface 2 depending on whether it outcrops in a negative or positive F_b region, the rapid shoaling of z_2 causes an abrupt response in y_2. For the down-going limb of the hysteresis loop, decreases in NADW flux cause mass convergence in the uppermost layer, which causes layers 1 and 2 to deepen. Because y_2 is in the positive buoyancy forcing region, it must move to the south as z_2 deepens in order to

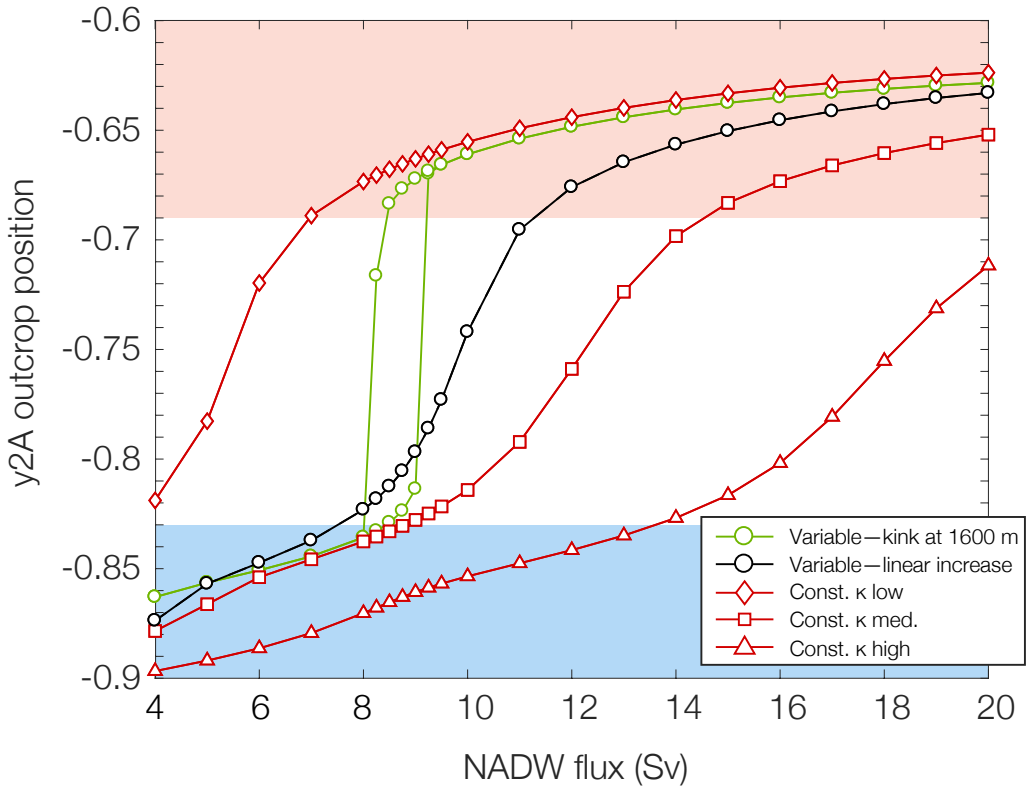

Figure 4.10: Outcrop position of y_2^A as a function of NADW flux for different vertical diffusivity profiles. The control experiment has a kinked κ profile (green). A series of experiments with constant κ (at values of 0.2×10^{-4}, 0.6×10^{-4}, and 1×10^{-4}; red) and an experiment with a linearly increasing κ profile (from 0.2×10^{-4} to 1×10^{-4}; black) are shown for comparison.

maintain a sufficiently shallow slope. Once z_2 enters the higher-κ region, it begins to deepen more quickly, pulling y_2 further to the south. Eventually, the slope of interface 2 steepens sufficiently that y_2 is forced to flip to the negative buoyancy region, causing z_2 to rapidly deepen as well.

Circulation configuration

In order to assess which combinations of NADW flux and density lead to a two-cell circulation configuration and which combinations lead to a figure-eight circulation configuration, we need to define a quantity that reflects 'figure-eight-ness'. The key to a figure-eight configuration is that deep water formed in the Atlantic needs to be transferred into the Indo-Pacific, before it diffusively upwells and is transferred back to the Atlantic in the upper layers to close the circulation loop. We therefore

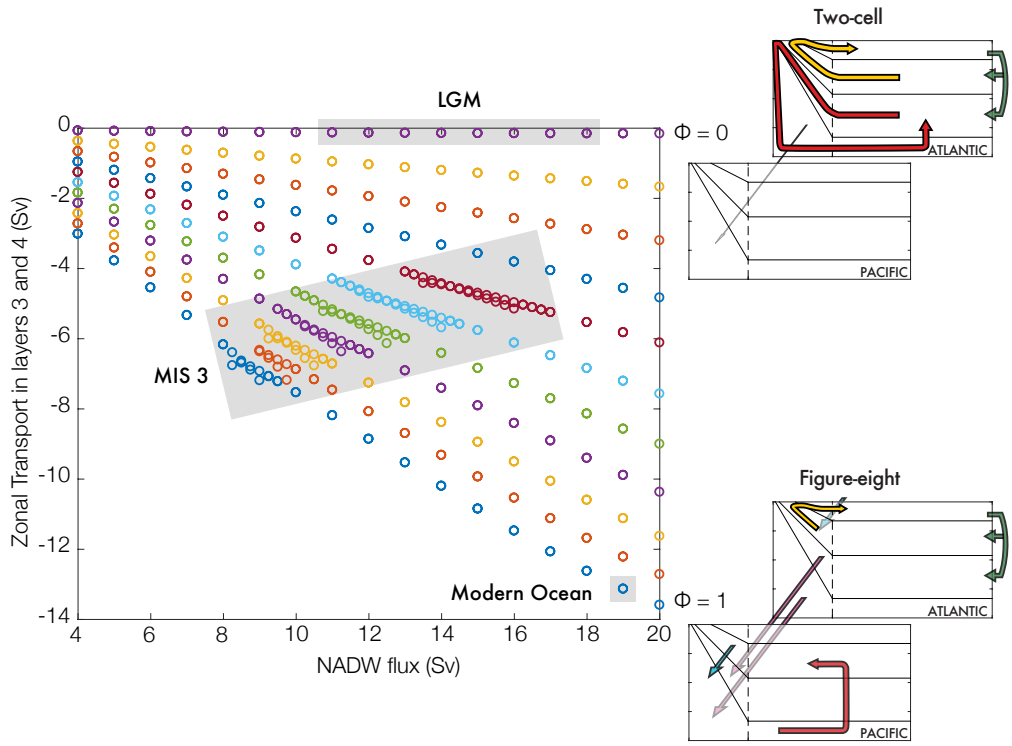

Figure 4.11: Assessment of circulation configuration for all ϕ experiments. Combinations of NADW strength and density that have very little zonal transport in layers 3 and 4 lead to a circulation configuration that is two-cell-like and combinations of NADW strength and density that have large zonal transport in layers 3 and 4 lead to a circulation configuration that is more figure-eight-like. Different colored circles represent different ϕ values from 0 (at top) to 1 (diagonal to lower right corner). Shaded regions show location of the modern ocean and approximate locations for the LGM and MIS 3. The high density of circles in the MIS 3 region mark the hysteresis loops, which show separation in outcrop position but not in circulation configuration.

look at the sum of T_{zonal} in layers 3 and 4. If this quantity is large, then more deep water from the Atlantic is going to the Pacific to upwell, and circulation is more figure-eight-like. If this quantity is small, then deep water from the Atlantic is upwelling instead in the Atlantic, and circulation is more two-cell-like (Figure 4.11). One important thing to note, however, is that by our metric circulation configuration exists on a continuum between figure-eight and two-cell—there is no cut-off value above which circulation is figure-eight and below which circulation is two-cell.

The first thing to notice in Figure 4.11 is that circulation configuration depends both on the strength and the density of NADW—strong dense NADW is the most figure-eight-like and weak light NADW is the most two-cell-like. However, as ϕ

decreases (i.e. NADW gets less dense), the dependence of T_{zonal} in layers 3 and 4 on NADW strength also decreases. The modern ocean has dense and strong NADW (~19 Sv, $\phi = 1$) and according to our metric a figure-eight circulation configuration. At the LGM, circulation may have been nearly as strong as the modern, but NADW was less dense ($\phi = 0$). Our configuration metric predicts that this would lead to a two-cell circulation configuration, matching paleo observations (Curry and Oppo, 2005; L. Skinner et al., 2017). During Marine Isotope Stage 3, there is evidence that NADW strength fluctuated and there are abrupt jumps in NGRIP δ^{18}O, indicating rapid flips between states in the climate system (Figure 4.1). The abrupt jumps in outcrop position and hysteresis that we see for many values of ϕ over a range of NADW fluxes is reminiscent of this period. Our configuration metric predicts that MIS 3 had some sort of intermediate circulation structure between the two-cell and figure-eight endmembers.

Relation to the Ferrari et al. model

The Ferrari et al. (2014) paper highlights key observations about the connection between the quasi-permanent sea ice position and the split between upper and lower meridional overturning circulation cells in the modern ocean, and they make some thought-provoking hypotheses about how these may have changed in the past. They note that expanded sea ice and shoaled NADW relative to AABW would lead to an overturning configuration with enhanced stratification at mid-depth and greater separation between the upper and lower circulation cells as the boundary between the cells moves out of the region with rough bottom topography. We compare our model results with three aspects of the Ferrari et al. (2014) theory: the relation between the quasi-permanent sea ice edge and the boundary between the upper and lower circulation cells, the role of rough bottom topography in determining the circulation configuration, and the role of the meridional sea ice extent in determining the circulation configuration.

In our model, we have defined a surface buoyancy forcing that is modeled after observed (from the Southern Ocean State Estimate) sea ice distribution and buoyancy fluxes with separated positive buoyancy flux and negative buoyancy flux regions to mimic freshwater input from sea ice melt and brine rejection due to sea ice formation. Although in our model we define the "sea ice edge" as the center of the positive buoyancy flux region associated with sea ice melt, this actually represents the seasonal ice region, therefore even isopycnals that outcrop south of our "sea ice edge" in this positive buoyancy flux region are north of the quasi-permanent

sea ice edge. Isopycnals that outcrop in the positive buoyancy forcing region by definition must participate in the upper cell and isopycnals that outcrop in the negative buoyancy forcing region must participate in the lower cell, in agreement with the Ferrari et al. (2014) observations.

The Ferrari et al. (2014) theory also notes that rough bottom topography, which is concentrated below 2000 m, greatly increases vertical mixing in the ocean (Polzin et al., 1997). To match this observed intensification of vertical mixing near the ocean bottom, our model has a kinked $\kappa(z)$ profile with enhanced vertical diffusivity in the deep ocean. We find that this non-linear vertical diffusivity distribution is crucial for generating the abrupt transitions in basin stratification and Southern Ocean isopycnal outcrop position that we observe. According to Ferrari et al. (2014), as stratification changes and the boundary between the upper and lower circulation cells moves into and out of the high mixing region, there should also be changes in configuration. In our model, however, these abrupt transitions in basin stratification and outcrop position do not lead to large changes in circulation configuration, however (see 'MIS 3' region in Figure 4.11).

Perhaps the most influential result from the Ferrari et al. (2014) paper is the hypothesis that expanded sea ice during the LGM led to a two-cell circulation configuration with shoaled NADW and enhanced stratification between the upper and lower circulation cells. There is an important dynamical step between sea ice expansion and the achievement of two-cell circulation configuration—the authors note that if sea ice is expanded, any NADW that sinks below the 2000 m depth would simply become part of the lower circulation cell and never return to the upper ocean. They note, importantly, that this deep penetration of NADW in a glacial configuration would only be possible transiently (since it would effectively drain the upper cell). They assert that the system would eventually adjust such that NADW was shoaled relative to AABW, since any NADW that was dense enough to sink below 2000 m would become part of the lower cell leaving the residual NADW less dense. In our model, NADW density is a separate parameter, so we cannot test the full Ferrari et al. (2014) mechanism exactly as they pose it in the paper (since ϕ does not evolve during a simulation). We can, however, test the two parts of this mechanism separately: the effect of expanded sea ice given a deep NADW of constant density ($\phi = 1$), and the effect of shoaled NADW given constant sea ice extent. We find that the density of NADW is much more important than the meridional extent of sea ice alone (compare Figures 4.11 and 4.12).

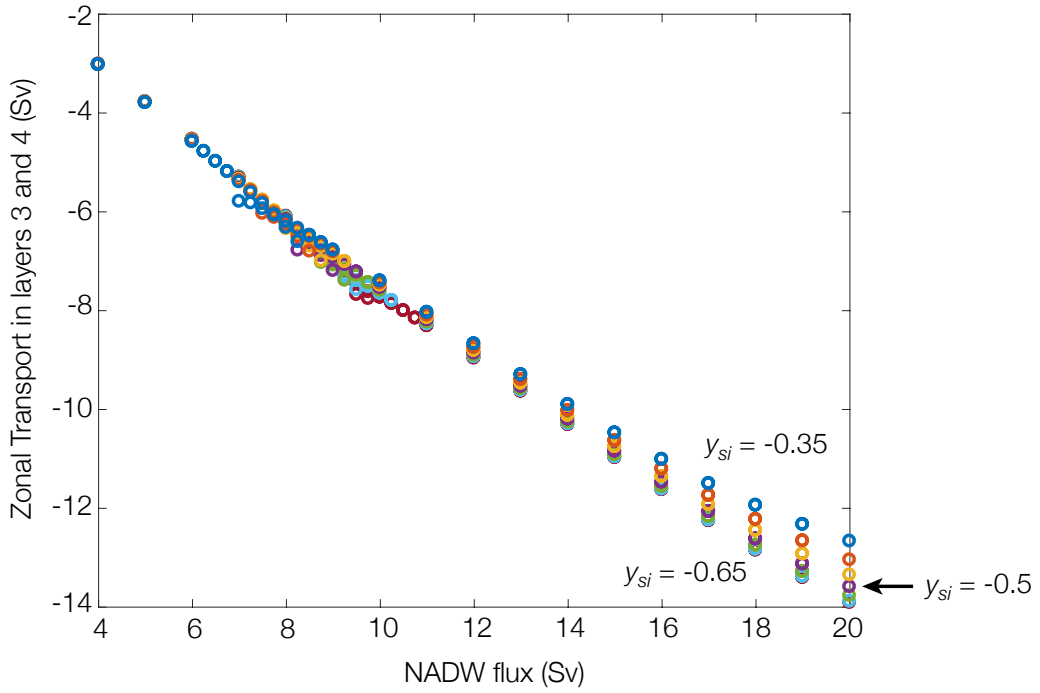

Figure 4.12: Assessment of circulation configuration for all y_{si} experiments. The relationship between NADW flux and circulation configuration is quite similar between all of the y_{si} experiments compared to the ϕ experiments (see Figure 4.11). The experiment with $y_{si} = -0.5$ is (labeled) is the same as the $\phi = 1$ experiment in Figure 4.11.

Dynamic versus forced responses in the model

One limitation of our model is that the external forcing lacks the ability to dynamically respond. In particular, the position of the "sea ice edge" in the Southern Ocean cannot respond to changes in isopycnal outcrop position. As was outlined in the Transient Interhemispheric Adjustment section, southward shifts of Southern Ocean isopycnals should increase the presence of warm (light) water at the surface and northward shifts of Southern Ocean isopycnals should increase the presence of cold (dense) water at the surface. This, in turn, should affect the position of Southern Ocean sea ice, contracting or expanding it, respectively.

One simple way to dynamically couple the sea ice would be to pin the sea ice edge to an interface in the model. If the sea ice edge were pinned to interface 2 (the isopycnal that splits NADW and PDW density classes), then the model would not be able to produce abrupt transitions in stratification or Southern Ocean outcrop position, which are the result of interface 2 flipping between the positive and negative buoyancy forcing regions. Interface 1, on the other hand, always sits in the positive

buoyancy forcing region, but does not move very much in response to changes in NADW flux (a change in NADW from 4 to 20 Sv moves $y1A$ 7% of the way across the channel for a ϕ value of 1, roughly equivalent distance to one y_{si} increment in Figure 4.6). There are no real data constraints for changes in sea ice position during the climate oscillations of MIS 3, but compiled sea ice reconstructions from the LGM indicate a northward shift of 7–10 ° latitude, $O(10^6)$ m, varying in different sectors of the Southern Ocean (Gersonde et al., 2005). In our model, this is equivalent to half the ACC domain width.

The main external forcing that drives our model is NADW formation flux. Most higher-complexity models that have been used to investigate climate variability associated with changes in NADW formation during MIS 3 are driven by changes in freshwater forcing in the North Atlantic (Buizert and Schmittner, 2015; Rahmstorf et al., 2005; Abe-Ouchi et al., 2016). However, changes in North Atlantic freshwater flux impact deep convection and thus lead to changes in NADW flux, making the ultimate driver similar. Many of these more complex models display hysteresis in Atlantic Meridional Overturning Circulation (AMOC) strength as a function of freshwater forcing, but they often have to resort to negative North Atlantic freshwater fluxes to get NADW formation to resume after a freshwater-induced shut-down. While our model is much simpler, it retains key elements of the ocean physics contained in these higher-order models, and explicitly contains residual mean theory. Most importantly, the origin of hysteresis in our model—separated positive and negative buoyancy forcing in the Southern Ocean and a kinked vertical diffusivity profile—is more physically meaningful than negative freshwater fluxes when it comes to the real ocean.

4.5 Conclusions

We have developed a two-basin time-dependent dynamical box model of the ocean, incorporating residual mean theory for describing circulation in the Southern Ocean. It is a coarse-resolution isopycnal model for the ocean with three isopycnal layers, each defined by two points: a depth in the basin and an outcrop position in the Southern Ocean. Separate Atlantic and Pacific basins allow the overturning circulation to occupy either a ‘figure-eight’ or ‘two-cell’ circulation and the basins can transfer mass via zonal convergence in the Southern Ocean. In the northern end of the Atlantic basin, North Atlantic Deep Water formation transfers mass from the uppermost layer into either the second or third layer, determined by the NADW density parameter, ϕ. This allows NADW to have a dense configuration like the

modern ocean, or a shoaled configuration like the LGM.

In a set of transient experiments, we find that abrupt changes in NADW flux cause rapid changes in basin stratification and Southern Ocean isopycnal outcrop position. The timescale associated with this rapid adjustment is ≈200 years, matching observations from synchronized Northern and Southern Hemisphere ice core records during MIS 3 (WAIS Divide Project Members, 2015). The dynamics of this transient adjustment provide a physical mechanism for the bipolar seesaw: a rapid increase (decrease) in NADW formation, associated with Northern Hemisphere interstadials (stadials), shoals (deepens) basin stratification and pushes Southern Ocean isopycnals to the north (south). This increases (decreases) the relative amount of cold dense water at the surface and cools (warms) the Southern Hemisphere.

In subsequent experiments where we run our time-dependent model to steady state, we find abrupt transitions and hysteresis in the outcrop position of interface 2 as a function of NADW strength. This behavior is driven by the separation of positive and negative buoyancy flux regions in the Southern Ocean and the kinked vertical diffusivity profile in the basin. Sufficiently large perturbations from one limb of the steady-state configuration in the hysteresis region are able to drive the system towards the other limb. This bifurcation is reached when the z_2 interface is perturbed into the region of higher vertical diffusivity. Experiments with constant or linear vertical diffusivity profiles do not show hysteresis and show much more gradual transitions in y_2^A outcrop position because the z position is able to adjust more smoothly as a function of NADW flux.

We find that the strength and the density of NADW are the most important factors for determining overturning circulation configuration. Circulation configuration is assessed based on the amount of zonal transport in the deepest two layers, with higher zonal transport leading to a more figure-eight-like circulation. Stronger denser NADW favors figure-eight circulation while weaker lighter NADW favors two-cell circulation. As expected, the modern ocean has a figure-eight circulation and the LGM has a two-cell circulation according to our metric. The combination of NADW strength and density that gives rise to abrupt transitions in Southern Ocean outcrop position and basin stratification, characteristic of MIS 3, has an intermediate circulation configuration between pure figure-eight and two-cell.

Our model results agree with the predictions of the Ferrari et al. (2014) paper with some exceptions. Our surface buoyancy forcing is modeled after sea ice dynamics and in our model, as in the paper, water that outcrops north of the quasi-permanent

sea ice edge participates in the upper overturning cell and water that outcrops south of the quasi-permanent sea ice edge participates in the lower overturning cell. We also find that the abrupt transitions in basin stratification and Southern Ocean outcrop position observed in our model depend strongly on the kinked vertical diffusivity profile in the ocean. These abrupt transitions are reminiscent of the DO events that characterize MIS 3, but do not lead to changes in circulation configuration. Although this is somewhat of a contradiction to the predictions of the Ferrari et al. (2014) paper, the authors put forward a mechanism whereby NADW adjusts its relative density in response to a sea ice expansion, and our model does not allow that sort of dynamic adjustment.

One limitation of our model that we hope to address in the future is that while basin stratification and overturning circulation can respond to changes in forcing, there are a few key parameters that cannot dynamically adjust, namely the position of Southern Ocean sea ice. According to the bipolar seesaw mechanism, reinvigoration of North Atlantic Deep Water (associated with Northern Hemisphere interstadials) should lead to cooler conditions in the Southern Hemisphere. While the dynamics of our model support this trend—strengthened NADW leads to a northward shift of Southern Ocean isopycnals and a greater fraction of cold dense water outcropping at the surface—Southern Ocean sea ice is not able to adjust its meridional extent in response. Because the distribution of surface buoyancy forcing associated with sea ice dynamics plays an important role in the behavior of our model, and the meridional extent of sea ice should change in response to hemispheric warming or cooling, this is an important area to investigate. Other interesting areas to investigate in the future are how to couple the strength and/or density of NADW to other aspects of the model, thereby allowing the ocean to create unforced DO oscillations or configuration changes.

References

Abe-Ouchi, A. et al. (2016). “Stability of AMOC and bipolar seesaw under different background climate in MIROC AOGCM”. In: *AGU Fall Meeting Abstracts*.

Abernathey, Ryan P. et al. (2016). “Water-mass transformation by sea ice in the upper branch of the Southern Ocean overturning”. In: *Nature Geoscience* 9.8, pp. 596–601.

Barker, Stephen et al. (2010). “Extreme deepening of the Atlantic overturning circulation during deglaciation”. In: *Nature Geoscience* 3.8, pp. 567–571.

Blunier, Thomas and Edward J Brook (2001). "Timing of Millennial-Scale Climate Change in Antarctica and Greenland During the Last Glacial Period". In: *Science* 291.5501, pp. 109–112.

Böhm, E et al. (2015). "Strong and deep Atlantic meridional overturning circulation during the last glacial cycle". In: *Nature* 517.7532, pp. 73–76.

Broecker, Wallace S. (1998). "Paleocean circulation during the last deglaciation: A bipolar seesaw?" In: *Paleoceanography* 13, pp. 119–121.

Buizert, C. and A. Schmittner (2015). "Southern Ocean control of glacial AMOC stability and Dansgaard-Oeschger interstadial duration". In: *Paleoceanography*.

Collins, William D. et al. (2006). "The Community Climate System Model Version 3 (CCSM3)". In: *Journal of Climate* 19, pp. 2122–2143.

Crowley, Thomas J (1992). "North Atlantic deep water cools the Southern Hemisphere". In: *Paleoceanography* 7, pp. 489–497.

Curry, William B. and Delia W. Oppo (2005). "Glacial water mass geometry and the distribution of δ13C of ΣCO2 in the western Atlantic Ocean". In: *Paleoceanography*.

Dansgaard, Willi et al. (1993). "Evidence for general instability of past climate from a 250-kyr ice-core record". In: *Nature* 364.6434, pp. 218–220.

Ferrari, R et al. (2014). "Antarctic sea ice control on ocean circulation in present and glacial climates". In: *PNAS* 111.24, pp. 8753–8758.

Gersonde, R et al. (2005). "Sea-surface temperature and sea ice distribution of the Southern Ocean at the EPILOG Last Glacial Maximum—A circum-Antarctic view based on siliceous microfossil records". In: *Quaternary Science Reviews* 24.7-9, pp. 869–896.

Gnanadesikan, A (1999). "A Simple Predictive Model for the Structure of the Oceanic Pycnocline". In: *Science* 283.5410, pp. 2077–2079.

Goodwin, P. (2012). "An Isopycnal Box Model with predictive deep-ocean structure for biogeochemical cycling applications". In: *Ocean Modelling* 51, pp. 19–36.

Kuhlbrodt, T et al. (2007). "On the driving processes of the Atlantic meridional overturning circulation". In: *Reviews of Geophysics* 45.

Lippold, Jörg et al. (2009). "Does sedimentary ^{231}Pa/^{230}Th from the Bermuda Rise monitor past Atlantic Meridional Overturning Circulation?" In: *Geophysical Research Letters* 36.12, p. 7.

Liu, Zhengyu and Mike Alexander (2007). "Atmospheric bridge, oceanic tunnel, and global climatic teleconnections". In: *Reviews of Geophysics* 45.2, p. 1769.

Liu, Z et al. (2009). "Transient Simulation of Last Deglaciation with a New Mechanism for Bolling-Allerod Warming". In: *Science* 325.5938, pp. 310–314.

Lumpkin, Rick and Kevin Speer (2007). "Global Ocean Meridional Overturning". In: *Journal of Physical Oceanography* 37.10, pp. 2550–2562.

Marshall, David P and Laure Zanna (2014). "A Conceptual Model of Ocean Heat Uptake under Climate Change". In: *Journal of Climate* 27.22, pp. 8444–8465.

Marshall, John and Timour Radko (2003). "Residual-mean solutions for the Antarctic Circumpolar Current and its associated overturning circulation". In: *Journal of Physical Oceanography* 33.11, pp. 2341–2354.

Marshall, John and Kevin Speer (2012). "Closure of the meridional overturning circulation through Southern Ocean upwelling". In: *Nature Geoscience* 5.3, pp. 1–10.

McManus, J F et al. (2004). "Collapse and rapid resumption of Atlantic meridional circulation linked to deglacial climate changes". In: *Nature* 428.6985, pp. 834–837.

Munday, David R, Helen L Johnson, and David P Marshall (2013). "Eddy Saturation of Equilibrated Circumpolar Currents". In: *Journal of Physical Oceanography* 43.3, pp. 507–532.

NGRIP members (2004). "High-resolution record of Northern Hemisphere climate extending into the last interglacial period". In: *Nature* 431, pp. 147–15.

Polzin, K L et al. (1997). "Spatial Variability of Turbulent Mixing in the Abyssal Ocean". In: *Science* 276, pp. 93–96.

Rahmstorf, Stefan et al. (2005). "Thermohaline circulation hysteresis: A model intercomparison". In: *Geophysical Research Letters* 32.

Skinner, L C et al. (2010). "Ventilation of the Deep Southern Ocean and Deglacial CO_2 Rise". In: *Science* 328.5982, pp. 1147–1151.

Skinner, L.C. et al. (2017). "Radiocarbon constraints on the glacial ocean circulation and its impact on atmospheric CO_2". In: *Nature Communications*.

Speer, Kevin, Stephen R. Rintoul, and Bernadette Sloyan (2000). "The Diabatic Deacon Cell". In: *Journal of Physical Oceanography*.

Stocker, T F (1998). "The Seesaw Effect". In: *Science* 282.5386, pp. 61–62.

Stocker, Thomas F and Sigfus J Johnsen (2003). "A minimum thermodynamic model for the bipolar seesaw". In: *Paleoceanography* 18.4.

Sun, S, I Eisenman, and A L Stewart (2016). "The influence of Southern Ocean surface buoyancy forcing on glacial-interglacial changes in the global deep ocean stratification". In: *Geophysical Research Letters*.

Talley, Lynne (2013). "Closure of the Global Overturning Circulation Through the Indian, Pacific, and Southern Oceans: Schematics and Transports". In: *Oceanography* 26.1, pp. 80–97.

Thompson, Andrew F., Sophia K. Hines, and Jess F. Adkins (*submitted*). "A Southern Ocean mechanism for climate transients through the last glacial period". In: *Nature*.

Thompson, Andrew F., Andrew L. Stewart, and Tobias Bischoff (2016). "A Multi-basin Residual-Mean Model for the Global Overturning Circulation". In: *Journal of Physical Oceanography* 46.9, pp. 2583–2604.

WAIS Divide Project Members (2015). "Precise interpolar phasing of abrupt climate change during the last ice age". In: *Nature* 520, pp. 661–664.

Wolfe, Christopher L and Paola Cessi (2011). "The Adiabatic Pole-to-Pole Overturning Circulation". In: *Journal of Physical Oceanography* 41.9, pp. 1795–1810.

Yeager, Stephen G. et al. (2006). "The Low-Resolution CCSM3". In: *Journal of Climate* 19, pp. 2545–2566.

Chapter 5

DEEP-SEA CORAL CLUMPED ISOTOPE AND RADIOCARBON RECORDS FROM NORTH ATLANTIC AND SOUTHERN OCEAN INTERMEDIATE WATER SPANNING THE MOST RECENT GLACIAL TERMINATION

5.1 Introduction

Ocean circulation plays a central role in glacial-interglacial climate. Of particular importance is the meridional overturning circulation (MOC), which transfers water from the surface to the deep ocean on ~1000-year timescales (Stuiver, Quay, and Ostlund, 1983). The deep ocean is a crucial carbon reservoir in the ocean-atmosphere system, and small changes in circulation rate and structure can have a large impact on the pCO_2 of the atmosphere, which is closely linked to glacial cycles (Barnola et al., 1987; Petit et al., 1999; Sigman and Edward A. Boyle, 2000).

On shorter timescales during glacial periods, it has long been recognized that there is an anti-phase relationship between high latitude temperatures in the Northern and Southern Hemispheres (Barker, Diz, et al., 2009; Blunier and Brook, 2001; Broecker, 1998; Crowley, 1992). Key to this observation are high resolution ice core stable isotope records from Greenland and Antarctica, which have also been supported by surface temperature reconstructions (Bard, 2000; Barker, Diz, et al., 2009; Lamy et al., 2007). Deeper ocean temperatures have not always followed surface temperature patterns, however. Clumped isotope and Mg/Ca records from the Nordic Seas show warmer temperatures in the high-latitude North Atlantic during the glacial than the Holocene (Cronin et al., 2012; Thornalley et al., 2015) and deep-sea coral clumped isotope temperatures from the New England Seamounts show an abrupt warming event that precedes the beginning of the Bølling-Allerød warm period in the Northern Hemisphere (Thiagarajan, Subhas, et al., 2014). Modelling experiments across the deglaciation also show an accumulation of heat in the deep and intermediate Atlantic preceding the Bølling-Allerød, potentially driven by freshwater forcing in the North Atlantic (Liu et al., 2009).

In order to understand the asynchronicity between the hemispheres, and the ability of the ocean to store more carbon during glacial times, it is necessary to understand both the pattern and rate of ocean circulation across the deglaciation. As was

nicely described by Talley (2013), in the modern ocean there is a 'figure-eight'-like circulation: North Atlantic Deep Water (NADW) that upwells in the Southern Ocean is far enough to the south that it experiences a negative surface buoyancy forcing and becomes part of sinking Antarctic Bottom Water (AABW). It is only once this AABW flows into the Indian or Pacific basins that it is able to diffusively upwell to density class where it can return to the Southern Ocean in a positive buoyancy forcing region, thus enabling the overturning circulation to close. There is evidence that the structure of the ocean at the Last Glacial Maximum (LGM) looked significantly different from the modern with a shoaled NADW, an expansion of AABW within the Atlantic basin and enhanced mid-depth stratification (Curry and Oppo, 2005; Lund, Adkins, and Ferrari, 2011). This shoaled NADW configuration would allow the overturning circulation to close within a single basin because NADW would no longer upwell in a negative buoyancy forcing region in the Southern Ocean. We therefore think of this LGM circulation configuration as 'two-cell'.

There is evidence not only that the structure of circulation during the LGM was distinct from the modern, but also that the stratification between northern and southern-source water was fundamentally different. Pore fluid measurements of ^{18}O and chlorinity, used as a direct measure of bottom water temperature and salinity, show that while the modern water column is dominantly temperature-stratified, the glacial ocean was instead salinity-stratified (Adkins, 2002). Subsequent modelling showed that this switch could be achieved simply by cooling NADW (Miller et al., 2012). In order to better constrain circulation configuration at the LGM and the transitions into and out of the LGM state, it is useful to have more records with multiple geochemical tracers, especially physical tracers such as radiocarbon and temperature. Reconstructions with multiple physical tracers can give insight into the mechanisms driving observed signals, because different mechanisms correspond to different vectors on a tracer-tracer plot.

Radiocarbon is a well-established tracer of deep ocean circulation. Carbon-14 atoms are produced in the atmosphere, where they become incorporated into CO_2. Atmospheric $^{14}CO_2$ is in equilibrium with surface ocean dissolved inorganic carbon, but when water leaves the surface, radiocarbon decays with a 5730-year half-life. Therefore, the radiocarbon content of deep water is a measure of the amount of time that has elapsed since that water was at the surface (once the radiocarbon age of the surface water is taken into account). Historically, radiocarbon has primarily been measured in planktic and benthic foraminifera, however it can also be measured

in deep-sea corals (Adkins, Griffin, et al., 2002), which have the added benefit of absolute age control via U/Th dating (Cheng et al., 2000; Lomitschka and Mangini, 1999).

Past deep ocean temperatures have been more difficult to constrain. Early measurements of oxygen isotopes on benthic foraminifera (Shackleton, 1967; Chappell and Shackleton, 1986; Emiliani, 1955) showed glacial-interglacial variation, however δ^{18}O of carbonate is affected by both temperature and the δ^{18}O of the water (which varies with the growth and decay of ice sheets). Subsequently, Mg/Ca ratios in planktic (Nürnberg, Bijma, and Hemleben, 1996) and benthic (Rosenthal, Edward A Boyle, and Slowey, 1997; Martin et al., 2002) foraminifera and surface corals (Mitsuguchi et al., 1996) were established as temperature proxies. Unfortunately, both of these methods for reconstructing paleo deep-water temperature have proved complicated in deep-sea corals due to 'vital effects', or ways in which the coral biology shifts isotope or elemental ratios away from theoretical values (Adkins, Edward A. Boyle, et al., 2003; Gagnon et al., 2007).

Recently, a new paleothermometer has been developed for carbonates based on the thermodynamics of homogeneous isotope exchange in carbonate minerals. At cold temperatures, heavy carbon and oxygen isotopes tend to 'clump' together within carbonate groups and at warm temperatures they tend to be more randomly distributed among carbonate groups within the mineral lattice (Z. Wang and E. Schauble, 2004; J. M. Eiler, 2007; Ghosh et al., 2006). An initial study by Thiagarajan, Adkins, and J. Eiler (2011) indicated that there were no apparent vital effects for clumped isotopes in corals, but recently this initial result has come into question (Spooner et al., 2016; Saenger et al., 2012). In shallow-water *Porites* corals, Saenger et al. (2012) found that offsets in clumped isotope value from the inorganic calibration line could be explained by incomplete equilibration of the CO_2 and DIC pools within the coral calcifying fluid as a result of rapid calcification. Deep-sea corals grow much slower than shallow-water corals, but a recent detailed study indicated that there are still small species-specific vital effects, with *Balanophyllia*, *Dasmosmilia*, and *Enallopsammia* affected most strongly and *Caryophyllia*, *Javania*, and *Desmophyllum* only minorly affected (Spooner et al., 2016). For the species *Desmophyllum*, used for this study, the vital effect is best described by pH—there are systematic differences in the clumped isotope values of the different dissolved inorganic carbon species (Hill, Tripati, and E. A. Schauble, 2014; Tripati et al., 2015) and corals elevate the pH of their calcifying fluid in order to precipitate carbonate (Venn et al., 2013). If carbon-

ate is precipitated fast enough that the solid is not completely in equilibrium, then clumped isotope values will be offset. While further inquiry into species-specific vital effects in deep-sea corals is warranted, our choice of *Desmophyllum dianthus* corals minimizes the possibility of bias and the mean offset of 0.005‰ is less than our average measurement error (Table 5.1) (Spooner et al., 2016).

In this chapter, we present paired radiocarbon and temperature time series from North Atlantic and Southern Ocean intermediate water derived from measurements of deep-sea corals. In the modern Southern Ocean, temperature and radiocarbon distributions are broadly similar and zonally symmetric (Figure 5.1A) (Key et al., 2004). These horizontal gradients at the surface are transferred into vertical gradients as water subducts along sloping isopycnals in the Southern Ocean. At intermediate water depths north of the Antarctic Circumpolar Current (ACC), this water mass distribution leads to two primary ways of generating signals in temperature and radiocarbon. The first mechanism, which can occur on short (decadal to centennial) timescales, is the movement of fronts at the surface in the Southern Ocean. Temperature and radiocarbon values are aligned with the major Southern Ocean fronts, so even without a change in circulation, frontal movement could change the initial value of water at the ventilation region, which would in turn change the value at depth. The second mechanism, which would tend to occur on longer timescales (centennial to millennial), is cross-isopycnal mixing between water at intermediate depths and deeper water masses, characterized by more depleted radiocarbon values. These mechanisms can be separated by combining temperature and radiocarbon data and visualized on a cross-plot of modern $\Delta^{14}C$ and potential temperature data (Figure 5.1B). Surface data are represented by yellow stars and have a fairly shallow slope in $\Delta^{14}C$ versus temperature space. Variability driven by frontal movement at the surface should follow this shallow slope. Variability that is instead driven by mixing with an older deep water mass, such as Pacific Deep Water (PDW), would follow a much steeper trend. Our sample location is marked by a star and has a modern temperature of ~2.3 °C and a modern $\Delta^{14}C$ value of ~ -150‰ (Figure 5.1).

In the North Atlantic, radiocarbon values are much younger than the Southern Ocean due to the influence of well-ventillated NADW. The influence of young NADW is strongest north of 40°N but persists south of 10°N between ~1000 and 3000 m. This well-ventillated NADW endmember is sandwiched between older AAIW and AABW (Figure 5.2A). In the $\Delta^{14}C$-potential temperature cross plot, there are three endmembers in the deep ocean: NADW, AAIW, and AABW. The Antarctic

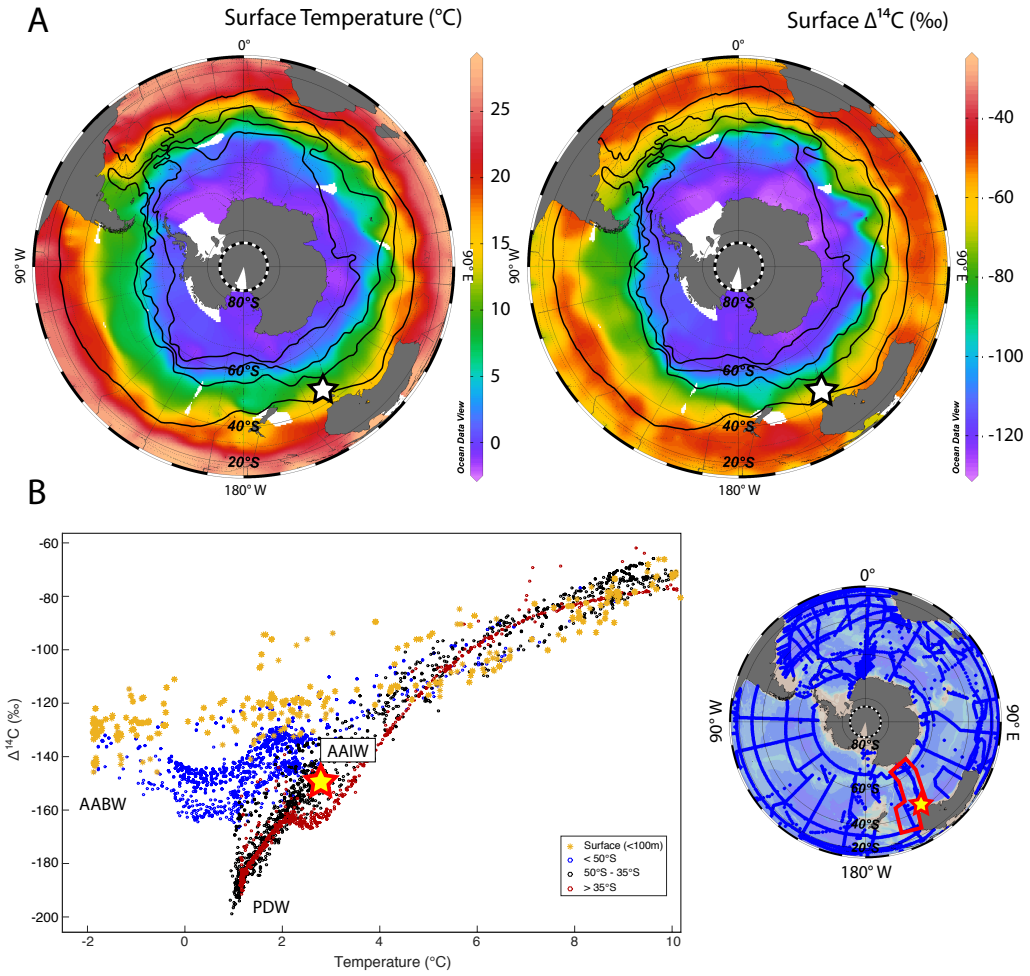

Figure 5.1: Modern hydrography from the Southern Ocean. A) Surface plots of temperature and $\Delta^{14}C$ (NAT14C variable from the GLODAP database) (Key et al., 2004). B) Cross-plot of modern potential temperature and $\Delta^{14}C$ data from section highlighted on map (lower right). Data are segregated by depth and latitude. Sample location is marked with a star.

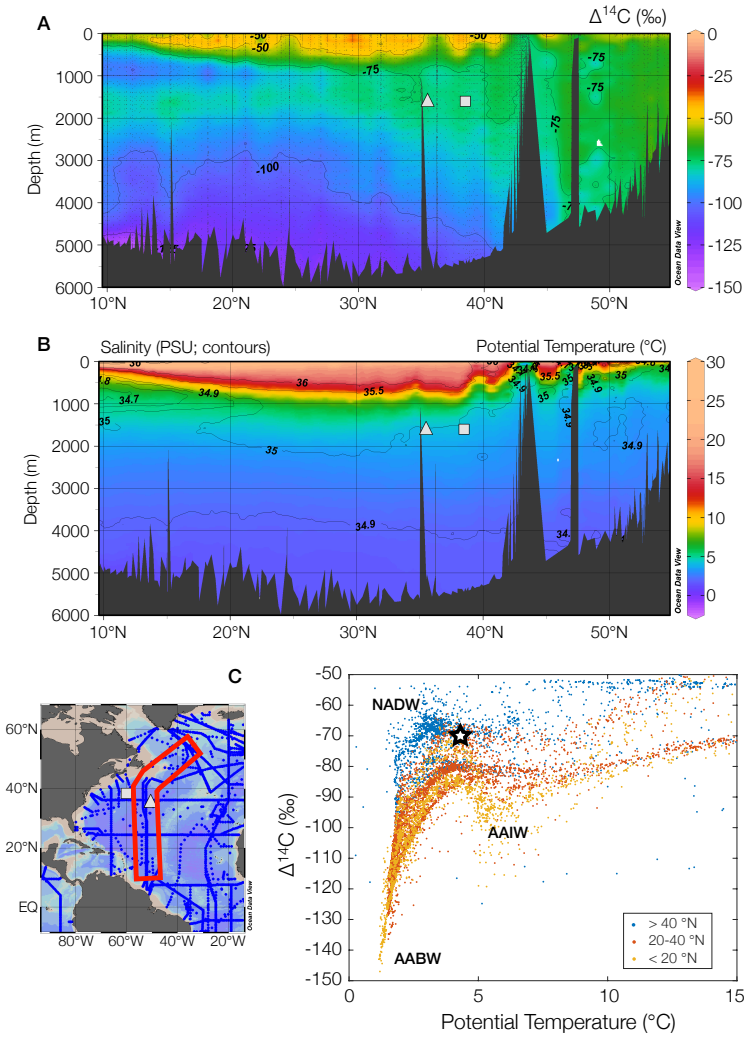

Figure 5.2: Modern hydrography from the North Atlantic. Sections of $\Delta^{14}C$ (NAT14C variable from the GLODAP database) (A) and potential temperature with overlaid salinity contours (B) (Key et al., 2004). Section highlighted on map. C) Cross-plot of data from sections segregated by latitude with water masses highlighted. On sections, the triangle marks location of Corner Rise Seamounts and the square marks location of New England Seamounts.

Intermediate Water endmember is most prominent south of 20°N (Figure 5.2C). Our sample location sits between the NADW and AAIW endmembers with a modern temperature of ~4 °C and a modern $\Delta^{14}C$ value of $\sim -70‰$ (Figure 5.2C).

5.2 Methods

Deep-sea corals used in this study were collected from seamounts south of Tasmania (43°S–47°S 144°E–152°E) during cruise TN-228 in 2008-2009 on the R/V

Thompson using the remotely operated deep submergence vehicle JASON, from the New England Seamounts in the Northwest Atlantic (38°N–39°N 50°W–61°W) during curise AT7-35 in 2003 on the R/V Atlantis using human-occupied deep submergence vehicle ALVIN, and from the Corner Rise Seamounts in the Northwest Atlantic (35°N–36°N 49°W–52°W) during cruise RB05-08 in 2005 on the R/V Ronald H. Brown using the remotely occupied deep submergence vehicle HERCULES. During these cruises around 16,500 deep-sea corals were collected from between 898–2395 m in the Southern Ocean and 1098–2763 m in the North Atlantic. All corals used for the construction of this time series were the scleractinian azooxanthellate *Desmophyllum dianthus*. The Southern Ocean time series presented here encompasses 32 samples from 1440–1900 m with 70% of samples from between 1500 and 1700 m. Three of these corals were sub-sampled for top-bottom ^{14}C and temperature measurements. The North Atlantic radiocarbon time series presented here consists of 38 samples from 1176–1751 m with 75% of samples from between 1494 and 1713 m, and the clumped isotope time series is subset of these samples. It consists of 19 samples from between 1494 and 1751 m.

U/Th and Radiocarbon dating

Previously, these samples had all been age screened at the NOSAMS lab at Woods Hole and the KCCAMS lab at UC Irvine (Hines, Southon, and Adkins, 2015; Thiagarajan, Gerlach, et al., 2013) following the methods of Burke, Laura F. Robinson, et al. (2010) and Bush et al. (2013), respectively. This age screening informed the selection of corals for further U/Th and high-precision radiocarbon dating (Hines, Southon, and Adkins, 2015, and references therein). Uranium and thorium were measured on the Neptune MC-ICPMS at Caltech using established methodologies (Hines, Southon, and Adkins, 2015). High-precision dating was done at the KCCAMS lab at UC Irvine, and background correction for the Southern Ocean samples were made based on replicate samples (n=8) of a "radiocarbon dead" deep-sea coral ($F_m = 0.0034 \pm 0.0007$) with a U/Th age of 205,000±3000 yr (Hines, Southon, and Adkins, 2015). North Atlantic data were measured in two separate blocks and corrected using the same radiocarbon dead coral, based on measurements made during those two measurement periods ($F_m = 0.0040 \pm 0.0013$ and $F_m = 0.0029 \pm 0.0010$, respectively). Combined U/Th ages and radiocarbon dates allow for the reconstruction of water Δ^{14}C:

$$\Delta^{14}C = \left(\frac{e^{-^{14}\text{C age/Libby Mean Life}}}{e^{-\text{U/Th age/True Mean Life}}} - 1 \right) \times 1000\,, \tag{5.1}$$

where the Libby Mean Life is 8033 yr and the True Mean Life is 8266 yr (Stuiver and Polach, 1977). This $\Delta^{14}C$ value corrects for the time elapsed since each coral sample grew, thereby extracting the $\Delta^{14}C$ value of the water it grew in, relying on the assumption that both the carbon isotope system and the U/Th isotope system have remained closed. In order to understand past changes in ocean circulation, it is more useful to compare reconstructed coral $\Delta^{14}C$ to the $\Delta^{14}C$ value of the contemporaneous atmosphere. This is done by converting the coral $\Delta^{14}C$ into epsilon notation:

$$\epsilon^{14}C = \left(\left[\frac{\frac{\Delta^{14}C_{sample}}{1000} + 1}{\frac{\Delta^{14}C_{atm}}{1000} + 1} \right] - 1 \right) \times 1000 \, . \tag{5.2}$$

Epsilon is a more correct measure of past ocean circulation changes than $\Delta\Delta^{14}C$ because it takes into account changes in atmospheric $\Delta^{14}C$ value itself. It is therefore the parameter that stays constant (for sufficiently slow ^{14}C production changes) if ocean circulation does not change.

Clumped Isotope Measurements

Clumped isotope temperatures were measured on a dual-inlet Finnegan MAT-253 IRMS connected to an automated carbonate sample preparation line (Passey et al., 2010; Ghosh et al., 2006). Deep-sea corals were first cut and physically cleaned to remove any ferromanganese crusts, which can skew measurements of the bulk coral (Thiagarajan, Subhas, et al., 2014; Thiagarajan, Adkins, and J. Eiler, 2011). Then samples were powdered for analysis. Approximately 8 mg of powder was used for each measurement. Carbonates were digested in 105% phosphoric acid at 90°C and purified in an automated line. Water was removed by passing gas through an ethanol/dry ice slush and CO_2 was trapped in liquid nitrogen. Other contaminants were removed by passing the CO_2 gas through a Porapak Q 120/80 mesh GC column at -20°C, then the resulting gas was transferred to the mass spectrometer. In the mass spectrometer, beams corresponding to masses 44–49 were simultaneously measured and used to calculate Δ_{47}, Δ_{48}, Δ_{49}, $\delta^{13}C$, and $\delta^{18}O$. R^{47} is defined as the sum of the mass-47 isotopologues ($^{17}O^{13}C^{17}O$ + $^{17}O^{12}C^{18}O$ + $^{16}O^{13}C^{18}O$) divided by the mass-44 isotopologue ($^{16}O^{12}C^{16}O$). Δ_{47} is defined relative to the stochastic distribution of isotopologues for a given isotopic composition:

$$\Delta_{47} = \left(\left[\frac{R^{47}_{\text{measured}}}{R^{47}_{\text{stochastic}}} - 1 \right] - \left[\frac{R^{46}_{\text{measured}}}{R^{46}_{\text{stochastic}}} - 1 \right] - \left[\frac{R^{45}_{\text{measured}}}{R^{45}_{\text{stochastic}}} - 1 \right] \right) \times 1000 \, . \tag{5.3}$$

Measurements at mass 48 were used to monitor for hydrocarbon contamination. Each aliquot of gas was measured for 8 acquisitions, which consisted of 7 cycles of sample-standard comparison with an integration time of 26 seconds.

Raw Δ_{47} values were corrected for nonlinearity and fragmentation within the mass spectrometer, converted into the 'absolute reference frame', and corrected for acid bath digestion temperature (Huntington et al., 2009; Passey et al., 2010; Dennis et al., 2011). Δ_{47} values were converted into temperature using the Ghosh calibration (Ghosh et al., 2006) as derived in the absolute reference frame by Dennis et al. (2011). This calibration was determined to be most appropriate for deep-sea corals by Thiagarajan, Adkins, and J. Eiler (2011), and was further supported by the recent work of Spooner et al. (2016). Typical errors on a single Δ_{47} measurement are ~0.01‰, which corresponds to ~2°C. Each deep-sea coral was measured 4–10 times to increase precision, and replicate measurements were averaged to make a single Δ_{47} value. Error for these averages are reported as the standard error of averaged replicate measurements.

Out of 345 individual measurements on 55 individual samples, 30 measurements were culled and excluded from averages. There are three reasons why measurements were culled: mass-48 excess (3 measurements), proximity to standards with unusually high residuals (25 measurements), and physically impossible temperatures (2 measurements). Mass-48 excess is determined by regressing a line through heated gases for a particular week in δ_{48} versus Δ_{48} space. The deviation of each sample from this '48 line' is measured, and samples with |48 excess| > 1 are flagged. Unusually high standard residuals are defined as standard residuals more than 2σ from zero, or a residual of > ±0.053. Samples that were measured immediately before or after these high-residual standards were culled. In addition to these 28 samples, two samples were marked for physically impossible temperatures. These two samples have uncorrected temperatures of −10.8 and −9.7 °C and corrected temperatures of −6.9 and −3.6 °C respectively, below the freezing point of seawater. Additionally, these samples fall more than 2σ away from the sample mean.

Clumped Isotope Temperature Accuracy

Five carbonate standards with different formation temperatures, TV03, TV04, CIT-Carrara, LB-001, and LB-002, were measured repeatedly with every sample session. CIT-Carrara is a marble with an accepted temperature of 119 °C, TV03 and TV04 are travertines with formation temperatures of 26 and 37 °C respectively (TV04

replaced TV03 when it ran out in December 2015), and LB-001 and LB-002 are deep-sea corals. LB-001 was collected live from south of Tasmania in 2009 and was measured throughout the entire measurement interval. LB-002 was also collected live in 2009 from the same location as LB-001 and was established in January 2017 as a new low-temperature lab standard. Over the course of the entire measurement interval (from April 2014–June 2017), there were temporally coherent shifts in the offset of these carbonate standards from their accepted values (Figure 5.3). Because of this, unknown deep-sea coral Δ_{47} values were corrected for this week-to-week instrument variability using the average offset of consistency standard LB-001 from its accepted value for that week. LB-001 was used to correct unknown deep-sea coral samples because it has a similar Δ_{47} value.

The growth temperature for deep-sea coral consistency standard LB-001 was determined using its known growth location and annual mean temperature for that location from the World Ocean Atlas 2013 1/4° gridded data product (Locarnini et al., 2013). LB-001 is from 2193 m water depth, 44.314 °S 147.447 °E. The nearest interpolated data point reported in the WOA13 is at 2200 m, 44.375 °S 147.625 °E and has a temperature of 2.07 °C. The nearest data point with repeat measurements reported in the WOA13 is at 2200 m, 44.375 °S 146.125 °E and has a temperature of 2.13 ± 0.02 °C for 7 measurements. In an effort not to introduce additional uncertainty due to the gridding algorithm used in the WOA13, we assign the temperature 2.13 °C to this sample. The corresponding Δ_{47} value in the absolute reference frame is 0.835. N.B.: If we choose a temperature of 2.07 °C, the Δ_{47} value in the absolute reference frame is also 0.835.

Deep-sea corals run by N. Thiagarajan (between 2009 and 2012) were also corrected for week-to-week variability using carbonate standards run during the same week, including a modern deep-sea coral 45923 from 1318 m water depth, 7.558 °N 56.417 °W. The nearest interpolated WOA13 grid point to this sample is at 1300 m, 7.625 °N 56.125 °W with a temperature of 4.71 °C, and the nearest grid point with actual measurements is at 1300 m, 7.625 °N 55.625 °W with a temperature of 4.72 °C. Both of these temperatures correspond to a Δ_{47} value of 0.819 in the absolute reference frame. Unfortunately, there was only one week where both modern corals (45923 and LB-001) were measured, because 45923 ran out. For this week, the average measured Δ_{47} value for LB-001 was 0.846 with a standard deviation of 0.005 (1σ, n=5) and the average measured Δ_{47} value for 45923 was 0.809 with a standard deviation of 0.015 (1σ, n=7). The difference between the measured Δ_{47} values,

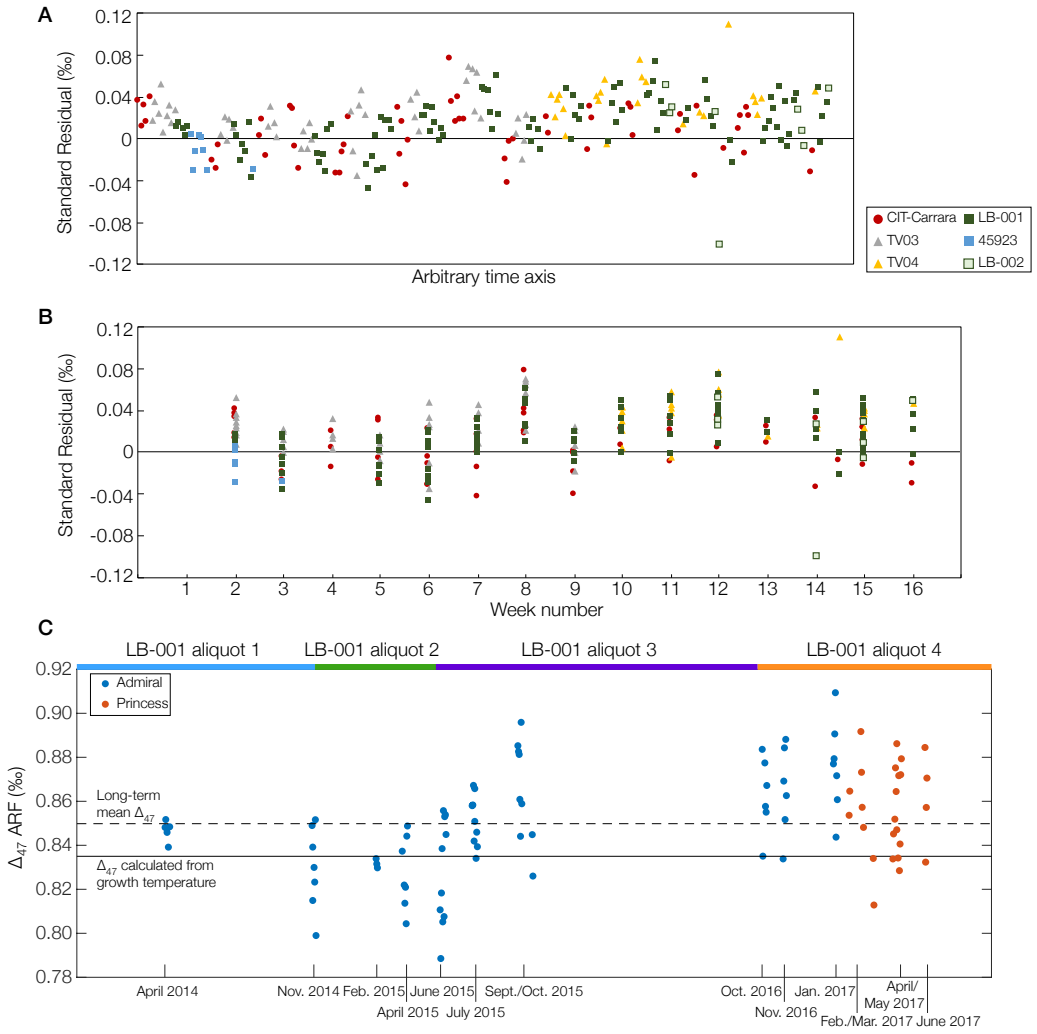

Figure 5.3: Summary of carbonate standard data. A) Plot of standard residuals in the absolute reference frame on an arbitrary time axis, where the standard residual is defined as: measured Δ_{47}−accepted Δ_{47}. B) Same data as in A, but now grouped by measurement week. C) Δ_{47} data for deep-sea coral standard LB-001 versus time, with measurement intervals labeled. Solid horizontal line is the long-term average Δ_{47} value for LB-001, 0.850, and dashed horizontal line is the accepted Δ_{47} from the coral growth temperature. Blue points were measured on the instrument 'Admiral Akbar' and red points were measured on the instrument 'Princess Leia'. Colored bars at the top of the plot indicate four separate aliquots of the coral that were cut and measured—long-term variation in measured Δ_{47} does not correspond to times when new aliquots were taken.

0.038, is more than twice the expected difference based on growth temperature, 0.016. While this Δ_{47} is larger than expected, we cannot rule out the possibility that this result is an analytical artifact.

As an additional accuracy check, we ran a deep-sea coral (sample SH-A008-S5) that was collected live from the same location as LB-001. It's standard-corrected average Δ_{47} value, 0.848±0.018, overlaps with the average Δ_{47} values of LB-001, 0.863±0.009, for weeks that they were run together within 2σ SE (and is barely outside 1σ SE).

Converting samples to the clumped isotope absolute reference frame requires both 'heated gases' (1000 °C) and 'equilibrated gases' (25 °C) (Dennis et al., 2011). Since the absolute reference frame was developed after N. Thiagarajan ran her deep-sea coral samples, we must resort to secondary method of retroactively transferring her values into the absolute reference frame using carbonate standards in order to compare our two deep-sea coral datasets. Because different carbonate standards were measured during different measurement sessions, we have decided to transfer averaged temperatures for each deep-sea coral from the Caltech reference frame (CRF) into the absolute reference frame (ARF) (Figure 5.4). The secondary transfer function was made using three materials: heated gas, carbonate standard NBS 19, and deep-sea coral standard 45923. Accepted ARF values for heated gases and these carbonate standards are from Dennis et al. (2011) (N.B. the corrected acid digestion fractionation was not used in the Dennis et al. (2011) paper, so 0.011 was added to the published Δ_{47} values for the carbonate standards to account for this error).

5.3 Results

Clumped isotope temperatures

Deep-sea coral samples were measured between 4 and 9 times each. Temperature errors ranged from 0.5 to 2.6 °C (1 SE), with an average value of 1.2 °C (Table 5.1). All three Southern Ocean corals that were sub-sampled for top-bottom temperature measurements differed outside of error. In addition to the 32 Southern Ocean and 19 North Atlantic fossil deep-sea corals, one additional Southern Ocean coral that had been collected alive was measured. It was collected from the same location as deep-sea coral standard LB-001. Replicate measurements of this sample, SH-A008-S5, have a mean that overlaps with replicate measurements of LB-001 for the weeks that they were measured together within 2σ SE.

North Atlantic and Southern Ocean clumped isotope temperature records are shown

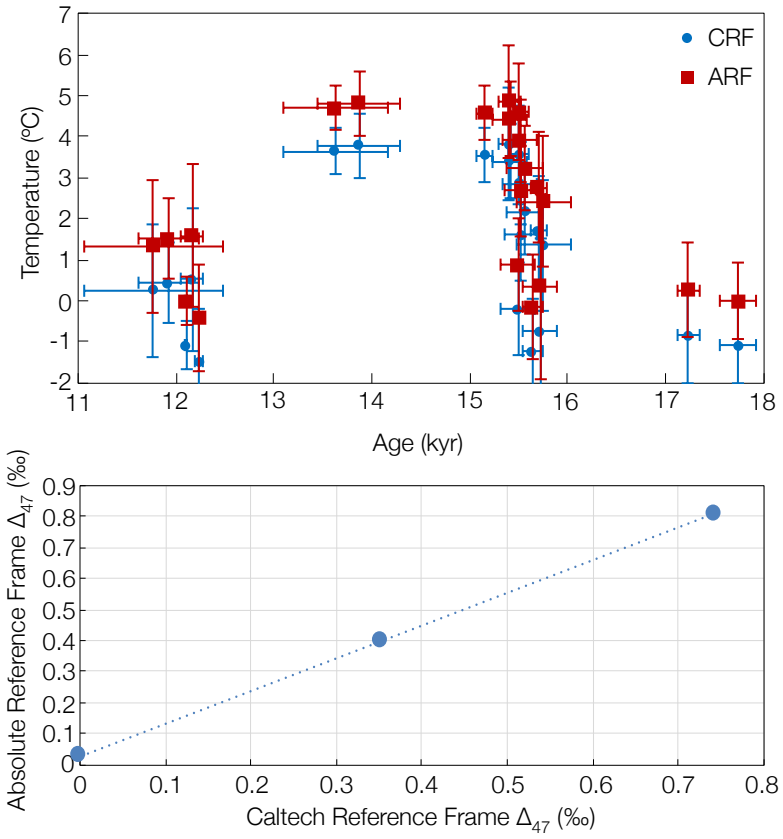

Figure 5.4: Transferring deep-sea corals run by N. Thiagarajan into the ARF. Secondary transfer function and deep-sea coral temperatures converted into the absolute reference frame.

in Figure 5.5. In the North Atlantic, there is some temperature variability early in the record, between 29 and 31 ka, with one extremely warm sample at 30 ka. Then, after a slight rise in temperature between 28 and 25 ka, there is a drop in temperature during Heinrich Stadial 2 (~24–27 ka). In Southern Ocean, there is also a drop in temperature during Heinrich Stadial 2, although it is not as large or abrupt. There is a large gap in the North Atlantic record during the LGM, between 17.6 and 23.3 ka. During the LGM, Southern Ocean temperatures rise, peaking at ~19 ka, then drop with some variability through ~17 ka. North Atlantic temperatures mirror this drop and then both records rise through the middle of Heinrich Stadial 1, with some variability. During the Antarctic Cold Reversal (ACR, ~13–14.7 ka) Southern Ocean temperatures show a high degree of variability on short timescales, reaching both the coldest and nearly the warmest temperatures observed in the whole Southern Ocean record.

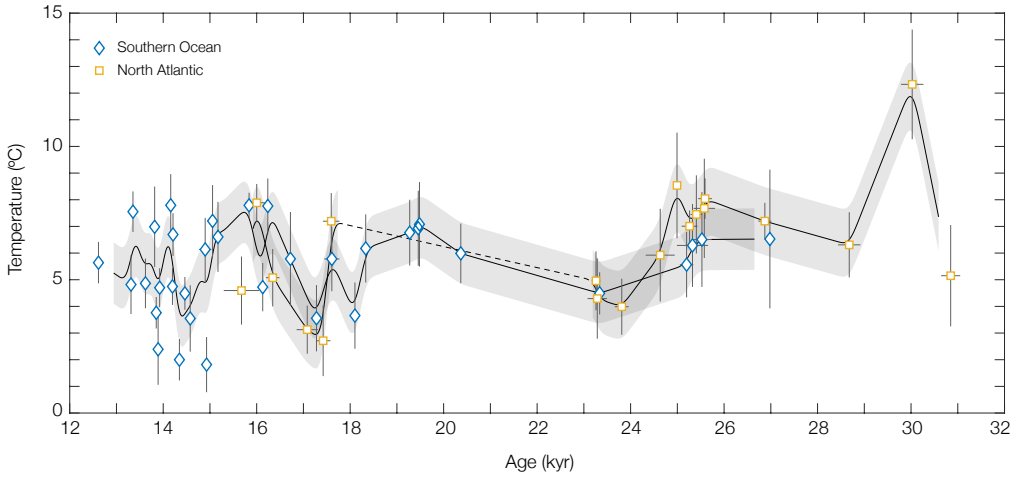

Figure 5.5: Clumped isotope temperature records for the North Atlantic and Southern Ocean. In order to better visualize long-term trends in the data, North Atlantic and Southern Ocean records were interpolated at 10-year resolution and smoothed using a 500-year Gaussian filter. Error envelope is average 1SE temperature error for North Atlantic and Southern Ocean (1.3 and 1.1 °C respectively).

North Atlantic U/Th and radiocarbon dates

In addition to the 44 Southern Ocean corals previously radiocarbon dated, including 8 that were subsampled (see Chapter 3), an additional 52 North Atlantic corals were U/Th dated (Table 5.2), and 38 of these samples were also radiocarbon dated (Table 5.3). U/Th dates were assessed based on two criteria: ^{232}Th concentration, which increases age error due to uncertainty in the initial ^{230}Th/^{232}Th ratio, and the initial δ^{234}U value (where $\delta^{234}U_i = \delta^{234}U_{meas}e^{\lambda t}$), which should be within error of the marine δ^{234}U value and assesses whether or not the sample has behaved like a closed system. We impose a ^{232}Th concentration cutoff value of 2000 ppt and assign a range of acceptable $\delta^{234}U_i$ values following IntCal09 (Reimer, Baillie, et al., 2009): 147 ± 7‰ for samples younger than 17 ka and 141.7 ± 7.8‰ for samples older than 17 ka. A much higher fraction of North Atlantic U/Th dates had high ^{232}Th compared to the Southern Ocean. 22 of the 52 North Atlantic samples had ^{232}Th concentrations higher than the cutoff value of 2000 ppt (compared to 14 out of 103 for the Southern Ocean). One North Atlantic sample even had a staggering 466, 000 ± 2000 ppt ^{232}Th. Two samples failed the $\delta^{234}U_i$ criterion, and three additional samples failed both criteria.

In general, we aimed to radiocarbon date samples that passed both age criteria, however due to the large number of samples that failed these criteria, we radiocarbon

dated 11 samples that failed the ^{232}Th criterion, one sample that failed the $\delta^{234}U_i$ criterion, and one sample that failed both. Of the samples that failed the ^{232}Th criterion, all but three had < 3000 ppt ^{232}Th (the other three had 5070, 3150, and 3100 ppt). Of the samples that failed the $\delta^{234}U_i$ criterion, one missed by 0.16‰ and the other missed by 3.14‰. Average relative radiocarbon age errors were 4.1‰ for samples younger than 15,000 ^{14}C-years, 4.7‰ for samples between 15,000–20,000 ^{14}C-years, 7.4‰ for samples between 20,000–25,000 ^{14}C-years, and 11.2‰ for samples older than 25,000 ^{14}C-years.

North Atlantic Δ^{14}C values are generally in agreement with Southern Ocean Δ^{14}C values (Figure 5.6). In the early part of the record, before the start of the LGM (at ~22 ka), there is a large amount of variability in Δ^{14}C value, and samples fall fairly close to the atmosphere, with two Southern Ocean samples and one North Atlantic sample lying above the IntCal13 atmospheric Δ^{14}C curve. There is a 5,600-year gap in the North Atlantic record during the LGM between 17.6 and 23.2 ka. During this time period, the Southern Ocean data generally parallel the atmosphere with one abrupt jump at ~19 ka. Starting at 17.6 ka, there is a well-resolved drop in North Atlantic Δ^{14}C of ~160‰ over 1600 years. There is also a drop in Southern Ocean Δ^{14}C between 15.8 and 16.7 ka, but it is shallower in slope. There are 43 Southern Ocean Δ^{14}C points younger than 15.1 ka and they show a great deal of short-timescale variability, particularly during the Antarctic Cold Reversal. There are only 5 North Atlantic samples younger than 16 ka, and they generally agree with the Southern Ocean data, except one sample at 14.4 ka that is very close to the atmosphere (ϵ^{14}C = −28‰).

Radiocarbon and temperature cross-plots

Compiled North Atlantic and Southern Ocean radiocarbon (converted into ϵ^{14}C) and potential temperature records are shown in Figure 5.7 and cross-plots of radiocarbon and potential temperature are show in Figure 5.8 with modern data in the background and the modern sample location marked. In both the North Atlantic and Southern Ocean, fossil corals fall far outside the range of modern data. For the Southern Ocean, LGM and HS1 samples (see figure caption for age ranges) are warmer and older than the modern and ACR and pre-LGM samples are younger and slightly colder. For the North Atlantic, there is a wide range of temperature and radiocarbon for all the data and samples tend to be much older than the modern. Unlike the Southern Ocean, pre-LGM and HS1 samples are interspersed in the North Atlantic, but there is a larger range of radiocarbon for the pre-LGM samples.

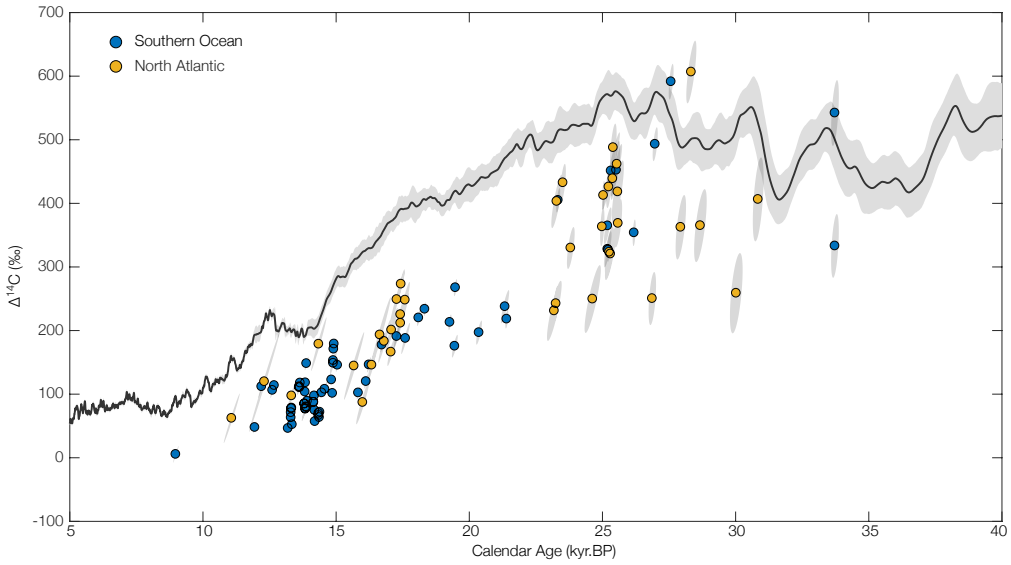

Figure 5.6: Δ^{14}C records from the North Atlantic and Southern Ocean. Coral Δ^{14}C values are plotted with 1σ error ellipses that take into account correlated U/Th age and ^{14}C date error. IntCal13 atmospheric Δ^{14}C record is also plotted for reference (Reimer, Bard, et al., 2013).

5.4 Discussion

To explore what can be learned about glacial ocean circulation from paired temperature and radiocarbon datasets in the North Atlantic and Southern Ocean we first look at a compilation of North Atlantic temperature and radiocarbon data spanning the late part of the last glacial period (from ~30–10 ka). We can try and interpret these data in the context of other key deglacial climate records (Figure 5.9). We then use insight gained from our dynamical box model (Chapter 4) to predict how changes in the North Atlantic would influence the temperature and radiocarbon distribution in the Southern Ocean across this same time period, and test these predictions against compiled radiocarbon and temperature data from the Southern Ocean.

North Atlantic radiocarbon and temperature

Before the start of the Last Glacial Maximum, there is a lot of short-timescale variability in radiocarbon and temperature (Figure 5.10). This time period, from ~35–22 ka, was punctuated by two Heinrich Events at 24 and 31 ka (Bond et al., 1993; Hemming, 2004). Accompanying these Heinrich Events were periods of reduced NADW formation, as indicated by Pa/Th from the Bermuda Rise (see Figure 5.9) (Lippold et al., 2009). NADW supplies the deep North Atlantic with a large volume of well-ventilated water rich in radiocarbon, and therefore when

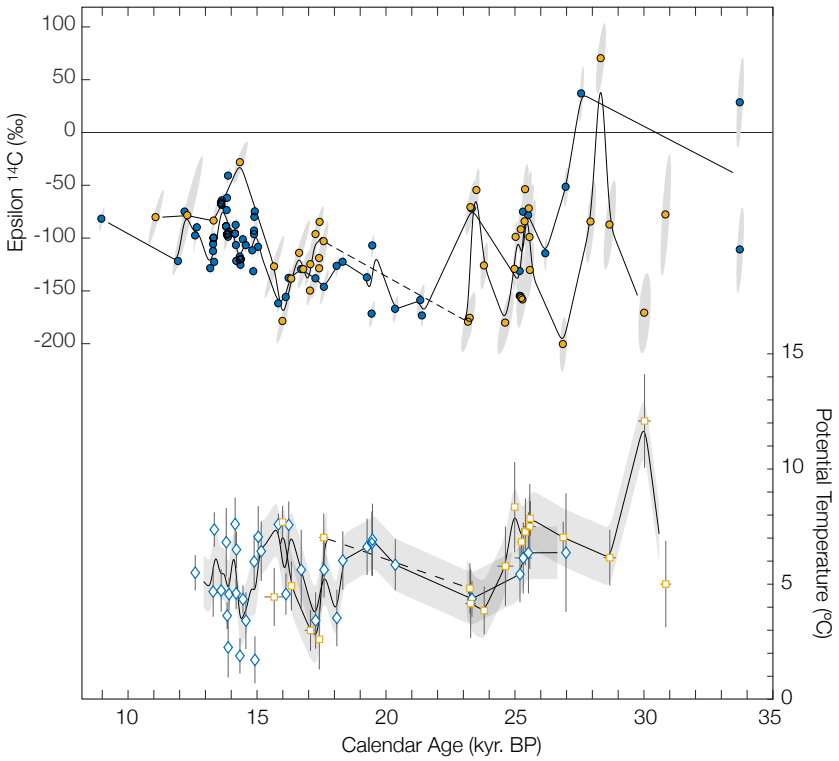

Figure 5.7: Deep-sea coral radiocarbon and temperature records from the North Atlantic (yellow) and Southern Ocean (blue). $\Delta^{14}C$ converted into $\epsilon^{14}C$ using the IntCal13 atmospheric radiocarbon curve (Reimer, Bard, et al., 2013). Temperature converted into potential temperature using each coral's collection depth and latitude.

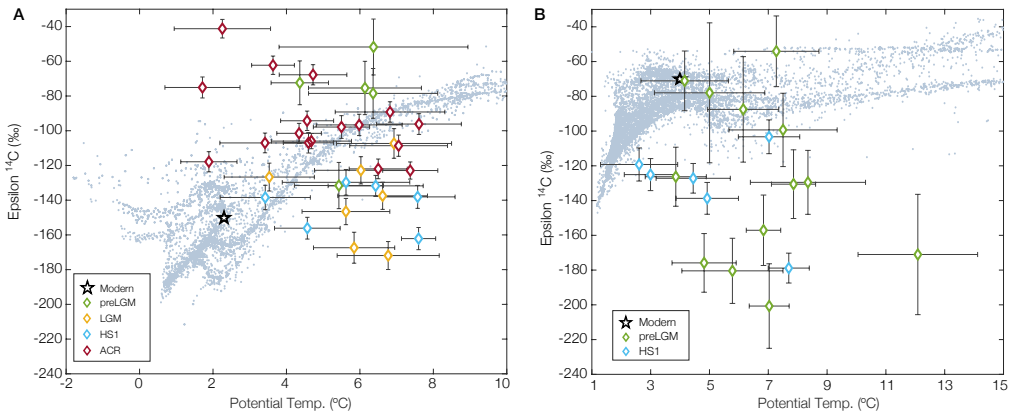

Figure 5.8: Cross-plots of Southern Ocean (A) and North Atlantic (B) radiocarbon and temperature data. Radiocarbon data are converted into $\epsilon^{14}C$ and temperatures are converted into potential temperature. Time periods are: 'pre-LGM' (>22 ka), 'LGM' (17.5–22 ka), 'HS1' (15.1–17.6 ka), and 'ACR' (<15.1 ka). Modern potential temperature and radiocarbon ('NAT14C') data from the GLODAP database are plotted in the background (Key et al., 2004). Modern value is marked with a black star.

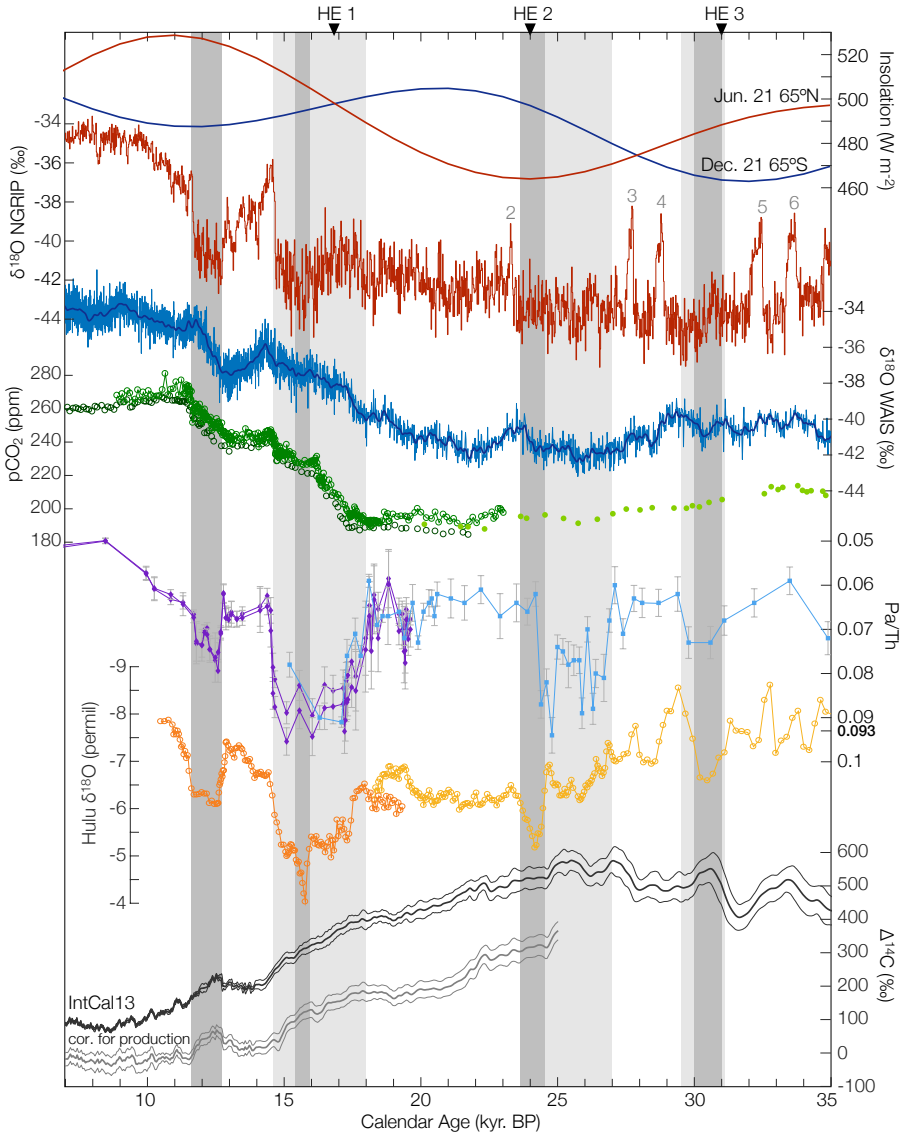

Figure 5.9: Compiled climate records spanning the late glacial. From top: High-latitude insolation curves (Huybers and Eisenman, 2006), North GRIP δ^{18}O on the GICC05 chronology (Rasmussen et al., 2014; Andersen et al., 2004), WAIS δ^{18}O on the WD2014 chronology (WAIS Divide Project Members, 2013; Buizert et al., 2015), atmospheric pCO_2 from WAIS (open circles and line) (Marcott, Bauska, et al., 2014), EDC (circles) (Monnin et al., 2001; Lemieux-Dudon et al., 2010), and Taylor Dome (filled circles) (Indermühle et al., 2000), Pa/Th from the Bermuda rise (purple diamonds) (McManus et al., 2004) and ODP 1063 (blue squares) (Lippold et al., 2009), Hulu cave δ^{18}O from stalagmites PD (orange) and MSD (yellow) (Y. J. Wang et al., 2001), atmospheric Δ^{14}C from IntCal13 (Reimer, Bard, et al., 2013), and the atmospheric Δ^{14}C record corrected for production (Hain, Sigman, and Haug, 2014). Light grey bars mark times of decreased NADW flux according to Pa/Th, dark grey bars mark weak monsoon intervals, and dates of Heinrich events are marked by triangles at the top of the figure (Hemming, 2004).

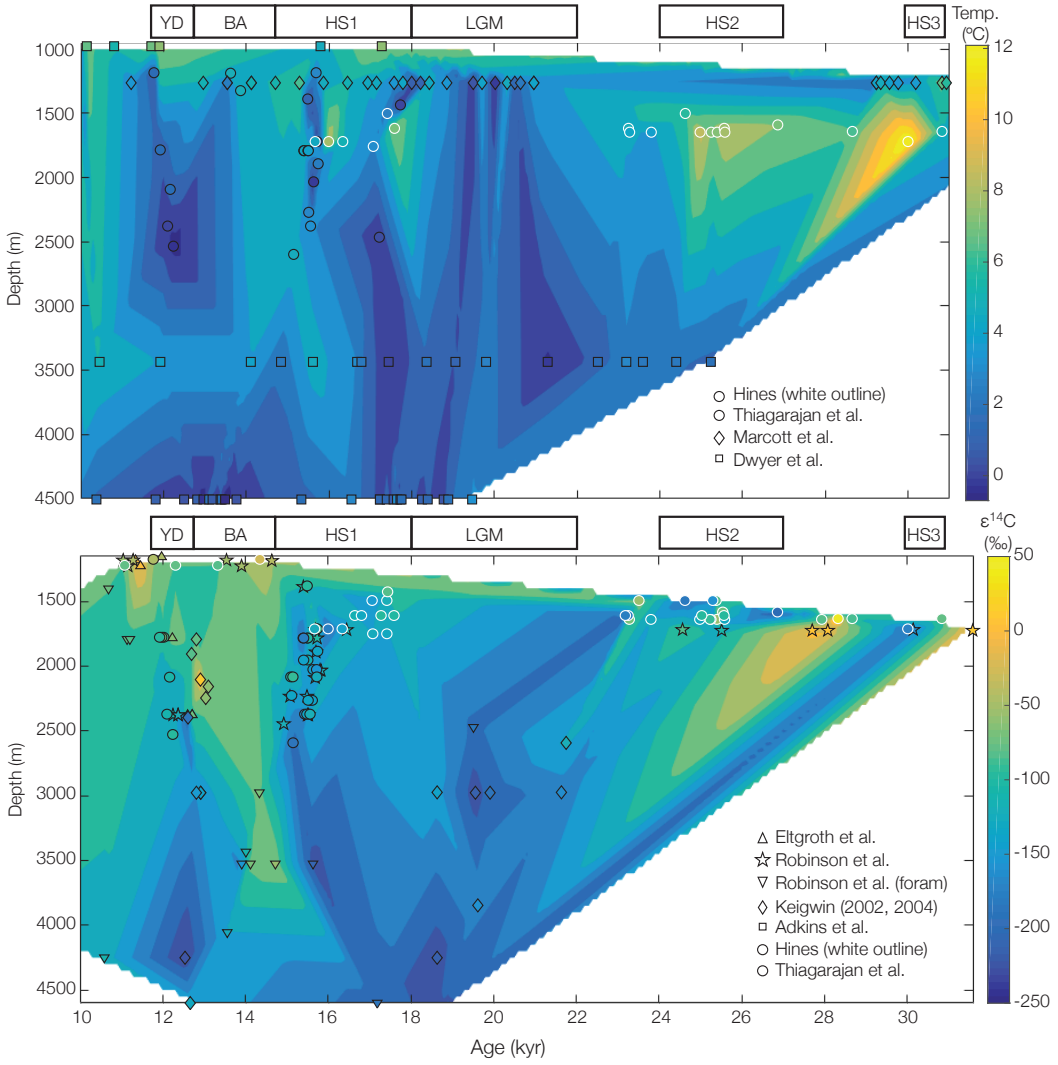

Figure 5.10: Contour plots of temperature (top) and radiocarbon (bottom) from the western North Atlantic. Compiled temperature records are based on deep-sea coral clumped isotope measurements (Thiagarajan, Subhas, et al., 2014, and this study) and benthic foram (Marcott, Clark, et al., 2011) and ostracode (Dwyer et al., 2000) Mg/Ca measurements. Deep-sea coral (Eltgroth et al., 2006; Laura F. Robinson et al., 2005; Adkins, Cheng, et al., 1998; Thiagarajan, Subhas, et al., 2014, and this study) and benthic foram (Laura F. Robinson et al., 2005; Keigwin and Schlegel, 2002; Keigwin, 2004) $\Delta^{14}C$ values were converted into $\epsilon^{14}C$ using the IntCal13 atmospheric radiocarbon curve (Reimer, Bard, et al., 2013).

this supply is reduced deep and intermediate waters in the North Atlantic become radiocarbon depleted.

It is imperative to note, however, that changes in the supply of radiocarbon to the deep ocean are very different from changes in the reservoir of radiocarbon.

Because of its long half-life, radiocarbon as a tracer has a long memory of past circulation regimes. As a result, the only way to record abrupt shifts in ϵ^{14}C in paleoceanographic archives, such as a deep-sea coral, is to have radiocarbon fronts in the water column that move and pass by the coral. From our modeling work in Chapter 4, we have shown that changes in NADW flux can cause abrupt shifts in basin isopycnal structure due to mass convergence. Therefore, these abrupt changes in ϵ^{14}C were likely driven by radiocarbon fronts passing by the deep-sea coral sites as a result of changes in NADW production. In turn, these changes in NADW production also help sustain ϵ^{14}C gradients by variably supplying radiocarbon to deep water.

Intermediate water temperature is also quite variable during this time period, and generally of opposite phase, although the temperature resolution is lower than the radiocarbon resolution (Figure 5.10). As several authors have pointed out, decreases in NADW production should be associated with increases in temperature at intermediate depths (Marcott, Clark, et al., 2011; Liu et al., 2009; Shaffer, Olsen, and Bjerrum, 2004). In the absence of a supply of cold surface water via NADW production at high latitude, intermediate water warms by downward diffusion of heat from the thermocline. In the North Atlantic cross-plot, this is clearly visible as a warm, radiocarbon-depleted endmember (Figure 5.8 B).

This association of warm and radiocarbon-depleted water breaks down during the late part of Heinrich Stadial 2 (starting at ~25.6 ka), as the warm radiocarbon-depleted endmember becomes colder but equally radiocarbon-depleted. Heinrich Stadial 2 is different from other Heinrich Stadials because it marks the transition into the peak glacial. Northern Hemisphere insolation, which strongly impacts ice sheet growth, declines during Heinrich Stadial 2, reaching a minimum at ~24 ka, and contributing to the final build-up of ice at the LGM (Figure 5.9). Low-latitude Northern Hemisphere insolation also declines during this time interval, potentially affecting heat uptake by intermediate water and contributing to the observed decrease in intermediate water temperature.

During the LGM, there is a gap in all measured deep-sea coral records, but a few points exist from other records. It is generally thought that LGM circulation was 'two-cell', with southern-source water occupying the ocean deeper than ~2000 m (Curry and Oppo, 2005; Ferrari et al., 2014). From the sparse data in Figure 5.10, there appears to be some temperature stratification during this time period and radiocarbon-depleted water at around 3000 m. It is not necessarily surprising,

however, that thermal stratification during the LGM is weak—pore water-based reconstructions of LGM temperature and salinity indicate that deep water was near the freezing point and salinity-stratified, rather than temperature stratified (Adkins, 2002). Some authors have suggested that this shift from temperature stratification to salinity stratification occurred much earlier, when Northern Hemisphere SSTs dropped at the MIS 5–4 transition (80–65 ka) via the mechanism proposed by Miller et al. (2012) (Kohfeld and Chase, 2017). Another consequence of salinity stratification during Stage 2 is that it permits a larger range of deep and intermediate water temperatures while still remaining stably stratified.

After the LGM, during Heinrich Stadial 1, there is still stratification in the water column, with younger warmer water shallower than ~2000 m and colder older water below (Figure 5.10). This is consistent with the persistence of a 'two-cell' circulation structure, and it is in line with the radiocarbon compilation of Laura F. Robinson et al. (2005). There is some-short timescale variability in intermediate water radiocarbon, however the magnitude of the variability is much smaller than during the pre-LGM interval. Between ~17.5–16 ka, there is a drop in ϵ^{14}C, coupled with a rise in temperature. This rise in temperature is matched by a gradual temperature rise observed in the southeast Labrador Sea at 1251 m (Marcott, Clark, et al., 2011) and the abrupt temperature rise and radiocarbon depletion observed at the New England and Corner Rise seamounts (Thiagarajan, Subhas, et al., 2014). These observations are consistent with the accumulation of heat at intermediate depths due to a reduced supply of cold NADW. As hypothesized by Thiagarajan, Subhas, et al. (2014), this heat build-up at depth stores potential energy that can be released catastrophically due to the thermobaric properties of seawater (Adkins, Andrew P Ingersoll, and Pasquero, 2005; Su, Andrew P. Ingersoll, and He, 2016).

At the start of the Bølling, reinvigorated NADW formation ventilates North Atlantic water down to ~3500 m (Figure 5.10 and 5.9). Younger ϵ^{14}C values are accompanied by warm temperatures down to a similar depth. This deep penetration of young, relatively warm NADW suggests that circulation may have transitioned from the 'two-cell' LGM configuration to a more modern-like 'figure-eight' configuration. At intermediate depths it is difficult to specifically say more about changes in circulation during this time period because there are relatively few samples.

During the Younger Dryas, following the Bølling-Allerød, there is a slight depletion in ϵ^{14}C at depth, but much of the water column above ~2500 m remains seemingly well-ventilated. However, the temperature contour plot tells a different story, with

much colder water between 2000–2500 m (Figure 5.10). This is evidence that during this time period, the long memory of radiocarbon may be obscuring the true history of ventilation.

Southern Ocean radiocarbon and temperature

Based on the compiled North Atlantic temperature and radiocarbon records, we can use intuition gained from our dynamical box model (Chapter 4) to make predictions about what should happen in the Southern Ocean, and then check these predictions against compiled temperature and radiocarbon records from the Southern Ocean. The schematic in Figure 5.11 summarizes the progression of circulation changes detailed in the previous section. The main interhemispheric mechanism from the model is: reinvigorated NADW formation, during a Northern Hemisphere 'interstadial', converges mass at depth and rapidly shoals isopycnals in the basin. This, in turn, adjusts the outcrop positions of these isopycnals in the channel to the north. As outcropping isopycnals in the Southern Ocean move to the north, cold, deep density classes occupy a larger area of the surface, which drives cooling in the south. During a Northern Hemisphere 'stadial', reduced NADW formation converges mass in the upper layers of the ocean and deepens stratification in the basin. This causes isopycnals to outcrop further to the south, and allows warmer, shallower density classes to occupy a larger area of the Southern Ocean, driving warming in the south. By the classic bipolar seesaw mechanism, times of enhanced (reduced) North Atlantic Deep Water formation should be accompanied by reduced (enhanced) Antarctic Bottom Water formation. Our bipolar seesaw mechanism, on the other hand, does not require the amount of deep water formed in the south to be so closely tied to the amount of deep water formed in the North. This permits there to be a disconnect between the surface expression of the bipolar seesaw (which is also recorded in ice cores) and subsurface changes associated with these circulation shifts.

While our time-dependent dynamical box model can be helpful for gaining insight into circulation configuration across the late glacial period and connecting observations in the North Atlantic and Southern Ocean, there are a few key ways in which the model does not accurately represent the ocean. These differences may lead to discrepancies between what the model predicts for the Southern Ocean given some change in the North Atlantic, and what actually occurs. Most importantly, the model is primarily forced in the North—the flux of NADW and the density of NADW are prescribed and drive the response of the model in many ways. In the Southern Ocean, the buoyancy distribution is fixed and cannot dynamically respond

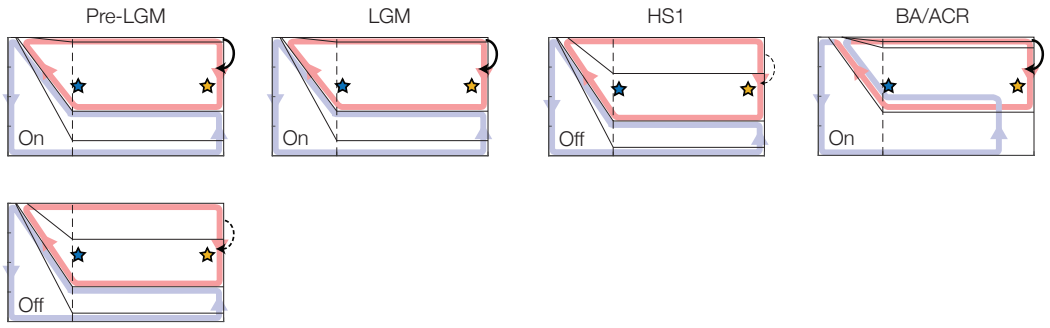

Figure 5.11: Schematic of circulation changes across the late glacial. North and south deep-sea coral approximate sample locations marked with stars.

to changes in NADW. In the real ocean, changes in the outcrop position of isopycnals in the Southern Ocean, driven by changes in NADW flux and/or density, should affect the sea ice position and therefore the surface buoyancy distribution, and changes in the Southern Hemisphere can lead to changes in the strength or relative density of NADW. Additionally, the model does not have any atmospheric component, so changes in insolation or atmospheric CO_2 are not taken into account.

During the pre-LGM time period, there are many similarities between the Northern and Southern Hemisphere records (Figures 5.10 and 5.12). Since there are no deep North Atlantic samples during this time period, we can only directly compare the intermediate-depth deep-sea corals. These samples are at roughly the same depth, so they should therefore be in approximately the same isopycnal class. Since circulation is still in its 'two-cell' configuration, there are no major basin asymmetries that would cause samples in the Indo-Pacific to behave differently than North Atlantic samples in the same layer. Despite this, even by our dynamical box model mechanism, we expect anti-phase behavior between the hemispheres in temperature and radiocarbon. Interestingly, North Atlantic and Southern Ocean samples instead show similar patterns of variability in $\epsilon^{14}C$ and temperature. This suggests, surprisingly, that Southern Ocean intermediate water is more sensitive to changes in Northern Hemisphere insolation and the supply of freshly-ventilated NADW than shifts in the distribution of radiocarbon and temperature at the surface in the south.

During the LGM, there is a clear and persistent radiocarbon minimum at ~3500 m. This radiocarbon bulge has been noted before as additional evidence for a 'two-cell' circulation configuration. In a 'two-cell' circulation configuration with enhanced mid-depth stratification, oldest water should be in the upper return limb of the lower cell, not at the bottom of the ocean (Burke, Stewart, et al., 2015).

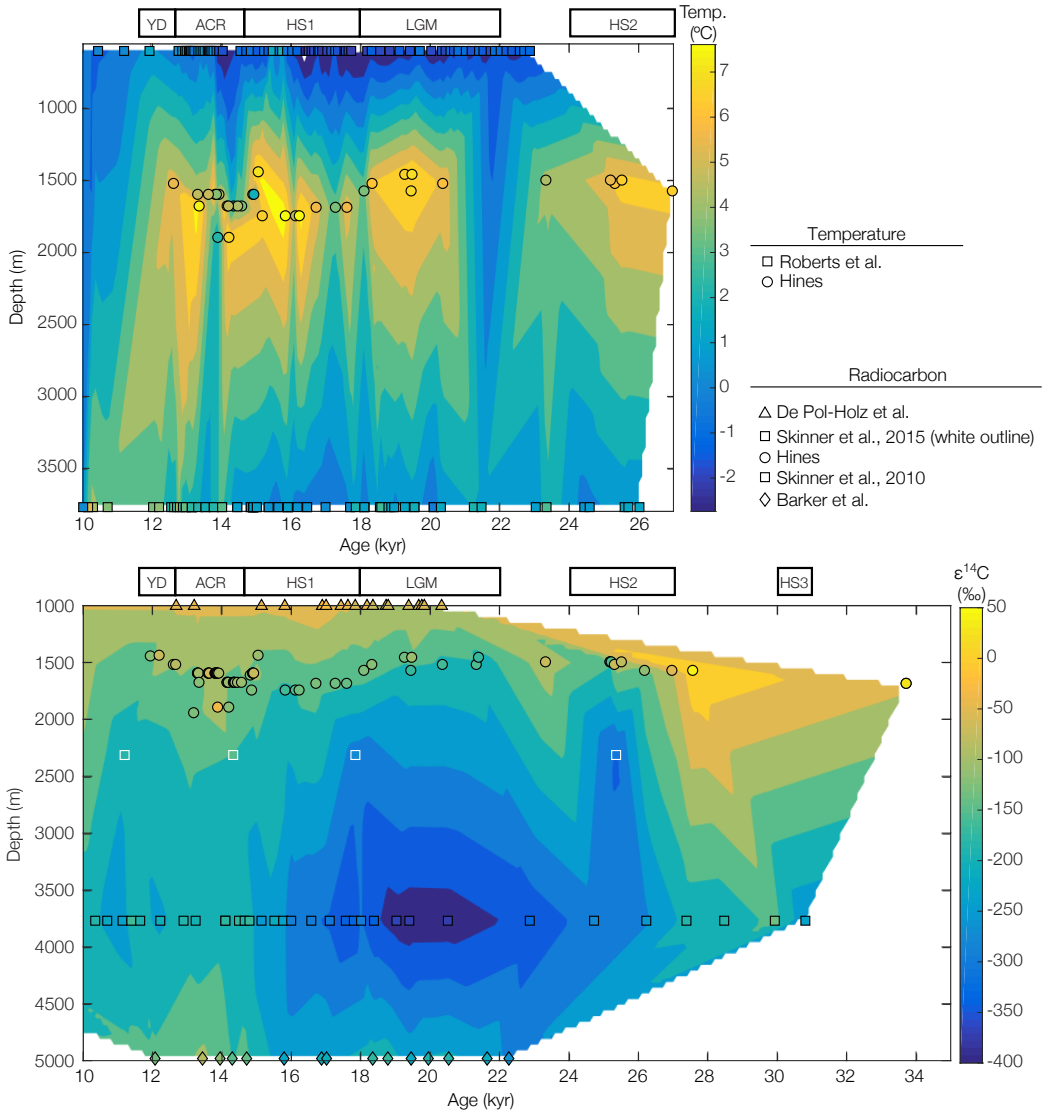

Figure 5.12: Contour plots of temperature (top) and radiocarbon (bottom) from the Southern Ocean. Temperature records based on Mg/Ca measurements on benthic foraminifera (Roberts et al., 2016) and clumped isotope measurements on deep-sea corals (this study). Radiocarbon measurements from benthic foraminifera (De Pol-Holz et al., 2010; L. Skinner et al., 2015; L. C. Skinner et al., 2010; Barker, Knorr, et al., 2010) and deep-sea corals (Hines, Southon, and Adkins, 2015). $\Delta^{14}C$ values were converted into $\epsilon^{14}C$ using the IntCal13 atmospheric radiocarbon curve (Reimer, Bard, et al., 2013).

Intermediate water deep-sea coral samples have roughly the same $\epsilon^{14}C$ value as modern water at this site—evidence that they are in the upper circulation cell and therefore shielded from the old deep water below. Unlike radiocarbon, which remains largely constant, Southern Ocean deep-sea coral temperatures rise during the later part of the LGM. Interestingly, while Northern Hemisphere insolation is low during this time period, this Southern Ocean temperature rise just lags the maximum in high-latitude Southern Hemisphere summer insolation. These observations, taken with data from the pre-LGM interval, indicate that while the Southern Ocean fossil corals are more sensitive to changes in the north during the pre-LGM transient state, they are sensitive to local changes during the LGM quasi-steady-state.

After the LGM, NADW formation slows during Heinrich Stadial 1 (Figure 5.9) (McManus et al., 2004). According to our dynamical model mechanism, this would cause a deepening of basin stratification, due to mass convergence in the upper ocean, and a southward shift in Southern Ocean isopycnals. Consequently, the lower cell should speed up due to the inverse relationship between layer thickness and diffusive transport. This fits nicely with the Southern Ocean radiocarbon data—we see a decrease in $\epsilon^{14}C$ at depth (i.e. in the lower cell) indicating that as the lower cell spins up, old carbon is being released into the atmosphere (Figure 5.12). This also fits nicely with atmospheric $\Delta^{14}C$ and CO_2 records, which show a decrease in atmospheric radiocarbon and an increase in atmospheric CO_2 (Figure 5.9).

At intermediate depth, we see a pronounced warming starting at ~17.3 ka, just before the Heinrich Event at 16.8 ka (Hemming, 2004). This warming trend is also seen at intermediate depth in the North and Equatorial Atlantic (Marcott, Clark, et al., 2011; Weldeab et al., 2016; Thiagarajan, Subhas, et al., 2014). While commonly attributed to downward heat diffusion from low latitudes, this Southern Hemisphere warming could also be the result of local insolation (which is high in the south during the LGM, see Figure 5.9). Our dynamical box model mechanism would also predict a shift toward warmer temperatures, since deepened stratification leads to a southward shift in Southern Ocean isopycnals, which would bring warmer water to the intermediate water source region.

During the ACR (contemporaneous with the Bølling-Allerød in the Northern Hemisphere), reinvigorated NADW formation should shoal basin stratification, leading to cooler temperatures in the south. Deep penetration of well ventilated water in the North Atlantic also indicates that Bølling-Allerød/ACR circulation is more 'figure-eight'-like. Indeed, we see colder temperatures throughout the water column

during the ACR than earlier in Heinrich Stadial 1, with more pronounced cooling at shallower depths. For our intermediate water deep-sea corals, there is also a lot of high-frequency variability in temperature.

On first pass, there are many similarities between the deep-sea coral radiocarbon and temperature records. This supports the frontal movement mechanism, which operates on short timescales and should drive positively correlated changes in radiocarbon and temperature (Figure 5.1). Upon closer inspection, however, there are a few notable and problematic differences between the records (Figure 5.13A). The most obvious being the difference in the direction of change for two of the three top-bottom corals that were sampled. Indeed, a cross plot of the data ordered by age shows a negative correlation between radiocarbon and temperature for most of this time period (Figure 5.13B).

One way we can explore how this apparent negative correlation between radiocarbon and temperature may have arisen is by attempting to reconstruct the depth-latitude section of radiocarbon during the ACR, focused on intermediate water depths. We do this using our radiocarbon data from south of Tasmania and data from the Drake Passage (Figure 5.14) (Burke and L F Robinson, 2012; Chen et al., 2015). Looking at the time series of these data, there is a surprising arrangement of water masses during the ACR compared to the times before and after—Drake Passage AAIW is ~50‰ older than contemporaneous Tasmanian water and seemingly older than Drake Passage UCDW (although there is a gap in the UCDW record, Figure 5.14A). Throughout the rest of the record, Tasmanian samples lie between Drake Passage UCDW and AAIW, with AAIW being the youngest.

In the depth-latitude section, there is an inversion in radiocarbon with the oldest values near the surface and younger values at depth. One way this arrangement of water could be achieved is if sea ice extended past the source water region for the Drake Passage AAIW samples and effectively capped the water from exchanging with the atmosphere. Both data (Gersonde et al., 2005) and climate models (Roche, Crosta, and Renssen, 2012) predict much more extensive sea ice during the LGM compared to the modern. There has been no comprehensive evaluation of how sea ice extent at the ACR compared to the LGM, but a maximum ACR estimate could be similar to the LGM. Sea ice is a very effective barrier for CO_2 exchange between surface water and the atmosphere, with piston velocities of at least 1 order of magnitude lower (Rutgers van der Loeff et al., 2014). Therefore, shallow samples could be strongly affected by reduced surface exchange with the atmosphere due to

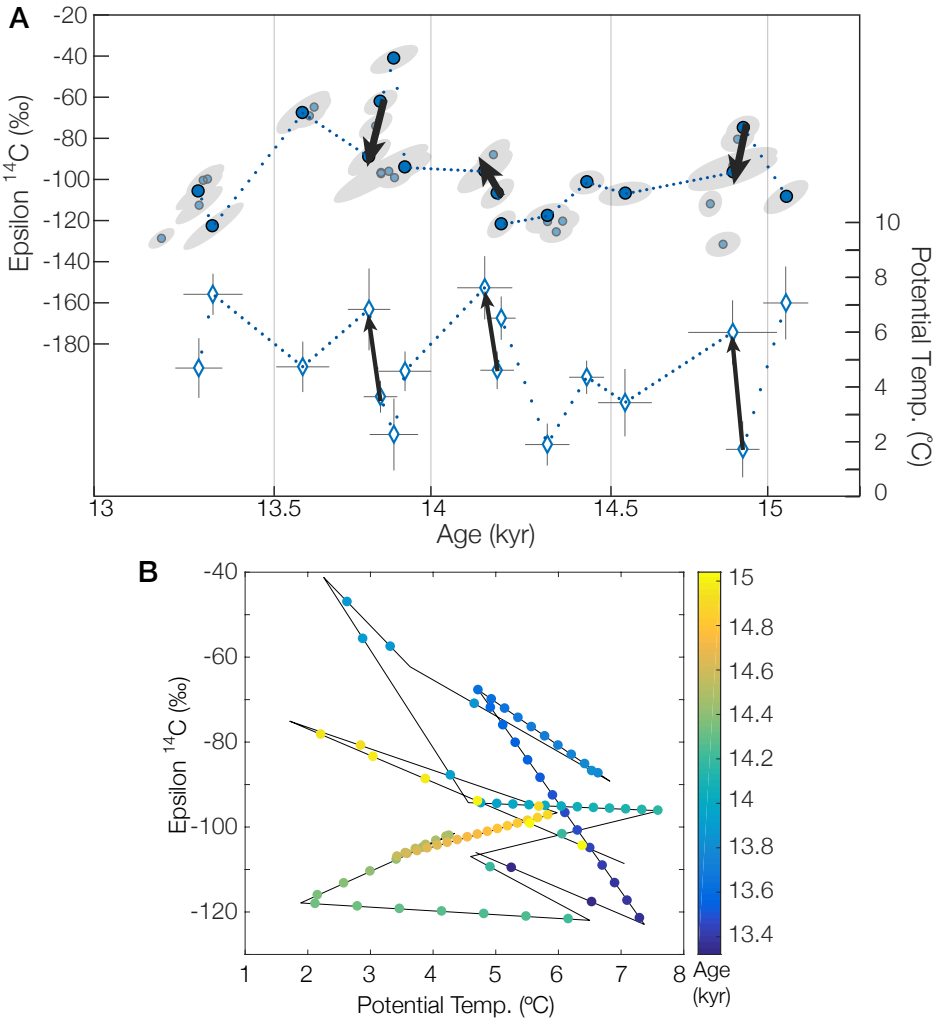

Figure 5.13: Correlation between ϵ^{14}C and potential temperature. A) ϵ^{14}C and potential temperature records with interpolated data. Arrows show the direction of change for top-bottom radiocarbon and temperature data. B) Cross plots of interpolated ϵ^{14}C and potential temperature with black line connecting actual measured data points. Colorbar shows age in kiloyears.

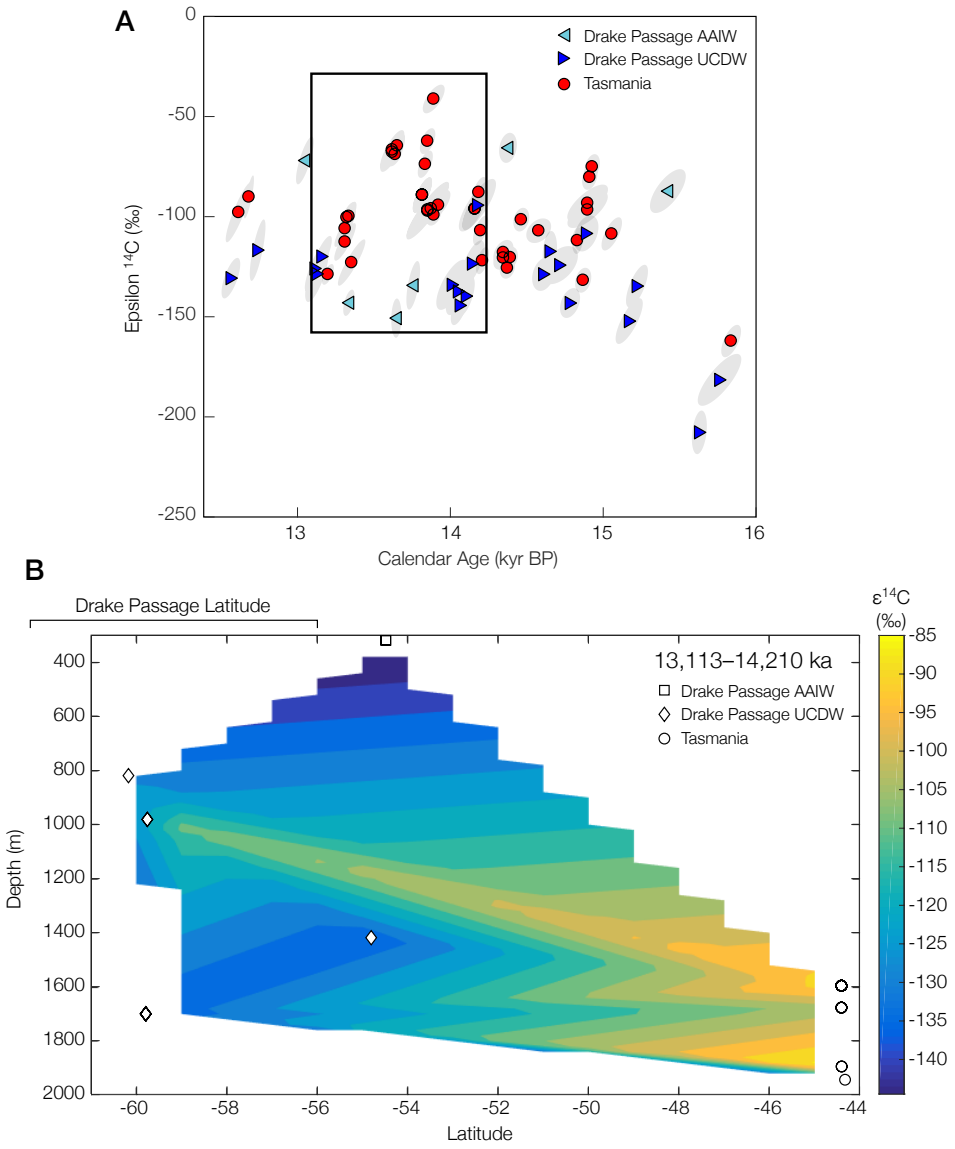

Figure 5.14: Deep-sea coral intermediate water radiocarbon data from the ACR. A) Time series of ϵ^{14}C from south of Tasmania and the Drake Passage (Burke and L F Robinson, 2012; Chen et al., 2015). B) Latitude-depth contour plot of ϵ^{14}C from 14.2–13.1 ka (boxed interval in panel A). Locations of deep-sea coral data marked with open symbols and approximate Drake Passage latitude marked at top.

a sea ice lid, while deeper samples could be more strongly influenced by newly-ventilated northern-source water.

One final complication with this interpretation is that the Tasmanian deep-sea coral samples are in the Indo-Pacific sector, not the Atlantic. While there is some NADW that makes its way directly to the region south of Tasmania (Supplemental Figure 5.15), this water sits deeper in the water column. In the modern ocean, the water mass with the greatest influence at our sample site (~44.5°S, 1600 m) is Pacific Deep Water. This water is characterized by low dissolved oxygen concentrations and depleted radiocarbon, and it likely contributes to the lack of modern deep-sea corals growing at this depth in the modern ocean (Chapter 2, Figure 2.1A). During the ACR, on the other hand, there is a depth excursion and abundance peak in the deep-sea coral population. This indicates that while several pieces of evidence point to a 'figure-eight'-like circulation configuration at the Bølling-Allerød/ACR, there must have been some configurational (or property) differences from the modern ocean.

5.5 Conclusion

Our high-resolution paired radiocarbon and temperature reconstructions from intermediate water deep-sea corals in the North Atlantic and Southern Ocean provide an unprecedented physical view of the glacial ocean. Our data, in combination with other published radiocarbon and temperature datasets from the North Atlantic and Southern Ocean, allow us to constrain changes in ocean circulation across the late part of the last glacial period.

During the early part of MIS 2, there is variability in NADW production in the North Atlantic. Changes in NADW production drive abrupt shifts in basin stratification, which lead to the observed variability in radiocarbon. North Atlantic temperature rises during Heinrich Stadial 3, in agreement with other North Atlantic records and supporting the hypothesis that reduced NADW formation leads to heat accumulation at depth due to downward diffusion from low latitudes. In contrast, during Heinrich Stadial 2 there is a coherent drop in both North Atlantic and Southern Ocean temperature, tracking Northern Hemisphere insolation and signaling a shift into the glacial maximum.

At the LGM there is a 'two-cell' circulation configuration with minimal radiocarbon depletion at intermediate depths and strong depletion around 3500 m in the South Atlantic. North Atlantic temperatures are cold but do not show strong gradients

with depth, indicating that salinity plays a larger role in glacial stratification than temperature. In the intermediate depth Southern Ocean, temperatures are relatively warm during the later part of the LGM and seem to follow local insolation.

During Heinrich Stadial 1, there is a drop in radiocarbon and a rise in temperature at intermediate depth in both the Southern Ocean and North Atlantic, starting at ~17.3 ka, just before the Heinrich Event at 16.8 ka. These trends are likely the result of shut down NADW, which reduces the supply of cold well-ventilated water and deepens basin stratification, pushing southern ocean isopycnals to the south and bringing warmer water to the Southern Ocean intermediate water source region. This North Atlantic intermediate-depth warming before the start of the Bølling primes the water column for catastrophic convection.

Reinvigorated NADW ventilates the North Atlantic down to ~3500 m during the Bølling-Allerød/ACR, indicating a switch from the LGM 'two-cell' circulation configuration to a 'figure-eight' circulation somewhat like the modern. In the Southern Ocean, expanded sea ice reduces exchange with the atmosphere and leads to depleted values near the surface. At depth, intermediate water is more strongly influenced by young NADW. Frontal movement during the ACR and strong tracer gradients within the water column lead to high-frequency variability in Southern Ocean intermediate water radiocarbon and temperature.

References

Adkins, Jess F. (2002). "The Salinity, Temperature, and δ^{18}O of the Glacial Deep Ocean". In: *Science* 298.5599, pp. 1769–1773.

Adkins, Jess F., Edward A. Boyle, et al. (2003). "Stable isotopes in deep-sea corals and a new mechanism for "vital effects"". In: *Geochimica et Cosmochimica Acta* 67.6, pp. 1129–1143.

Adkins, Jess F., Hai Cheng, et al. (1998). "Deep-Sea Coral Evidence for Rapid Change in Ventilation of the Deep North Atlantic 15,400 Years Ago". In: *Science* 280, pp. 725–728.

Adkins, Jess F., Sheila Griffin, et al. (2002). "Radiocarbon Dating of Deep-Sea Corals". In: *Radiocarbon* 44, pp. 567–580.

Adkins, Jess F., Andrew P Ingersoll, and Claudia Pasquero (2005). "Rapid climate change and conditional instability of the glacial deep ocean from the thermobaric effect and geothermal heating". In: *Quaternary Science Reviews* 24, pp. 581–594.

Andersen, Katrine K et al. (2004). "High-resolution record of Northern Hemisphere climate extending into the last interglacial period". In: *Nature* 431.7005, pp. 147–151.

Bard, Edouard (2000). "Hydrological Impact of Heinrich Events in the Subtropical Northeast Atlantic". In: *Science* 289.5483, pp. 1321–1324.

Barker, Stephen, Paula Diz, et al. (2009). "Interhemispheric Atlantic seesaw response during the last deglaciation". In: *Nature* 457.7233, pp. 1097–1102.

Barker, Stephen, Gregor Knorr, et al. (2010). "Extreme deepening of the Atlantic overturning circulation during deglaciation". In: *Nature Geoscience* 3.8, pp. 567–571.

Barnola, J. M. et al. (1987). "Vostok ice core provides 160,000-year record of atmospheric CO2". In: *Nature* 329, pp. 408–414.

Blunier, Thomas and Edward J Brook (2001). "Timing of Millennial-Scale Climate Change in Antarctica and Greenland During the Last Glacial Period". In: *Science* 291.5501, pp. 109–112.

Bond, Gerard C et al. (1993). "Correlations between climate records from North Atlantic sediments and Greenland ice". In: *Nature*.

Broecker, Wallace S. (1998). "Paleocean circulation during the last deglaciation: A bipolar seesaw?" In: *Paleoceanography* 13, pp. 119–121.

Buizert, C et al. (2015). "The WAIS Divide deep ice core WD2014 chronology—Part 1: Methane synchronization (68–31 ka BP) and the gas age-ice age difference". In: *Climate of the Past* 11, pp. 153–173.

Burke, Andrea and L F Robinson (2012). "The Southern Ocean's Role in Carbon Exchange During the Last Deglaciation". In: *Science* 335.6068, pp. 557–561.

Burke, Andrea, Laura F. Robinson, et al. (2010). "Reconnaissance dating: A new radiocarbon method applied to assessing the temporal distribution of Southern Ocean deep-sea corals". In: *Deep-Sea Research Part I-Oceanographic Research Papers* 57.11, pp. 1510–1520.

Burke, Andrea, Andrew L. Stewart, et al. (2015). "The Glacial Mid-Depth Radiocarbon Bulge and Its Implications for the Overturning Circulation". In: *Paleoceanography*.

Bush, Shari L. et al. (2013). "Simple, rapid, and cost effective: a screening method for ^{14}C analysis of small carbonate samples". In: *Radiocarbon* 55, pp. 631–640. DOI: 10.1017/S0033822200057787.

Chappell, J and N. J. Shackleton (1986). "Oxygen isotopes and sea level". In: *Nature* 324, pp. 137–140.

Chen, Tianyu et al. (2015). "Synchronous centennial abrupt events in the ocean and atmosphere during the last deglaciation". In: *Science* 349.6255, pp. 1537–1541.

Cheng, Hai et al. (2000). "U-Th dating of deep-sea corals". In: *Geochimica et Cosmochimica Acta* 64, pp. 2401–2416.

Cronin, T M et al. (2012). "Deep Arctic Ocean warming during the last glacial cycle". In: *Nature* 5, pp. 631–634.

Crowley, Thomas J (1992). "North Atlantic deep water cools the Southern Hemisphere". In: *Paleoceanography* 7, pp. 489–497.

Curry, William B. and Delia W. Oppo (2005). "Glacial water mass geometry and the distribution of δ13C of ΣCO2 in the western Atlantic Ocean". In: *Paleoceanography*.

De Pol-Holz, Ricardo et al. (2010). "No signature of abyssal carbon in intermediate waters off Chile during deglaciation". In: *Nature Geoscience* 3.3, pp. 192–195.

Dennis, Kate J et al. (2011). "Defining an absolute reference frame for 'clumped' isotope studies of CO_2". In: *Geochimica et Cosmochimica Acta* 75.22, pp. 7117–7131.

Dwyer, G S et al. (2000). "Changes in North Atlantic deep-sea temperature during climatic fluctuations of the last 25,000 years based on ostracode Mg/Ca ratios". In: *Geochem Geophysics Geosystems* 1.

Eiler, John M. (2007). ""Clumped-isotope" geochemistry—The study of naturally-occurring, multiply-substituted isotopologues". In: *Earth and Planetary Science Letters* 262.3-4, pp. 309–327.

Eltgroth, Selene F et al. (2006). "A deep-sea coral record of North Atlantic radiocarbon through the Younger Dryas: Evidence for intermediate water/deepwater reorganization". In: *Paleoceanography* 21.4.

Emiliani, Cesare (1955). "Pleistocene Temperatures". In: *The Journal of Geology* 63.6, pp. 538–578.

Ferrari, R et al. (2014). "Antarctic sea ice control on ocean circulation in present and glacial climates". In: *PNAS* 111.24, pp. 8753–8758.

Gagnon, Alexander C et al. (2007). "Sr/Ca and Mg/Ca vital effecgts correlated with skeletal architecture in a sclaractinian deep-sea coral and the role of Rayleigh fractionation". In: *Earth and Planetary Science Letters* 261, pp. 280–295.

Gersonde, R et al. (2005). "Sea-surface temperature and sea ice distribution of the Southern Ocean at the EPILOG Last Glacial Maximum—A circum-Antarctic view based on siliceous microfossil records". In: *Quaternary Science Reviews* 24.7-9, pp. 869–896.

Ghosh, Prosenjit et al. (2006). "^{13}C-^{18}O bonds in carbonate minerals: A new kind of paleothermometer". In: *Geochimica et Cosmochimica Acta* 70.6, pp. 1439–1456.

Hain, Mathis P, Daniel M Sigman, and Gerald H Haug (2014). "Distinct roles of the Southern Ocean and North Atlantic in the deglacial atmospheric radiocarbon decline". In: *Earth and Planetary Science Letters* 394.C, pp. 198–208.

Hemming, S R (2004). "Heinrich Events: Massive late Pleistocene detritus layers of the North Atlantic and their global climate imprint". In: *Review of Geophysics* 42.

Hill, Pamela S, Aradhna K Tripati, and Edwin A Schauble (2014). "Theoretical constraints on the effects of pH, salinity, and temperature on clumped isotope signatures of dissolved inorganic carbon species and precipitating carbonate minerals". In: *Geochimica et Cosmochimica Acta* 125, pp. 610–652.

Hines, Sophia K.V., John R. Southon, and Jess F. Adkins (2015). "A high-resolution record of Southern Ocean intermediate water radiocarbon over the past 30,000 years". In: *Earth and Planetary Science Letters* 432, pp. 46–58. DOI: 10.1016/j.epsl.2015.09.038.

Huntington, K W et al. (2009). "Methods and limitations of 'clumped' CO_2 isotope (Δ_{47}) analysis by gas-source isotope ratio mass spectrometry". In: *Journal of Mass Spectrometry* 44.9, pp. 1318–1329.

Huybers, P and I Eisenman (2006). *Integrated summer insolation calculations*. NOAA/NCDC Paleoclimatology Program Data.

Indermühle, Andreas et al. (2000). "Atmospheric CO_2 concentration from 60 to 20 kyr BP from the Taylor Dome Ice Core, Antarctica". In: *Geophysical Research Letters* 27.5, pp. 735–738.

Keigwin, L D (2004). "Radiocarbon and stable isotope constraints on Last Glacial Maximum and Younger Dryas ventilation in the western North Atlantic". In: *Paleoceanography* 19.

Keigwin, L D and M A Schlegel (2002). "Ocean ventilation and sedimentation since the glacial maximum at 3 km in the western North Atlantic". In: *Geochemistry, Geophysics, Geosystems* 3.6.

Key, RM et al. (2004). "A global ocean carbon climatology: Results from Global Data Analysis Project (GLODAP)". In: *Global Biogeochemical Cycles* 18.4.

Kohfeld, K E and Z Chase (2017). "Temporal evolution of mechanisms controlling ocan carbon uptake during the last glacial cycle". In: *Earth and Planetary Science Letters* 472, pp. 206–215.

Lamy, Frank et al. (2007). "Modulation of the bipolar seesaw in the Southeast Pacific during Termination 1". In: *Earth and Planetary Science Letters* 259.3-4, pp. 400–413.

Lemieux-Dudon, Benedicte et al. (2010). "Consistent dating for Antarctic and Greenland ice cores". In: *Quaternary Science Reviews* 29.1-2, pp. 8–20.

Lippold, Jörg et al. (2009). "Does sedimentary $^{231}Pa/^{230}Th$ from the Bermuda Rise monitor past Atlantic Meridional Overturning Circulation?" In: *Geophysical Research Letters* 36.12, p. 7.

Liu, Z et al. (2009). “Transient Simulation of Last Deglaciation with a New Mechanism for Bolling-Allerod Warming”. In: *Science* 325.5938, pp. 310–314.

Locarnini, R A et al. (2013). *World Ocean Atlas 2013, Volume 1: Temperature*. Ed. by S Levitus and A Mishonov. NOAA Atlas NESDIS 73, p. 40.

Lomitschka, Michael and Augusto Mangini (1999). “Precise Th/U-dating of small and heavily coated samples of deep sea corals”. In: *Earth and Planetary Science Letters* 170.4, pp. 391–401.

Lund, D C, Jess F. Adkins, and R Ferrari (2011). “Abyssal Atlantic circulation during the Last Glacial Maximum: Constraining the ratio between transport and vertical mixing”. In: *Paleoceanography* 26.1.

Marcott, Shaun A, Thomas K Bauska, et al. (2014). “Centennial-scale changes in the global carbon cycle during the last deglaciation”. In: *Nature* 514, pp. 616–619.

Marcott, Shaun A, Peter U Clark, et al. (2011). “Ice-shelf collapse from subsurface warming as a trigger for Heinrich events”. In: *PNAS* 108.33, pp. 13415–13419.

Martin, Pamela A. et al. (2002). “Quaternary deep sea temperature histories derived from benthic foraminiferal Mg/Ca”. In: *Earth and Planetary Science Letters* 198, pp. 193–209.

McManus, J F et al. (2004). “Collapse and rapid resumption of Atlantic meridional circulation linked to deglacial climate changes”. In: *Nature* 428.6985, pp. 834–837.

Miller, M D et al. (2012). “The role of ocean cooling in setting glacial southern source bottom water salinity”. In: *Paleoceanography* 27.3, PA3207.

Mitsuguchi, Takehiro et al. (1996). “Mg/Ca Thermometry in Coral Skeletons”. In: *Science* 274.5289, pp. 961–963.

Monnin, Eric et al. (2001). “Atmospheric CO_2 concentrations over the last glacial termination”. In: *Science* 291.5501, pp. 112–114.

Nürnberg, Dirk, Jelle Bijma, and Christoph Hemleben (1996). “Assessing the reliability of magnesium in foraminiferal calcite as a proxy for water mass temperatures”. In: *Geochimica et Cosmochimica Acta* 60.5, pp. 803–814.

Passey, Benjamin H et al. (2010). “High-temperature environments of human evolution in East Africa based on bond ordering in paleosol carbonates”. In: *Proceedings of the National Academy of Sciences* 107.25, pp. 11245–11249.

Petit, J. R. et al. (1999). “Climate and atmospheric history of the past 420,000 years from the Vostok ice core, Antarctica”. In: *Nature* 399, pp. 429–436.

Rasmussen, Sune O et al. (2014). “A stratigraphic framework for abrupt climatic changes during the Last Glacial period based on three synchronized Greenland ice-core records: refining and extending the INTIMATE event stratigraphy”. In: *Quaternary Science Reviews* 106, pp. 14–28.

Reimer, Paula J., Mike G. L. Baillie, et al. (2009). "IntCal09 and Marine09 radiocarbon age calibration curves, 0–50,000 years cal BP". In: *Radiocarbon* 51.

Reimer, Paula J., Edouard Bard, et al. (2013). "IntCal13 and Marine13 radiocarbon age calibration curves 0–50,000 years cal BP". In: *Radiocarbon* 55.4, pp. 1869–1887.

Roberts, Jenny et al. (2016). "Evolution of South Atlantic density and chemical stratification across the last deglaciation". In: *PNAS*, p. 201511252.

Robinson, Laura F. et al. (2005). "Radiocarbon Variability in the Western North Atlantic During the Last Deglaciation". In: *Science* 310, pp. 1469–1473.

Roche, D M, X Crosta, and H Renssen (2012). "Evaluating Southern Ocean sea-ice for the Last Glacial Maximum and pre-industrial climates: PMIP-2 models and data evidence". In: *Quaternary Science Reviews* 56, pp. 99–106.

Rosenthal, Yair, Edward A Boyle, and Niall Slowey (1997). "Temperature control on the incorporation of magnesium, strontium, fluorine, and cadmium into benthic foraminiferal shells from Little Bahama Bank: Prospects for thermocline paleoceanography". In: *Geochimica et Cosmochimica Acta* 61.17, pp. 3633–3643.

Rutgers van der Loeff, Michiel M et al. (2014). "The influence of sea ice cover on air-sea gas exchange estimated with radon-222 profiles". In: *Journal of Geophysical Research: Oceans* 119.5, pp. 2735–2751.

Saenger, Casey et al. (2012). "Carbonate clumped isotope variability in shallow water corals: Temperature dependence and growth-related vital effects". In: *Geochimica et Cosmochimica Acta* 99.C, pp. 224–242.

Shackleton, N. J. (1967). "Oxygen Isotope Analyses and Pleistocene Temperature Re-assessed". In: *Nature* 215, pp. 1–3.

Shaffer, G, S M Olsen, and C J Bjerrum (2004). "Ocean subsurface warming as a mechanism for coupling Dansgaard-Oeschger climate cycles and ice-rafting events". In: *Geophysical Research Letters*.

Sigman, Daniel M and Edward A. Boyle (2000). "Glacial/interglacial variations in atmospheric carbon dioxide". In: *Nature* 407, pp. 859–869.

Skinner, L C et al. (2010). "Ventilation of the Deep Southern Ocean and Deglacial CO_2 Rise". In: *Science* 328.5982, pp. 1147–1151.

Skinner, L et al. (2015). "Reduced ventilation and enhanced magnitude of the deep Pacific carbon pool during the last glacial period". In: *Earth and Planetary Science Letters* 411.C, pp. 45–52.

Spooner, Peter T et al. (2016). "Clumped isotope composition of cold-water corals: A role for vital effects?" In: *Geochimica et Cosmochemica Acta* 179, pp. 123–141.

Stuiver, M and H A Polach (1977). "Reporting of ^{14}C Data—Discussion". In: *Radiocarbon* 19.3, pp. 355–363.

Stuiver, M, P D Quay, and H G Ostlund (1983). "Abyssal Water Carbon-14 Distribution and the Age of the World Oceans". In: *Science* 219.4586, pp. 849–851.

Su, Zhan, Andrew P. Ingersoll, and Feng He (2016). "On the Abruptness of Bølling-Allerød Warming". In: *Journal of Climate* 29, pp. 4965–4975.

Talley, Lynne (2013). "Closure of the Global Overturning Circulation Through the Indian, Pacific, and Southern Oceans: Schematics and Transports". In: *Oceanography* 26.1, pp. 80–97.

Thiagarajan, Nivedita, Jess F. Adkins, and John Eiler (2011). "Carbonate clumped isotope thermometry of deep-sea corals and implications for vital effects". In: *Geochimica et Cosmochimica Acta* 75.16, pp. 4416–4425.

Thiagarajan, Nivedita, Dana Gerlach, et al. (2013). "Movement of deep-sea coral populations on climatic timescales". In: *Paleoceanography* 28, pp. 227–236.

Thiagarajan, Nivedita, Adam V. Subhas, et al. (2014). "Abrupt pre-Bolling-Allerod warming and circulation changes in the deep ocean". In: *Nature* 511, pp. 75–78.

Thornalley, D J R et al. (2015). "A warm and poorly ventilated deep Arctic Mediterranean during the last glacial period". In: *Science* 349.6249, pp. 706–710.

Tripati, Aradhna K et al. (2015). "Beyond temperature: Clumped isotope signatures in dissolved inorganic carbon species and the influence of solution chemistry on carbonate mineral composition". In: *Geochemica et Cosmochimica Acta* 166, pp. 344–371.

Venn, Alexander A. et al. (2013). "Impact of seawater acidification on pH at the tissue-skeleton interface and calcification in reef corals". In: *PNAS* 110, pp. 1634–1639.

WAIS Divide Project Members (2013). "Onset of deglacial warming in West Antarctica driven by local orbital forcing". In: *Nature* 500, pp. 440–444.

Wang, Y J et al. (2001). "A High-Resolution Absolute-Dated Late Pleistocene Monsoon Record from Hulu Cave, China". In: *Science* 294.5550, pp. 2345–2348.

Wang, Z and EA Schauble (2004). "Equilibrium thermodynamics of multiply substituted isotopologues of molecular gases". In: *Geochimica et Cosmochimica Acta*.

Weldeab, Syee et al. (2016). "Strong middepth warming and weak radiocarbon imprints in the equatorial Atlantic during Heinrich 1 and Younger Dryas". In: *Paleoceanography*, pp. 1–13.

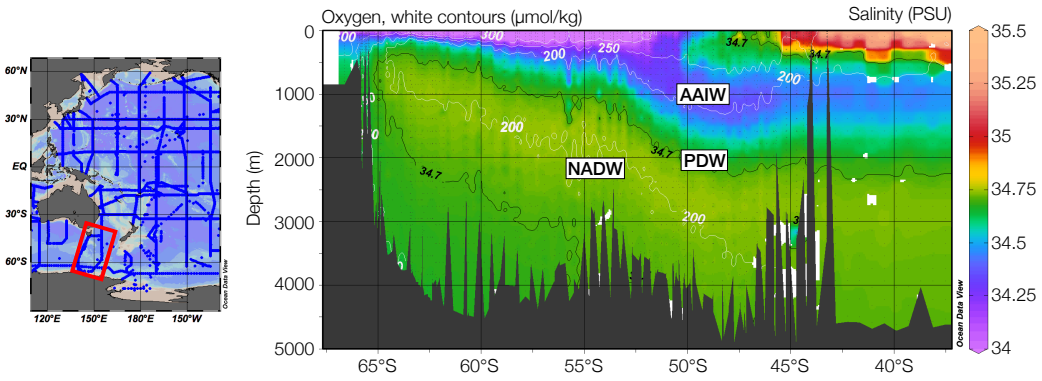

Figure 5.15: Modern salinity section from south of Tasmania with contours of dissolved oxygen. Labels mark the relative position of water masses in the area south of Tasmania. Deep-sea corals sit at ~44.5°S, 1600 m, near the boundary between AAIW and PDW.

Table 5.1: Summary of Southern Ocean and North Atlantic clumped isotope temperature data. All reported Δ_{47} values and temperatures have been corrected with deep-sea coral standard LB-001.

										Corrected with LB-001		
Name	LabID	Depth	Age	err.	ClumpedID	n	Ave. Δ_{47}	1σ SD	1σ SE	Ave. Temp.	1σ SD	1σ SE
TN228-J2-382-1216-1350-03-1523-002	SH_SOI_F01-2	1523	12615	87	SH-A002-S1	5	0.8137	0.0102	0.0046	5.6	1.7	0.8
TN228-J2-387-1226-1148-20-1680-005	SH_SOI_H01	1680	13353	88	SH-A002-S2	9	0.8026	0.0130	0.0043	7.6	2.3	0.8
TN228-J2-387-1226-1148-20-1680-013	SH_SOI_H02	1680	14347	66	SH-A002-S3	6	0.8355	0.0116	0.0047	2.0	1.9	0.8
TN228-J2-387-1226-1635-23-1599-020	SH_SOI_G15-2	1599	13924	78	SH-A002-S4	9	0.8193	0.0129	0.0043	4.7	2.2	0.7
TN228-J2-387-1226-1148-20-1680-017	SH_SOI_H03	1680	14578	80	SH-A002-S5	9	0.8264	0.0222	0.0074	3.5	3.7	1.2
TN228-J2-387-1226-1148-20-1680-003	SH_SOI_B09	1680	14464	52	SH-A002-S6	6	0.8205	0.0090	0.0037	4.5	1.5	0.6
TN228-J2-387-1225-1253-11-1898-002	SH_SOI_K07	1898	13891	72	SH-A003-S1	4	0.8332	0.0161	0.0080	2.4	2.7	1.3
TN228-J2-387-1226-0615-17-1748-009	SH_SOI_C09	1748	15172	62	SH-A003-S2	4	0.8081	0.0150	0.0075	6.6	2.6	1.3
TN228-J2-393-0112-0730-13-1442-003	SH_SOI_J02-2	1442	15056	67	SH-A003-S3	10	0.8050	0.0247	0.0078	7.2	4.3	1.3
TN228-J2-387-1226-1635-23-1599-005	SH_ACR_05-T	1599	14898	132	SH-A003-S4	7	0.8109	0.0183	0.0069	6.1	3.1	1.2
TN228-J2-387-1226-0615-17-1748-014	SH_SOI_K05	1748	15837	65	SH-A003-S5	4	0.8011	0.0054	0.0027	7.8	0.9	0.5
TN228-J2-387-1226-0615-17-1748-020	SH_SOI_K04	1748	16129	71	SH-A003-S6	9	0.8192	0.0163	0.0054	4.7	2.7	0.9
TN228-J2-387-1226-1635-23-1599-005	SH_ACR_05-B	1599	14928	50	SH-A003-S7	5	0.8366	0.0141	0.0063	1.8	2.3	1.0
TN228-J2-387-1226-1635-23-1599-002	SH_ACR_02-T	1599	13817	63	SH-A004-S1	7	0.8062	0.0229	0.0087	7.0	4.0	1.5
TN228-J2-387-1226-1635-23-1599-002	SH_ACR_02-B	1599	13851	50	SH-A004-S2	4	0.8248	0.0071	0.0035	3.8	1.2	0.6
TN228-J2-387-1226-1635-23-1599-003	SH_ACR_03-T	1599	13620	79	SH-A004-S3	6	0.8183	0.0134	0.0055	4.9	2.3	0.9
TN228-J2-387-1226-1635-23-1599-004	SH_ACR_04-T	1599	13311	70	SH-A004-S4	6	0.8186	0.0161	0.0066	4.8	2.7	1.1
TN228-J2-387-1226-1148-20-1680-008	SH_SOI_C02-T	1680	14161	82	SH-A004-S5	7	0.8013	0.0177	0.0067	7.8	3.1	1.2
TN228-J2-387-1225-1253-11-1898-001	SH_SOI_K08	1898	14210	43	SH-A005-S1	5	0.8075	0.0105	0.0047	6.7	1.8	0.8
TN228-J2-387-1226-1148-20-1680-008	SH_SOI_C02-B	1680	14198	50	SH-A005-S2	5	0.8189	0.0092	0.0041	4.7	1.5	0.7
TN228-J2-387-1226-0615-17-1748-015	SH_SOI_K03	1748	16238	76	SH-A006-S1	4	0.8013	0.0119	0.0060	7.8	2.1	1.0
TN228-J2-387-1226-0615-17-1748-014	SH_SOI_H05	1689	16722	64	SH-A006-S2	7	0.8133	0.0275	0.0104	5.8	4.7	1.8
TN228-J2-382-1216-1010-01-1689-004	SH_SOI_H06	1689	17279	109	SH-A006-S3	6	0.8262	0.0183	0.0075	3.6	3.0	1.2
TN228-J2-382-1216-1010-01-1689-009	SH_SOI_H09	1689	17608	164	SH-A006-S4	5	0.8129	0.0159	0.0071	5.8	2.7	1.2
TN228-J2-383-1217-0725-01-1575-006	SH_SOI_A04	1575	18102	65	SH-A006-S5	6	0.8256	0.0180	0.0073	3.7	3.0	1.2
TN228-J2-382-1216-1350-03-1523-007	SH_SOI_F06	1523	18333	38	SH-A006-S6	7	0.8108	0.0196	0.0074	6.2	3.4	1.3
TN228-J2-383-1217-1320-05-1460-008	SH_SOI_E03	1460	19274	57	SH-A006-S7	6	0.8072	0.0176	0.0072	6.8	3.0	1.2
TN228-J2-383-1217-1320-05-1460-009	SH_SOI_E04	1460	19483	61	SH-A006-S8	6	0.8056	0.0223	0.0091	7.1	3.9	1.6

							Corrected with LB-001					
Name	LabID	Depth	Age	err.	ClumpedID	n	Ave. Δ_{47}	Δ_{47} SD	Δ_{47} SE	Ave. Temp.	Temp. SD	Temp. SE
TN228-J2-383-1217-0725-01-1575-023	SH_SOI_G10-2	1575	19457	108	SH-A006-S9	7	0.8064	0.0211	0.0080	6.9	3.7	1.4
TN228-J2-382-1216-1350-03-1523-006	SH_SOI_F05	1523	20367	109	SH-A006-S10	6	0.8117	0.0160	0.0065	6.0	2.7	1.1
TN228-J2-395-0114-0057-09-1500-002	SH_SOI_E06	1500	23338	75	SH-A008-S1	5	0.8205	0.0104	0.0047	4.5	1.8	0.8
TN228-J2-382-1216-1350-03-1523-010	SH_SOI_F08	1523	25324	333	SH-A008-S2	4	0.8100	0.0181	0.0090	6.3	3.1	1.6
TN228-J2-395-0114-0057-09-1500-010	SH_SOI_E12	1500	25198	144	SH-A008-S3	5	0.8142	0.0161	0.0072	5.6	2.7	1.2
TN228-J2-395-0114-0057-09-1500-008	SH_SOI_E10	1500	25526	209	SH-A008-S4	5	0.8089	0.0230	0.0103	6.5	4.0	1.8
TN228-J2-383-1217-0725-01-1575-010	SH_SOI_F13	1575	26980	96	SH-A011-S1	4	0.8090	0.0300	0.0150	6.5	5.2	2.6
ALV-3892-1315-001-009	SH-NAI-G06	1713	15675	379	SH-A008-S6	5	0.8200	0.0170	0.0076	4.6	2.9	1.3
ALV-3892-1315-001-004	SH-NAI-G04	1713	16001	251	SH-A008-S7	6	0.8006	0.0099	0.0041	7.9	1.7	0.7
ALV-3892-1315-001-012	SH-NAI-G08	1713	16343	144	SH-A009-S1	5	0.8170	0.0144	0.0064	5.1	2.4	1.1
RBDASS05-H01_0812-2157-101-003-1751	SH-NAI-G11	1751	17082	228	SH-S009-S2	5	0.8286	0.0122	0.0055	3.1	2.0	0.9
RBDASS05-h09-0823-0349-217-007-1494	SH-NAI-A01	1494	17422	155	SH-A009-S3	5	0.8313	0.0180	0.0081	2.7	3.0	1.3
RBDASS05-H09-0823-0225-216-022-1610	SH-NAI-A09	1610	17595	177	SH-A009-S4	4	0.8046	0.0122	0.0061	7.2	2.1	1.1
RBDASS05-h09-0823-0225-216-006-1610	SH-NAI-A08	1610	23259	93	SH-A009-S5	5	0.8177	0.0148	0.0066	5.0	2.5	1.1
RBDASS05-H06_0819-1631-210_5-013-1640	SH-NAI-C10	1640	23287	208	SH-S009-S6	6	0.8219	0.0218	0.0089	4.3	3.7	1.5
RBDASS05-H06_0819-1631-210_5-009-1640	SH-NAI-C09	1640	23811	149	SH-A009-S7	4	0.8235	0.0141	0.0063	4.0	2.4	1.1
RBDASS05-H09_0823-0349-217-017-1494	SH-NAI-H13	1494	24634	310	SH-A010-S1	6	0.8124	0.0247	0.0101	5.9	4.3	1.7
RBDASS05-H06_0819-1631-210_5-004-1640	SH-NAI-C08	1640	24993	82	SH-A010-S2	8	0.7977	0.0316	0.0112	8.5	5.6	2.0
RBDASS05-H06_0819-1631-210_5-003-1640	SH-NAI-D02	1640	25262	170	SH-A010-S3	5	0.8057	0.0076	0.0034	7.0	1.3	0.6
RBDASS05-H06-0819-1631-210-5-020-1640	SH-NAI-B04	1640	25407	123	SH-A010-S4	5	0.8033	0.0190	0.0085	7.4	3.3	1.5
RBDASS05-H09_0823-0225-216-014-1610	SH-NAI-H06	1610	25577	230	SH-A010-S5	5	0.8022	0.0242	0.0108	7.7	4.2	1.9
RBDASS05-H06_0819-1631-210_5-005-1640	SH-NAI-D03	1640	25592	147	SH-A010-S6	5	0.7997	0.0097	0.0043	8.0	1.7	0.8
RBDASS05-H03-0815-0156-304-005-1583	SH-NAI-A05	1583	26872	139	SH-A011-S2	6	0.8046	0.0098	0.0040	7.2	1.7	0.7
RBDASS05-H03_0814-2151-301-002-1634	SH-NAI-C02	1634	28678	239	SH-A011-S3	4	0.8098	0.0141	0.0071	6.3	2.4	1.2
ALV-3892-1315-001-001	SH-NAI-G03	1713	30025	240	SH-A011-S4	6	0.7763	0.0278	0.0113	12.3	5.0	2.1
RBDASS05-H03_0814-2151-301-008-1634	SHNAI_C06	1634	30848	204	SH-A011-S5	5	0.8169	0.0253	0.0113	5.2	4.2	1.9
TN228-J2-395-0113-0902-01-2193-L003	**MODERN**	2193	0		SH-A008-S5	5	0.8212	0.0203	0.0091	4.4	3.5	1.5

Table 5.2: Summary of North Atlantic U/Th dates including measured uranium and thorium concentration and uranium isotope ratios. Corrected age takes into account initial thorium using an atom ratio of $^{230}Th/^{232}Th = 80\pm80$. $\delta^{234}U_i$ is initial $\delta^{234}U$ corrected using measured age. Both raw and corrected ages are in yr since 1980.

$*$ samples flagged for high ^{232}Th (>2000 ppt). † samples flagged for non-marine $\delta^{234}U_i$ (where marine is defined as 147±7 for samples younger than 17 ka and 141.7±7.8 for samples older than 17 ka by IntCal09). ‡ samples are flagged for both criteria.

Name	Depth	Lab Code	^{238}U	err.	^{232}Th	err.	$\delta^{234}U_m$	err.	$^{230}Th/^{238}U$	err.	Age raw	Age Corr.	Age err.	$\delta^{234}U_i$	err.	Note
			ppb		ppt		‰		Activity		years BP	years BP		‰		
ALV-3891-1646-004-006	1180	UAO04	4707.86	2.24	7974.65	9.93	144.86	0.48	0.1061	0.0001	10534	9751	772	148.93	0.59	*
ALV-3891-1758-006-001	1222	UAM20	3623.19	1.53	20501.71	13.53	145.57	0.42	0.1345	0.0001	13538	10904	2602	150.16	1.19	*
ALV-3892-1315-001-009	1713	SH-NAI-G06	3190.65	2.24	2601.91	14.20	148.23	0.36	0.1580	0.0002	16048	15674	379	154.98	0.41	‡
ALV-3892-1315-001-011	1713	SH-NAI-G07	3115.28	1.60	1662.34	10.17	136.43	0.35	0.3265	0.0002	36650	36405	250	151.24	0.40	†
ALV-3892-1315-001-012	1713	SH-NAI-G08	3532.88	2.22	1100.56	12.46	144.89	0.41	0.1615	0.0001	16486	16342	144	151.77	0.43	
RBDASS05-H03_0814-2151-301-005-1634	1634	SH-NAI-C03	3061.43	2.11	15324.58	18.27	143.46	0.39	0.1908	0.0002	19790	17464	2297	150.74	1.07	*
RBDASS05-H01_0812-2157-101-001-1751	1751	SH-NAI-G09	3480.98	1.35	3480.50	7.73	144.20	0.36	0.1695	0.0001	17384	16923	455	151.29	0.43	*
ALV-3892-1315-001-004	1713	SH-NAI-G04	4285.51	2.39	2359.97	10.77	143.18	0.46	0.1592	0.0001	16254	16000	251	149.83	0.50	*
ALV-3892-1315-001-005	1713	SH-NAI-G05	2874.69	1.30	4061.35	9.16	144.94	0.39	0.1636	0.0001	16712	16061	648	151.70	0.49	*
RBDASS05-H01_0812-2157-101-003-1751	1751	SH-NAI-G11	3217.13	2.06	1573.07	12.84	141.51	0.38	0.1684	0.0002	17306	17081	228	148.53	0.41	
RBDASS05-h09-0823-0349-217-007-1494	1494	SH-NAI-A01	3439.54	1.29	1167.01	7.21	142.95	0.37	0.1710	0.0002	17577	17421	155	150.19	0.39	
RBDASS05-H09-0823-0225-216-022-1610	1610	SH-NAI-A09	3296.51	1.89	1258.02	11.40	141.78	0.38	0.1726	0.0001	17770	17594	177	149.04	0.40	
RBDASS05-H06_0819-1631-210_5-013-1640	1640	SH-NAI-C10	3420.89	1.62	1534.59	9.44	137.70	0.31	0.2217	0.0002	23493	23286	208	147.09	0.35	
ALV-3891-1725-005-B2	1222	UBB10	3799.36	2.24	25935.81	21.87	143.98	0.48	0.1322	0.0001	13306	10115	3230	148.18	1.45	*
ALV-3892-1315-001-001	1713	SH-NAI-G03	4557.57	3.19	2413.31	15.08	129.14	0.40	0.2747	0.0002	30205	29959	249	140.58	0.45	*
RBDASS05-h09-0823-0225-216-006-1610	1610	SH-NAI-A08	3257.45	2.06	625.28	13.48	138.68	0.37	0.2201	0.0002	23281	23193	91	148.10	0.39	
RBDASS05-H06_0819-1631-210_5-009-1640	1640	SH-NAI-C09	3778.91	2.88	1193.85	16.34	137.04	0.37	0.2249	0.0002	23891	23745	148	146.58	0.41	
RBDASS05-H06-0819-1631-210-5-020-1640	1640	SH-NAI-B04	3075.98	3.11	789.02	21.75	136.46	0.40	0.2379	0.0002	25460	25342	124	146.62	0.43	
RBDASS05-H03-0815-0156-304-001-1583	1583	SH-NAI-A04	3986.74	3.38	1022.65	18.15	135.89	0.41	0.2390	0.0002	25602	25484	122	146.06	0.45	
RBDASS05-H06_0819-1631-210_5-005-1640	1640	SH-NAI-D03	3942.96	2.73	1255.32	14.84	134.51	0.38	0.2393	0.0001	25673	25526	148	144.60	0.42	
RBDASS05-H06_0819-1631-210_5-003-1640	1640	SH-NAI-D02	3134.23	3.45	1136.15	23.75	136.35	0.40	0.2371	0.0003	25364	25197	169	146.44	0.44	
RBDASS05-H03_0814-2151-301-001-1634	1634	SH-NAI-C01	3517.14	3.43	3466.57	21.29	133.31	0.46	0.2672	0.0002	29136	28680	450	144.60	0.53	*
RBDASS05-H06_0819-1631-210_5-008-1640	1640	SH-NAI-D01	3731.57	2.76	810.95	15.86	137.27	0.42	0.2365	0.0002	25275	25175	105	147.42	0.46	

Name	Depth	Lab Code	^{238}U	err.	^{232}Th	err.	$\delta^{234}U_m$	err.	^{230}Th/^{238}U	err.	Age raw	Age Corr.	Age err.	$\delta^{234}U_i$	err.	Note
			ppb		ppt		‰		Activity		years BP	years BP		‰		
RBDASS05-H03-0815-0156-304-005-1583	1583	SH-NAI-A05	3341.89	2.70	997.31	17.39	136.99	0.37	0.2503	0.0002	26944	26806	142	147.80	0.41	
RBDASS05-H03_0814-2151-301-002-1634	1634	SH-NAI-C02	4268.57	3.74	2177.72	19.03	131.30	0.39	0.2644	0.0002	28849	28612	238	142.39	0.43	*
RBDASS05-H06_0819-1631-210_5-014-1640	1640	SH-NAI-D09	3383.03	2.77	1432.74	17.64	137.92	0.38	0.2597	0.0002	28072	27876	199	149.26	0.42	
ALV-3891-1758-006-009	1222	UBB05	4699.58	4.53	3148.28	5.91	143.86	0.69	0.1142	0.0001	11390	11081	304	148.47	0.72	*
ALV-3891-1758-006-001	1222	UAM20	3900.26	5.20	5067.26	10.12	144.44	0.62	0.1285	0.0002	12909	12310	581	149.58	0.69	*
ALV-3891-1725-005-006	1222	UAN10	3811.37	3.49	1414.20	4.73	143.60	0.66	0.1340	0.0001	13503	13332	173	149.14	0.69	
ALV-3891-1459-003-018	1176	UAN06	4173.59	10.12	2608.29	14.14	144.80	0.81	0.1446	0.0003	14638	14350	291	150.82	0.85	*
RBDASS05-H03-0815-1004-314-3-001-1427	1427	SH_NAI_G01	3847.84	5.03	1125.50	6.91	142.63	0.63	0.1704	0.0002	17509	17375	136	149.83	0.67	
RBDASS05-H01_0812-2157-101-002-1751	1751	SH_NAI_G10	3071.18	3.33	2138.77	6.05	144.42	0.63	0.1722	0.0002	17678	17357	318	151.71	0.67	*
RBDASS05-H06_0819-1631-210_5-004-1640	1640	SHNAI_C08	3304.66	3.31	568.27	5.16	140.15	0.57	0.2355	0.0002	25073	24993	82	150.43	0.61	
RBDASS05-h09-0823-0349-217-012-1494	1494	SHNAI_A03	3016.48	2.38	595.52	4.03	138.23	0.51	0.2384	0.0002	25479	25388	93	148.54	0.55	
RBDASS05-H06-0819-1631-210-5-012-1640	1640	SHNAI_B02	3368.19	4.28	2803.14	7.57	135.09	0.60	0.2435	0.0002	26178	25793	384	145.33	0.66	*
ALV-3889-1404-004-002	1700	SH_NAI_G02	3593.82	16.00	466070.62	2039.74	137.60	1.61	0.6797	0.0009	96875	11469	94961	142.16	38.41	*
RBDASS05-H03_0814-2151-301-006-1634	1634	SHNAI_C04	3337.66	3.89	1379.80	6.22	134.20	0.61	0.2620	0.0002	28462	28271	190	145.38	0.67	
RBDASS05-H03_0814-2151-301-008-1634	1634	SHNAI_C06	3416.16	3.38	1478.69	5.37	132.52	0.53	0.2822	0.0002	31049	30848	204	144.62	0.59	
ALV-3889-1444-005-004	1649	SHNAI_E01	3038.44	4.78	5698.90	12.17	138.02	0.74	0.3174	0.0003	35391	34526	869	152.19	0.89	3
RBDASS05-H09_0823-0225-216-004-1610	1610	SH-NAI-H01	3300.31	1.54	1951.01	4.28	137.93	0.52	0.2215	0.0001	23466	23193	276	147.30	0.57	
RBDASS05-H09_0823-0349-217-008-1494	1494	SH-NAI-H02	3793.63	2.31	4535.62	6.92	135.05	0.41	0.2271	0.0001	24197	23643	564	144.41	0.50	*
RBDASS05-H09_0823-0225-216-011-1610	1610	SH-NAI-H03	3629.95	2.37	2224.22	6.83	145.56	0.44	0.1707	0.0001	17497	17216	285	152.84	0.48	*
RBDASS05-H09_0823-0225-216-008-1610	1610	SH-NAI-H04	3532.87	1.76	3103.35	5.19	143.96	0.46	0.1665	0.0001	17053	16648	404	150.93	0.52	*
RBDASS05-H09_0823-0225-216-013-1610	1610	SH-NAI-H05	3341.32	2.96	1659.55	9.23	145.01	0.38	0.1659	0.0001	16971	16743	225	152.07	0.41	
RBDASS05-H09_0823-0225-216-014-1610	1610	SH-NAI-H06	4325.81	2.81	2179.11	6.76	133.87	0.38	0.2402	0.0001	25811	25577	230	143.93	0.42	*
RBDASS05-H09_0823-0225-216-016-1610	1610	SH-NAI-H07	3010.93	2.33	2125.37	8.15	152.22	0.38	0.1681	0.0001	17100	16778	326	159.65	0.43	‡
RBDASS05-H09_0823-0225-216-019-1610	1610	SH-NAI-H08	3109.76	2.03	341.23	6.62	143.06	0.43	0.2357	0.0001	25024	24974	54	153.55	0.46	†
RBDASS05-H09_0823-0349-217-010-1494	1494	SH-NAI-H09	3479.38	1.72	1078.55	4.91	144.45	0.45	0.1674	0.0001	17143	17000	143	151.59	0.47	
RBDASS05-H09_0823-0349-217-011-1494	1494	SH-NAI-H10	3503.16	2.01	798.17	5.75	136.60	0.46	0.2226	0.0001	23625	23520	107	146.01	0.49	
RBDASS05-H09_0823-0349-217-014-1494	1494	SH-NAI-H11	2984.83	1.34	1351.94	4.47	136.17	0.46	0.2378	0.0001	25450	25240	212	146.26	0.50	
RBDASS05-H09_0823-0349-217-016-1494	1494	SH-NAI-H12	3234.86	2.08	4447.02	7.39	134.11	0.35	0.2434	0.0001	26192	25555	644	144.19	0.46	*
RBDASS05-H09_0823-0349-217-017-1494	1494	SH-NAI-H13	3528.63	1.78	2332.76	5.19	137.46	0.40	0.2338	0.0001	24939	24634	310	147.40	0.45	*

Table 5.3: Summary of radiocarbon dates used for calculating $\Delta^{14}C$.
$*$ samples flagged for high ^{232}Th (>2000 ppt). † samples flagged for non-marine $\delta^{234}U_i$ (where marine is defined as 147±7 for samples younger than 17 ka and 141.7±7.8 for samples older than 17 ka by IntCal09). ‡ samples are flagged for both criteria.

Name	Lab Code	Depth (m)	Age (yrBP)	Age err.	^{14}C age (^{14}C yr)	^{14}C err.	Note
ALV-3892-1315-001-009	SH-NAI-G06	1713	15675	379	14150	60	‡
ALV-3892-1315-001-012	SH-NAI-G08	1713	16343	144	14790	70	
ALV-3892-1315-001-004	SH-NAI-G04	1713	16001	251	14880	70	$*$
RBDASS05-H01_0812-2157-101-003-1751	SH-NAI-G11	1751	17082	228	15130	70	
RBDASS05-h09-0823-0349-217-007-1494	SH-NAI-A01	1494	17422	155	15300	70	
RBDASS05-H09-0823-0225-216-022-1610	SH-NAI-A09	1610	17595	177	15320	70	
RBDASS05-H06_0819-1631-210_5-013-1640	SH-NAI-C10	1640	23287	208	19910	130	
ALV-3892-1315-001-001	SH-NAI-G03	1713	30025	240	27330	330	$*$
RBDASS05-h09-0823-0225-216-006-1610	SH-NAI-A08	1610	23259	93	20860	150	
RBDASS05-H06_0819-1631-210_5-009-1640	SH-NAI-C09	1640	23811	149	20850	140	
RBDASS05-H06-0819-1631-210-5-020-1640	SH-NAI-B04	1640	25407	123	21500	160	
RBDASS05-H03-0815-0156-304-001-1583	SH-NAI-A04	1583	25549	120	21780	160	
RBDASS05-H06_0819-1631-210_5-005-1640	SH-NAI-D03	1640	25592	147	22350	170	
RBDASS05-H06_0819-1631-210_5-003-1640	SH-NAI-D02	1640	25262	170	22300	180	
RBDASS05-H06_0819-1631-210_5-008-1640	SH-NAI-D01	1640	25241	104	21680	160	
RBDASS05-H03-0815-0156-304-005-1583	SH-NAI-A05	1583	26872	139	24320	230	
RBDASS05-H03_0814-2151-301-002-1634	SH-NAI-C02	1634	28678	239	25370	250	$*$
RBDASS05-H06_0819-1631-210_5-014-1640	SH-NAI-D09	1640	27942	197	24670	230	
ALV-3891-1758-006-009	UBB05	1222	11081	304	10285	40	$*$
ALV-3891-1758-006-001	UAM20	1222	12310	581	11055	40	$*$
ALV-3891-1725-005-006	UAN10	1222	13332	173	12210	45	

Name	Lab Code	Depth (m)	Age (yrBP)	Age err.	^{14}C age (^{14}C yr)	^{14}C err.	Note
ALV-3891-1459-003-018	UAN06	1176	14350	291	12625	50	*
RBDASS05-H06_0819-1631-210_5-004-1640	SH-NAI-C08	1640	24993	82	21800	160	
RBDASS05-h09-0823-0349-217-012-1494	SH-NAI-A03	1494	25388	93	21750	160	
RBDASS05-H03_0814-2151-301-008-1634	SH-NAI-C06	1634	30848	204	27240	320	
RBDASS05-H09_0823-0225-216-004-1610	SH-NAI-H01	1610	23193	276	20870	150	
RBDASS05-H09_0823-0225-216-008-1610	SH-NAI-H04	1610	16648	404	14760	70	*
RBDASS05-H09_0823-0225-216-014-1610	SH-NAI-H06	1610	25577	230	22050	170	*
RBDASS05-H09_0823-0349-217-011-1494	SH-NAI-H10	1494	23520	107	19970	130	
RBDASS05-H09_0823-0349-217-017-1494	SH-NAI-H13	1494	24634	310	22150	170	*
RBDASS05-H03-0815-1004-314-3-001-1427	SH_NAI_G01	1427	17441	136	15010	60	
RBDASS05-H01_0812-2157-101-002-1751	SH_NAI_G10	1751	17423	319	15390	60	*
RBDASS05-H03_0814-2151-301-006-1634	SHNAI_C04	1634	28337	191	23730	160	
RBDASS05-H09_0823-0225-216-011-1610	SH-NAI-H03	1610	17282	286	15010	60	*
RBDASS05-H09_0823-0225-216-013-1610	SH-NAI-H05	1610	16809	226	14985	55	
RBDASS05-H09_0823-0225-216-019-1610	SH-NAI-H08	1610	25040	55	21560	120	†
RBDASS05-H09_0823-0349-217-010-1494	SH-NAI-H09	1494	17066	143	15350	60	
RBDASS05-H09_0823-0349-217-011-1494	SH-NAI-H11	1494	25306	213	22360	140	

Chapter 6

CONCLUSION

In the introduction, we laid out two fundamental questions that this thesis sought to answer: how did the structure of ocean circulation change across the deglaciation, and how did these changes impact global climate? In order to answer these questions, we have taken a two-pronged approach, combining data and theory. Paleoceanographic reconstructions are essential to answering these questions, because they provide direct access to conditions in the past ocean and they can be used to validate models of past ocean states. I believe that a robust understanding of modern ocean physics is also important for interpreting paleoceanographic data, because it sets the parameters for what ocean processes are possible in the past. The difficulty of relying on the modern ocean to inform paleoceanographic reconstructions is that the modern ocean is more or less at steady state, and for many of the time periods that we are most interested in learning about in the past are likely not (the ocean can take thousands of years to reach steady state).

Deep-sea corals have many advantages as paleoceanographic archives—they are large, unbioturbated and U/Th-dateable. However, when it comes to seeing the big-picture ocean changes that happen across the deglaciation, for example, their advantage can become somewhat of a hindrance. Because they are unbioturbated, deep-sea coral records are particularly sensitive to all of the gradients present in the chaotic deglacial ocean. On one hand, they are uniquely capable of revealing the variability that exists, but their records are aliased. Seeing beyond this aliased variability is a necessary challenge. One way to do this is by resisting the urge to interpret every detail of the record. By compiling multiple records, it can be easier to see what the data says about the broader circulation. Using multiple proxies and making cross plots can also aid in visualizing the different endmembers that are influencing water properties in a particular region.

When interpreting paleoceanographic data in the context of large-scale ocean circulation, it is extremely valuable to have models to compare with and make predictions based on. The Ferrari et al. (2014) model has been particularly influential in the paleoceanographic community, as it provides relatively simple mechanisms and predictions for changes in large-scale circulation that have been supported by paleo

data (Curry and Oppo, 2005). However, as our time-dependent box model results highlight, it can be misleading to think about circulation configuration as either figure-eight or two-cell. Our model shows that circulation configuration exists on a continuum, so while it is simpler to draw schematic diagrams that show circulation as either figure-eight or two-cell, the data may support a configuration that has aspects of both.

An interesting result that has shown up in the deep-sea coral reconstructions presented here is the pervasiveness of warm intermediate water during the glacial. At first pass, this contradicts many glacial observations, such as lower high-latitude temperature (as inferred from ice core records) and the dramatic expansion of ice sheets on land. However, if the glacial ocean was salinity stratified instead of temperature stratified, as some evidence suggests (Adkins, 2002), then there would be much more room for intermediate water temperature to vary while still maintaining stable vertical stratification. Intermediate water is volumetrically much smaller than other deep water masses, such as North Atlantic Deep Water, Pacific Deep Water, and Antarctic Bottom Water, so its contribution to carbon cycle changes at the Last Glacial Maximum were relatively minor. Its role as a heat capacitor during glacial times could be significant, however. Intermediate water lies just below the main thermocline, therefore it is the first water mass to receive low-latitude heat that is constantly diffusing downward. There is evidence that warm intermediate water could contribute to the destabilization of ice shelves and initiation of Heinrich Events (Marcott et al., 2011), and it could have triggered the Bølling during the deglaciation (Thiagarajan et al., 2014). As Tzedakis et al. (2017) point out, maybe it is more important to think of glacial cycles as the build-up and release of potential energy in the climate system, and warm intermediate water represents an important potential energy reservoir.

Taking all of our circulation reconstructions together, it appears that ocean circulation retained many aspects of the glacial configuration through at least Heinrich Stadial 1. During the Bølling-Allerød, there is evidence for more vigorous circulation (McManus et al., 2004) and some evidence for deeper penetration of North Atlantic Deep Water (Thiagarajan et al., 2014, see Extended Data Figure 8). However, if the circulation configuration was fully figure-eight during that time, then we would not expect such an abundance of deep-sea corals at a depth characterized by low oxygen in the modern. According to our box model, the two parameters that control figure-eight-ness are the flux and density of North Atlantic Deep Water.

Therefore, it is likely that at least one of these parameters was not yet at its modern value by the start of the Bølling.

Moving forward, the time-dependent model we have explored dynamically in this thesis could also be modified to tackle other questions central to glacial-interglacial climate. It should be fairly straightforward to add more layers to our model for higher vertical resolution, or an atmosphere and simple biogeochemical tracers in order to explore carbon cycle changes, and it is something we plan to do in the future. Although potentially more difficult to implement, it could be possible to break up density into its constituent parameters, temperature and salinity. This would allow us to explore dynamics associated with the build-up of heat in intermediate waters that we observe throughout our records.